VRIJE UNIVERSITEIT

# Spatial organization of the bacterial cell: *in vivo* imaging across scales

ACADEMISCH PROEFSCHRIFT

ter verkrijging van de graad Doctor of Philosophy
aan de Vrije Universiteit Amsterdam,
op gezag van de rector magnificus
prof.dr. V. Subramaniam,
in het openbaar te verdedigen
ten overstaan van de promotiecommissie
van Faculteit der Bètawetenschappen
op dinsdag 29 januari 2019 om 9.45 uur
in de aula van de universiteit,
De Boelelaan 1105

door
Jacopo Solari
geboren te Orbetello, Italie

promotor : prof.dr. T. S. Shimizu

This thesis was reviewed by:

| | |
|---|---|
| prof. dr. E.J.G. Peterman | Vrije Universiteit Amsterdam |
| prof. dr. A. Briegel | Universiteit Leiden |
| prof. dr. L.W. Hamoen | University van Amsterdam |
| prof. dr. S. Jun | UCSD, San Diego |
| dr. R.T. Dame | Universiteit Leiden |
| dr. S. van Teeffelen | Institut Pasteur, Paris |


The research described in this thesis was performed at AMOLF, Science Park 104, 1098 XG Amsterdam, The Netherlands. This work is part of the research programme of the Netherlands Organization for Scientific Research (NWO).

Cover Design: Jacopo Solari
Printed by : Ipskamp Printing, Amsterdam

ISBN 978-94-92323-22-4

A digital copy of this thesis is available online at *www.ub.vu.nl* and *www.amolf.nl*.
Printed copies available on request via library@amolf.nl.

# Table of contents

# Chapter 1

# Introduction

## 1.1 The importance of quantitative *in vivo* approach in biophysical studies

Life is all but easy.
If this statement is generally accurate for most human lives, it is definitely true when attempting to understand the functioning and behavior of living systems. Life is indeed very complicated. Living systems can accomplish incredibly complex tasks at an incredibly wide range of length and time scales. Consider a mammal for example. Its size lies usually on the meter length scale while its vital organs are one order of magnitude smaller. In turn organs like the intestine or the brain are often composed of subunits lying again one lower order of magnitude in size and each organ subunit and tissue is ultimately composed of cells, the building bricks of life, which are six orders of magnitude smaller than the individual itself.

In order to carry out complex vital tasks, all the cells forming multicellular organisms are capable of differentiation, tissues formation, coordination, interaction and communication amongst different cell types, such as to provide the individual with astonishing abilities like moving around in space, growing and reproducing (just to cite some of the most important ones). Nowadays, we are still far from understanding in deep how such interactions emerge and are organized. In fact a comprehensive mechanistic and predictive description of the underlying phenomena at the basis of such complex behaviors is still elusive and sometimes presents mysterious features (e.g. think about self awareness and conscious thought originating from the interplay among billions of neurons in a human brain).

Physicists are used to simplify a problem when it seems too complicated to describe mathematically, by reasoning on what are the essential features and "degrees of freedom" that can explain most of the behavior of a process, still giving major insights on the actual nature

of the system. When modeling a purely physical phenomenon the "higher order corrections" are often identified and neglected. Nevertheless when trying to apply this approach to experimental biology, biophysicists face many difficulties. Following a reductionist approach, e.g. similar to that adopted by solid state or statistical physics where the properties of the macroscopic system are linked by the theory to the features and interactions of single atoms or molecules, it makes sense to start studying life from its fundamental constituents: cells.

It turns out cells are not really mere 'bricks' of life but are on the contrary incredibly complicated out-of-equilibrium entities composed essentially of organic macromolecules, water, metabolites and ions that are also capable of coordinating, interacting and communicating between themselves again on a wide range of length scales (from microns to nanometers, three orders of magnitude). Think of the "simplest" single-celled organisms: bacteria. They are composed of a lipid bilayer membrane (some of them like E. coli have even two and a cellular rigid sugar wall between them) which encloses millions of proteins [1] and the whole genetic information necessary to grow and reproduce. All in just $\simeq 1\mu m^3$ volume. Proteins and genes inside cells can interact in wonderful ways via a dense network of transactions such as to provide bacteria with the ability to move, sense food (chemotaxis), produce energy, grow, measure sub-cellular position, divide via binary fission, replicate and segregate their chromosomes, adapt to different environments, respond to specific stress with specific expression patterns, exchange DNA with other bacteria, acquire resistance to antibiotics,change their phenotype according to the environment, and the list could continue for a while..

Just have a look at the modeled metabolic network in E. Coli shown in Fig.1.1.1 , covering only a very small fraction of all the types of interactions mentioned above.

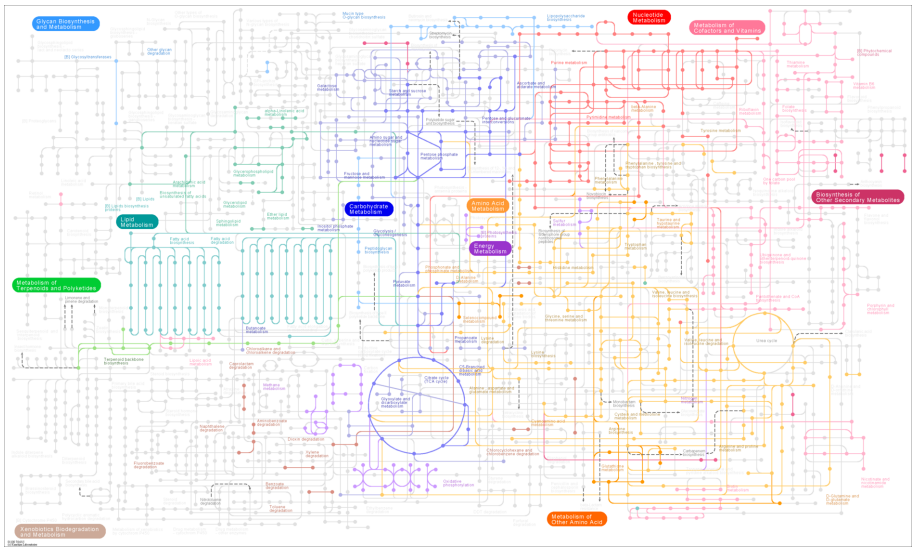

Fig. 1.1.1 Recent model of the metabolic network of E. coli (K12, MG1655) obtained from the KEGG database

Looking at Fig. 1.1.1 it looks like every single cell is already quite a universe on its own!A very different system from solid state physics where mean field theories and nearest neighbor interactions are already enough to beautifully capture and predict the properties of a crystal for instance. In fact, most cellular components have multiple (known) interaction partners and often times multiple functions and 'tasks' as well. The number of different cellular constituents is just too high to attempt a purely reductionist approach, given such a dense interaction network.

In a way this issue is reminiscent of how Newtonian dynamics failed to describe the macroscopic behavior of thermodynamic systems by solving the equation of motion of $10^{23}$ number of particles. Statistical mechanics solved this problem in the most elegant way. Nevertheless, if on one hand statistical mechanics was able to link the microscopic and macroscopic features of thermodynamical systems composed of order of Avogadro's number of particles in thermodynamic equilibrium, life is on the contrary and by definition an out of equilibrium system. Life needs to produce and consume energy to sustain itself. Thus not all the branches of statistical mechanics, which can still give many insights into biological systems, can be employed to describe what is happening inside cells and for sure cannot provide (so far) a precise predictive power not even of single cells behavior.

Of course there is some degree of reductionism that can be employed when studying living cells, for instance by identifying subcellular structure and components and studying them separately. In bacteria one can define the membrane, nucleoid, cytoskeleton, and more in detail identify specific sets of proteins or genes to study separately. Though, differently from solid state physicists, biophysicists working with living systems should always keep in mind that the cell is not the a bare collection of passive components but rather an incredibly complex network of active interactions (look at Fig. 1.1.1 again) and processes that are intrinsically intertwined. Thus the biophysicist should always maintain a holistic approach to the study of life at all scales. Given the complexity of biology, there is a lot of value in studying cells and organisms in vivo, where all the interactions mentioned before are taking place naturally but under controlled conditions.

The modern approach of biophysicists consists in applying models, data collection and analysis methods borrowed from physics to biological data (often from living cells). Many incredibly successful applications of the theories of diffusion, optics, statistical mechanics and electronics (amongst many others) to biological data and experimentation on biological system are found in the literature. Feeding quantitative data into theories coming from classical physics is providing very deep insights on the mechanistic nature of biological processes, insights that are unaccessible when attempting qualitative descriptions. From **in vivo** biophysical studies we know the localization patterns and dynamics of many important

proteins in many different organisms, we know a lot about how DNA is organized, stored and replicated, how cell grow and divide, how they move and so on.

Nevertheless, when studying biological systems *in vivo*, it becomes key to try interpreting results and experimental data acquired on specific cellular components (as is possible only to measure few of the many observables in a cell) at the system level, thinking in holistic terms and being aware that the measured data is always the output of many intricate intracellular transactions with different weights.

## 1.2 Localization and mobility: two fundamental features of proteins in bacteria

Though very complicated, bacteria are amongst the simplest living systems one can study. A lot of scientific work has been carried out since the discovery of microorganisms (which happened between 1665 and ca. 1678 [2]) to an extent that the gram-negative bacterium *E. coli* became with time a model organism for microbiology. Throughout few centuries of research we gained an astonishing control and reproducibility on bacterial growth, physiology and genome editing such that a huge variety of genome engineering tools, molecular biology assays combined with high-tech imaging techniques are nowadays available to researchers approaching the study of bacteria in vivo [3]. With these cutting-edge tools and techniques is possible (just to cite the most relevant for this work) to knock in or out specific genes of interest on the chromosome, introduce expression-controlled plasmids producing protein of interest inside the cell and fuse fluorescent proteins to target proteins to visualize them in living cells using fluorescent microscopy [4].

Thanks to such technical advances it became possible, since a couple of decades ago, to design complex and well controlled experiments where specific proteins or set of proteins species are monitored over time with high spatio-temporal resolution and throughput in living bacteria. In recent years researchers employing such methods reported a huge variety of evidence about the importance of precise sub-cellular localization of specific protein species (see[5–9] and [10] for a general review on the topic of protein localizations in bacteria). Alongside with that, the ability of some other protein species to move by means of passive diffusion in the cytoplasm or on the membrane became clearly essential for many vital cellular processes like protein complexes assembly, cellular division and motility [11–13].

One of the most striking process requiring both precise cellular localization and mobility of proteins, which are the topics at the core of this thesis work, is binary fission (one of the mechanism for bacterial reproduction) where an elongated growing cell bearing at least two

copy of the bacterium's chromosome splits into two daughter-cells of approximately the same length, volume and DNA content [14]. This process is extremely steady, reproducible and under certain growth conditions it can take place as fast as every 20 minutes [15].

In order for binary fission to take place, bacteria like *E. coli* need to gather some kind of positional information about where the middle cell is and then pinch the membrane at that location shrinking it until the mother cell is divided into two. Membrane pinching is accomplished by a protein named FtsZ which polymerizes in ring-shaped bundles precisely at middle cell and contracts to squeeze the membrane and achieve division [16], providing a fundamental example of how protein localization is key for bacteria.

On the other hand the position at which FtsZ polymerizes is dictated by a very peculiar process involving protein mobility. Among other proteins with related functions, the so called "min system" includes a protein (MinD) that is capable of producing spatial oscillations of its concentration on the inner side of the cytoplasmic membrane. These oscillations form on average an inhomogeneous spatial profile as the oscillating proteins spend more time at the poles than at the middle cell. Researchers have found convincing anti-correlation between the minD density along the cell long axis and the position of the division site and FtsZ polymerization [17] which happens where the average concentration of minD is minimum (see Fig 1.2.1).

v

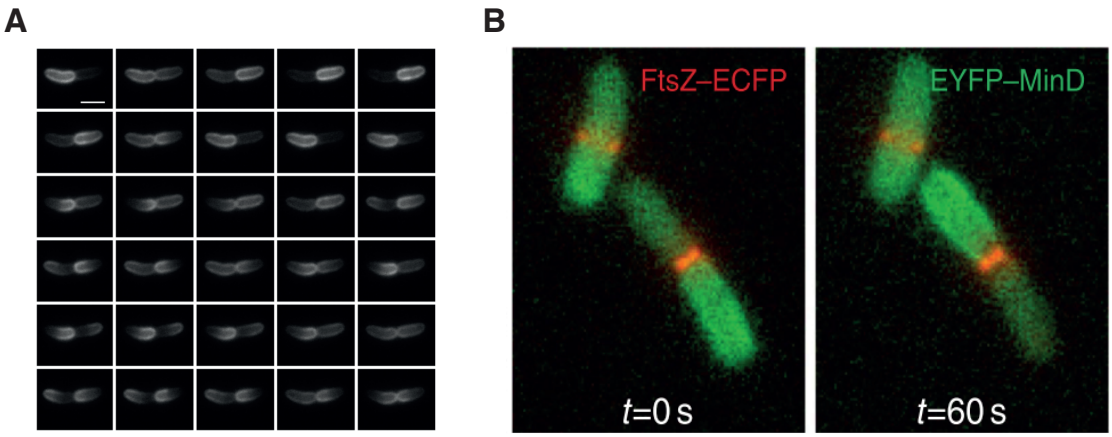


Fig. 1.2.1 **An example of the importance of localization of mobility *in vivo*: minD oscillations determine the position of FtsZ ring formation (A)** MinD::EGFP oscillations. Each frame (from left to right) is acquired every 7s, image adapted from [18] **(B)** Overlay of MinD and FtsZ fluorescence images. Oscillatory movement of MinD drives FtsZ polymerization at mid-cell.

Another relevant cellular process which requires precise protein localization, assembly and mobility is chemotaxis [19]. The chemotaxis network is a relatively simple protein network providing bacteria with the ability of to sense food or repellent gradients and swim in the direction of a favorable environment. For this network to function, a set of mobile signaling cytoplasmic proteins serving as signal carriers and a set of clustered membrane proteins, serving as attractant/repellent concentration sensors, are required. Details about the chemotaxis network can be found later in this chapter. Importantly, many of these proteins have to be placed at specific cellular positions while others need to be able to displace from a cellular region to another for the network to function.

The spatio-temporal organization of the nucleoid also provides plenty of examples showing how specific proteins have to be mobile and/or precisely localized. Obvious examples are repressors and transcription factors which have to be both mobile to find their binding DNA target sequence by diffusion [20] and also to have a high affinity for their specific target and, in the case of repressors, be able to precisely co-localize with a specific gene promoter region. Also a set of so-called Nucleoid Associated Proteins (discussed more in detail later in the book) are know to co-localize with the nucleoid in order to spatially organize it by different binding modes [21], but still exhibiting mobility [22], indicating a binding-unbinding dynamics on the nucleoid.

Finally we mention the protein MreB as an example of spatial organization and mobility of proteins. This protein can polymerize on the inner membrane in different patterns and it's activity is related to building new cell wall material as the cell is growing [23]. Experimental evidences in the literature show that its mobility on the membrane, which is associated with energy consumption, could in turn influence the mobility of other proteins that are not associated with ATP burning [24]. We could go on with many other examples where both localization and mobility are key to bacterial homeostasis but in this work we will focus on chemotaxis proteins and proteins involved in nucleoid spatial organization.

## 1.3 Spatial organization of membrane receptor proteins is key to bacterial chemotaxis

Motile bacteria are usually equipped with molecular machineries that provide them with the ability to move towards more favorable environments, where attractants concentrations are higher. This process goes under the name of chemotaxis. Micro-organisms can sense food gradients and escape from higher repellents concentrations. Many bacteria like *E. coli, Salmonella, R. sphaeroides, Pseudomonas* and *Vibrio* have a dedicated set of proteins

forming a biochemical network of molecular interactions and signal feedbacks which goes under the name of chemotaxis network [25].

In *E. coli* the input of such network is an extracellular change in concentration of either attractants or repellents while the response integrates to a bias in the rotation of flagella which influences the frequency at which the bacterium changes direction of swimming. This bias, in the framework of the so called 'run-and-tumble' motility [26], is sufficient to make bacteria climb up food gradients and run down repellent gradients [27].

Thus chemotaxis defines the ability of an organism to move in response to a chemical stimulus by biasing its swimming in the direction parallel to the concentration gradient of food or antiparallel to the concentration gradient of repellents. More in detail, the chemotaxis signaling network modulates cell swimming by regulating the switch between the counter-clock wise (CCW) and clock-wise (CW) rotation biases of the flagella. CW rotation makes flagella bundle together thus producing a directed propulsion that results in a straight swimming 'run' state. On the other hand when flagella spin CCW the flagellar bundle falls apart and the cell randomly reorient its body during the so-called 'tumble' state. After tumbling, the bacterium initiate a new 'run' following a 'run-and-tumble' dynamics which at large times can be considered as a random walk. This random walk becomes biased in the presence of a gradient of attractant or repellent.

From a biochemical point of view, transmembrane chemoreceptors sense changes in the concentration of chemical attractants in the periplasm and control the activity of the cytoplasmic receptor-associated kinase CheA, which in turn regulates motor rotation. When phosphorylated, CheA transfers the phosphoryl group to the response regulator CheY, which then induces cell tumbling by binding to the switch complex and changing the direction of motor rotation from CCW to CW. Other proteins are involved in the chemotaxis signaling network. The receptors-associated CheA and CheW, the signal terminator CheZ and the adaptors proteins CheR and CheB. CheR and CheB constitute the adaptation system that is used to restore sensitivity of the system in the presence of sustained attractant stimulation thus enabling measurement of changes in attractant concentrations, rather than absolute levels. This adaptation is mediated through the methylation of receptors on five of their glutamate residues which influences CheA activity in different ways for different methylation states. A sketch of the chemotaxis biochemical network is given in Fig. 1.3.1.

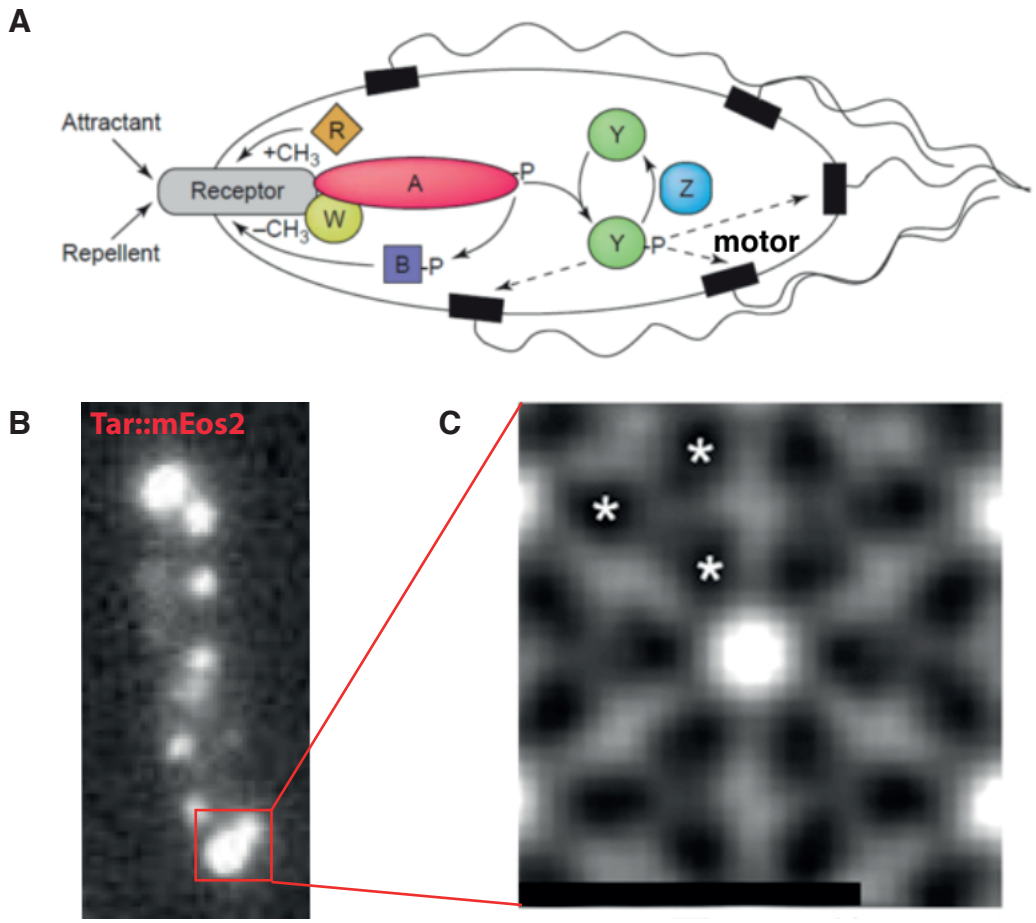


Fig. 1.3.1 **(A) Chemotaxis network and clustering of chemoreceptors.** Ligand molecules are bound by transmembrane receptors (gray) and the chemotactic signal is transmitted to the CheA kinase that gets subsequently phosphorylated and becomes active. CheR and CheB (orange and purple) constantly methylate/demethylate the receptors providing sensory adaptation. The activated CheA reach the motors (black) at the base of the flagella and transmit the chemotactic signal to the flagella. CheZ (cyan) is responsible for dephosphorylation of active CheA. **(B)** Fluorescence image of labeled Tar receptors in live E. coli.**(C)** Average of EM sub-tomograms of clustered receptors showing the hexagonal arrangement of single trimers of dimers. Asterisks indicate position of single receptor dimers. Scale bar 12nm. Image adapted from [28].

Chemoreceptors are known to assemble into clusters of various size forming a crowded environment [5, 29] on the cytoplasmic membrane (see Fig. 1.3.1B and C). Clusters are composed of trimers of dimers forming an hexagonal array as shown in Fig. 1.3.1C. Many independent researchers have shown that receptor clustering is functional for signal sensing, namely providing amplification of the signal by receptor cooperativity [30] allowing bacteria to sense extremely small concentration change. If much is known about the steady-state

function of receptor clusters, not many investigations have been carried out on their dynamics and stability under different ligand stimulation condition. Some results from literature actually draw contrasting conclusion about chemoreceptor cluster stability upon ligand binding ([31–36]).

First, chemical cross linking experiments suggest that receptors tend to form less dense clusters upon attractant binding while repellent binding tends to stabilize the clusters of *E.coli* cells [32], [33]. Yet another study (also using electron cryo-tomography) reported no change in the hexagonal packing, either upon stimulation or under different growth conditions [34]. Studies which employed optical diffraction-limited imaging have also reported conflicting results. On one hand, using immuno-fluorescence labeling, a number of studies have reported a nearly complete disruption of polar clusters in fixed E.coli and B.subtilis cells. In these works, strong increases in the fraction of cells exhibiting lateral clusters or diffuse localization patterns was observed upon stimulation with attractant, and the localization was restored after adaptation [31, 35]. In one of these studies, stimulus-dependent redistribution of receptors between clusters was observed not only with immuno-fluorescence, but also with receptors directly fused to the green fluorescent protein in live (unfixed) B. subtilis cells [35]. On the other hand, in a study that monitored receptor clusters via fluorescent fusions of CheZ, which tends to localize at the receptor complexes, no change in localization upon attractant stimulation was apparent in live E.coli cells [36].

In this thesis work we present the results of our attempt to clarify this controversy, using a combined approach of super resolution imaging in fixed cells (similar to [5]) and live-cell single-particle tracking to estimate cluster size and mobility before and after introducing a saturating ligand stimulation.

## 1.4 Macromolecular crowding in biological systems

Macromolecular crowding is a physico-chemical phenomenon causing attraction of macromolecules in solution at high concentration of total solute, mainly due to excluded volume interactions. The non-specific repulsion originating from the impenetrability of macromolecules in crowded environments, can generate purely entropic depletion forces [37] as the volume available for each single macromolecule to occupy is limited by the presence of the others. For example, if two large molecules in a crowded medium are found in close spatial proximity (e.g. due to thermal motion), they will exclude smaller crowders from the space in correspondence of their minimal distance point and feel a depletion attractive force as illustrated in Fig. 1.4.1. This phenomenon will create a depletion layer around each macromolecule and they will feel an attractive force every time their depletion layers (whose

size will depend on the size of the other crowders in solution) will overlap. Nevertheless we should keep in mind that this particular case does not cover all the possible scenarios and all the effects that can arise in macromolecular crowded environments: the magnitude, the nature and the implications of excluded volume effects can indeed strongly depend on the size distribution of the macromolecules in solution [38].

Inside living cells, about 20-30% of the cytoplasm is occupied by biological macromolecules like proteins or RNA [39] and thus excluded volume effects can be ubiquitous. The cytoplasm is indeed a very crowded environment as illustrated in Fig. 1.4.1A showing a data-driven artist impression of a cellular inside.

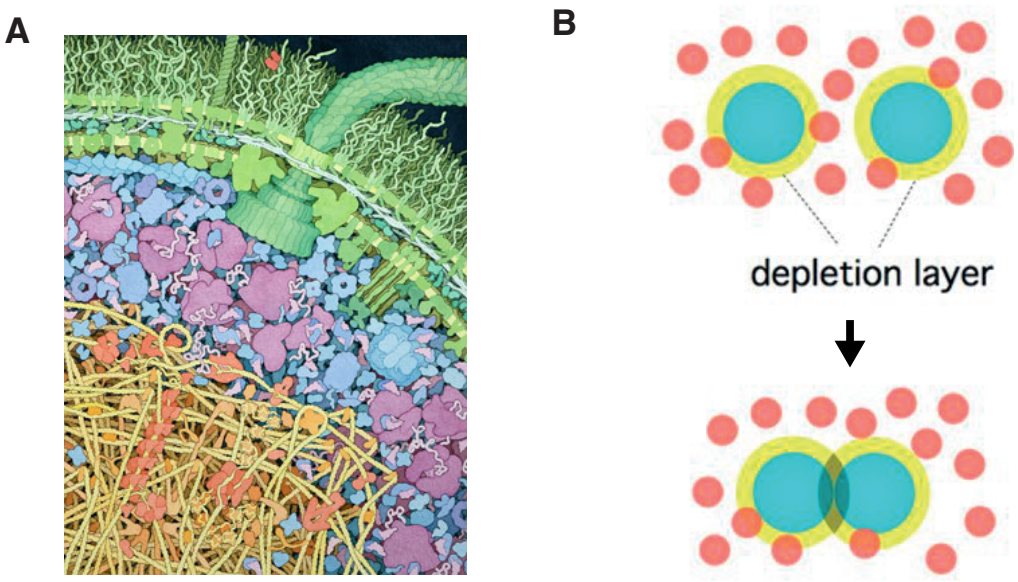


Fig. 1.4.1 **Intracellular crowding generates depletion forces due to excluded volume.** **(A)** Data-driven artist impression of bacterial cytoplasm giving an illustrating the high degree of crowding inside the cytoplasm of living cells (image courtesy of Goodsell lab.) **(B)** Illustration of depletion attraction due to excluded volume. Red smaller circles represent crowders while bigger cyan circles represent larger particles in solution. when crowders are excluded from the volume in between the larger particles, i.e. their depletion layers overlap, the larger particles feel an effective attractive force.

The constituents of the cytoplasm come in a very wide range of different sizes and thus effects of crowding can be very diverse on different protein species for example. As a consequence of macromolecular crowding, cytoplasmic diffusivity decreases with protein size and crowding levels [40, 41]. In addition, the cytoplasm (in which water is the most abundant component) contains many charged or polar molecular species and excluded volume effects can influence the rate of reactions depending on electrostatic, Van Der Waals or hydrophobic interactions

[42]. Importantly, crowding and excluded volume effects has also been shown to influence the size of bacterial chromosomes inside artificial crowders solutions [43] also in the absence of the native Nucleoid Associated Proteins [44]: a higher crowding level leads to a more compact configuration of isolated chromosomes and this effect is thought to be important for nucleoid spatial organization inside living cells too [45].

Crowding effects seems to be relevant also in cellular membranes, it is indeed estimated that membrane proteins occupy 30-50% of the total membrane area [46]. Simulations on membrane diffusivity also show a decrease in diffusion coefficients of both lipids and protein with increased membrane crowding [47] and results from theory showed that crowding can affect the gating energies of mechanosensitive channels [48]. Experiments employing Fluorescence Correlation Spectroscopy (FCS), Fluorescence Recovery After Photobleaching (FRAP) and Single-Particle Tracking (SPT) also point in the same direction (see [49] for a review on the topic).

Since excluded volume influences diffusion of proteins both on the membrane and in the cytoplasm, crowding is likely to be involved in protein localization, mobility and clustering, thus affecting the processes described in the previous section of this chapter. Importantly for the cell, crowding has been shown to (differently) affect a variety of reaction rates in the cytoplasm both *in silico* [50] and *in vitro* [51]. Thus, vital functions like transport, enzymatic reactions, protein association, transcription, DNA replication protein polymerization and protein folding must cope with or exploit the high crowding levels in both the cytoplasm and the membrane. In this context, a recent review on the topic introduced the concept of crowding homeostasis highlighting the importance of crowding inside living systems and proposing the idea of crowding being actively maintained at certain levels throughout the life of a cell [52]. Despite crowding is raising increasing research interest, whether cells use it in their favor, what is its interplay with active processes and in general how important it is for the life of a cell is still subject of intense discussion and research. This is also due to the fact that testing the effect of crowding perturbations *in vivo* is experimentally challenging [53]. In fact, until recently [54] it was not possible to precisely quantify crowding levels in living cells. Also, introducing controlled perturbations to crowding without perturbing physiology or triggering unwanted cellular responses is not trivial due to the sensitivity of bacteria to external perturbations and to their variety of adaptation mechanisms.

## 1.5 Bacterial nucleoids are not random polymers and live in the crowded cytoplasm

Looking at bacterial chromosomes under electron or optical microscopes, gives the impression that they consist of a completely disorganized random polymer thrown into the cell's cytoplasm [55]. By looking at electron micro-graphs, the contrast with eukaryotic DNA is pretty striking (see Fig 1.5.1A) : as bacteria do not have histones, they don't undergo mytosis and they lack a nuclear envelope enclosing their genetic material, the nucleoid at first glance looks like a completely random polymer blob. For this reasons the bacterial chromosome was historically named 'nucleoid' as to clearly state the difference with the eukaryotic nuclear organization.

By contrast, in recent years the nucleoid has been proven to possess a very fascinating and high degree of spatio-temporal organization, which is plausible given the wide variety of processes it has to carry out throughout the cell cycle. Such organization seems to be mediated by a set of DNA-binding proteins like Nucleoid Associated Proteins (NAPs, proteins like H-NS, Fis and HU have been shown to be capable of drastically influencing DNA folding both in vitro and in vivo [56–61]), Structural Maintenance of Chromosome proteins (SMCs) [62–64] but also by the passive action of intracellular crowding [43, 65, 66] acting via depletion forces resulting from purely entropic effects. Recent estimates report indeed a concentration of $\sim 3^{*}10^{6} proteins/\mu m^{3}$ for the cytoplasm [67].

The volume of a typical bacterial cell is very small ($\sim 1\mu m^{3}$) and the nucleoid, which is one thousand times longer than the cell long axis when unraveled ( 1mm as opposed to 1um), has to fold approximately one thousand times to fit in the cellular volume reaching a very high degree of compaction already in the absence of crowding. Nevertheless, we know from polymer physics that a flexible polymer in a neutral solution and confined in a space much smaller than its radius of gyration would tend to occupy all the space available since that would be the most entropically favorable state [68]. Though, bacterial nucleoids do not fill the entire cellular space but only a fraction of it and this fraction is dependent on growth conditions (Fig. 1.5.1 C). Given the variety of (in vitro) experimental ad theoretical results on crowding cited earlier in this chapter, it is thought that intracellular crowding plays an important role in compacting the nucleoid to a size smaller than the cellular volume. Some recent experiments on isolated nucleoids from lysed living cells showed indeed that the chromosomes are somewhat similar to loaded spring: if the membrane of living E. coli is digested, the nucleoid undergoes a sudden, rapid and reproducible expansion [43], the main compressing force probably being crowding.

In addition, results in literature suggests that also active processes like RNAP activity contribute in shaping nucleoid morphology *in vivo* [69]. Consistently, when the metabolism of the cell is shut down, for instance by exposing cells to dinitrophenol (DNP), the nucleoid undergoes an expansion phase until it fills almost the whole cellular volume [70]. Thus, nucleoid compaction is likely to originate from the interplay of passive and active mechanisms but testing and studying the effect of crowding and active processes on nucleoid morphology inside living cells has remained experimentally challenging.

In this thesis work we present the results of our experimentations on the nucleoid organization under controlled crowding perturbations induced by osmotic shock *in vivo* (Chapter 5) in the physiologically relevant experimental framework provided by the mother machine PDMS device (described later in this chapter). This part of the work was aimed at clarifying the role of crowding in organizing the nucleoid in living cells and its relation to active cellular processes.

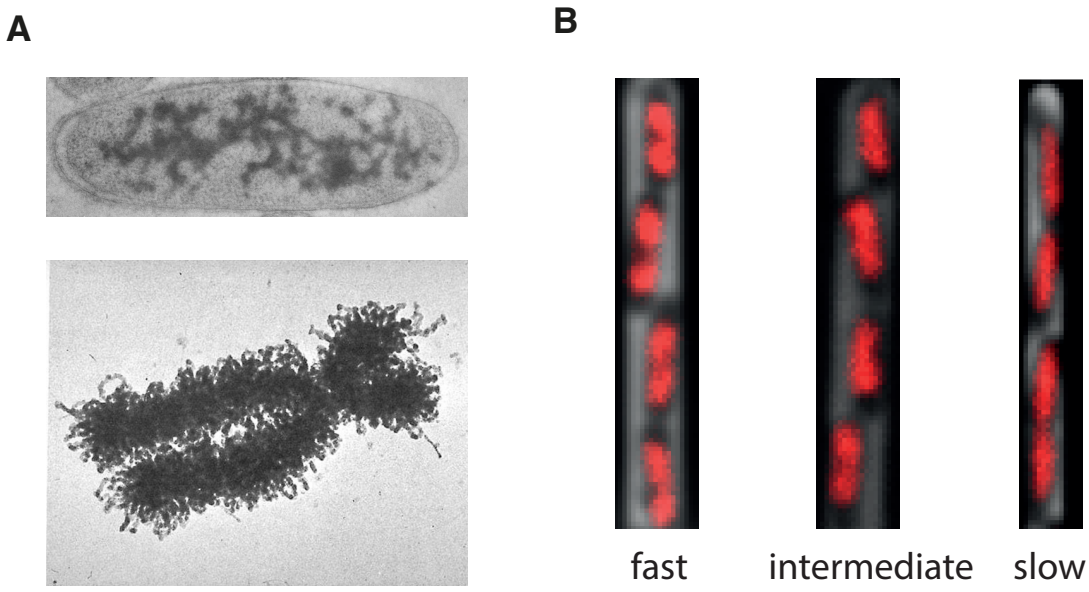


Fig. 1.5.1 **Bacterial nucleoid arrangement in the cell. A.** comparison between electron micrographs of a bacterial nucleoid ([71], upper panel) and a mitotic human chromosome (DuPraw1968, lower panel). **B.** Live E. coli nucleoids labeled with HU::mCherry under different growth rate conditions showing distinct nucleoid morphologies.

## 1.6 Single molecule fluorescence imaging approach allow for studying protein organization, mobility and interactions

Recent technical advances in fluorescence microscopy and fluorescent protein engineering have opened the way for a wide range of new experimental possibilities both in live and fixed cells [72, 73]. In particular super resolution techniques have overcome the resolution limitations of wide-field fluorescence imaging due to diffraction limit which restricts the maximum resolution that can be achieved with an optical imaging system to half the wavelength of the emitted light. This hard physical limit states that any emitter object smaller than half the wavelength of the emitted light, would appear when imaged under an optical microscope as a bell shaped function called Point Spread Function (PSF, Fig 1.6.1A). The width of the PSF is about half of the wavelength of the emitted light. With the advent of Super Resolution (SR) techniques like PALM, STORM and STED ([74–76]) it became possible to image sub-cellular structures with ten times higher resolution and resolve spatial patterns that would otherwise result in a blurred image when employing diffraction limited imaging techniques. Super resolution though, come usually at the cost of fixing cells and thus give up on measuring dynamics of the cellular process under study in real time.

Both PALM and STORM rely on the ability to image single fluorescent molecules and estimate their position by fitting their PSF with a bell-shaped two dimensional function, usually a Gaussian. With the high sensitivity of modern detectors it is now pretty standard to image single fluorescent proteins in living and fixed cells. Another requirement for both PALM and STORM is to image single molecules in a well-separated fashion, avoiding PSF overlap in order to unambiguously estimate the position of individual emitters.

Producing a well-separated spatial profile of individual emitters became much easier with the introduction of photo-activatable (or photo-switchable) fluorophores which are special fluorescent protein that can be pushed from a dark state to an emitting one by UV light irradiation. Before the advent of such fluorophores, producing a sparse emitter spatial profile was challenging in living cells for most of the times the protein of interest comes in large copy number in the cell and the PSFs of individual labeled proteins tend to overlap rendering the single molecule position estimation hard if not impossible. The use of photo-activatable fluorophores [77] in biophysical experiments allows for stochastically activating the emission state of a subset of the total fluorophore population in the cell, by shining UV light on the sample. By tuning the intensity of UV irradiation is possible to acquire time lapse images having only few well-separated PSFs produced by stochastically photo-activated fluorophores

in the sample. Such images (see Fig 1.6.1B) are suitable for estimation of emitters' position at nanometer precision via 2D Gaussian fitting.

PALM and STORM imaging protocols consist of an image acquisition part, a data processing and an image reconstruction part. In the image acquisition phase, many (on the order of thousands) subsequent image frames with few well-separated emitting fluorophores each are recorded. In the data processing and image reconstruction part each such single frame is analysed and the PSFs of all the fluorophores in the frame are fitted to estimate the emitters' positions with higher spatial precision. The localization precision will depend on the number of collected photons for each single PSF and neglecting higher order corrections can be estimated as $\Delta \sim \frac{\sigma}{\sqrt{N}}$ where N is the number of collected photons [78]. After each data frame has been processed this way, localizations are filtered for duplicates, multiple localization of the same emitter and sample drift [79] and eventually a single super-resolved image is produced by showing all the localizations coming from each data frame at the same time (see Fig. 1.6.1B).

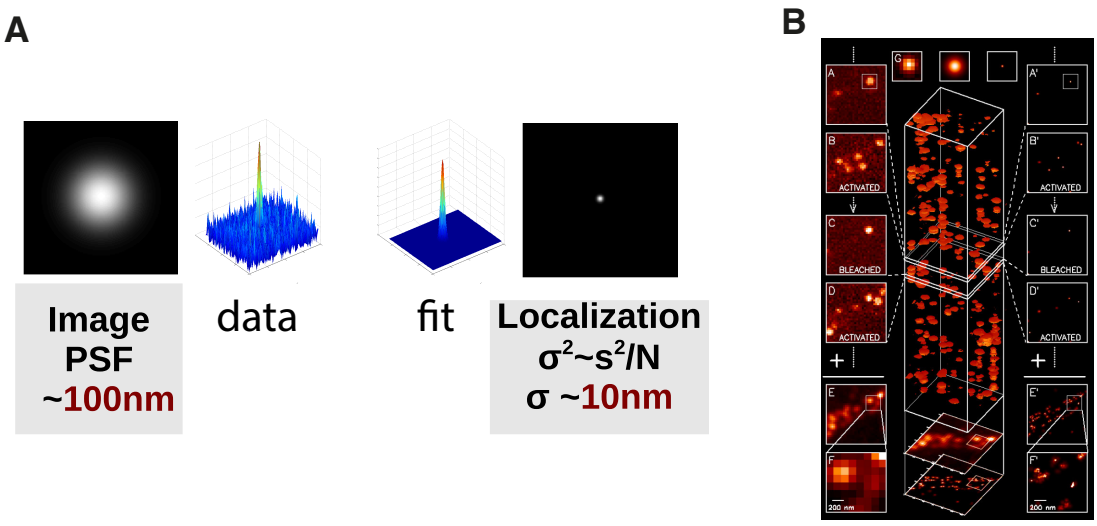


Fig. 1.6.1 **PALM analysis protocol** **(A)** Representative image of a Point Spread Function and successive fitting procedure. After fitting the PSF with a 2D Gaussian distribution the emitter is localized with an average precision of 10nm. **(B)** After collecting multiple frames with well-separated emitters each PSF in each frame is fitted to localize the emitter with high precision. Subsequently all the super-resolved frames are superimposed to reconstruct the full SR image (image adapted from [74]).

PALM can also be employed for experiments *in vivo* [80, 81]. The main limitation of using PALM in living systems is that most of the labeled proteins inside cells are highly mobile and they can diffuse over large distances in the time required to complete PALM imaging. Thus, the final super-resolved image will be blurred by protein motion. On the other

hand such limitation can be turned into an advantage: by activating the emission of single labeled-proteins one can then perform single-molecule tracking on even very dense spatial profiles of labeled proteins [82, 83] to study their mobility (PALM-tracking). Nevertheless, since PALM tracks come from single fluorophores, they are limited by bleaching and if a decent localization precision is desired the excitation power has to be relatively high thus producing on average short (<10 frames) tracks.

To overcome the limitations of PALM-tracking we developed a hybrid single-particle tracking (SPT) technique that allows for reliable tracking of clustered proteins in crowded environments while achieving a much longer (up to a factor of 10) tracklength when compared to usual PALM tracking. Instead of using a wide-field 405nm activation profile, we focus the activation light into a diffraction limited spot and deliver a short (<10ms) focused 405nm pulse onto immobilized bacteria. When clustered proteins, like membrane chemoreceptors, are labeled with photo-switchable fluorophores multiple fluorophores belonging to the same clusters will become active after a localized activation pulse. Their bleaching behavior will not follow a single exponential curve and tracklength distributions will exhibit much longer tails as compared to those produced by PALM tracking. See Chapter 2 for a more detailed description of the technique.

## 1.7 Mother machine allows for nucleoid imaging in E. coli under physiological growth

When studying nucleoid organization in live bacteria, great care has to be taken in order to minimize perturbations to physiology. This is mainly because nucleoid morphology can vary a lot depending on growth conditions, stress and changes in the environment [71, 84, 70] or also in response to perturbations to other cellular processes or proteins [85, 86]. In general, cellular physiology can be strongly perturbed by standard experimental protocols for microscopy, that often expose bacteria to abrupt changes in buffer solutions, temperature and osmotic pressure (among others) during cell harvesting, sample preparation and imaging. Thus an ideal tool for experimental studies on nucleoid spatio-temporal organization would be a device allowing imaging experiments under well defined and steady physiological conditions, to minimize external perturbations that could trigger uncontrolled cellular and nucleoid responses. In many cases, it is indeed desirable to perform imaging on bacteria undergoing a precise growth phase. In fact nucleoid morphology, together with cell size and metabolic activity, can also drastically change throughout the different phases of bacterial growth [87, 88, 86].

Bacterial growth of an initial population in a finite volume of growth medium follows 4 different phases: the lag phase (where no growth is observed), the exponential phase, the stationary phase (when nutrients start to be scarce and growth is arrested) and finally the death phase. The standard growth phase at which cells are harvested from (liquid) cultures in most bacterial studies, is exponential growth. During exponential phase cells are healthy and growing at the maximum rate for that given growth condition. In practice it is quite difficult to achieve steady growth and keep cells in a precise growth phase while at the same time having them immobilized on a glass surface for carrying out microscopy on the nucleoid. Some techniques like agar or poly-acrylamide pads [89, 90] are capable of providing steady exponential growth and immobilization of cells but at a cost: medium exchange (for instance if a step-like perturbation mediated by a certain chemical needs to be introduced in the system) is pretty slow, challenging and inefficient.

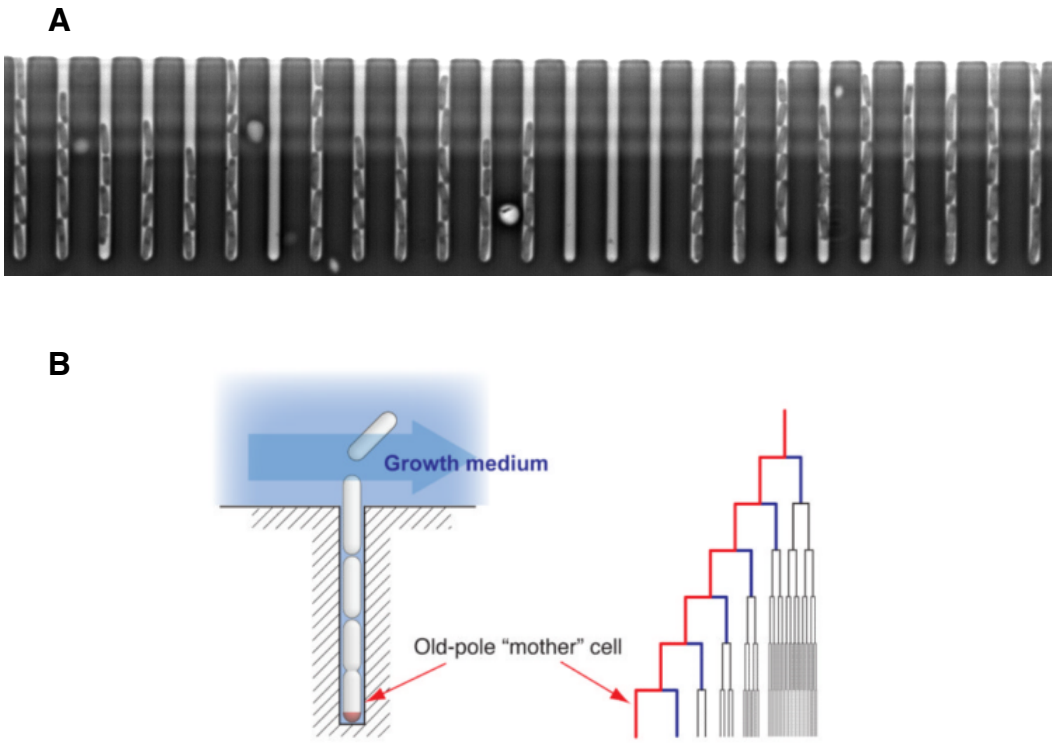


Fig. 1.7.1 **(A)** Phase-contrast image of a representative field of view in a typical mother machine experiment. The upper ends of the growth channels are facing the main channel where fresh medium is continuously flowing. **(B)**Schematic of a mother machine device. Growth medium is constantly exchanged in the growth channels such that cells in the growth channels can grow exponentially at all times. The 'mother' cell (indicated with 'old pole' in the figure) will never get swiped away by the flow while all the other daughter cells eventually will. Image adapted from [14]

On the other hand standard microfluidic flow cells [91] allow for fast medium exchange but often utilize some chemical treatment of the glass surface (like Poly-L-Lysine, PLL) or antibody attachment that can perturb growth, cell shape and physiology [92]. A microfluidic tool that overcomes all these difficulties is the so called "mother machine" which allow for both rapid medium exchange and steady exponential growth of bacterial cells during imaging experiments [93]. See Fig 1.7.1A for an example of a typical field of view in a mother machine experiment.

The mother machine is a PDSM microfluidic device ([94]) consisting of few thousands of parallel growth channels of about 1 um in width and 20$\mu$m in length arranged in a comb fashion. Each growth channel is closed at one end while the other open end is facing the main channel where fresh growth medium is usually flowing. Inlet and outlet are placed at both ends of the main channel. Thus, the main channel can provide continuous fresh growth medium flow, bypassing the nutrient limitations leading to stationary and death phase and ensuring that cells in the growth channels are always in exponential phase. Each growth channel can fit a line of (about 6) single cells. As they grow and elongate, the closest cell to the open end of the growth channel is periodically swept away by the medium flow. At the other closed end of each channel is where the 'mother cell' lie (see Fig. 1.7.1B). The name is appropriate since that is the only cell (or better the only 'pole') that will never be washed away by medium flow and is also the reason why the device itself is called 'mother machine'. In addition to these features, the medium flowing in the main channel can be exchanged rapidly by connecting the inlet to a different medium source.

The mother machine opened the way for a new class of experiments with unprecedented physiological relevance which in recent years unveiled fundamental features of bacterial growth, size regulation and gene expression [14, 95–98]. We decided to employ this device for our studies on nucleoid spatial organization under controlled crowding perturbations via osmotic shock. In this work, we took advantage of both the efficiency of medium switching and the non perturbative nature of the mother machine device to conduct pioneering experiments investigating the relationship between nucleoid morphology, macromolecular crowding and active processes inside the cell (see Chapter 5).

## 1.8 Application of Super Resolution imaging to non-biological systems

The features of super resolution techniques like PALM can also be exploited for investigations on non-biological systems [99–101]. The techniques developed in our laboratory for the

study of bacterial chemoreceptors and nucleoid (PALM in particular), turned out to be instrumental for a completely different problem which is light-matter interaction at the nanometer scale. In collaboration with Garnett's lab from AMOLF, I developed a novel protocol for super-resolution imaging of the absorption profile of silicon nanowires, employing caged fluorophores in a viscous solution. Our combined efforts resulted in a publication [102] which, despite being out of the scope of this thesis, represent part of the output of my PhD and thus is given in Appendix 1.

## 1.9 Thesis outline and scope

This thesis lies in the framework of a quantitative description of diffusion, binding and positioning of a series of different proteins in relation to fundamental biological processes inside living bacteria. The quantitative *in vivo* approach at the basis of this work aims at understanding better the role of protein and DNA spatial organization, focusing on bacterial chemotaxis and nucleoid morphology in the context of macromolecular crowding.

In **Chapter 2** I describe the techniques we utilized for the experimental part of this work on chemoreceptor spatial organization (Chap

ter 4). First I introduce the PALM imaging approach and protocol for measuring chemoreceptor cluster size in fixed bacteria. I describe the detailed protocol for cluster size estimation under different attractant stimulation conditions. Subsequently I describe the technique I developed for reliable "single-particle" tracking of a population of fluorescently labeled proteins forming a crowded environment both in the cytoplasm and on the membrane. We named this technique Localized Photo-Activation Single-Particle Tracking (LPA-SPT). By genetically fusing the protein of interest to photoswitchable fluorophores (of the Eos family) we are able to locally switch the fluorescent emission from state1 to state2 of a subset of fluorophores falling in the vicinity of a diffraction-limited spot generated by focusing a 405nm laser onto the sample plane. This way only a small (tunable) fraction of the whole protein population will be in emitting state2, thus making it easy to track them even in crowded environments. This chapter has been published.

In **Chapter 3** I describe a set of experimental tools we developed and implemented in our laboratory for imaging experiments on bacterial nucleoids at a low level of physiological perturbation. I introduce a novel DNA-label (H-NS-dbd) produced by truncation of an endogenous DNA-binding protein (H-NS). Our construct can be expressed *in vivo* and a set of results from different tests and validations show that H-NS-dbd interfere less with the nucleoid compared to labels based on the full H-NS. We find indeed a lower DNA binding affinity for H-NS-dbd. I show that H-NS-dbd is suitable for labeling chromosomes in cell

species that do not express the native H-NS. In addition, our toolkit includes techniques like PALM, 3D PALM and PALM-tracking for high resolution studies on nucleoid associated proteins. We present preliminary experiments that paved the way for future studies on global nucleoid spatial organization. Our efforts in developing a low perturbative assay for linking DNA compaction and gene expression resulted in a set of Fluorescent Repressor Operator System (FROS) strain with couples of specific labeled loci at controlled genomic distances. Preliminary tests showed how our FROS system is suitable for measuring end to end distances and tracking, even though the labels rely on the binding of only 6 TetR::YFP or LacI::mCherry. Finally, I describe the mother machine based experimental protocol that we employed to measure the crowding perturbations on nucleoid size and morphology under physiologically relevant conditions (see Chapter 5).

In **Chapter 4** I present a study on the spatial distribution and mobility of clustered membrane chemoreceptors upon ligand binding. By means of PALM imaging and our novel single-particle tracking technique (LPA-SPT) we show that ligand binding can perturb cluster organization, mobility and size distribution of transmembrane chemoreceptor clusters. In particular, by combining these two approaches we provide orthogonal evidences indicating that the average size of clusters is modulated by sustained ligand binding in a time-dependent manner. Employing adaptation-deficient mutants we show that cells capable of chemotactic adaptation also restore their cluster size distribution to pre-stimulus levels while *cheRB* mutants do not. Our findings suggest that cluster size might be an important dynamic variable in chemotaxis and that cells seems to be able to modulate cluster size and mobility distributions under different stimulation conditions. Taker together, our spatial resolution experiments clarified the long standing controversy about stability of chemoreceptors clusters upon cognate ligand stimulation.

In **Chapter 5** we employ a FRET crowding sensor to measure the level of molecular crowding inside live *E. coli* together with morphology, size and dynamics of fluorescently labeled chromosomes in growing cells subjected to osmotic shocks. We show that variations in intracellular crowding, induces by hyper osmotic shock, produce variations in nucleoid (and cell) size *in vivo* and for different growth conditions. On the contrary, nucleoids in cells subjected to hypo osmotic shock expands, suggesting that crowding is important for nucleoid compaction. By shutting down metabolism, we investigate the interplay between active and passive (e.g. crowding) mechanisms in steady state nucleoid morphology and during dynamic responses to osmotic shock. Taken together, our results provide insight into the different roles of intracellular crowding in nucleoid spatial organization in living cells, connecting nucleoid morphology to the properties of the cytoplasm and to metabolism.

In **Appendix A** I present a work done in collaboration with Eric Garnett's group (AMOLF)

where I designed and executed the experimental part which involved a novel protocol for PALM imaging. The experiments were aimed at measuring carbon nanowires absorption profile at high spatial resolution, by measuring the intensity of single emitters stochastically activated at different distances from the wire. This work has been published.

# Chapter 2

# Bacterial Chemoreceptor Imaging at High Spatiotemporal Resolution Using Photoconvertible Fluorescent Proteins

We describe two methods for high-resolution fluorescence imaging of the positioning and mobility of E. coli chemoreceptors fused to photoconvertible fluorescent proteins. Chemoreceptors such as Tar and Tsr are transmembrane proteins expressed at high levels (thousands of copies per cell). Together with their cognate cytosolic signaling proteins, they form clusters on the plasma membrane. Theoretical models imply that the size of these clusters is an important parameter for signaling, and recent PALM imaging has revealed a broad distribution of cluster sizes. We describe experimental setups and protocols for PALM imaging in fixed cells with $\sim$10 nm spatial precision, which allows analysis of cluster-size distributions, and localized-photoactivation single-particle tracking (LPA-SPT) in live cells at $\sim$10 ms temporal resolution, which allows for analysis of cluster mobility.

## 2.1 Introduction

The use of fluorescent proteins such as GFP allows for in vivo labeling of native proteins at high specificity to achieve high-contrast imaging of their spatial organization within a cellular context. Yet information attainable by traditional fluorescence microscopy is fundamentally limited by the so-called diffraction limit of spatial resolution—even with microscope objectives of highest performance, one can only achieve resolution of roughly half the wavelength of light ($\sim$250 nm for green fluorescence). This means that molecules separated by less than this distance cannot be distinguished from one another, placing strong

constraints on practical applications that are particularly relevant for the bacterial cell (which measures only several-fold larger than this diffraction-limited length scale). There are at least two ways in which the diffraction limit can hinder practical applications. For situations in which the spatial arrangement of molecules is of interest, the diffraction limit effectively blurs the image of the arrangement, thereby obscuring relevant details regarding shape and/or size of cellular structures. For situations in which the spatial dynamics of molecules are of interest, the diffraction limit hinders reliable tracking of movement, as the blurred image of molecules or molecular assemblies often overlap with one another.

Here, we describe two imaging methods that utilize photo convertible fluorescent proteins to overcome each of these difficulties, and our experimental protocols for applying them to bacterial chemoreceptors. Photoactivation localization microscopy (PALM [74]) allows one to image chemoreceptors with increased spatial resolution within fixed samples. Localized photoactivation single-particle tracking (LPA-SPT) allows one to study the movement of individual clusters of receptors within the crowded environment of live cells. In both techniques, the photoactivatable protein probe is initially dark and can be converted into a fluorescent state using Fig. 2.1.1 near-UV (405 nm) light, as schematized in Fig. 2.1.1, to separate a small subset of the proteins of interest from the bulk of the population. If the spatial extent of this subset is smaller than the diffraction limit, its microscopic image is a spot of a size determined by the diffraction limit, also known as the point-spread function (PSF) of the imaging system. As illustrated in Fig. 2.1.1, the width s of a fitted bell-shaped function to this spot cannot be smaller than the diffraction-limited width of the PSF of the microscope (typically $\sim$100 nm). However, its position can be estimated at a precision that increases with the number (N) of collected photons as

$$\frac{s}{N^{\frac{1}{2}}} \tag{2.1}$$

and readily reaches near-nanometer precision for typical fluorophores, from which >103 photons can be collected [78].

The amount of information one can extract from fluorescence measurements is fundamentally limited by the number of photons that fluorophores emit before they bleach, commonly referred to as the "photon budget" of the experiment. The two techniques described in this chapter make use of this finite photon budget in contrasting manners. Whereas PALM expends the entire photon budget of each fluorophore in a single image frame to maximize the localization precision of single molecules in fixed cells (where protein mobility is negligible), LPA-SPT distributes the photon budget over multiple frames, to obtain information about the mobility of protein clusters in live cells. Figure 2.1.2 provides an overview of the workflow for the two methods.

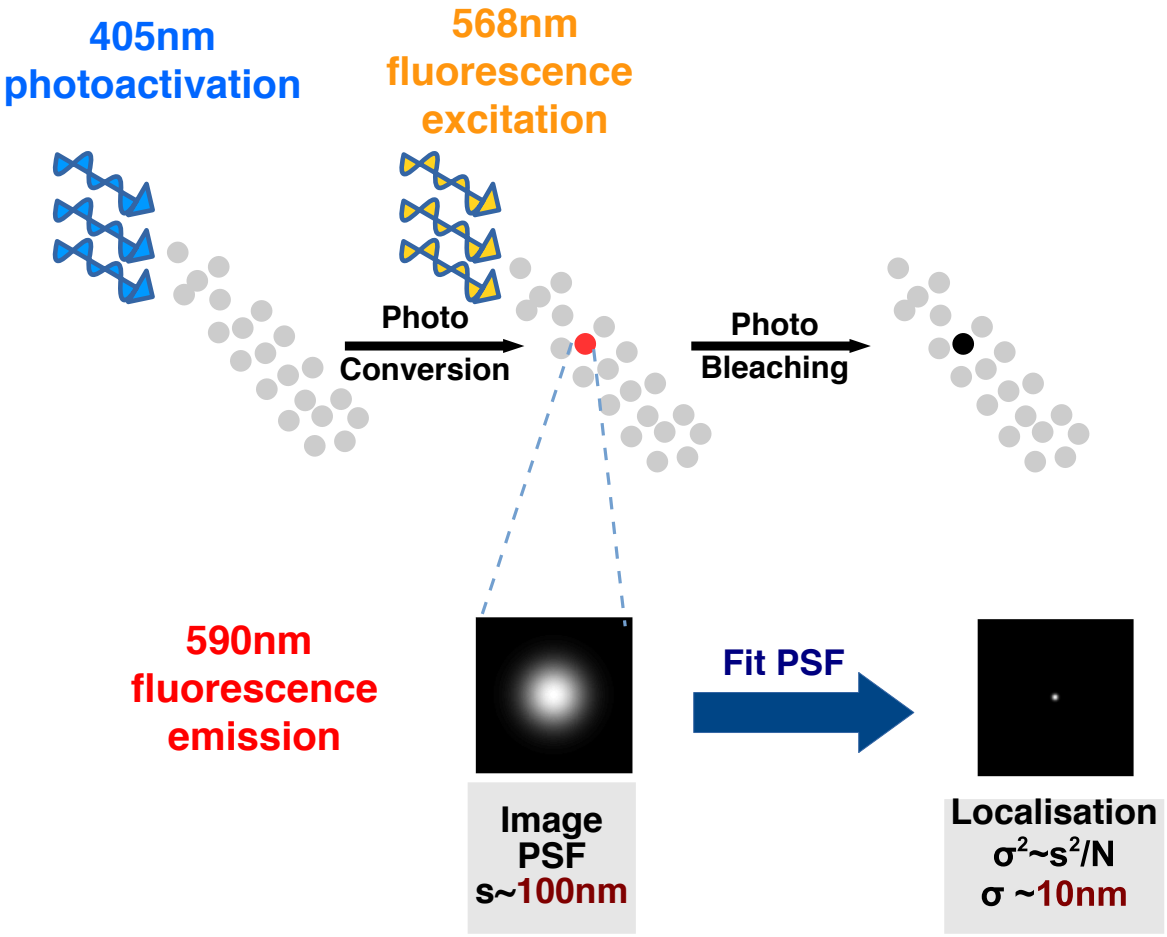


Fig. 2.1.1 **Photoactivation and precise localization of photoconvertible fluorophores.** The two techniques described here, PALM and LPA-SPT, both take advantage of photoconvertible fluorophores to enable precise localization of the labeled protein, even in "crowded" samples in which such molecules (gray) are present at high density. The labels can be converted from a dark (inactive) state to a bright (active) state by irradiation with 405 nm light. Subsequent exposure to light of the excitation wavelength (568 nm in our experiments) leads to emission that is imaged as a diffraction-limited point-spread function (PSF). Fits to a bell-shaped (usually Gaussian) function allows the position of objects to be estimated at ~10 nm precision if $\sim 10^3$ photons can be counted from each fluorophore before irreversible bleaching

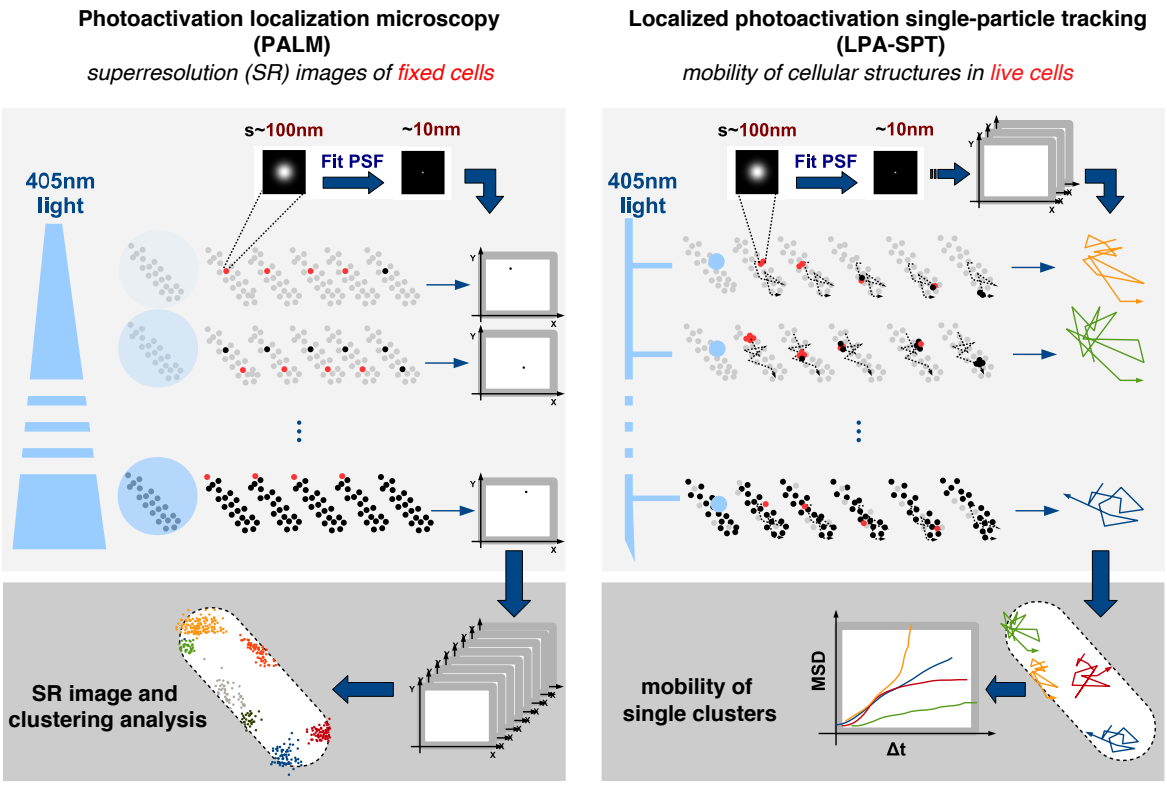


Fig. 2.1.2 **Comparison of workflow between PALM and LPA-SPT.** Because of their limited photostability, each fluorescent label provides only a finite photon budget for measurements. A compromise must be found between the localization precision and the number of frames over which a particle can be followed. The two methods presented in this chapter make contrasting use of the photon budget. (a) For PALM imaging, one expends the full photon budget on localization precision, by imaging each individual fluorophore within a single image frame. Light of the photoactivation wavelength (405 nm) homogeneously illuminates the sample, and fluorophores stochastically switch to their bright state. The activation power is kept sufficiently low to ensure that two fluorescently active molecules will be, on average, separated by more than the microscope resolution. Fluorescent labels are progressively photobleached over the course of the experiment, thus depleting the pool of photoactivatable labels in the sample. The intensity of the photoactivation light is thus progressively increased to maintain a nearly constant activation rate. All single molecules positions, estimated with ∼10 nm precision, are then assembled to form a super-resolution image. (b) For LPA-SPT, the photon budget is distributed across multiple image frames, thereby obtaining information about mobility at the cost of decreased precision of localization. The choice of imaging parameters must strike a balance between length (longer is better), density (lower is better) and localization precision (the higher the better) of tracks. Localized photoactivation relieves the fundamental trade-off between track length and localization precision (which benefits from stronger photoactivation) and track density (which benefits from weaker photoactivation) by providing strong photoactivation within a small fraction of the sample volume. Photoactivation light is delivered in pulses. Particles are then localized in subsequent image frames and tracked to obtain trajectories. This photoactivation/ acquisition sequence is iterated to obtain data for several trajectories per cell, which are tracked and analyzed to build up statistics for individual tracks, single cells, as well as the entire ensemble of tracks.

### 2.1.1 PALM Imaging and Cluster-Size Analysis of Bacterial Chemoreceptors

In recent years, a number of fluorescence imaging techniques have emerged that allow one to overcome the aforementioned diffraction limit of spatial resolution in optical microscopy [103–105] . PALM belongs to this family of so-called super-resolution (SR) imaging techniques. This technology depends on the capability to image single molecules and takes advantage of the simple principle that, if the density of light emitters is low enough, their diffraction-limited images do not overlap in space. Thus, the position of each emitter can be localized at a much higher precision than the width of the diffraction-limited spot [78, 106]. PALM allows the application of this principle to samples with a high spatial density of labeled molecules. It does so by utilizing photoactivatable (or photoswitchable) fluorescent proteins to limit the number of actively emitting labels at any moment in time to a small fraction of total population [74]. The imaging experiment proceeds in an iterative fashion, with a small subset of the total fluorophore population being photoactivated, imaged and bleached. The process is repeated until unbleached labels in the sample are exhausted. In short, PALM allows one to work around the diffraction limit by separating, in time, the appearance of individual fluorophores, which would be indistinguishable as independent emitters if imaged simultaneously. From the sequence of acquired images (typically $10^3 - 10^5$ in number, depending on the sample), a single SR image is constructed by superposition of the probability density functions for the positions of all detected emitters (Fig. 2.1.2). Given that one can usually collect $10^2 - 10^3$ photons from a single fluorescent protein before bleaching, it can be localized at a precision of $200nm/\sqrt{(10^2 - 10^3)} = 5 - 20nm$, an order-of-magnitude improvement over conventional wide-field or confocal imaging.

Our protocol for PALM imaging of labeled chemoreceptors (in this case Tar-mEos2) in fixed bacteria is detailed in Section 2.3.1 was pioneered by Greenfield et al. [5], and our protocol closely follows their approach. Our protocol additionally includes modifications for exploring chemoreceptor organization under ligand stimulation (in this case $\alpha$-methyl-d/l-aspartate, hereafter referred to as MeAsp). A feature of primary biological interest in the nanoscale spatial organization is the size distribution of chemoreceptor arrays, which we quantify using a simple clustering algorithm applied to the localized PALM coordinates.

### 2.1.2 LPA-SPT Analysis of Chemoreceptor Mobility

Single-particle tracking is a powerful method for characterizing the mobility of molecules and subcellular structures within cells, but its utility is usually limited to samples with low object densities because frequent collisions and near encounters preclude reliable tracking.

The latter problem is particularly severe in bacteria, given their small size (cell dimensions of 2-4 × 1 $\mu$m), only an order of magnitude greater than the PSF for a typical fluorescence microscope ($\sim 0.2\mu$m). Thus, only objects with a very low copy number per cell are typically trackable. PALM tracking (also known as "spt- PALM") overcomes this limitation [81] by using photoactivatable fluorophores, which can be switched on and tracked one at a time. PALM tracking has been successfully applied by many investigators [107, 108, 83], but the track lengths are limited by the relatively low photostability of photoactivatable proteins. In practical applications, individual photoactivated proteins tend to bleach within <10 frames, on average.

In Section 2.3.2, we describe a modified PALM tracking technique that allows tracking over a greater number of frames, under conditions in which the tracked particles contain multiple fluorophore labels. As in PALM tracking, this method utilizes photoactivatable fluorophores to enable tracking within a high density of labeled particles. However, instead of activating one fluorophore at a time using uniform illumination, it concentrates the photoactivation beam onto diffraction-limited spots to enhance the probability activating multiple fluorophores for particles that happen to lie within these photoactivation "hot spots." We have found this localized photoactivation single-particle tracking (LPA-SPT) method to be particularly useful for tracking bacterial chemoreceptors, which form a dense arrangement of arrays on the plasma membrane. However, the technique is, in principle, applicable to any oligomeric protein complex in which each subunit is fluorescently labeled, or even to single molecules if they are engineered to contain multiple fluorophore labels.

## 2.2 Materials

### 2.2.1 Strains and Plasmids

1. Strains and plasmids used in this study are listed in Table 4.1 and Table 4.2. For both methods introduced in Section 2.1, any photoswitchable or photoactivatable protein can be employed as a fluorescent fusion to the protein of interest. Experiments described here utilized Tar-mEos2 (except in Fig. 2.3.3, where CheA-mEos3.2 was used). Plasmid pSJAB4 expresses Tar-mEos2 from an IPTG inducible promoter, a C-terminal fusion of mEos2 fused to the coding region of the tar gene with a six amino-acid (GSGGGG) linker. Strain UU1250, a gift from J.S. Parkinson, is a derivative of the chemotaxis wild-type strain RP437 with all chemoreceptors deleted [Δaer-1 Δtsr-7028 Δ(tar-tap)5201 Δtrg-100]. The induction level of fusion proteins (Tar-mEos2 or CheA-mEos3.2) was chosen to be the level that maximizes the rate of chemotactic

ring expansion on soft agar motility plates ([27]) prepared with tryptone broth (TB). The functionality of the Tar-mEos2 fusion protein was tested via CheY-CheZ FRET assays [109].

2. Cell culturing: Strains TSS902, TSS1020, and TSS1836 were inoculated from a glycerol stock into tryptone broth (TB) and grown overnight until saturation at 30 °C in the presence of 100 $\mu$g/ml ampicillin for TSS902 and TSS1020 and 34 $\mu$g/ml chloramphenicol for TSS1836. The next morning, the saturated culture was inoculated 1:100 into fresh H1 minimal medium (100 $\mu$l in 10 ml) supplemented with 0.5% glycerol, 20 $\mu$M IPTG for TSS1020 and TSS902, and 6 $\mu$M NaSal for TSS1836 containing the following amino acids at 1 mM concentration: histidine, leucine, L-methionine, threonine. The medium was supplemented with 100 $\mu$g/ml of ampicillin for TSS902 and TSS1020 and 34 $\mu$g/ml chloramphenicol for TSS1836. After 6 h and 15 min growth at 33.5 °C to $OD_{600nm}$ = 0.2, cells were harvested by centrifugation at for 5 min. The supernatant was discarded, and the cells were resuspended and washed with motility medium (see Section 2.2.3). The centrifugation and washing step was repeated twice. About 30 min after the washing was completed, cells were considered ready for microscopy.

| **Plasmid** | **Gene** | **Backbone** | **Resistance** | **Source** |
|---|---|---|---|---|
| pSJAB4 | *tar-mEos2* | pTrc99A [110] | Ampicillin | this work |
| pSJAB93 | *hns-mEos3.2* | pBAD33 [111] | Chloramphenicol | this work |
| pGP53 | *cheA-mEos3.2*, *cheW* | pKG116 [112] | Chloramphenicol | J.S. Parkinson |

Table 2.1 Plasmids used in this study

| **Strain** | **Parent** | **Source** | **Parent strain genotype** | **Plasmid** |
|---|---|---|---|---|
| TSS902 | UU1250 | [113] | $\Delta tsr, \Delta tartap, \Delta trg, \Delta aer$ | pSJAB4 |
| TSS1020 | VH1 | [114] | $\Delta tsr, \Delta tartap, \Delta trg, \Delta aer$ $\Delta cheRBYZ$ | pSJAB4 |
| TSS1836 | UU1607 | [115] | $\Delta cheAW$ | pGP53 |
| TSS1893 | HS1 | [116] | $\Delta hns$ | pSJAB93 |

Table 2.2 Bacterial strains used in this study

### 2.2.2 Growth Media

1. Tryptone broth (TB): 1% Bacto tryptone, 0.5% NaCl.

2. H1 minimal salts medium: 50 mM $KPO_4$, 7.6 mM $(NH_2)_4SO_4$, 0.5 mM $MgSO_4$, 1.25 $\mu M$ $Fe_2(SO_4)_3$, 0.01% thiamine, 67 mM $NaCl$, 1 mM histidine,1 mM leucine, 1 mM L-methionine, 1 mM threonine, pH 7.4. All chemicals used in growth media preparation were purchased from Sigma-Aldrich.

### 2.2.3 Buffer Solutions

All imaging experiments, including those involving chemical fixation and ligand stimulation, were conducted in motility buffer medium, with which cells were washed and resuspended after growth. All chemicals used for preparation of buffers were purchased from Sigma-Aldrich.

1. Motility medium: 10 mM KPO, 0.1 mM EDTA, 10 mM lactic acid, 1 $\mu$M methionine, pH 7.

2. 1 mM MeAsp motility medium: Dissolve final amount of MeAsp acid in half the final volume of motility medium, which results in a turbid white solution. Add saturated NaOH until the solution clears, and then add motility medium to the final volume. Add saturated NaOH until pH 7 is reached (see Note 1).

3. 4% w/v paraformaldehyde motility medium: Dissolve 4 g of paraformaldehyde powder in 80 ml of motility medium and put it on a magnetic shaker hot plate at 80 °C. Add saturated NaOH (around 200 $\mu$l) until the solution clears. Add 37% HCl until pH 7.

### 2.2.4 Coverslip Cleaning

Extremely clean coverslips are essential both for PALM and LPA-SPT. In fact, every scattering particle coming from "dirt" that is smaller than $\sim$250 nm in diameter will produce a PSF that can be challenging for the analysis software to distinguish from an emitting fluorescent protein, thereby giving rise to false positive artifacts. Our protocol for coverslip cleaning requires the following:

1. Deionized milli-Q water.
2. Hydrogen peroxide, 50% w/v.
3. 100% ethanol.

4. 100% acetone.
5. Hellmanex detergent.
6. A sonicator.
7. Filtered pressurized nitrogen.

The protocol steps are:

1. Place the coverslip in a coverslip holder that fits in a beaker.
2. Rinse the coverslip with an abundance of milli-Q water.
3. Leave the coverslip in 1% Hellmanex dissolved in milli-Q water for >5 h (overnight is best).
4. Rinse thoroughly with milli-Q water.
5. Fill the beaker with 100% acetone. Submerge coverslips and sonicate for 15 min.
6. Rinse thoroughly with milli-Q water.
7. Fill the beaker with 100% ethanol. Submerge coverslips and sonicate for 15 min.
8. Rinse thoroughly with milli-Q water.
9. Fill the beaker with 50% hydrogen peroxide. Submerge coverslips and incubate at 80 °C overnight.
10. Safely dispose of the hydrogen peroxide and rinse thoroughly with milli-Q water.
11. Dry the coverslips with filtered pressurized nitrogen.
12. Coverslips can be kept in air for about 2 weeks, provided that the beaker containing them is properly sealed with Parafilm or aluminum foil.

### 2.2.5 Cell Attachment and Drift Correction

To correct for sample drift, which can occur during the long acquisition time of PALM, we employ 100 nm-wide gold-coated silica beads as fiducial markers within the imaging field of view. We use poly-l-lysine to attach both gold-coated beads and fixed cells to cleaned glass coverslips.

For LPA-SPT, we employ anti-flagellar antibodies for attaching cells to the coverslip. (Anti-FliC antibodies bind specifically to bacterial flagellar filaments and non-specifically to the glass surface.)
We utilize:

1. Poly-l-lysine solution 0.1% w/v (Sigma-Aldrich).
2. Gold-coated polystyrene beads (diameter < 200 nm, Sigma-Aldrich).
3. Anti-FliC antibodies (rabbit polyclonal, a gift of H.C. Berg).

### 2.2.6 Preparation of PALM Imaging Chamber

1. $25 \times 75\ mm^2$ glass slides.
2. Rubber spacer (1 mm thick, silicon isolator, Press-to-Seal series, Sigma).
3. $25 \times 75\ mm^2$; 200 $\mu$m thick coverslips.

### 2.2.7 LPA-SPT Consumables for Flow Cell

1. Round coverslips (ø 12 mm, bioWORLD, thickness=0.17mm).
2. Vacuum grease (Apiezon L).

### 2.2.8 General Microscopy

PALM and LPA-SPT equipment requirements mostly overlap, and an optical path for localized photoactivation can be easily added to an existing PALM setup. We list here all the components needed to build a PALM setup and the additional optics required for building a localized photoactivation path for LPA-SPT. We provide a sketch of our setup in PALM mode in Fig. 2.3.1, and in LPA-SPT mode in Fig. 2.3.7. We note that, by simply removing the microlens array, it is possible to switch between the two modes.

1. Nikon Ti-E inverted microscope with Perfect Focus System (PFS).
2. Automated XY stage (Mad City Labs).
3. Halogen lamp for bright field imaging.
4. High numerical aperture (1.49 NA) 100× TIRF objective lens (Nikon).
5. Filter cubes, used for mEos2 green-state and red-state imaging (for green state: EX R405/491/561/635 multi-edge, EM FF01- 525/45-25. For red state: EX R405/491/561/635 multi-edge, EM NF02 405S-25/NF03 561E-25/FF01-607/70-25).
6. Optical table.
7. Temperature/humidity controlled room.

8. Solid-state lasers for fluorophore excitation and photoactivation: 405 nm (Coherent CUBE 100 mW), 491 nm (Cobolt Calypso 200 mW), 515 nm (Cobolt Fandango 150 mW), 568 nm (Coherent Sapphire 200 mW). Acousto-optic tunable filter (AOTF, AA, France) for shutter ing/pulsing excitation lasers (see Note 2).
9. Acousto-optic tunable filter (AOTF, AA, France) for shuttering/pulsing excitation lasers (see Note 2).
10. Signal generator for analog control.
11. Back-thinned, electron-multiplying CCD (EMCCD) camera (Princeton Instruments ProEM and Andor iXon 897).
12. General optomechanics and accessories (Thorlabs and Radiant Dyes).
13. Computer interface hardware (National Instruments).
14. Data acquisition PC (running Microsoft Windows).

### 2.2.9 Additional Component for PALM

1. Neutral density filter wheel (Thorlabs).

### 2.2.10 Additional Components for LPA-SPT

1. Microlens array (Flexible Optical B.V., APO-GB-P1500-R13.9, BK-7 glass, F $\simeq$ 25 mm, pitch = 1500 $\mu$m, 36 lenses, $10 \times 10 mm^2$).
2. Mechanical shutter (Uniblitz) with automated control for 405 nm laser.

### 2.2.11 Fluidics

1. Gold-plated flow cell [91].
2. Fluidic pump (Harvard Apparatus, PHD-2000).
3. Polyethylene fluidic tubing (PORTEX fine bore polyethylene tubing, 0.58 mm ID, 0.96 mm OD).
4. Fluidic switch (Hamilton HVM 3-2).

## 2.3 Methods

### 2.3.1 PALM Imaging of Bacterial Chemoreceptors

Cells are first cultured as described above and then left in neutral buffer for ∼45 min prior to fixation with 4% paraformaldehyde, coverslip attachment, and incubation in PALM imaging chamber. For experiments in which a ligand stimulus is applied, the buffer suspension is aliquoted into two or more parts and subjected to ligand stimuli of different concentration and/or duration (but always leaving one part as unstimulated control) prior to fixation, and a separate PALM imaging chamber is prepared for each aliquot. PALM image analysis and filtering of localizations are achieved by either custom-written Matlab code or by means of open-source GUI-based software. The resulting PALM localizations are then grouped into clusters by means of a simple distance-based clustering algorithm. These analyses yield the number of localizations falling within each cluster, as well as an estimate of the area occupied by each cluster.

### 2.3.2 PALM Setup Summary

Requirements and typical microscopy setups for PALM imaging have been discussed extensively in the literature [74]. Here we provide a brief description of our PALM imaging setup, which is also used for LPA-SPT with slight modifications. Our setup is built around the Nikon Ti-E inverted microscope (see Fig. 2.3.1 for a detailed scheme).

1. Excitation path: 491 nm and 568 nm lasers for exciting the green and red states, respectively, of mEos2/mEos3.2 are passed through an acousto-optic tunable filter (AOTF), which is used as a shutter to convert the continuous laser illumination into excitation light pulses of desired timing. The excitation light is then magnified 10× via a telescope. The collimated expanded beam is focused on the objective back focal plane via a tube lens (focal length of 300 mm for our setup) placed immediately in front of the rear aperture of the microscope, yielding (after the microscope objective) a nearly parallel beam that passes through the sample plane with a size of approximately 60 $\mu$m (full width at half maximum). The 568 nm power is set to 50 mW at the laser module, of which 25 mW is transmitted to the sample plane in our setup.

2. Photoactivation path: The photoactivation 405 nm beam illuminates the sample continuously at low power in a typical PALM experiment. In our setup, a dichroic mirror combines the photoactivation (405 nm) laser with the excitation (568 nm) laser. The 405 nm beam is also focused onto the back focal plane of the objective, creating a

photoactivation beam that passes through the sample plane with approximately the same dimensions as the excitation beam. Neutral density (ND) filters placed in a filter wheel in front of the 405 nm laser, as well as analog control of laser power, are used to modulate the intensity of the photoactivation beam over the course of the experiment in order to keep the number of activated fluorophores per image frame approximately constant.

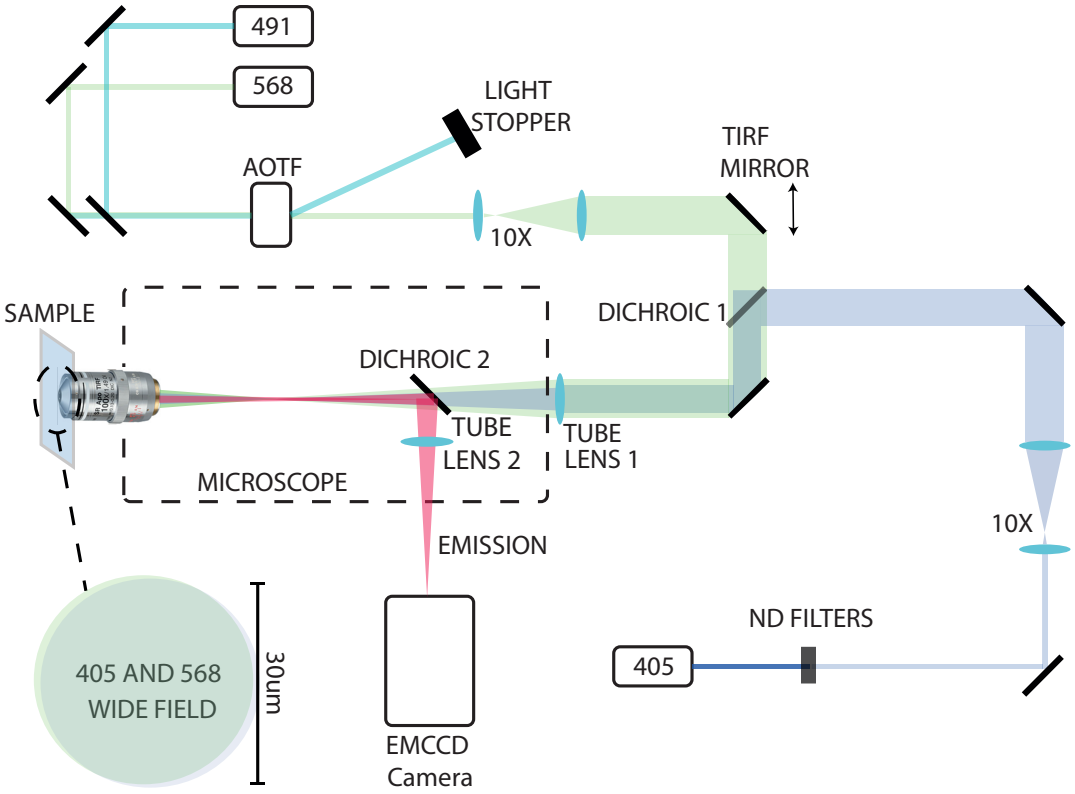


Fig. 2.3.1 **Optical setup for PALM imaging.** Excitation and activation paths are shown in green and blue, respectively. An AOTF placed in the excitation path allows laser exposure times to be controlled separately from the camera's frame interval (e.g., for stroboscopic illumination). The excitation (561 nm) beam is expanded by a 10× telescope and focused on the back focal plane of the objective to achieve EPI illumination with a flat profile across the camera field of view. Translation of one of two mirrors ("TIRF mirror") placed between the telescope and tube lens is used to achieve highly inclined illumination to minimize reflections of the excitation beam. A 488 nm laser is also coupled to the same excitation path for green-state wide-field imaging of mEos2 and mEos3.2. The activation (405 nm) beam is also expanded 10× and combined with the excitation path through a dichroic mirror (Dichroic1) to achieve EPI illumination. The activation intensity is modulated via both a neutral density filter wheel and analog computer control of the power of the 405 nm laser. Light emitted from the sample (red) is collected through the objective, reflected by a second dichroic mirror (Dichroic2) and imaged by an EMCCD camera

3. Imaging path: The emitted light is collected via the 100× 1.49NA Nikon TIRF objective and passed through a series of emission filters to block both the 405 and 568 nm light (405 and 561 notch filters in series, Semrock) and to band-pass the emission of the red state of mEos2. The filtered emission is then passed through 1.5× magnifier built into the microscope and imaged on the EMCCD sensor via the microscope tube lens. The total magnification is thus 150×, and the effective pixel size is 106.7 nm.

4. Sample positioning: We use a standard sample holder for regular microscopy slides to position our imaging chamber for imaging. The imaging chamber consists of a rubber spacer sandwiched by a rectangular coverslip and a standard glass microscope slide (Fig. 2.3.2). The holder is coupled to a motorized stage that allows for computer-controlled movement of the sample.

5. Acquisition software: We employ custom-written software to control our microscopy and data-acquisition hardware. The program allows precise control of laser and camera timings and other experimental parameters. For PALM experiments, we use continuous 405 nm illumination with analog control of the power level, and 568 nm excitation with an exposure time of 60-100 ms per camera frame.

### 2.3.3 Chamber Preparation

Rectangular coverslips are cleaned as described in Section 2.2.4. The coverslip has to be chemically treated to firmly attach fixed bacteria on its glass surface, and the following steps describe such a treatment employing poly-l-lysine, which we employ for fixed-cell attachment to glass surfaces. To prepare the coverslip for attachment we follow the steps below.

1. Deposit 40 $\mu$l of poly-l-lysine (PLL) at the center of the coverslip by pipetting (see Note 3) and let sit for $\sim$20 min.

2. Thoroughly rinse with milli-Q water by pipetting to remove excess PLL from the glass surface.

3. Deposit 5 $\mu$l of 1% v/v solution of gold-coated silica beads, which are sonicated for 5 min previous to deposition on the PLL-coated region and let sit for 15 min.

4. Rinse twice with motility medium by pipetting.

5. Incubate bacterial suspension on the area covered with PLL for 15 min.

6. Rinse three times with motility medium.

### 2.3.4 Bacterial CellPreparation

Cells are cultured as described in Section 2.2.1 (see Note 4), harvested by centrifugation (4165 × g, 5 min washing twice with 50 ml of motility medium), and finally resuspended in 1 ml motility medium. Incubate at room temperature for 45 min prior to fixation and PALM imaging. For experiments with ligand stimulation, the suspension is aliquoted into three parts prior to fixation.

1. Unstimulated cells: Cells are held in neutral motility medium before fixation.

2. Cells shortly after stimulation: Cells are exposed to 1 mM MeAsp for a duration of ∼10 min prior to fixation.

3. Cells under prolonged stimulation: Cells are exposed to 1 mM MeAsp for a duration much longer than the chemotactic adaptation time, usually 1 h.

4. Each sample is chemically fixed with 4% paraformaldehyde (PFA) as described below prior to attachment to the coverslip.

5. Fixation: Because PALM depends on iteratively accumulating many images of fluorophore subpopulations, the acquisition sequence for a single PALM image can extend over long times (often >1 h). PALM images will thus reflect cellular structures accurately only if the labeled structures are stationary over the course of the acquisition. Chemical fixation is thus desirable for most PALM experiments, to ensure that movement of cellular structures is negligible. For this purpose, PAF powder is dissolved in motility medium to a final concentration of 4% w/v, as described in Section 2.2. We find that paraformaldehyde solution should be prepared fresh on the day of the PALM experiment to minimize false positives in the sample. Just before the fixation step, cells suspended in motility medium (with or without ligand stimulation) are centrifuged (4165 × g, 5 min), and the supernatant is decanted to achieve an OD of about 2. We add 40 ml of the fixative solution to the cell pellet. Fixation proceeds by incubation at room temperature for 10 min (see Note 5). For best imaging results, perform the fixation of each sample just prior to PALM imaging. We find that this procedure minimizes false positive localizations and maximizes quantitative reproducibility of the PALM experiment. If multiple samples (e.g., different stimulation conditions) are to be imaged on the same day, it is advisable to fix the different samples at different times.

6. Imaging chamber: We perform PALM imaging in a sealed chamber filled with motility medium, assembled on a conventional microscope slide by means of a square piece

of 1 mm-thick microscopy rubber, out of which a circular hole 2 cm in diameter has been carved, as illustrated in Fig. 2.3.2. The multiuse rubber spacer is first cleaned in H2O2 at ∼100 °C for 15 min, then rinsed with milli-Q water and acetone to maximize adhesion to glass. It is then placed on the microscopy slide so as to create an open circular chamber. The chamber is filled with 170 $\mu$l of motility medium and sealed with the treated coverslip on which bacteria were immobilized (see Note 6).

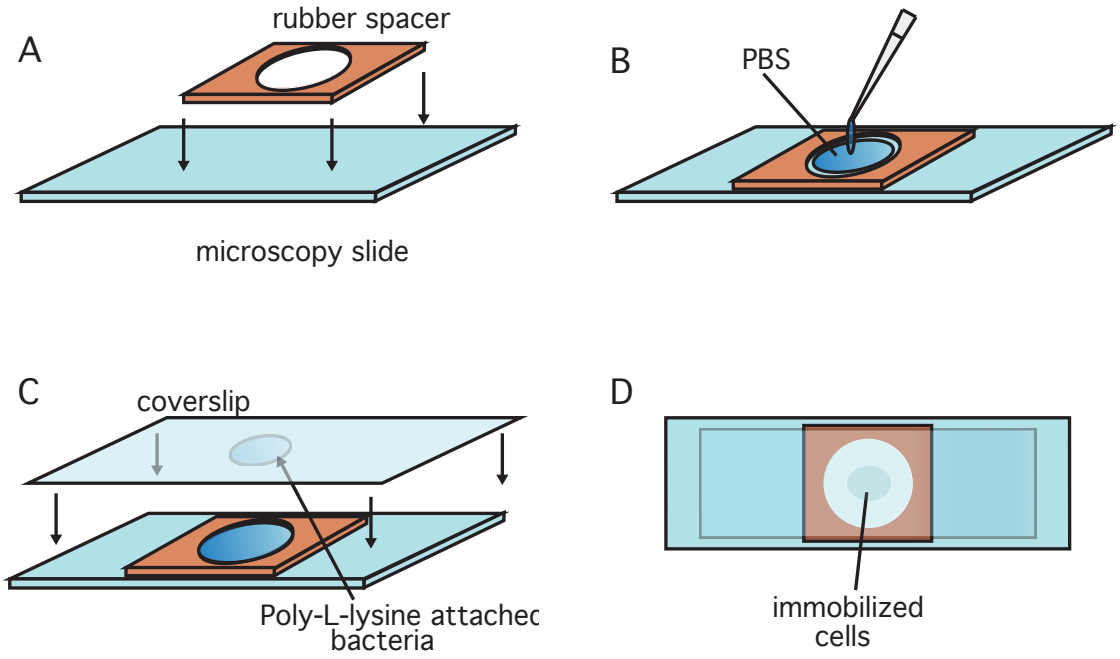


Fig. 2.3.2 **Preparation of the PALM imaging chamber.** (a) A rubber spacer with a circular hole is placed on a clean microscopy slide. (b) The circular chamber is filled with PBS buffer. (c) The chamber is sealed with a coverslip on which fixed bacteria are immobilized using poly-l-lysine. (d) The chamber is ready for imaging

### 2.3.5 PALM Imaging Protocol

After positioning the sample and focusing with the objective, a suitable field of view (FOV) is chosen in brightfield (see Note 7). The criteria for choosing a good FOV are as follows.

1. Presence of at least one (bright) fiducial marker.
2. Good cell attachment (cells are not wobbling and lie parallel to the glass surface).
3. Cells in the FOV are non-overlapping and well separated.

4. After choosing the FOV, we record a brightfield image and switch the microscope to fluorescence mode. A typical chemoreceptor imaging experiment under our conditions involves the acquisition of about 80,000 frames. In our PALM imaging protocol, both the photoactivation and the excitation illumination are continuous. Care should be taken to limit the 405 nm intensity to avoid overactivation. When the photoactivation rate is too high, the chances of switching on two fluorophores within the DL area become significant and lead to complications and/or artifacts in the PSF fitting procedure. We control the photoactivation rate by both analog control of the 405 nm laser power and by a double filter wheel equipped with neutral density filters of optical density (OD) ranging from 0.1 to 0.8 on the first wheel and from 1.0 to 4.0 in the second wheel. Because the number of activatable fluorophores will decay exponentially over time if the photoactivation beam intensity is constant, we increase its intensity over time accordingly to maintain an approximately constant activation rate. 405 nm power is ramped up exponentially by analog control over 20,000 frames, at which point the neutral density filter is switched to one of a lower OD, and the process is repeated. Depending on the power losses occurring in the optical paths, which can vary for different microscopy setups, these parameters might need to be adjusted accordingly. Our imaging protocol is summarized in Table 2.3.

5. Excitation is carried out at high power to minimize the occurrence of activated fluorophores that continue to emit across more than one frame. In practice, some emission across frames is unavoidable, but minimizing this fraction facilitates analysis, especially when PALM is used not only to localize molecules, but also to count them.

| | **0-20k frames** | **20-40k frames** | **40-60k frames** | **60-80k frames** |
|---|---|---|---|---|
| Frame duration | 100ms | 100ms | 100ms | 100ms |
| Frame rate | 10 fps | 10 fps | 10 fps | 10 fps |
| Excitation power (568nm) | 50 mW | 50 mW | 50 mW | 50 mW |
| Activation power 405nm[a] | $V0 \times e^{(1.6 \times n/n_{max})}$ | $V0 \times e^{(1.6 \times n/n_{max})}$ | $V0 \times e^{(1.6 \times n/n_{max})}$ | $V0 \times e^{(1.6 \times n/n_{max})}$ |
| Neutral density filter O.D. | 3.8 | 3.1 | 2.4 | 1.7 |

Table 2.3 Experimental parameters for PALM imaging

[a] In each 20k-frame segment, n ranges from 0 to nmax, where nmax = 20,000 and V0 = 20 mW

### 2.3.6 PALM data analysis

1. Image reconstruction: Our PALM image analysis procedure makes use of the freely available software ThunderStorm developed and described in [79]. This program is implemented in Fiji (imageJ) as a plugin which can be downloaded at https://github.com/zitmen/thunderstorm/wiki/Installation. The software takes as its input the set of raw images from the PALM experiment in the form of an "image stack". As in any other standard PALM analysis protocols, ThunderStorm first finds the positions of the maxima corresponding to the emitter PSFs in each image and uses those positions as initial-guess parameters for fitting a two-dimensional Gaussian function to each PSF to localize the fluorophore. After this procedure is repeated for each frame, an SR image is constructed by superimposing all localizations from all frames. We also make use of the "drift correction" function in ThunderStorm in the mode "fiducial markers" to compute the sample drift over time by means of the localizations corresponding to the gold-coated silica beads deposited on the coverslip.

2. Drift correction: We employ immobilized 100 nm diameter gold-coated silica beads as described in 3.3 Chamber preparation to correct for the sample drift in the x–y directions. The position of the beads is recorded at each frame, and the position of all the other localizations in that frame is translated by the difference vector between the initial position of the fiducial marker and the position of that marker at that frame. Given the long acquisition time of our experiments (around 100– 150 min), correcting for sample drift is essential (Fig. 2.3.3).

3. Additional postprocessing: In our protocol we consistently apply two additional post-processing routines to the raw list of localizations. First, remove duplicate localizations (localizations that converged to the same position). Second, eliminate all localizations belonging to the same molecule in consecutive frames, or molecules that are blinking instead of bleaching. This last phenomenon (fluorophore blinking) is one of the main causes of artifacts in PALM images, as it can produce "clusters" of localizations that are actually coming from multiple localizations of the same protein. Such localizations can be combined into one single localization based on a specified distance within which molecules are merged together in the subsequent frames, and accounting for an allowed number of frames in which the molecule can disappear. Routines for both corrections

are implemented in ThunderStorm. A representative PALM image of receptor clusters is shown in Fig. 2.3.4.

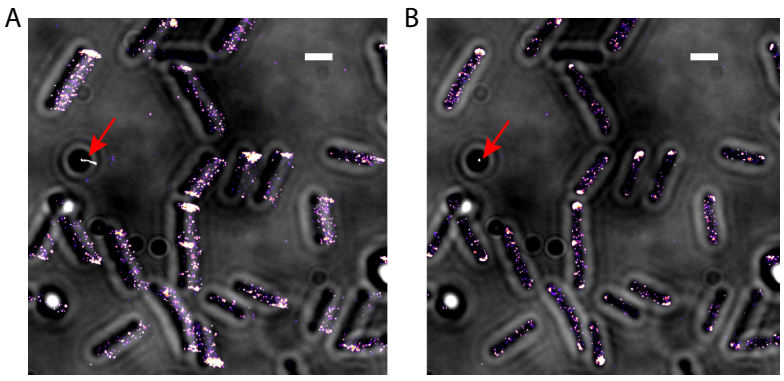


Fig. 2.3.3 **Drift correction by use of fiducial markers.** (a) Uncorrected PALM image (prior to drift correction) overlaid with brightfield image of cells acquired at the start of the experiment. Considerable sample drift over the duration of PALM acquisition (150 min) is clearly visible, both in the trace of the fiducial marker (indicated by red arrow) and by the large number of PALM localizations outside of the initial cell positions in the brightfield image. (b) PALM image after drift correction. The trace of the fiducial marker is reduced to a point and the features of the sample (CheA clusters in this case) are recovered. Scale bar: 1 $\mu$m. Strain used: TSS1836. Genotype: *Delta*cheAW cells (UU1607) expressing CheW and CheA::mEos3.2 from plasmid (pGP53) at 6$\mu$M NaSal induction. See Table 2.3 for imaging conditions

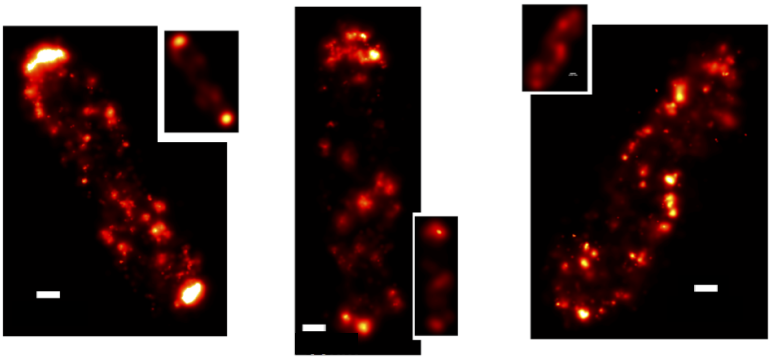

Fig. 2.3.4 **Representative PALM images of a strain expressing Tar-mEos2.** There is considerable diversity in the nanoscale organization of chemoreceptors, as exemplified by these three cells. The insets show simulated diffraction-limited images constructed by convolving each PALM image (main panels) with a Gaussian function of the same width as the PSF of our microscope. Scale bar: 200 nm. Strain used: TSS902 (see Table 4.1 and Table 4.2 for details)

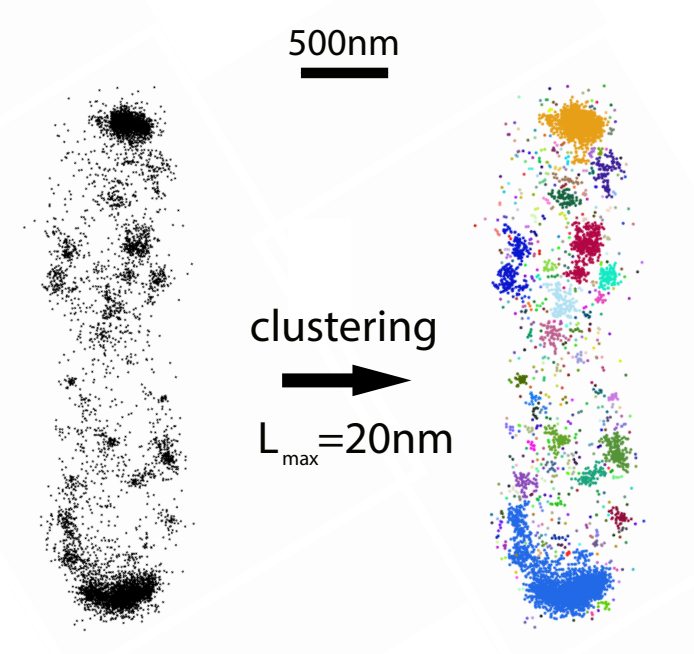


Fig. 2.3.5 **Example input and output of clustering algorithm.** The full set of single-molecule PALM localizations within a cell (left, black points) are partitioned into clusters (right, colored points) by a simple criterion: localizations separated by a distance less than a threshold Lmax (here set to 20 nm) are assigned to the same cluster. Each identified cluster is represented in a different color. Scale bar: 500 nm. Strain used: TSS902 (see Table 4.2 and 4.1 for details)

### 2.3.7 Cluster Analysis

Once the raw list of localizations has been generated, we can proceed with cluster identification. For our purposes, the following simple algorithm yields satisfactory results.

1. Compute all the pairwise distances between localizations in a cell.
2. Assign two localizations to the same cluster if their distance is <20 nm.

A sample output of our code is presented in Fig. 2.3.5. We also tried to implement more sophisticated algorithms such as DBSCAN [117], but a comparable cluster identification efficiency was obtained. Each cluster identified by our algorithm is depicted in a different color in Fig. 2.3.5. After the localizations are grouped into clusters, we can count the number of localizations for each cluster in the cell and repeat the procedure for each cell in the PALM image. Upon collecting enough statistics, we can build a cluster size distribution for each sample (Fig. 2.3.6). In agreement with [5], we find that the distribution of cluster size, N, is

extremely broad, ranging from single localizations to >2000 localizations. Large clusters (N > 100) make up only a few per cent of the cluster population (Fig. 2.3.6,inset), but contain more than half of the receptor population (Fig. 2.3.6, main panel).

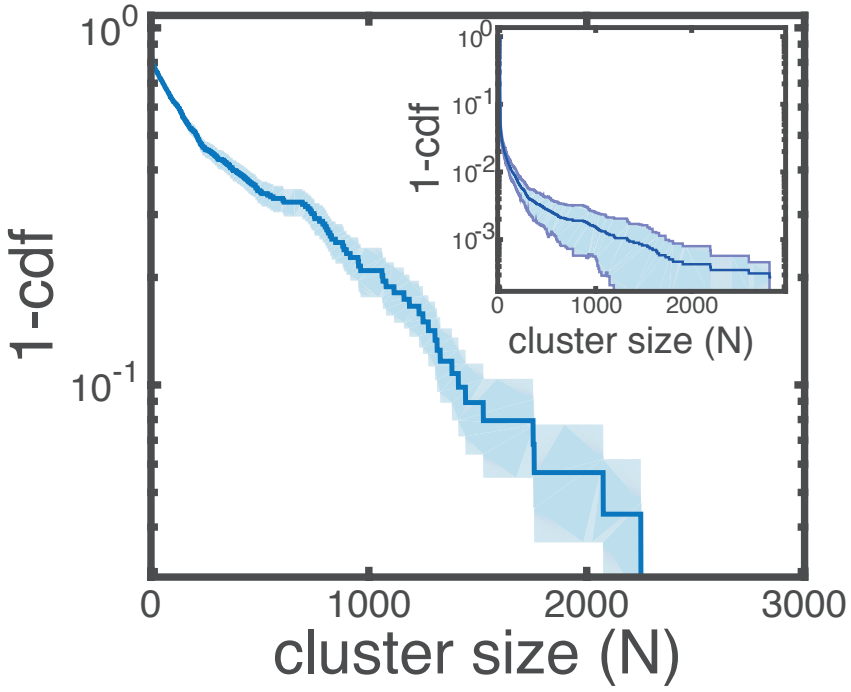


Fig. 2.3.6 **PALM cluster-size statistics for a strain expressing Tar-mEos2.** The main panel shows the cumulative distribution function (1-cdf) for the probability that a localized receptor is found in a cluster of size N (or equivalently, the fraction of receptors found in clusters of size smaller than or equal to N). Inset: Cumulative distribution function (1-cdf) for the probability that a cluster is of size N (or equivalently, the fraction of clusters with size smaller than or equal to N)

### 2.3.8 Localized Photoactivation Single-Particle Tracking (LPA-SPT) of Chemoreceptors

Cells expressing labeled chemoreceptors are cultured according to standard procedures (see Section 2.2.1), immobilized on a round coverslip, and incubated in a flow cell [91] under buffer flow. By use of a micro-lens array, we generate a squared grid of twenty-five diffraction-limited (DL) foci of the 405 nm laser at the sample plane that switch mEos2 fluorophores from the green-emitting (inactive) to red-emitting (active) state in the vicinity of the DL

photoactivation spots. Upon translating the sample to a new field of view (FOV), the X–Y position of the stage is fine-tuned manually to ensure a good overlap of the photoactivation spots with immobilized bacteria. We then deliver a short 405 nm laser pulse and image the red state of mEos2 by means of a 568 nm laser until all activated fluorophores are bleached. Before the pulse, no mEos2 fluorophores are visible in the red channel. After the pulse, a few Tar-mEos2 clusters appear in the FOV as mEos2 labels that happen to lie near the DL photoactivation foci are switched to the red-emitting state as a result of 405 nm irradiation. Because the 405 nm photoactivation pulse is focused to a diffraction-limited spot, one can obtain a low enough spatial density of activated clusters for reliable tracking. In addition, by tuning the energy of this photoactivation pulse, one can photoactivate, on average, more than one fluorophore per cluster. By adjusting the intensity of the 568 nm excitation, the number of image frames over which Tar- mEos2 clusters can be tracked before photobleaching can be increased.

### 2.3.9 Localized Photoactivation Path

The optical path for localized photoactivation is implemented on the same PALM setup described earlier. A microlens array is placed in the 405 nm laser path to create a telescope with the tube lens at the aperture of the microscope (Fig. 2.3.7; see Note 8). This creates a bundle of parallel beams organized in an array that converges at, and overfills, the back focal plane of the microscope objective. The beams are focused on the sample by the microscope objective, creating an array of diffraction limited spots for localized photoactivation. By inserting/removing the microlens array, one can switch between the PALM and LPA-SPT configurations.

### 2.3.10 LPA-SPT Sample Preparation

1. Coverslip treatment and preparation: Round coverslips (ø 12 mm, bioWORLD, thickness=0.17mm) are cleaned as described in Section 2.2.4. For sealing purposes, a ring-like pattern of vacuum grease must be deposited at the rim of the round coverslip. To achieve this, we use a short cylindrical hollow metal tube, which has the same diameter as the round coverslip and a wall thickness of about 1 mm. One end of the tube is dipped into a thin film of vacuum grease prepared by sandwiching the grease between two microscope slides and rubbing.

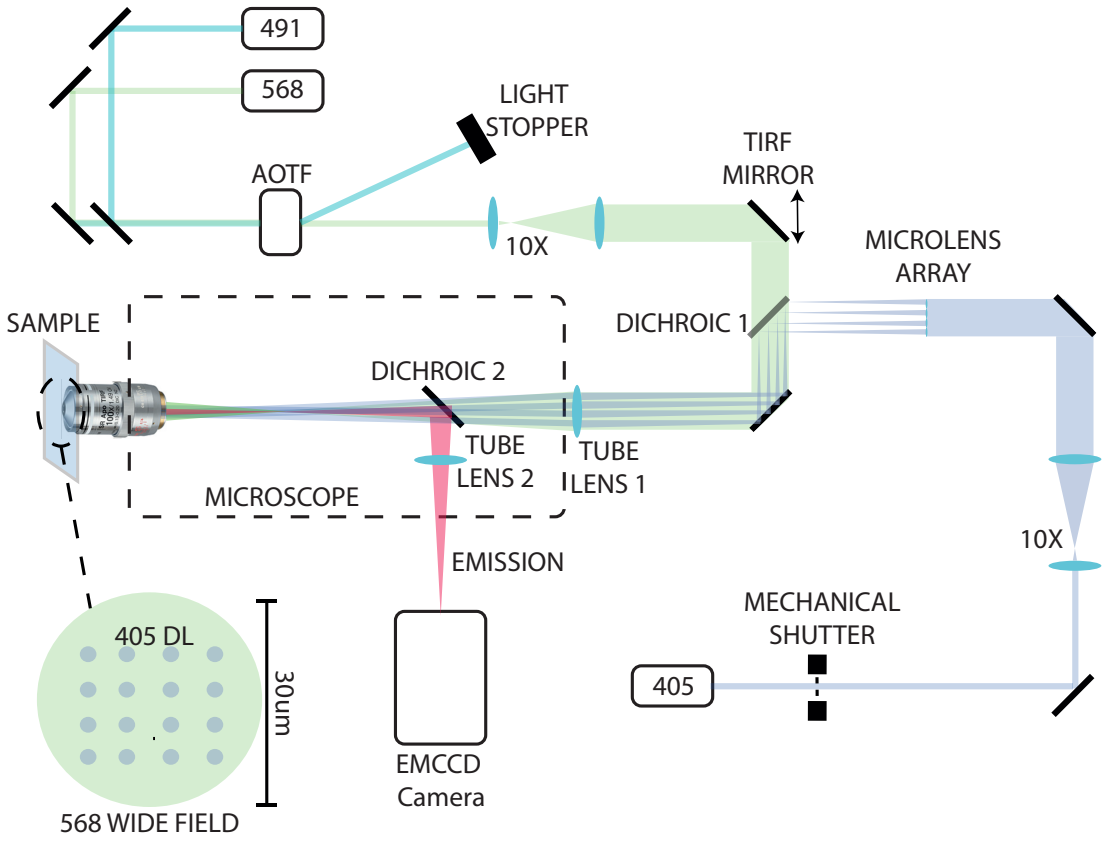


Fig. 2.3.7 **Optical setup for Localized PhotoActivation Single-Particle Tracking (LPA-SPT).** The excitation path is identical to that described in Fig. 2.3.1 for PALM imaging. The activation path is also unchanged except that in this localized activation mode, the 405 nm activation beam is not attenuated and passes through a mechanical shutter to generate millisecond pulses and is converted into a beamlet bundle by a micro-lens array that forms a telescope with the tube lens. Each expanded beamlet leaving the micro-lens tube-lens telescope overfills the back focal plane of the objective with a different angle of incidence to yield an array of diffraction-limited (DL) activation spots on the sample plane

The grease spreads homogeneously on the circular face of the tube, which is then applied to the coverslip by placing the greased face of the tube onto the coverslip and gently rotating several times before removal. For LPA-SPT experiments we usually use anti-FliC antibodies to attach the cells, as we have found that use of PLL often leads to less reproducible results with live cells, possibly because of perturbations of cell physiology [118]. Anti-FliC antibodies bind non-specifically to the glass surface of the coverslip and very specifically to bacteria's flagella.

2. Cells are concentrated via centrifugation to a final OD $\sim$ 2 in motility medium.

3. Fifteen microliter of concentrated cells is deposited on the round coverslip on the side with the deposited vacuum grease, and 1.5 $\mu$l of antibody solution (2 ng/ml) are immediately added.

4. After 20 min incubation at room temperature, the coverslip is ready to be mounted on the flow cell.

### 2.3.11 Cleaning of Flow Cell

Prior to mounting the treated coverslip, the flow cell has to be cleaned to remove impurities (dirt and unwanted particles or chemicals coming from previous experiments). For cleaning, we connect a syringe to polyethylene tubing and flow solvents through the inlet and the outlet of the flow cell to clean and also purge air bubbles that tend to form in the vicinity of the inlet and outlet. Our flow cell cleaning protocol consist of the following steps.

1. Ethanol 100% is flushed into the flow cell by means of a syringe on either side successively.

2. Acetone is flushed into the flow cell by means of a syringe on either side successively.

3. Ethanol 100% is flushed into the flow cell by means of a syringe on either side successively.

4. Check if any air bubbles are in the vicinity of the inlets (see Note 9). If so, repeat step 3.

5. Connect the flow cell to the fluidic pump and seal with an empty greased coverslip.

6. Flow Milli-Q-water for 5 min at 400 $\mu$l/min.

7. Flow buffer for 5 min at 400 $\mu$l/min.

### 2.3.12 Coverslip Mounting

The flow cell is sealed with the coverslip on which bacteria are attached. To seal the flow cell without air bubbles, it is essential that some liquid is present in the chamber. After the last step of the cleaning protocol, flow is stopped and the empty coverslip removed. The buffer-air interface at the now open top window of the flow cell is allowed to bulge and form a convex dome-like droplet by gradually raising the buffer reservoir at the end of the feed tube above the height of the flow cell to apply a gentle gravity flow. The coverslip with attached bacteria is then gently laid on the droplet, the side with the cell suspension

face down, and flow is switched on immediately by applying negative pressure at the flow cell outlet connected to a syringe pump. As liquid is sucked away, the bulge on which the coverslip rests recedes. The coverslip is assisted to its seat at the top face of the flow cell by a gentle push with a wooden toothpick, to achieve sealing of the flow cell just before the bulge disappears. The flow cell is now ready for imaging.

### 2.3.13 Fluidic Switch Valve

Use of a fluidic switch valve allows for media exchange in the flow cell. For tracking receptor clusters in the presence or absence of stimulation, we feed buffer through one inlet of the switch and buffer with stimulus (e.g., 1 mM MeAsp) through the other. The switch is operated manually to perform tracking experiments in the presence and absence of stimulus.

The syringe pump is operated in suction mode, and thus using a 50 ml syringe and a flow rate of 400 $\mu$l/min, measurements can proceed uninterrupted for up to 2 h. For experiments of longer duration, one can stop the flow and empty the syringe, being careful not to create air bubbles in the chamber or to compromise the grease seal of the coverslip by perturbing pressure in the flow cell.

### 2.3.14 LPA-SPT Imaging Protocol

Cells are continuously perfused with fresh motility medium (at 400 $\mu$l/min) in the flow cell assembled as described above. Focal drift in the z-direction is minimized by closed-loop feedback (Perfect Focus System, Nikon). A joystick is used to control the X–Y positioning of the motorized stage for fine adjustments of the field-ofview (FOV) to enhance overlay of the DL 405 nm photoactivation spots with the immobilized bacteria. In our standard protocol, image acquisition in each FOV consists of four repeats of the following sequence: one photoactivation frame, in which a 405 nm pulse is delivered to the sample for localized photoactivation, followed by 249 tracking frames, during which time a 568 nm pulse is delivered for widefield excitation and imaging of fluorescence emission via the camera. Unless otherwise stated, the data described here use a frame rate of 15 fps (frame duration = 65 ms), excitation laser pulse of 30 ms, and an activation pulse of 5 ms. Thus, the number of image frames per FOV is 1000, and the acquisition lasts 65 s. With these settings, we find an average number of tracks per FOV of Ntracks = 604 ± 144 (mean ± stdev.) and an average track length of L = 10 ± 9 (mean ± stdev.).

These parameters were chosen empirically for our experiments, but they can be adjusted for each type of sample to achieve a good balance between track length, throughput (i.e., number of tracks per unit of acquisition time), and precision of localization (see Note 10). The

key parameter is the duration of the 405 nm pulse, which determines the density of activated clusters after each localized activation pulse. If this duration is too long, the frequency of collisions/ near-encounters becomes too high for reliable tracking. If the duration is too short, trajectories will be fewer in number and shorter in length, limiting the quality and quantity of data.

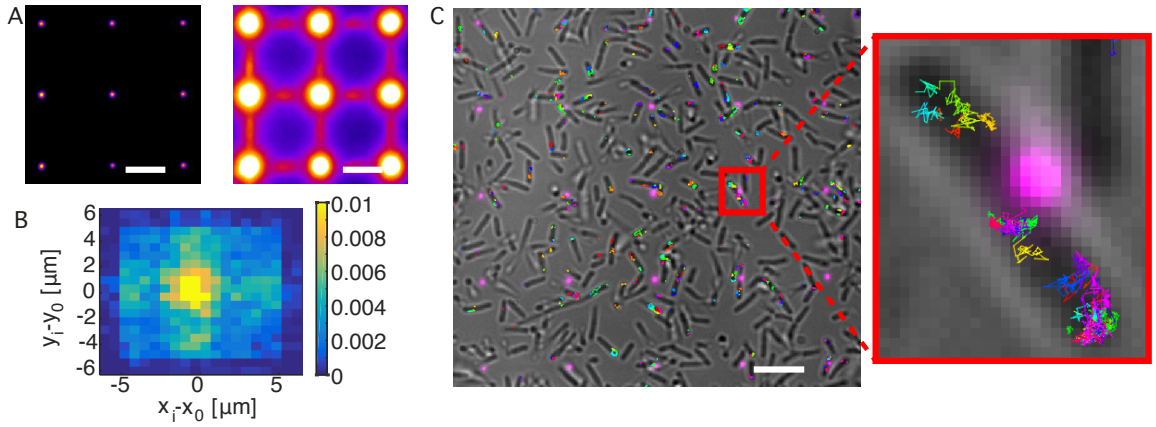


Fig. 2.3.8 **Localized photoactivation and sample trajectories.** (a) Low-contrast and high-contrast images of the micro-lens-generated array of photoactivation spots at the sample plane (left and right image, respectively). The high-contrast image reveals the presence of a pattern of low-intensity 405 nm light between the diffraction-limited foci that form photoactivation hot spots. (b) Two-dimensional histogram (probability mass function) for the initial position of tracks $[x_i, y_i]$ relative to the nearest photoactivation hot spot $[x_0, y_0]$. Photoactivation density is clearly peaked at the hot spots ($[x_i - x_0, y_i - y_0] = [0,0]$), but a considerable fraction of localizations also occur outside of this central peak, with a pattern that closely resembles the unit cell of the repeating pattern in the high-contrast image of panel A. Data from 25 FOVs, number of tracks $\sim$ 30,000, strain used: TSS1020. (c) Typical field of view (left) with image of photoactivation hot spots (violet) and receptor-cluster trajectories overlaid. Zoomed view of a cell lying near a photoactivation hot spot (right) reveals the diversity of trajectories, which vary with respect to their length, mobility, and cellular location. Scale bar: 5 $\mu$m. Localized-activation pulse: 5 ms, 405. Power: 100 mW. N tracks = 631. Only tracks lasting for five or more frames were retained. Strain used: TSS1020 (see Table 4.2 and 4.1)

The LPA-SPT imaging sequence described above is repeated for many FOVs across the field of coverslip-attached cells. Using a motorized stage, we sample the coverslip in an approximately periodic 2-D grid across the square window of the flow cell, using a motorized stage to initialize the positioning of FOVs in a periodic array (with pitch 500 $\mu$m). We use manual fine-tuning of FOV position to maximize coincidence between the DL 405 nm photoactivation spots and attached bacteria. By systematically sampling FOVs in a well-

spaced grid, we avoid imaging the same cells twice. This grid-like sampling of FOVs with sufficient spacing was found to be important for reproducible results, as tracking results were found to depend on the number of imaging cycles a cell has undergone (presumably due to the relatively strong 405 nm irradiation, which can perturb cell physiology). Combined with sufficient care to keep acquisitions within each field of view reasonably short (see above), we found that reproducible results are achievable in LPA-SPT.

The 405 nm intensity at the DL photoactivation spots is ∼100 times higher than that for the area outside the spots, so the efficiency of activation is concomitantly high at, and very close to, each photoactivation spot. However, the entire FOV is exposed to a finite intensity of 405 nm irradiation, with a non-uniform intensity profile in the region between spots that is determined by the square-grid arrangement of microlenses in the array (see high-contrast and low-contrast images of the microlens-generated spots provided in Fig. 2.3.8a). Given that the total FOV area is much greater than that of all spots combined, there is also a considerable fraction of "off-spot" activation events (see Fig. 2.3.8b). In our typical analyses, we also include tracks originating in off-spot photoactivation to increase tracking statistics.

### 2.3.15 LPA-SPT Data Analysis

Tracks are obtained from LPA-SPT image sequences using the u-track package [119], integrated into custom MATLAB scripts to automate data handling. The tracking algorithm performs very well on LPA-SPT data, which consist of low-background images of point emitters with well-separated trajectories. An example FOV (Fig. 2.3.8c) demonstrates the efficiency of tracking under our standard conditions for Tar-mEos2 imaging (∼500 tracks of length >5 frames per FOV, in which 1000 frames are acquired). Track length is also enhanced in LPA-SPT, relative to PALM tracking, as shown in Fig. 2.3.9a.

The brightfield image of each FOV is segmented to extract masks for cellular position analyses of tracks. For each track we identify the bacterium to which it belongs, as well as its location along the long axis of the cell. Positional information about individual tracks is useful, for example, in looking at differences between the mobility of chemoreceptor clusters residing at the cell poles ("polar clusters") and those residing elsewhere ("lateral clusters"). These two cluster types have been found, through diffraction-limited imaging, to have contrasting mobilities, with polar clusters moving more rapidly than lateral ones [120]. With LPA-SPT, we also find a strong difference between mobility of polar and lateral Tar-mEos2 clusters (Fig. 2.3.9b), but with the signs reversed (i.e., polar clusters move more slowly than lateral ones).

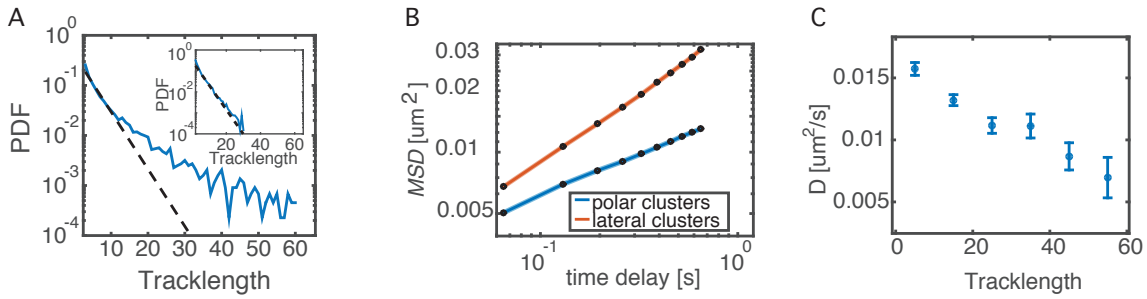


Fig. 2.3.9 **Example tracking statistics from LPA-SPT experiments.** (a) Comparison of track-length distributions from a typical LPA-SPT experiment (main panel) and PALM tracking (inset). LPA-SPT tracks are significantly enriched for long trajectories that give the distribution a broad tail. Dashed lines are fits of the initial decay by an exponential $a\ e^{-bn}$, where n is the number of frames and b = 0.26 for the main panel, and b = 0.25 for the inset. For the main panel, the mean, standard deviation and maximum track length were 8, 9, and 61, respectively, and the number of tracks was ∼4400, collected from ∼600 cells in ten FOVs. For the inset, the mean, standard deviation and maximum track-length were 4, 3, and 31, respectively, and the number of tracks was ∼6000. (b) Mobility of clusters in different cellular locations. The mean-squared displacement (MSD) grew sublinearly with time. Fitting a linear function to the first three points of the MSD versus time curve yielded an apparent diffusivity $D_{lin} = (6.0 \pm 0.8) \times 10^{-3} \mu m^2/s$ for polar clusters and $D_{lin} = (13.5 \pm 0.8) \times 10^{-3} \mu m^2/s$ for lateral clusters. Errors on $D_{lin}$ were obtained from the covariance matrix of the linear fitting parameters. Fitting with a power law ($MSD \sim D_{PL} t^{\alpha}$) yielded $\alpha = 0.4 \pm 0.01$ and $D_{PL} = (21.7 \pm 0.4) \times 10^{-3} \mu m^2/s$ for polar clusters, $\alpha = 0.69 \pm 0.02$ and $D_{PL} = (42.3 \pm 0.7) \times 10^{-3} \mu m^2/s$ for lateral clusters. Polar clusters were defined as those spending 80% or more of their time in regions within 15% of the cell length from the cell pole. Lateral clusters were defined as those spending 80% or more of their time beyond 15% of the cell length from the cell pole. (c) Relationship between mobility and length of tracks. The negative correlation is consistent with the expectation that, on average, tracks for larger clusters are longer (because they will have more photoactivated fluorophores), and larger clusters diffuse less rapidly. The number of tracks was ∼5000, collected from ∼1100 cells in nine FOVs. Strain used: TSS1020, except for panel (a) inset, which used strain TSS1893. See Table 4.1 and 4.2 for strain information, and Table 2.4 for imaging conditions

The reason for this apparent discrepancy merits further study, but it likely reflects the depth of sampling. The diffraction-limited imaging employed n [120] resolves only the largest clusters in the cell, whereas LPA-SPT enables tracking across the full range of cluster sizes, from single receptor dimers to the largest clusters in the cell.

LPA-SPT can photoactivate multiple fluorophore labels per tracked cluster, and the expected number of activated labels increases with cluster size. Combined with the expectation that larger clusters will tend to move slower (because of increased viscous drag), we expect

a negative correlation between mobility and track length. Such a trend is indeed observed in our SPT data (Fig. 2.3.9c). Thus, the length distribution of tracks from LPA-SPT carries information about the size of clusters.

| | **Excitation power, mW** | **Excitation duration, ms** | **Frame duration** | **Activation pulse, ms** | **Activation power, mW** | **Activation frequency** | **Number of frames** |
|---|---|---|---|---|---|---|---|
| LPA-SPT | 60 | 30 | 65ms (15fps) | 1 | 100 | 1/250 frames | $10^3$ |
| PALM-SPT | 100 | 5 | 65ms (15fps) | N.A. | 0.01 | continuous | $10^4$ |

Table 2.4 Experimental parameters for single-particle tracking

### 2.3.16 Notes

1. Care should be taken when pH-ing the MeAsp solution as the pH curve of MeAsp is extremely steep around pH 7. If pH 7 is exceeded and HCl has to be added to lower the pH, salts will form and this should be avoided. Use very small NaOH volume increments or increase the temperature to $\sim$80 °C to facilitate dissolution.

2. The use of an AOTF in the excitation path is optional in both PALM and LPA-SPT—it is possible to localize single or clustered emitters also with continuous illumination. Use of the AOTF provides more flexibility in the design of the single-particle tracking protocol in LPA-SPT experiments, by enabling stroboscopic illumination (i.e., excitation times shorter than the camera exposure).

3. In preparing PALM coverslips, care should be taken in obtaining a round droplet on the coverslip. The poly-l-lysine tends to slip away from very clean glass, so a perfectly flat surface is recommended.

4. An experimental variable that strongly affects the frequency of false-positive detections is growth medium. We successfully perform PALM imaging of cells grown in a well-defined medium (H1 for our experiments). However, our attempts to image cells grown in less controlled culture media failed. Indeed control cells expressing no fluorescent protein exhibited a large number of false-positive detections when cells are grown in TB. By contrast, the false-positive rate was negligible when the same cells are grown in H1 minimal medium. Extensive washing with buffer of cells prior to imaging does not eradicate such false positives. Growth on minimal salts medium is thus recommended for PALM imaging.

5. For PALM imaging, optimal values for fixation time and temperature may vary considerably between different organisms/ strains/growth conditions. We find that room temperatureand fixation for 10 min in 4% PFA is a suitable protocol for chemoreceptor imaging. Temperature does not affect the efficiency of fixation while longer fixation time gives rise to increased false-positive localizations in our hands.

6. In constructing the PALM imaging chamber, the sealing step requires some practice. In particular, care should be taken to avoid wetting the top surface of the rubber spacer, as this can impair the integrity of the seal between the spacer and treated coverslip. Poor sealing in turn leads to increased sample drift and, in extreme cases, to leakage. To minimize wetting of the spacer, sealing should be executed with care and as rapidly as possible. In the event of accidental wetting, the seal may yet be rescued if the amount of liquid wetting the surface is small, by carefully drying it from the sides of the chamber with absorbent paper.

7. False-positive PALM localizations can result from many variables that are not under control of the experimenter, e.g., impurities in the sample, autofluorescence of cellular components, products of fixation. Our experience is that cleaning every component (including the rubber spacer and the glass slides) of the PALM chamber with H2O2 at $\sim$100 °C helps reduce the number of false positives. We performed tests in cells that do not express labeled proteins and we nevertheless find false positives even under the most careful cleaning conditions. In Fig. 2.3.10, we present cumulative distribution functions of the number of localizations per cell for two experiments, one in which the number of false positives is much smaller than the labeled proteins (leading to saturation of the cumulative distribution curve), and another in which a high incidence of false positives leads to continued increase of the cumulative emitter count over $\sim$105 frames (and severely corrupts data to preclude reliable analyses, e.g., cluster size estimation).

8. The specifications for the LPA-SPT micro-lens array (focal length at 405 nm F $\simeq$ 25 mm, pitch = 1500 $\mu$m, array of 6 × 6 = 36 micro lenses) must be chosen to match those for the objective lens and other components of the imaging system. In our setup, the tube lens in the excitation/photoactivation path has a focal length of 300 mm ("Tube Lens 1" in Figs. 2.3.1 and 2.3.7). To fill the back aperture of the 100× NA1.49 objective (diameter $\simeq$ 17 mm), we had to expand about 12× each 1500-$\mu$m beamlet from the micro lens array, leading to the requirement F $\simeq$ 300/12 = 25 mm. The pitch was chosen such that the distance between activation spots at the sample plane was about 10 $\mu$m. Using 150× magnification for imaging, this pitch gives 5 × 5

= 25 photoactivation spots within the FOV of our EMCCD camera (chip size = 8192 × 8192 $\mu m^2$).

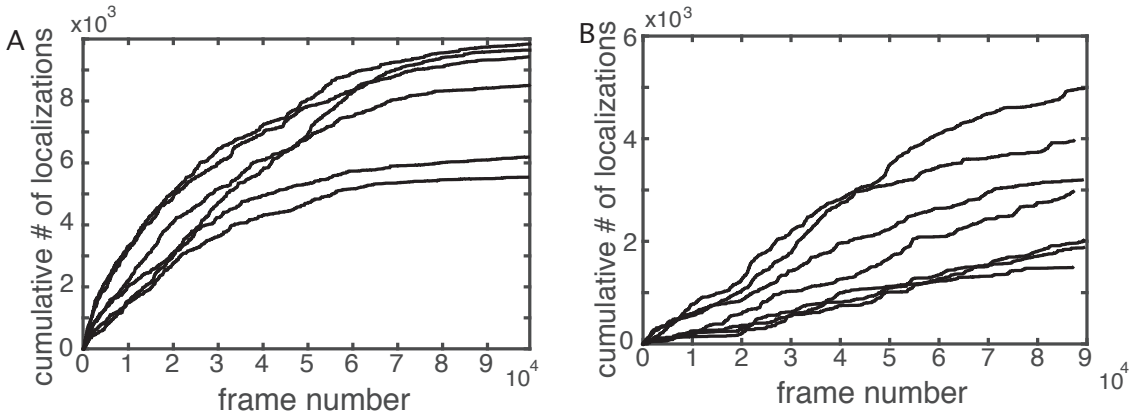


Fig. 2.3.10 **Optical setup for Localized PhotoActivation Single-Particle Tracking (LPA-SPT).** The excitation path is identical to that described in Fig. 2.3.1 for PALM imaging. The activation path is also unchanged except that in this localized activation mode, the 405 nm activation beam is not attenuated and passes through a mechanical shutter to generate millisecond pulses and is converted into a beamlet bundle by a micro-lens array that forms a telescope with the tube lens. Each expanded beamlet leaving the micro-lens tube-lens telescope overfills the back focal plane of the objective with a different angle of incidence to yield an array of diffraction-limited (DL) activation spots on the sample plane

9. Removing air bubbles is particularly important, as they can drastically perturb cell attachment, flow profile, the imaging quality and integrity of the vacuum-grease seal; an air bubble reaching the imaging chamber often forces one to terminate the experiment prematurely.

10. For reliable tracking in LPA-SPT, it is essential to limit the photoactivation pulse energy so as to avoid excessive emitter crowding, which can cause problematic collisions and near encounters between tracked objects. Conversely, insufficient photoactivation energy leads to a lower throughput and shorter track lengths. The optimal imaging parameters thus depend not only on the properties of the fluorophore labels and mobility of tracked particles, but also on the density of the tracked particles/ clusters and the number of fluorophore labels per particle/ cluster. For optimizing imaging conditions, it is thus advisable to test a number of acquisition parameter sets, not only for each strain/labeled-protein combination, but also whenever expression levels or protein labeling is modified significantly

## 2.4 Acknowledgments

We thank J.S. Parkinson and G. Pinas for strains, plasmids, and helpful discussions; A.S.N. Seshasayee for strain HS1; and H.C. Berg and K.A. Fahrner for the gift of anti-FliC antibody. This work was supported by NWO/FOM and the Paul G. Allen Family Foundation.

# Chapter 3

# Development of a fluorescent toolkit for quantitative *in vivo* imaging of bacterial chromosomes

Bacterial chromosomes are highly compacted but yet very dynamic and understanding their behavior *in vivo* requires orthogonal approaches at a range of time and length scales. Fluorescence microscopy is the most used tool for studies on the nucleoid spatio-temporal organization *in vivo* but even cutting edge experimental techniques are often limited by diffraction, perturbative labeling and sample preparation protocols. In this chapter, we describe our methodological efforts to implement a suite of fluorescence microscopy tools for imaging the bacterial nucleoid. Most of the described techniques are adaptations of existing imaging and labeling techniques, and for these, we describe the specifics of our local implementation, together with representative data. In addition, we developed a novel in situ DNA label derived from the *E. coli* nucleoid associated protein H-NS, which allows for high-resolution, low-perturbation imaging of chromosomes in both bacterial and eukaryotic cells. Our fluorescent toolkit includes implementations and extensions of 2D-3D PALM that were tested on a H-NS photo-switchable fusion. In a complementary way we implement single-particle tracking and inverse FRAP for DNA-binding proteins mobility estimation. Our toolkit features also a low-perturbation FROS system that was designed and tested to measure distances between labeled loci and an optimized high-throughput mother machine setup and analysis work-flow that can be combined with most of the techniques we describe. Our efforts resulted in a valuable, well characterized toolkit for low-perturbative studies on nucleoid spatial organization in live and fixed bacteria at a wide range of temporal and spatial scales that will be used in the future for comprehensive studies on nucleoid spatial organization in relation to DNA associated proteins and transcription.

## 3.1 Introduction

Studying the nucleoid via quantitative imaging presents challenges due to the broad range of relevant temporal and spatial scales, as well as sensitivity to physiological conditions that can be perturbed by imaging protocols that could impair or bias interpretation of results. Despite its extreme compaction and its seemingly random organization when visualized under a microscope, researchers in the field have figured out by means of orthogonal approaches that the nucleoid is highly spatially organized *in vivo* and such organization seems to be coordinated by many different factors, spanning a wide range of length scales. [121–123, 21, 124, 58, 125, 14, 126, 62]. The nucleoid has also been shown to be very dynamic throughout the cell cycle and in response to external cues, being able to coordinate short time scale processes like transcription with longer time scale processes like DNA replication and segregation as well as modulating its morphology in response to changes in the environment [127, 128, 69, 129, 84].

To understand such an intertwined spatio-temporal organization, researchers have employed a wide variety of microscopy and DNA labeling techniques such as super resolution (PALM, STORM), fluorescent repressor-operator system (FROS), diffraction-limited fluorescence, single-particle tracking, DAPI and endogenous labeling via HU fluorescent fusions [130] among others. Nevertheless, each of these techniques presents different pros and cons. PALM for instance ([74]) provides resolution on the order of 10nm but it requires fixation thus suppressing dynamics and potentially introducing structural perturbations via cross-linking. By contrast, with nucleic acid staining (e.g. via DAPI, SYTOX [131]) and single-particle tracking of labeled loci or single fluorescent proteins is possible to investigate the temporal evolution of global and local nucleoid morphology but at low spatial resolution and short length scale respectively. Importantly, nucleic acid staining and tracking often involve complicated incubation protocols and cells are subjected to abrupt changes in their environment before the imaging experiment that could perturb physiology and trigger uncontrolled cellular responses. The mother machine overcomes this limitation by allowing imaging during exponential growth but cells are usually wobbling in the growth channels and precise localization of subcellular components have to be carried out in some other way e.g. by agarose pad immobilization. Though, agar pads render controlled medium switching challenging, a feature that on the other hand the mother machine possesses. Another example of this pros and cons scheme is FROS, where the high spatial and genomic resolution is a trade-off with the amount of genetic engineering effort for producing the strains.

Thus, quantitative studies on nucleoid spatial organization throughout the cell cycle cannot be carried out exhaustively employing a single microscopy technique: a wide range of spatial and temporal scales needs to be investigated to understand the dynamic nature

of bacterial chromosomes and each of the available techniques exhibit a trade-off between spatio-temporal resolution, physiological perturbation, amount of genetic engineering work and other experimental parameters.

With this in mind, we developed a set of microscopy, DNA labeling and genetic engineering tools for quantitative experiments on nucleoid spatio-temporal organization trying to minimize physiological perturbations and covering the relevant range of length and time scales for nucleoid transactions. Here we describe our toolkit for fluorescence microscopy comprising of a novel *in situ* DNA label and a series of implementations of modern experimental techniques described earlier that were tested and improved to minimize perturbation.

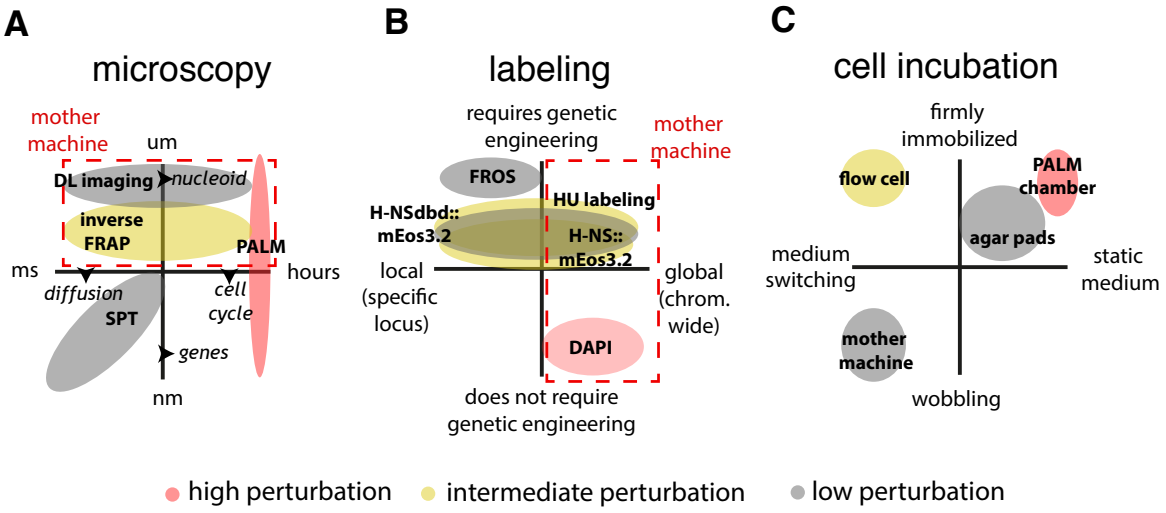


Fig. 3.1.1 **Overview of our toolkit for fluorescent microscopy on the nucleoid.** **(A)** Time and length scales accessible by the microscopy techniques we implemented and developed . Ellipses represent different microscopy techniques and their position and extension shows the temporal and spatial scale at which they are usable for experiments. Here, as in the other panels, colors indicate different levels of physiological perturbation (grey=low, yellow=intermediate, red=high) **(B)**. The DNA labeling techniques described in this chapter present different degrees of genetic engineering efforts and are suitable for local genetic spatial organization studies (e.g. FROS) or global (e.g. DAPI). **(C)** Our toolkit provides different cell incubation protocols with different immobilization-medium switching trade-offs.

Figure 3.1.1 shows the techniques in our toolkit in relation to some of the more important variables for studies on the nucleoid: time-length scale, perturbation degree, medium switching, cell immobilization and amount of required genetic engineering. Figure 3.1.1 shows that by applying our tools to the study of a particular question related to nucleoid organization, it is possible to cover a relevant fraction of the phase space generated by the aforementioned

experimental parameters including a subset of experiments that can be carried out at low physiological perturbation.

To minimize perturbations to endogenous protein function and DNA structure we designed a novel DNA label based on an endogenous DNA-biding protein from *E. coli*. We produced fluorescent fusions to a truncated version of H-NS lacking the dimerization domain responsible for the formation of higher order binding modes of the full H-NS, leaving the DNA binding domain alone with the fluorescent tag (mEos2 and mEos3.2). We named the unlabeled truncated H-NS construct "H-NS-dbd", for H-NS DNA-binding-domain. Our fusion, which can be expressed *in situ* without any chemical treatment, has a lower affinity to DNA when compared to the full H-NS and can be used in both eukaryotic and bacterial cells. Our construct does not perturb H-NS functions as opposed to endogenous labeling of DNA-binding proteins e.g. HU fluorescent fusions [130].

Our toolkit for nucleoid fluorescence imaging features a set of photo-switchable fusion (mEos2 and mEos3.2 [132]) to the full version of the DNA-binding protein H-NS that we constructed for high-resolution imaging of labeled chromosomes. In combination with astigmatism-based 3D PALM, our fusions allow for 3D super resolution image reconstruction of labeled nucleoids.We also combined our fluorescent fusions with inverse FRAP via localized photo-activation (LPA, see Chapter 2) or live-cell PALM tracking, providing a complementary framework for studies of mobility of labeled DNA-binding protein in crowded environments.

For live-cell studies on the local organization of genetic material in bacteria, we developed a two-color FROS labeling system consisting of only 6 operator repeats for each of the two insertions and found experimental conditions where we could reliably track and measure distances between labeled loci over many frames despite the low photon budget. We report here proof of principles experiments on one of the designed strains, characterizing and verifying our FROS system under different angles.

We also discuss here our expanded (capable also of measuring FRET signals) mother machine experimental and analysis setup that was used to investigate the dynamics of nucleoid response under osmotic shocks in relation to intracellular crowding (see chapter 5) and discuss its expanded capabilities when combined with other techniques.

By employing our toolkit we will be able in the future to approach questions related to DNA organization from orthogonal angles overcoming the trade-offs of single techniques. The toolkit will be employed in experiments aimed at understanding the interplay between the complex DNA spatio-temporal organization in prokaryotes and the robust and vital process of gene expression and gene regulation as well as the interplay between chromosome compaction and crowding. The power of our suite of tools for fluorescent microscopy resides

in the wide range of spatio-temporal scales that it covers, in the low perturbation degree of our implementations for live-cell imaging and in the possibility to combine and/or apply each technique to the same research question.

## 3.2 Results

### 3.2.1 A novel fluorescent DNA label for *in vivo* chromosome imaging derived from the H-NS DNA binding domain (HNS-dbd).

Fluorescent DNA labeling for live-cell microscopy imaging experiments usually involves some kind of perturbation to physiology and DNA structure due to e.g. intercalation, buffer switching or fixation (see Introduction section). We describe here a novel *in situ* DNA-label based on genetic editing of the nucleoid-associated protein H-NS that bypasses the aforementioned physiological perturbation. H-NS is an abundant DNA-structuring and regulator protein that binds unspecifically to DNA via its DNA-binding domain and that can associate with other H-NSs via its multimerization domain. We reasoned that if we could remove the multimerization domain, the truncated H-NS would still bind the DNA unspecifically but without perturbing the endogenous H-NS function and exhibiting lower DNA binding affinity. For these reasons it would be ideal for unperturbative DNA labeling. We constructed such a truncated version of the *hns* gene and fused it to mEos3.2 leaving the fluorophore alone with the DNA binding domain with no chances of multimerization. We called our fusion H-NS-dbd::mEos3.2 ("dbd" standing for "DNA-Binding-Domain"). We then cloned our construct into a plasmid (pBAD33) under the control of an arabinose inducible promoter and transformed into MG1655 *E. coli* strain.

When we first expressed and imaged the construct in live and fixed *E. coli* we could not observe efficient nucleoid labeling: some cells exhibited a fluorescence spatial distribution reminiscent of the nucleoid shape while in most cells the fluorescence signal was pretty homogeneous and did not colocalize strongly with DAPI (see Fig3.2.1A,B, and C). These results suggested that the H-NS-dbd::mEos3.2 had a lower affinity than the full length H-NS for DNA, which is actually a desirable feature to avoid interference with DNA transactions. Though, the labeling efficiency was too low under these conditions for a reliable readout of the nucleoid. We hypothesized that a possible cause of this observation could have been binding competition with endogenous H-NS.

We then characterized the mobility of the H-NS-dbd::mEos3.2 in a wild type strain and in an *hns* knockout and compared with the mobility of the full length H-NS fused to mEos3.2 and with that of mEos3.2 alone. Here, we aimed at characterizing the labeling efficiency of

the H-NS-dbd construct via mobility of its labeled version: a higher mobility as compared to the full H-NS version would suggest a weaker binding labeling efficiency and thus strengthen the competition hypothesis. The results of our PALM single-particle tracking experiments are shown in Fig3.2.1D.

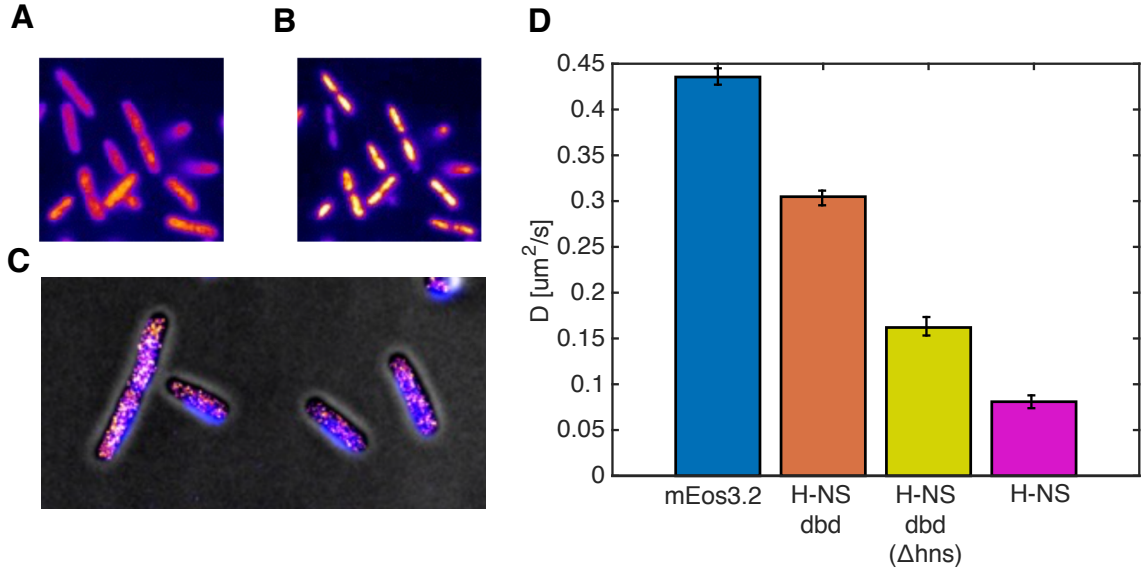


Fig. 3.2.1 **H-NS-dbd::mEOS3.2 is competitively excluded from the nucleoid in the presence of wildtype H-NS. (A)** Diffraction limited image of H-NS-dbd::mEos3.2 in MG1655 (TSS1833) **(B)** DAPI images of the same cells. **(C)** PALM images of H-NS-dbd::mEos3.2 from TSS1833 superimposed with the DAPI profile. DAPI is shown in blue. (**D**) Comparison of mobility of H-NS-dbd in wild type, H-NS-dbd in H-NS knockout, H-NS in wild type and mEos3.2 alone. From left to right: PALM tracking average apparent diffusion coefficient from TSS1843 (blue) expressing mEos3.2 only, N = 1320, <D> = 0.44$\mu m^2$/s , $\sigma$= 0.33$\mu m^2$/s. PALM tracking average apparent diffusion coefficient from: TSS1833 expressing H-NS-dbd::mEos3.2 together with the endogenous H-NS (orange), N = 3768, <D> = 0.31$\mu m^2$/s , $\sigma$=0.26$\mu m^2$/s, TSS1924 expressing H-NS-dbd::mEos3.2 in an H-NS knockout (yellow), N = 1796, <D> = 0.16$\mu m^2$/s, $\sigma$= 0.22$\mu m^2$/s, TSS1779 expressing fluorescent H-NS (magenta), N = 3559, <D> = 0.08$\mu m^2$/s, $\sigma$= 0.15$\mu m^2$/s. Errorbars represent standard error of the mean.

To our initial surprise the estimated diffusion coefficient for the mEos fluorophore alone was one order of magnitude smaller than previously reported values [107]. Such a prominent difference in our estimation can be understood in terms of motion blur and subdiffusivity in relation to our imaging conditions i.e. camera/laser exposure time and interframe interval respectively. In fact, the subdiffusive nature of proteins in the cytoplasm caused by cellular confinement makes the estimated diffusion coefficient depend on the sampling time interval

used for tracking: the larger the sampling time interval, the lower the diffusivity ([107]) and our sampling time interval (20ms) is 20 times larger than the one used in [107]. In addition, motion blur imposes a detection threshold on the speed of a cytoplasmic molecule [133] as the photons will be spread over a larger area and the blurred PSF can fall below the background fluorescence noise. We think that for this reason we are probably missing the population of fast diffusing mEos fluorophores under our imaging conditions. Despite these sampling and motion blur biases, PALM tracking suggested that the affinity of the dbd construct in wild type *E. coli* lies in between that of mEos3.2 alone and that of the full H-NS fusion. In fact our estimate of H-NS-dbd::mEos3.2 mobility was more similar to that of mEos3.2, which suggests that the binding affinity is comparatively low. We note that H-NS is a 15kDa protein and that the absence of the dimerization domain ($\simeq$47 amino acids, about 30% of the full protein, [134]) cannot account for the difference in mobility from the full version of H-NS (for cytoplasmic proteins a 30% change in mass is expected to result in an average change of about 10% in diffusivity [40]). Thus, the factor of 3 in the mobilities we measured for H-NS::mEos3.2 and H-NS-dbd::mEos3.2 by tracking cannot be explained by a difference in mass, on the contrary it suggests a difference in DNA binding affinity. In support of the competition hypothesis when we performed PALM tracking of H-NS-dbd::mEos3.2 in an *hns* knockout strain, we measured a mobility lying in between that of H-NS-dbd::mEos3.2 in wild type and that of H-NS in wild type, also confirming the lower binding affinity of our construct with respect to endogenous H-NS.

The H-NS-dbd::mEos3.2 construct (moved to a inducible plasmid) was also tested in eukaryotic cells, which lacks the endogenous bacterial H-NS protein (Fig.3.2.2). In mammalian cells the signal nicely overlapped with the Hoecst and DAPI staining (Fig.3.2.2A,B and C) and when the fluorophore was trasfected alone in the same cells, without H-NS-dbd::mEos3.2, we measured fluorescent signal inside nucleoli and nuclear colocalization was lost as shown in Fig. 3.2.2D, E and F. These results also strengthened the hypothesis of a binding competition with the endogenous H-NS.

We finally tested the binding competition hypothesis by imaging the construct in an H-NS knockout strain and in *B.Subtilis* which does not express the endogenous H-NS. As shown in Fig. 3.2.3 these qualitative results also support our hypothesis since the nucleoid was labeled with high efficiency (as shown by the large dark area in the cells shown in Fig. 3.2.3C and D) both in *B.Subtilis* and in the *hns* knockout.

In conclusion, we proved our H-NS-dbd::mEos3.2 fusions to be able to transiently bind the nucleoid providing a less perturbative readout of nucleoid shape leaving the native H-NS unperturbed.

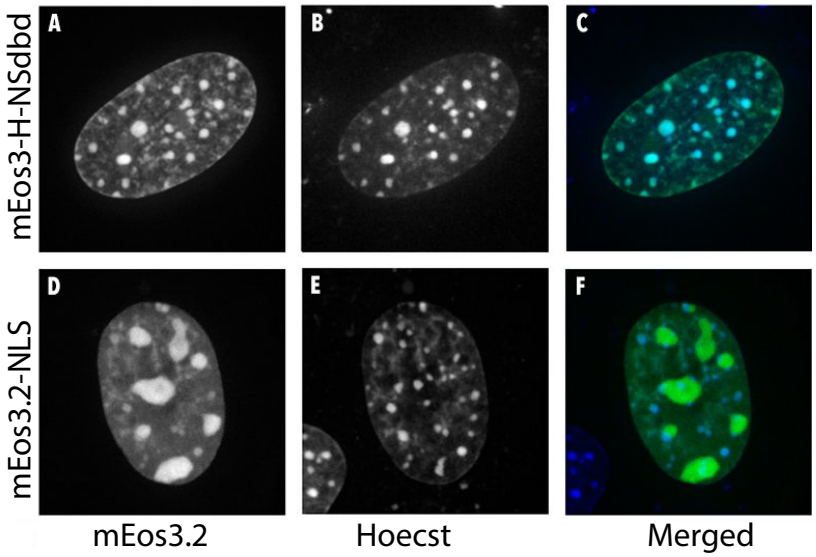


Fig. 3.2.2 **H-NS-dbd::mEOS3.2 efficiently labels chromosomal DNA in eukaryotic cells (U2OS cell line).** **(A)** H-NS-dbd::mEos3.2 labeling appears as several discrete and dense foci and to less extend at the nucleus periphery. **(B)** Stained nuclei inside cells visualized by Hoecst labeling in the same cell shown in (A). **(C)** Overlay of the mEos3.2 and the Hoecst channels shows colocalization of H-NS-dbd::mEos3.2 and Hoecst. **(D)** mEos3.2 alone expressed in the same cell type as in (A-C) is mostly restricted to the nucleoli. **(E)** Stained nuclei inside cells visualized by Hoecst labeling in the same cell shown in (D). **(F)** Overlay of the mEos3.2 and the Hoecst channels shows no colocalization of mEos3.2 and Hoecst. H-NS-dbd::mEos3.2 shows a higher degree of colocalization with DAPI with a PCC of 0.758 than NLS-mEos3.2 (PCC = 0.005)

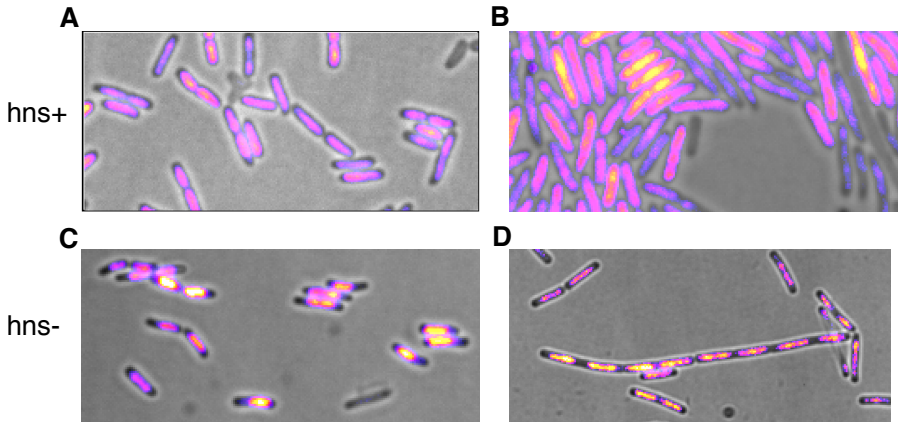


Fig. 3.2.3 **H-NS-dbd::mEOS3.2 efficiently labels the nucleoid in hns- E. coli , as well as B. subtilis cells.** **(A)** H-NS::mEos3.2 in wild type MG1655 (TSS1833) **(B)** mEos3.2 fluorophore alone in wild type MG1655 (TSS1843) **(C)** H-NS::mEos3.2 in ΔH-NS MG1655 (TSS1924) **(D)** H-NS::mEos3.2 in wild type B. Subtilis (TSS2005)

In bacterial strains lacking the endogenous H-NS (e.g. *B.Subtilis*) our construct seems to bind DNA much more efficiently and we provide evidences for a binding competition with the native H-NS protein.

### 3.2.2 High-resolution 2D and 3D imaging of nucleoids labeled via fluorescent H-NS

To explore the local arrangement and structure of the chromosome at a much smaller length scale compared to diffraction-limited imaging, localization-based super-resolution techniques such as PALM require the use of photo-activatable (or photo-switchable) fluorophores that can be localized at the single-molecule level under low intensity UV irradiation which induces stochastic photoconversion of fluorophores. We produced photo-switchable fluorescent fusions (mEos2 and mEos3.2) to the nucleoid associated protein H-NS gene to image the spatial organization of bacterial nucleoids in living cells via fluorescent imaging at high spatial resolution and also used them to compare the binding affinity of H-NS-dbd with that of full-length H-NS (see Fig. 3.2.1). In addition, we set up an experimental framework for 3D PALM reconstruction in order to visualize nucleoid structure in 3D at high spatial resolution. For this purposes, we cloned our fusions into an inducible plasmid and expressed it in *E. coli* to first verify whether we could achieve a readout of nucleoid morphology by fluorescent H-NS DNA labeling.

Our H-NS::mEos3.2 fusion is able to effectively label the nucleoid as shown in Fig. 3.2.4A. After confirming nucleoid labeling via DAPI colocalization with diffraction-limited imaging we proceeded with 2D PALM imaging (the lateral resolution we could achieve via PALM is $\sim$ 10nm). PALM images revealed smaller scale features of our labeled nucleoids that appear blurred with diffraction-limited imaging. Peaks of the DAPI spatial profile are spatially resolved with PALM (Fig. 3.2.4 B,C) and peaks in the projected high resolution PALM reconstruction image coincide with peaks in the projected DAPI image (Fig3.2.4D,E, $p>0.95$). We conclude that our fusions are indeed labeling the nucleoid with high accuracy and that we can observe higher resolution DNA structures by our 2D PALM implementation (Fig3.2.4B and C)

Subsequently, we measured the 3D spatial distribution of the H-NS fusion. We asked whether we could resolve structures that would otherwise be obscured by projection on the xy plane , or by the lower spatial resolution of diffraction-limited fluorescence imaging. Following the approach pioneered in [135] we implemented an astigmatism-based 3D PALM setup by inserting a cylindrical lens in the imaging path of the setup (described in Chapter2).

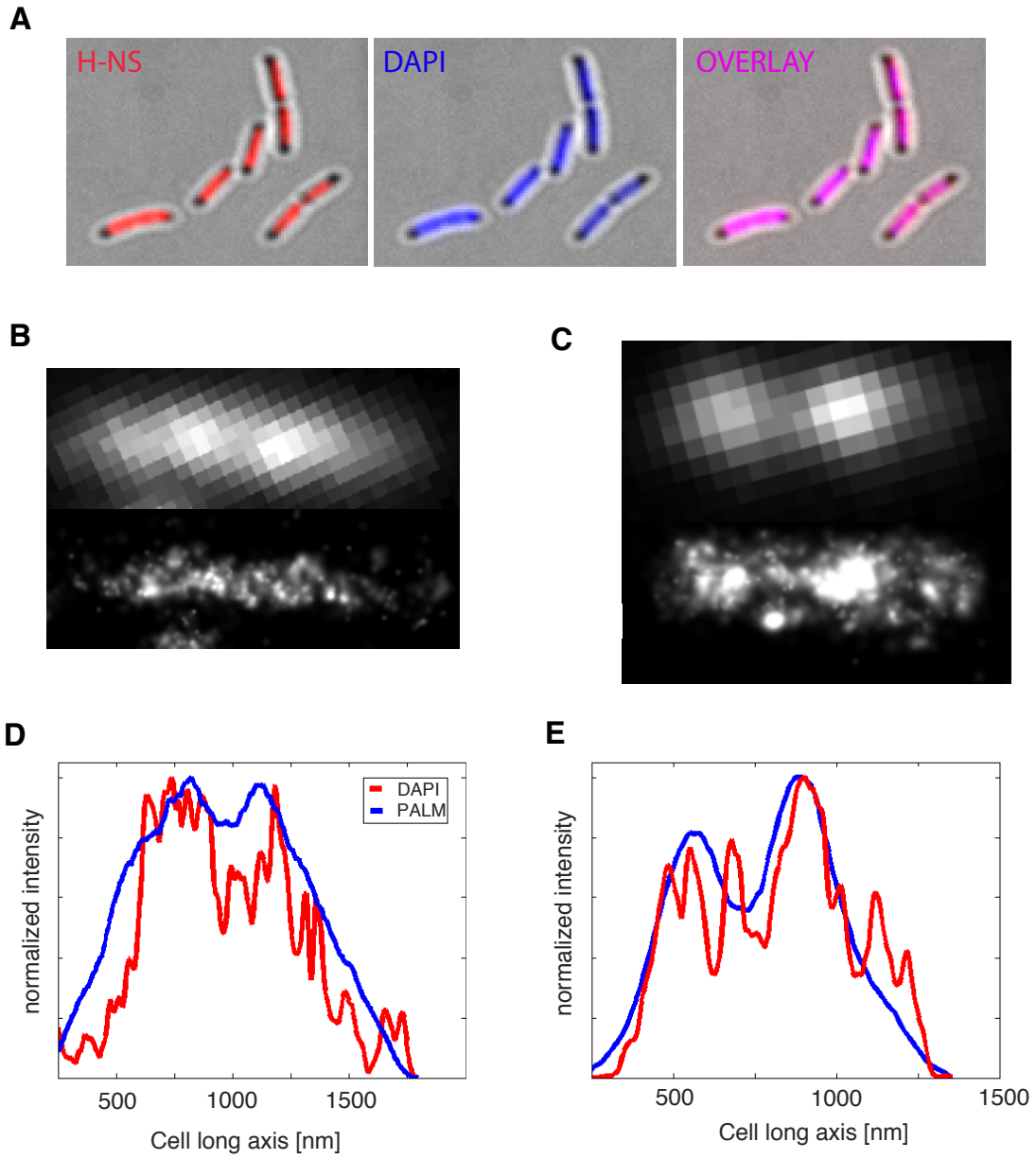


Fig. 3.2.4 **H-NS::mEOs3.2 colocalizes with the standard nucleoid label DAPI. (A).** H-NS::mEos3.2 in TSS1360 (left), DAPI in the same cells (center) and overlay (right). **(B,C,D,E).** DAPI and H-NS::mEos3.2 2D PALM images of two representative cells from our colocalization experiments (upper panel) and their intensity profile projected (summed) over the long axis of the cell (lower panels). diffraction-limited peaks in the projected DAPI intensity are found in correspondence of higher resolution ones in PALM projected intensity profiles.

Upon calibrating the dimensions of the elliptic single-molecule image produced by the cylindrical lens with controlled piezo movements in the z direction, we mapped the shape of the deformed PSF to a z-coordinate value for each PALM localization event. A schematic of the optical system employed and the calibration curves for 3D estimation of the z-position of our PSFs are presented in Fig. 3.2.5A, B and C.

In some of the cells imaged, 3D PALM highlighted interesting features of the nucleoid. Fig. 3.2.5D,E shows an example of a cell with the nucleoid in a helical arrangement. Helical configurations have been predicted by theory for a confined supercoiled ring polymer and have been previously observed at lower resolution by diffraction-limited 3D deconvolution imaging in [129] and (in 2D) in B. subtilis [136]. Nevertheless for a conclusive demonstration of the helical arrangement of the nucleoid more statistics should be collected and experimental controls such as tuning the fluorophore expression level, using other photoactivatable fluorophores and employing complementary techniques like 3D SIM would be necessary.

These findings pave the way for further systematic studies on the 3D organization of nucleoids in bacteria. These labeling and microscopy tools, will enable exploration of the 3D architecture of nucleoids grown at different physiological conditions and under different perturbations e.g. osmotic shock (see Chapter 5).

### 3.2.3 Probing the mobility of DNA-associated proteins using photoconvertible fluorophores.

Despite its capacity for providing high-resolution information on the global spatial organization of bacterial chromosomes, PALM imaging of fixed cells cannot give insights on the dynamics of DNA associated proteins. However, the same photoconvertible fluorophores used in PALM can be utilized for experiments that inform on dynamics of DNA-associated proteins within live cells. Here we describe two different methods with which we have characterized the spatial dynamics of H-NS proteins labeled by photoconvertible fluorophores.

In the first approach, the same localized-photoactivation protocol employed in chapter 2 for localized photoactivation (LPA) was used to photoactivate a subpopulation of H-NS::mEos2 at a diffraction-limited spot within the cells, but the spatial density profile of the photoactivated population (rather than the trajectories of individual localized spots) was followed in subsequent image frames. By activating fluorophores only in a diffraction-limited area, we could follow the dynamics of that subpopulation of emitting H-NS::mEos2 fusion inside living cells. H-N::mEos2 has been shown to form clusters in living cells [137] and we tried to activate fluorophores in single clusters to follow their dynamics (if any) over time.

This approach is similar to a recently described method named Photo-Converted Intensity Profile

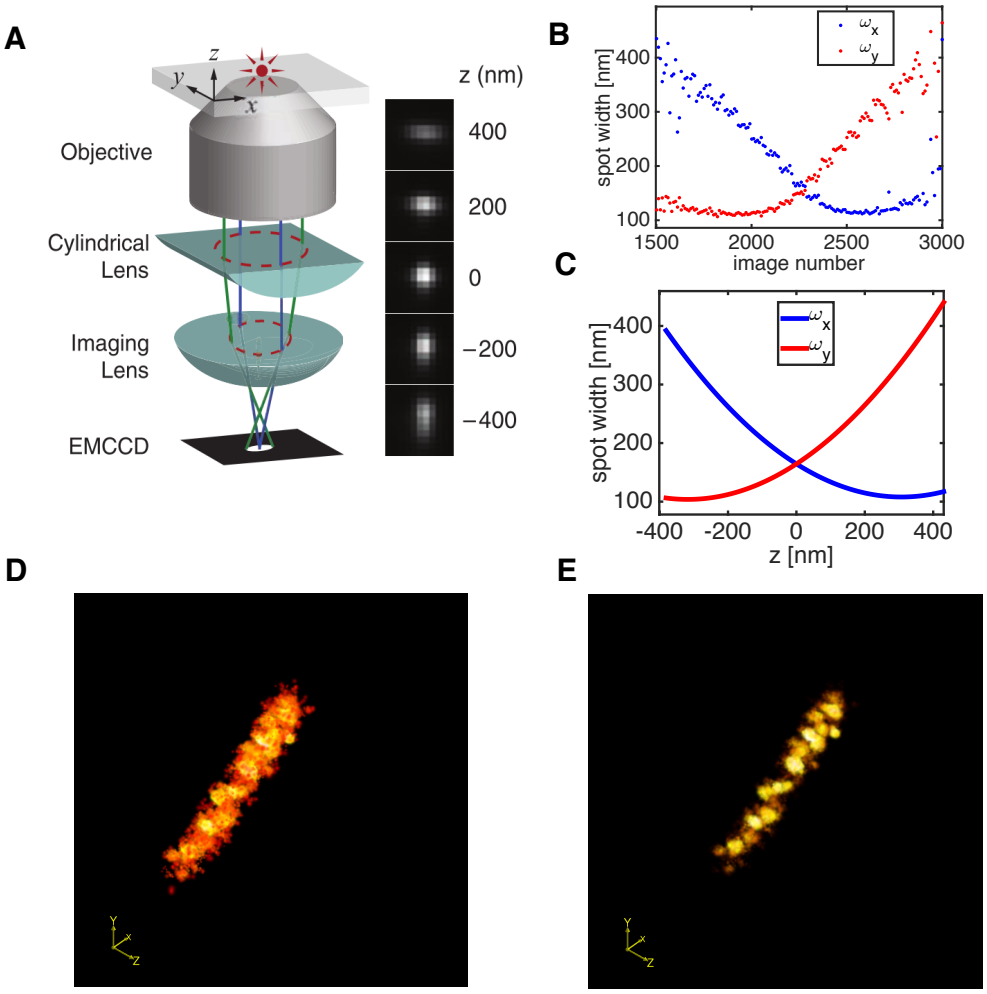


Fig. 3.2.5 **3D PALM setup and example calibration and image data. (A).** Optical scheme for astigmatic imaging. The cylindrical lens (f=1m, Thorlabs) is inserted between the objective and the tube lens placed before the camera. This way sub-diffraction limit emitters will produce asymmetric deformations of the PSFs as a function of the distance from the apparent focal plane, where the PSF is symmetric (image adapted from [135]). **(B,C).** Calibration curves (upper panel) obtained by moving the piezo stage in the z direction in steps of 20nm and measuring the width of the PSF as a function of distance form the apparent focal plane where the width of the PSF in the x and y direction crosses. Lower panel show a fit to the data in the upper panel (fitting function: $y = a(z - z0)^2 + b$ ), taking into account piezo stage movement. **(D).** Representative nucleoids imaged with our 3D PALM system by means of H-NS::mEos3.2 labeling. After performing PALM imaging as described in Chapter 2, we reconstruct 3D high resolution images of nucleoids showing a helical arrangement. **(E).** By filtering the localization over density, the helical arrangement becomes more visible and the regions of high DNA density are highlighted (right panel).

Expansion (PIPE, [138]), although we do not attempt to extract diffusion coefficients as in [138] but rather focus on the timescale over which the labeled H-NS::mEos2 binding proteins exchange between the multiple clusters they form when bound to the nucleoid [137]. A similar experimental framework has also been previously pioneered in [107].

We observed a surprisingly rapid turnover of labeled molecules that appear to hop from one initially photoactivated H-NS cluster to others until reaching within a few minutes a stable density profile in which photoactivated molecules are distributed across multiple H-NS clusters within the same cell. We note that the strong clustering of H-NS::mEos2 observed in the experiment of Fig. 1.2.6 might not be representative of the behavior of the native H-NS protein, as it has been shown that expression of H-NS::mEos2 can lead to fusion protein aggregation artifacts [132]). Although the relatively small data set from this exploratory experiment (Fig. 1.2.6) precludes conclusive quantitative statements, these preliminary observations suggests that the interaction of H-NS proteins with the nucleoid are highly dynamic, with their binding, unbinding, and movement spanning the nucleoid volume on a time scale of the order of minutes, even when fused to an aggregation-prone fluorescent protein.

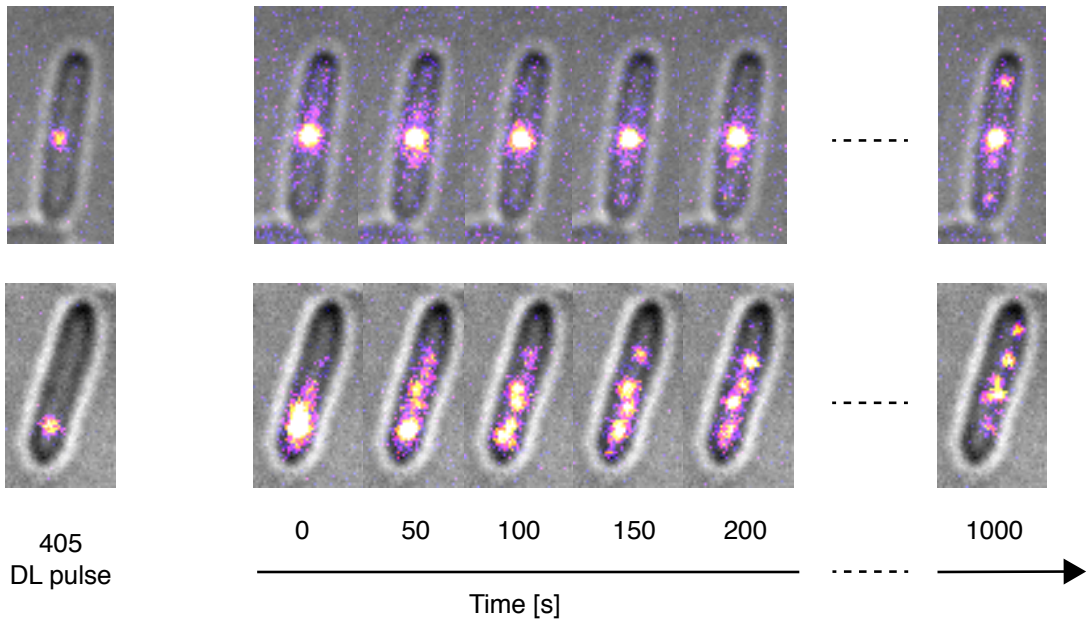


Fig. 3.2.6 **Mobility of H-NS::mEos2 is revealed by the evolution of the fluorescence intensity profile following localized photoactivation.** 405nm laser at 100mW power is focused onto a single cell (left panels). Subsequently the fluorescence signal from activated mEos2 is followed over time. Two representative cells where the activation spot was placed near a pole or in the middle cell are shown.

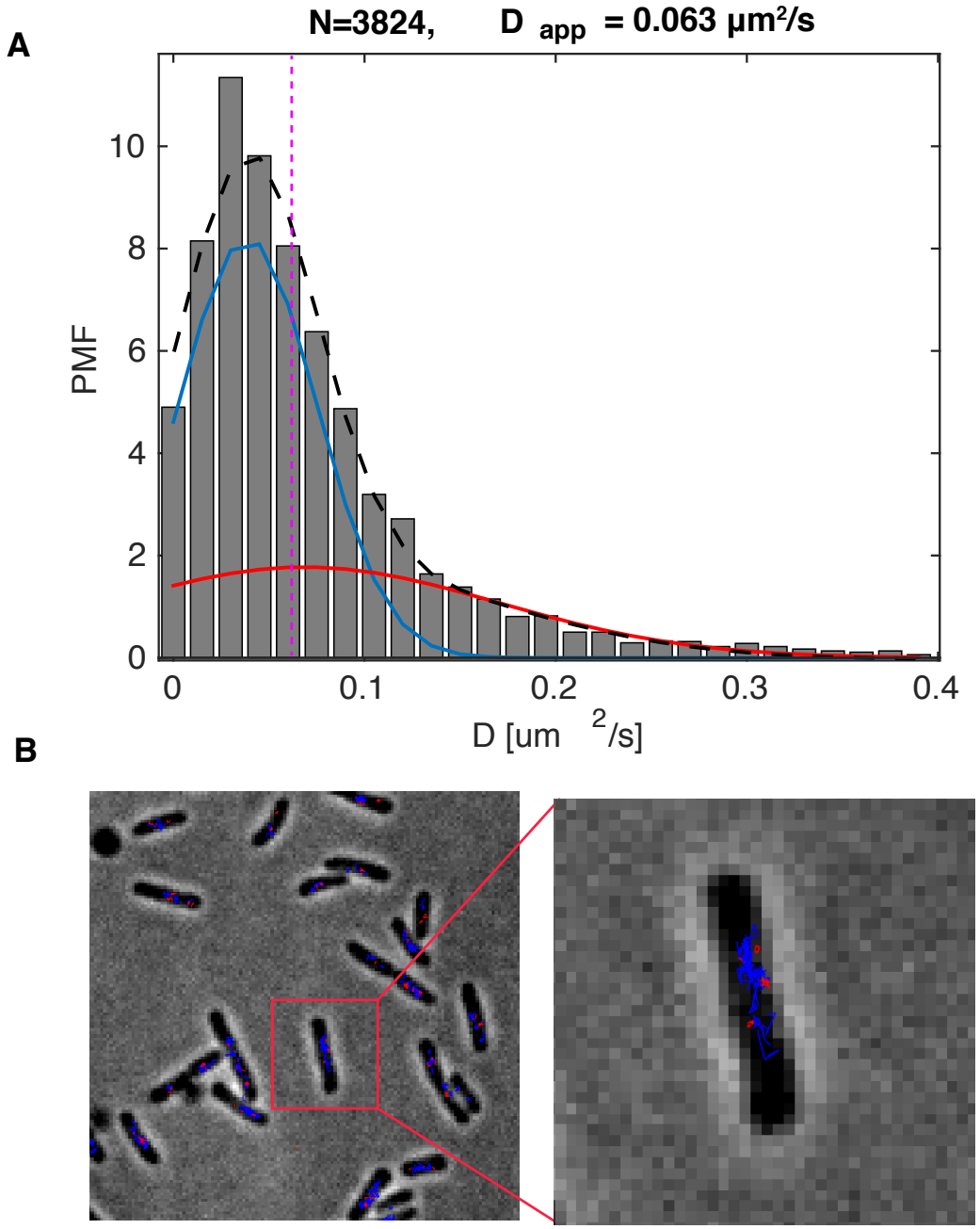


Fig. 3.2.7 **PALM tracking of H-NS::mEos3.2 .** **(A)** Histogram of single-track diffusion coefficient computed using the covariance-based unbiased estimator described in chapter 2. The distribution is not well fitted by a single Gaussian and was fitted with the sum of two Gaussians $f(D) = A_1 e^{(D-D_1^*)^2/\sigma_1^2} + A_2 e^{(D-D_2^*)^2/\sigma_1^2}$ to establish the threshold apparent diffusion coefficient for classifying the tracks as "bound" or "unbound". The fit results in the following parameters: $A_1 = 8.21$,$A_2 = 1.77$,$D_1^* = 0.048\mu m^2/s$,$D_2^* = 0.078\mu m^2/s$,$s_1 = 0.051\mu m^2/s$,$s_2 = 0.143\mu m^2/s$. The threshold value, obtained as the average of the two mean values of the fitting Gaussian ($(D_1^* + D_2^*)/2 = 0.063\mu m^2/s$) is indicated by the vertical pink line. **(B)** Bright field images and tracks overlay. Tracks classfied as "bound" are shown in red while "unbound" tracks in blue.

We used our H-NS::mEos3.2 fusion, which is less prone to aggregation, to perform live-cell PALM tracking [81] in order to estimate the fraction of our H-NS fusion bound to chromosomal DNA. Under these less perturbative conditions (mEos3.2 is more monomeric than mEos2), we found that the mobility statistics of labeled H-NS is consistent with a binding-unbinding dynamics as we were able to sort tracks into 2 families based on apparent diffusion coefficient estimations, following a simplified methodology of that employed in ref. [83]. We fit the diffusion coefficient distribution with two Gaussian functions and established a threshold to distinguish between bound and unbound H-NS proteins (Fig. 3.2.7), computed as the average value of the mean of the two fitting distributions.

The preliminary experiments presented here demonstrate two complementary methods utilizing photoconvertible fluorescent for investigating the dynamics of nucleoid associated proteins: (i) time-lapse imaging of fluorescence intensity profiles following localized photoactivation, (ii) single-particle PALM tracking. These techniques will be instrumental for future experiments aimed at understanding in a quantitative manner how DNA-binding proteins such as H-NS dynamically associate and dissociate with the nucleoid and provide insights on the role of DNA-binding proteins in determining nucleoid morphology and dynamics.

### 3.2.4 Low-perturbation FROS system for studies on local gene compaction

An approach pioneered by Hong et al [139] to quantify the compaction of specific chromosomal segments, and thus to investigate the correlation between gene compaction and gene expression, is to sandwich their ends with different fluorescent labels in order to localize them at the same time and estimate the end-to-end distance of the target segment. Fluorescent Repressor-Operator System (FROS, see Fig. 3.2.8A for an illustration of the technique) is a widespread approach to localize specific DNA loci along the chromosomes in living cells ([140–142, 90, 62, 143, 129, 144, 145]) exploiting the high affinity between repressor proteins and their cognate binding site. By inserting repeated artificial operator sequences near the target chromosomal location and expressing a fluorescently labeled repressor (usually LacI or TetR) at low levels, the fluorescent repressors will form repressor-operator complexes on the operator sequences repeats. As a consequence, a fluorescence focus will form next to the target location when the sample is imaged with sufficient excitation power.

We designed a series of FROS labels employing only 6 operator repeats (see Fig. 3.2.8B) in order to minimize perturbations to local DNA structure induced by long operator repeats. To further reduce the chance/degree of perturbations, we carefully chose the target locations

for the labeling. *E. coli*'s genome is indeed extremely dense in genes leaving very small room for non-coding sequences which would be ideal for inserting the operator arrays.

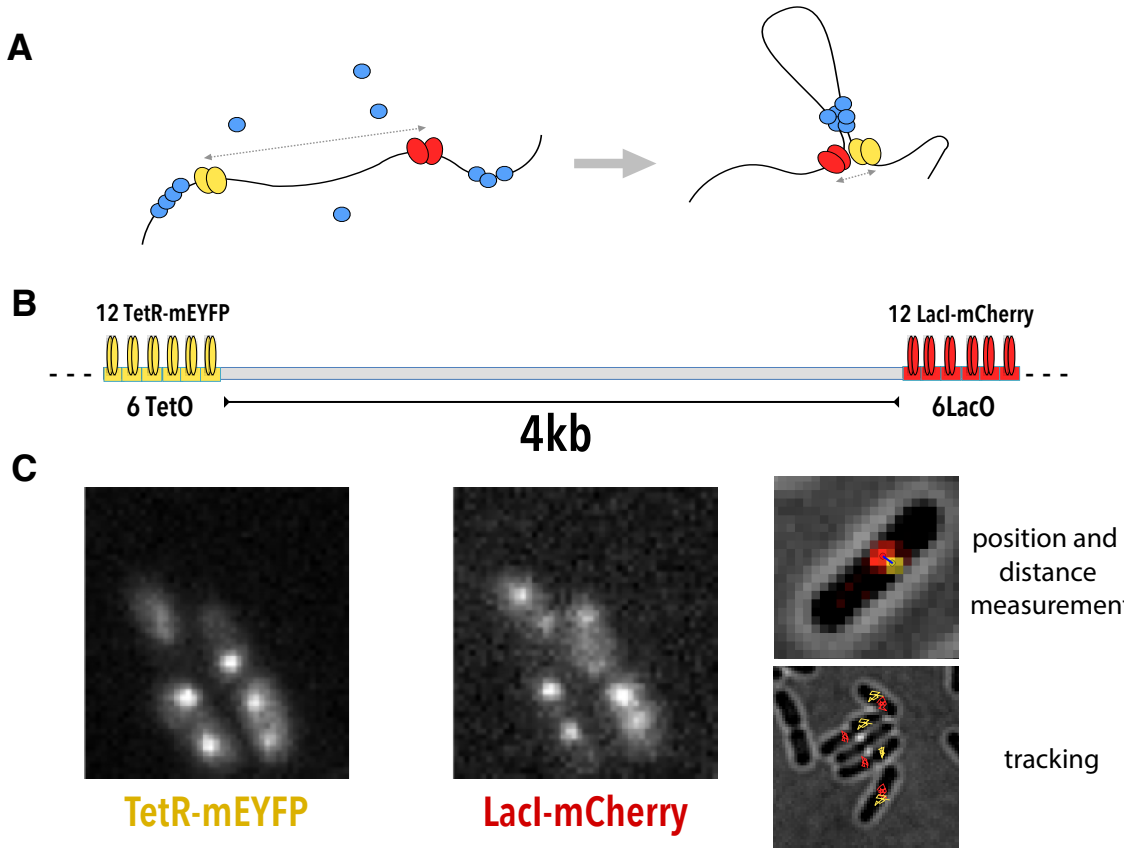


Fig. 3.2.8 **6TetO-6LacO test FROS system.** **(A)** Schematics of repression by looping. Our TetR and LacI fluorescent fusions are depicted in yellow and red. Cyan circles represent Nucleoid Associated Proteins inducing looping by a change in binding mode. Red and yellow ellipses represent our FROS labels. **(B)** Schematic of the genomic insertions of our arrays. The YFP and mCherry tags are separated by 4kb in the test strain (TSS1738). Repressors bind as dimers, leading to a maximum capacity of each 6x operator site to bind 12x fluorescent repression fusions. **(C)** From left to right: example of TetR::EYFP and LacI::mCherry foci, distance measurement (composite images of two fluorescent channels; TetR-mEYFP in yellow and LacI-mCherry in Red; overlaid with phase contrast channel) and tracking of foci (schematics).

Thus, randomly choosing the insertion positions along the genome can produce very drastic genetic perturbations. We selected only intergenic loci in which the two neighboring genes are oriented such that their terminus flanks the intergenic locus (with opposing transcription directions) in order to avoid perturbations to transcription initiation. Here we report the

results of multiple tests we conducted in one of our designed strains and some preliminary pilot experiments, discussing future research directions for investigating the details of transcriptional repression in relation to gene compaction employing a FROS labeling system.

**FROS dual labeling enables measurements of inter-locus distances and locus tracking**

We describe here a set of tests, validations and preliminary experiments on one of our functional strains that we used to thoroughly characterize our FROS system in order to prove it a suitable tool for investigating gene compaction in relation to gene expression.

We first wanted to verify that the number of bound fluorophores producing the FROS spots matched the number of operator repeats we introduced in that particular genomic location. The insertions were validated by sequencing but we wanted to measure the number of bound TetR::EYFP and LacI::mCherry inside living cells. To calibrate the conversion of spot intensity to the number of bound fluorescent molecules, we exploited the propensity of YFP to "blink" (i.e. cycling between an emitting "bright" state and a non-emitting "dark" state) upon high-intensity excitation, prior to irreversible photobleaching [146] in order to estimate the number of photons collected per single YFP molecule under our imaging conditions. We first immobilized cells on agar pads then bleached an entire field of view sufficiently before recording many single TetR::EYFP blinking events inside the cells to estimate the average number of photons collected from a single YFP molecule per frame under our imaging conditions. With this information in hand, it is then straightforward to divide the integrated intensity obtained by TetR::EYFP FROS spots by the intensity per frame of a single YFP molecule to estimate the number of bound YFPs per FROS focus. An example of an intensity trace coming from integrating the fluorescence signal from a single cell in which nearly all fluorophores were previously bleached is presented in figure 3.2.9A. We find that the average number of TetR per FROS spot was close to 12, as expected, given that each of six TetO insertions can accommodate a TetR::mEYFP dimer. When we repeated the procedure for a strain engineered with a 12 TetO repeats (2 of which were proven to be perturbed via sequencing and likely to be non-functional), the calibration yielded a fluorophore count close to 20, again consistent with the expected result as shown in Fig.3.2.9 B and C.

To determine the number of LacI::mCherry in our cells we had to follow a different approach as mCherry does not blink as much as YFP: we first measured bleaching curves of the test strain by exposing cells to a low intensity excitation laser (561nm for LacI::mCherry) until all the fluorophores in the field of view were bleached. Following [147] we then computed the pair-wise differences in intensity from single-cell bleaching curves according to the following formula.

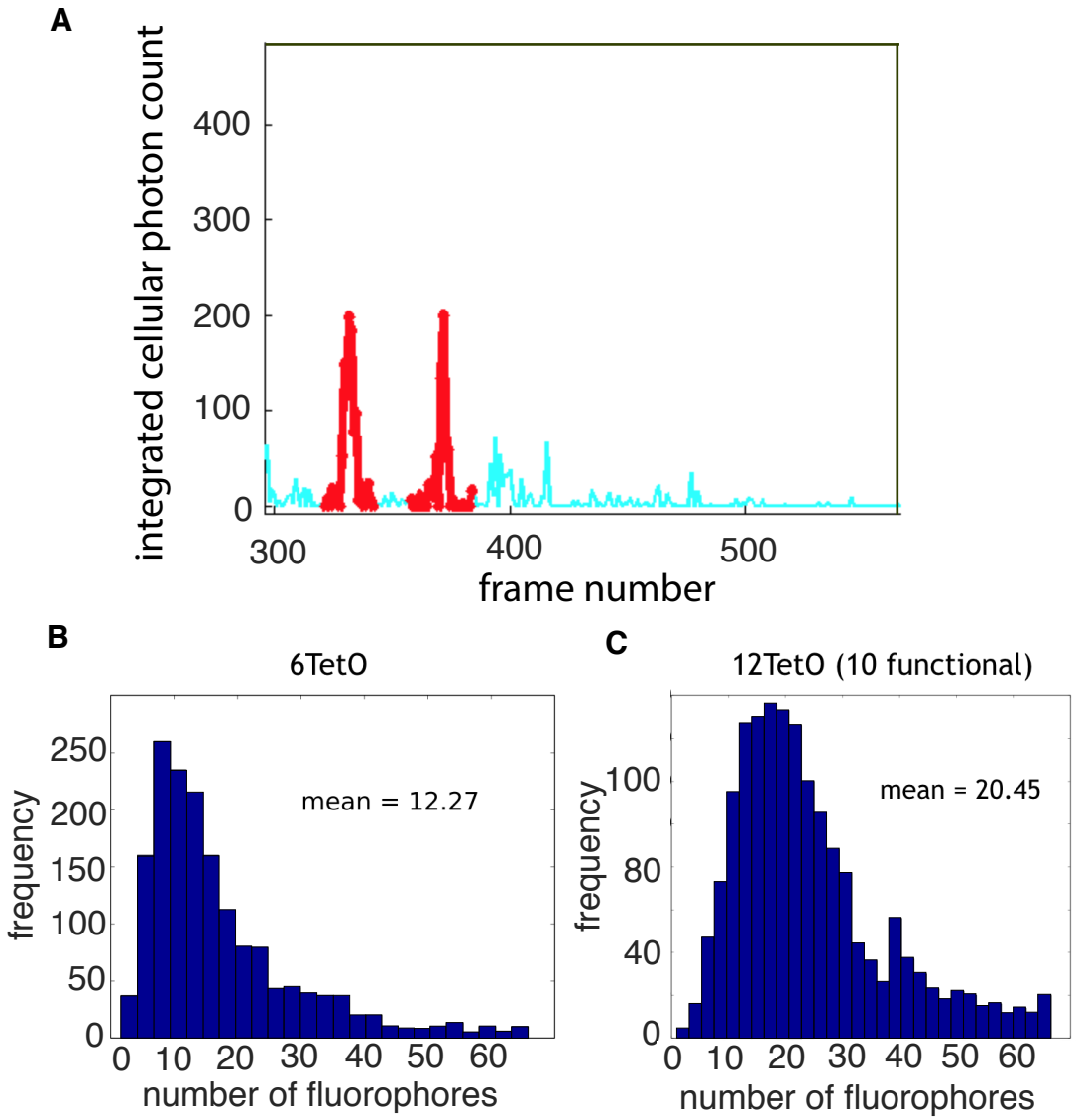


Fig. 3.2.9 **Calibration of EYFP single-molecule fluorescence intensity.** **(A)** Representative intensity time series of single-molecule blinking events following near-complete photobleaching. Intensity is measured after background subtraction, flatfield correction and integration over cell area via bright field image segmentation. In red are indicated blinking events. By averaging the peak values of the blinking events the average number of photons per single EYFP under our imaging conditions is estimated. Ncells=32, strain: TSS1658. **(B)** Histogram of estimated number of bound fluorophores per focus. Upon automated focus indentification from TSS1738 (6T6L, LacI::mCherry, TetR::EYFP) the fitted intensity of multiple YFP focuses are divided by the estimated intensity per single EYFP. **(C)** Same analysis for TSS1664 (12T, LacI::mCherry, TetR::EYFP). Sequencing reported only 10 out of the 12 arrays to be functional for TSS1664.

$$P(i,j) = I(i) - I(j) \quad , \quad for j > i \tag{3.1}$$

The pairwise difference histogram presents multiple peaks, which are approximately equally spaced. Those peaks are produced by subtracting intensity at time points i and j where the difference in intensity is an integer multiple of the intensity of a single mCherry fluorophore $I_{S.F.}$. We take the Fourier transform of the histogram data to identify the most prominent "frequencies" that capture those peaks. The result of the transform is shown in Fig.3.2.10C. We select those peaks in the Fourier transform that exceed $3\sigma$ (where $\sigma$ is the standard deviation of the distribution of the values from the Fourier transform) in amplitude and invert them to compute the number of photons per frame per fluorophore. The result of the analysis is presented in Fig 3.2.10d, showing that under our growth conditions cells have on average just enough fluorophores to fill the LacO arrays, which is consistent with the low background level in our mCherry imaging channel.

We performed tracking on our FROS foci by means of diffraction-limited imaging. Employing an adapted version of our LPA-SPT tracking software (see Chapter 2), we were able to compute the mean squared displacement of our FROS insertions in two different strains from tracks with an average length of 11.5 frames (Fig. 3.2.11B). In one strain (TSS1731) the TetR insertion we tracked (T1) is located inside the replication terminus region, while in another strain (TSS1733) the tracked locus (T2) is located in the left macrodomain. Mobility of chromosomal loci has been the subject of recent studies and is an important proxy for local nucleoid compaction [148, 90]. Previous work in the literature reported a subdiffusive nature of chromosomal loci diffusion and this is also visible in our MSD curves (Fig. 3.2.11C): the negative curvature of the MSD is a clear sign of subdiffusivity and thus, to estimate the apparent diffusion coefficient, we fit the curve with a power law function of the form

$$f(t) = D_{app} t^{\alpha} \tag{3.2}$$

By fitting we find apparent diffusion coefficients that are comparable with those reported in literature and a value of $\alpha = 0.35 +/- 0.03$ which indeed indicates subdiffusivity.

Using the YFP channel of the 6TetO-6LacO strain (TSS1738) we performed tracking of TetO-TetR::YFP complexes, harvesting cells in stationary and exponential phase (Fig.3.2.12A). To test mobility of loci under different growth conditions, we also tracked the arrays in cells grown in the same M9 medium but at 26C. Interestingly, the mobility of the YFP spots in stationary phase cells is strikingly similar to that of cells grown at 26C while for exponential phase cells grown at 37C the mobility is higher (all measurements were

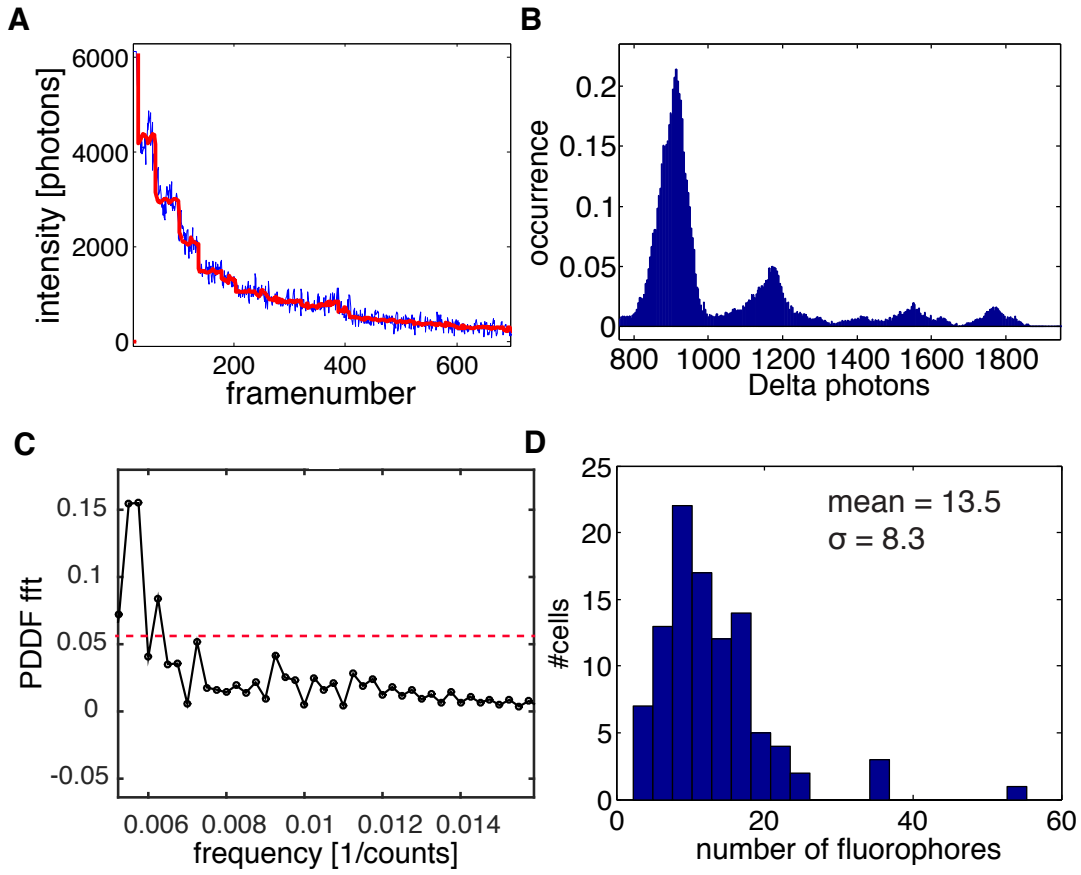


Fig. 3.2.10 **Calibration of mCherry single-molecule fluorescence intensity.** **(A)** Bleaching curve from TSS1658 imaged in the mCherry channel (blue) and corresponding Chung-Kennedy filtered curve (red). **(B)** Pairwise difference histogram peaks roughly correspond to integer multiples of a single mCherry intensity. **(C)** Fourier transform of the pair wise difference histogram (B), horizontal line corresponding to $3\sigma$ of the collection of data points is chosen as threshold to retain only the more prominent modes in the pairwise distribution. Inverting the peak values gives a value of $\sim$ 200 photons per single mCherry. **(D)** Final results from dividing the integrated LacI::mCherry intensity per cell by the single-mCherry intensity estimated before.

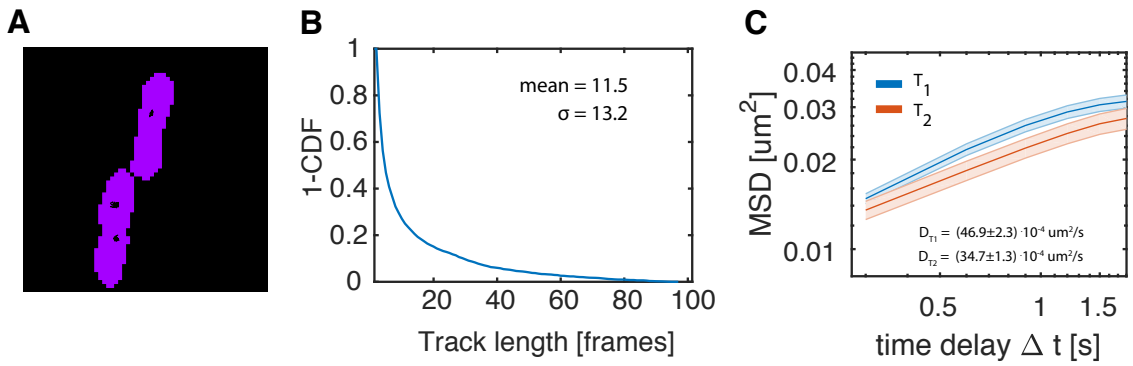


Fig. 3.2.11 **Tracking TetR::EYFP spots at the two FROS sites T1 and T2. (A)** Segmented cells and corresponding tracked TetR::EYFP foci at the T1 locus (black) in TSS1731. **(B)** Tracklength distribution from the tracking experiment on TSS1731 **(C)**, T1 (TSS1731) and T2 (TSS1733) mean squared displacements as a function of time. Apparent diffusion coefficients were estimated by fitting a linear function to the first 3 points of the MSDs curves.

conducted at room temperature, after harvesting). This is consistent with the nucleoid being more compacted in stationary phase [87].

By separately processing YFP and mCherry channels corresponding to TetR::YFP and LacI::mCherry respectively (schematics in Fig.3.2.12B) we compute interloci end-to-end distances and find a peaked distribution. We do so by means of a custom written python code extracting the position of the maxima in the images after maximum filtering, fitting it with a Gaussian function to estimate with high spatial precision the position of the arrays and then taking the distance to the closest YFP or mCherry spot in the cell. When cells had multiple YFP or multiple mCherry foci, we considered only the distance to the closest FROS spot and we discarded cells with odd numbers of foci in each channel (typically 1 or 3) to prevent analysis errors and artifacts.

Our distance estimation presents a clear peak around 150nm (Fig.3.2.12C). We note that the genomic distance between our 6TetO and 6LacO insertions is about 25kbp (kilo-base pairs) and the linear distance of such a DNA segment is $8x10^3$nm (the estimated length of a nucleotide is 0.34nm [149]) thus our measured end to end distances are about 55 times smaller than the linear distance and they is found, in independent cells of the same population, to be distributed around the same average value.

We measured interloci distances and cellular position of the foci along the cell long axis in cells grown in minimal M9 medium until exponential phase (O.D.=0.15) and repeated the same measurements harvesting the same batch culture in stationary phase (O.D.=2). As shown in Fig.3.2.12C the distribution of distances between the spots remained strikingly constant across the two physiological conditions, and we speculate that the genes "sandwiched" by our

LacO and TetO arrays are not involved in the physiological state change between exponential and stationary phase. On the other hand, the positions of the arrays relative to the cell long axis changed significantly (Fig.3.2.12D). In particular the TetO arrays are more likely to be found near the poles of the cell, while in stationary phase they reside more in the central region of the cell. This is again consistent with the idea of the nucleoid being more compact and less active during stationary phase.

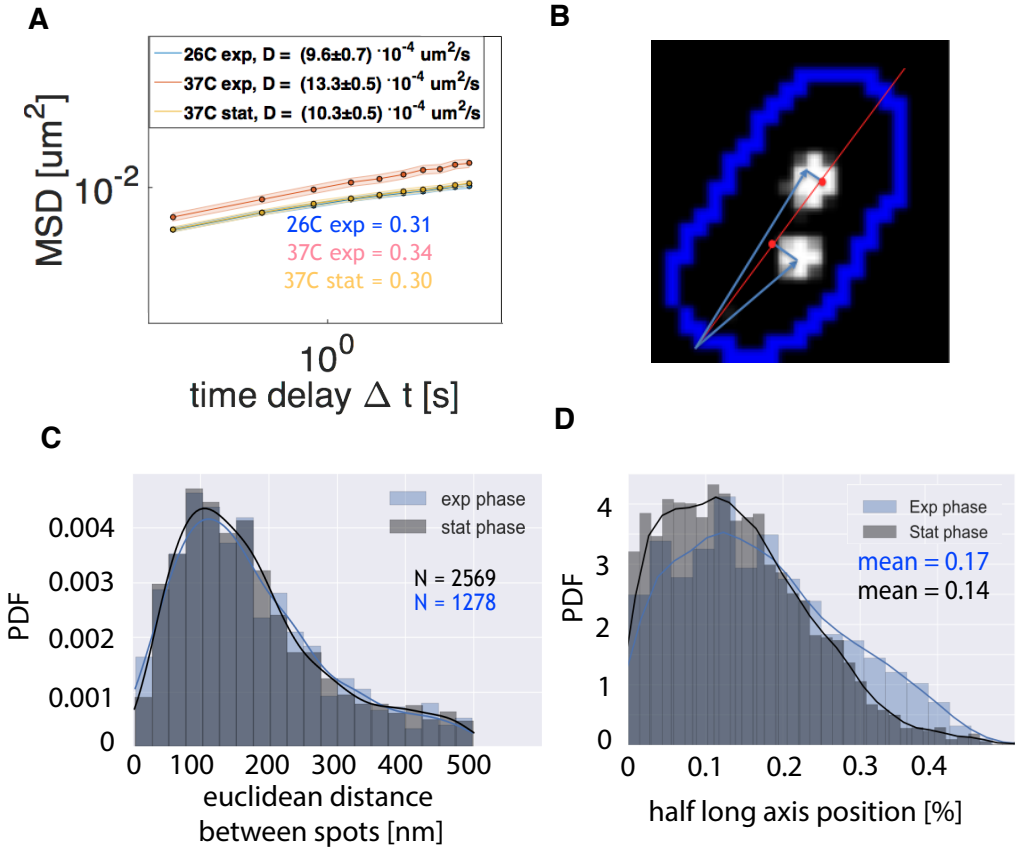


Fig. 3.2.12 **FROS foci localization, tracking and distance measurement under different physiological conditions.** **(A)** MSD of tracked YFP foci at 6tetO sites from cells harvested in exponential phase grown at 26C (blue), exponential phase grown at 37C (red), stationary phase grown at 3C (yellow) **(B)** Cellular position estimation procedure. The localizations of the foci are projected on the long cell axis and due to cell symmetry we consider the distance from middle cell only. **(C)** Distance distribution comparison between exponential phase (blue) and stationary phase (black) of TSS1738 cells grown at 37C **(D)** Cellular position histograms of TetR::EYFP foci histogram in exponential phase (blue) and stationary phase (black)

These exploratory experiments demonstrate that these relatively short (6x operator sites) FROS arrays are a reliable tool for studies on the organization of the bacterial nucleoid *in vivo* and provide some preliminary insights on the difference in physical state of the nucleoid across exponential and stationary phase. Future work will apply these methods to sets of strains bearing FROS insertions flanking specific genes suspected to be regulated by local changes in DNA conformation (e.g. the proU operon, the the flagellar operon) to investigate the relationship between DNA compaction and gene repression. Ideally such experiments would be carried out in a microfluidic device such as the "mother machine" (see below) where cells can be imaged while growing exponentially under controlled physiological conditions.

### 3.2.5 A microfluidic chemostat (mother machine) allows for *in vivo* quantitative measurements under physiological conditions

Given the sensitivity of the nucleoid spatial organization to environmental and physiological conditions ([63], [150], [151], [83]), it is desirable to have an imaging system allowing for fluorescent microscopy experiments during steady (exponential growth under continuous flow of growth media. The "mother machine" microfluidic device satisfies such requirements. We describe here a mother machine implementation, its capabilities as well as its applications to our research questions. The "mother machine" is a simple PDMS (Polydimethylsiloxane) microfluidic device (see materials and methods) that provides steady and continuous exponential growth while permitting fluorescence and phase contrast imaging. This is possible as PDMS is a transparent material and the device continuously provides fresh growth medium to, and removes excess cells from, an array of growth channels so that cells experience a stationary environment.

The design of the mother machine device we employed, which has been successfully applied in many recent *in vivo* studies on bacteria ([43, 93, 97, 14, 95]) is fairly simple (Fig. 3.2.13A). It consists of a main channel where medium can flow at a fixed rate, flanked by a series of smaller growth channels (around 1000) oriented perpendicular to the main channel. Growth channels are about $20\mu m$ long and $1\mu m$ wide so that growing cells from a single-file colony, with up to about 6 cells occupying each growth channel at a given instant during growth (Fig.3.2.13B). Medium diffusion is efficient throughout the entire length of the growth channels [93] so no bias in growth rate is observed along their long axis. We placed the whole microscopy and microfluidic setup in a temperature controlled room so that all the equipment and the buffers are at constant temperature throughout the experiment to minimize growth rate fluctuations.

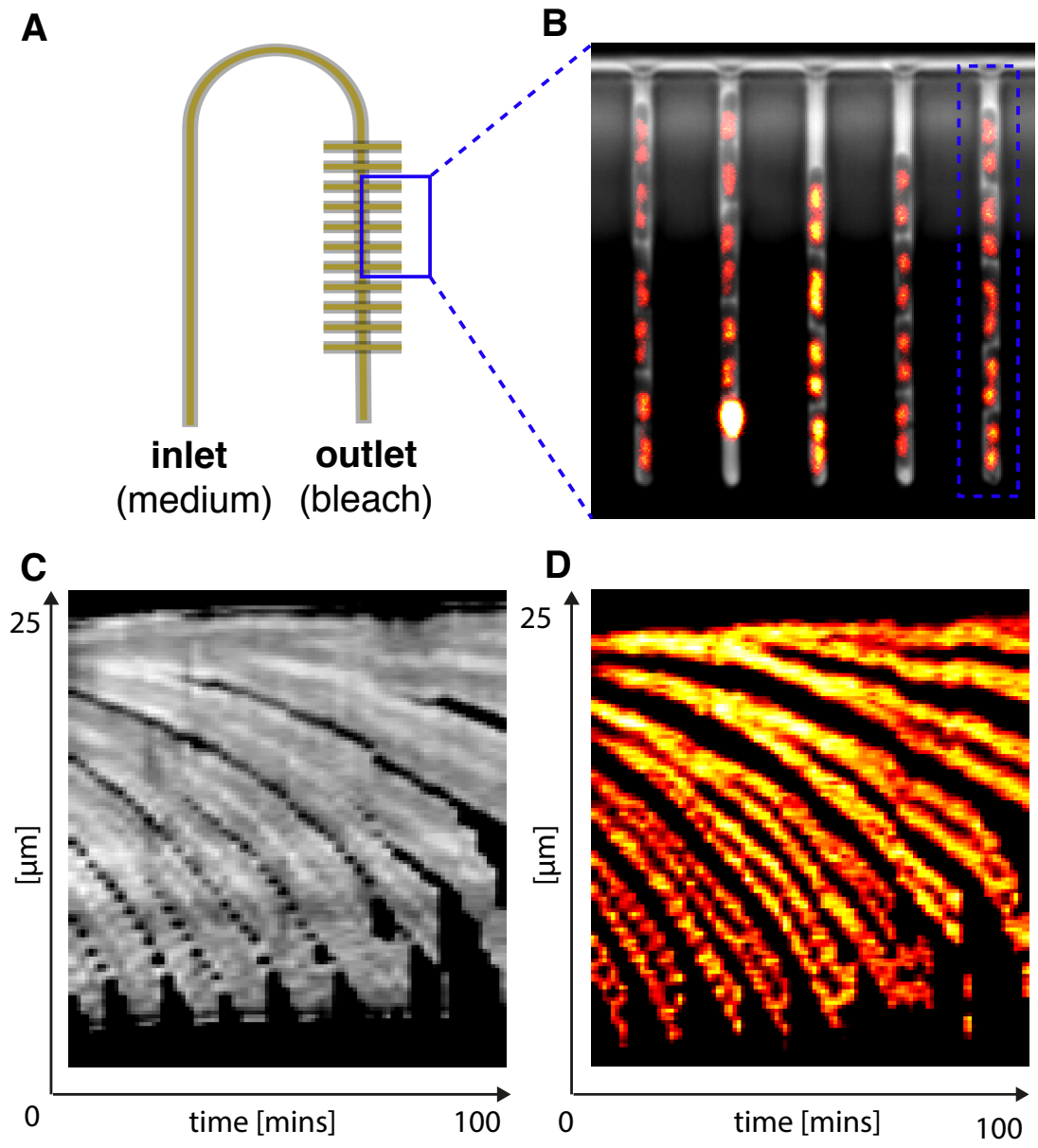


Fig. 3.2.13 **Mother machine schematics (SJ110 device, not to scale) and representative field of view.** **(A)** The curved line line represent the main channel (height = 25 $\mu m$, width = 100 $\mu m$) where fresh medium is constantly flowing while the shorter perpendicular lines represent growth channels (height and width $\simeq$ 1.2 $\mu m$, length = 25 $\mu m$) where non motile cells are centrifuged and cultured. **(B)** An example of a typical filed of view in our experiment. An overlay of the phase contrast and the labeled nucleoid (red) is shown **(C)** Line kymograph of phase contrast time series during exponential growth in a typical experiment. Black lines between grey areas correspond to cell poles boundaries and cell division. **(D)** Line kymograph of HU::mRuby2 labeled nucleoids in growing cells.

Under our experimental conditions, bacteria grow exponentially in the mother machine. A kymograph demonstrating steady exponential cell growth in a mother machine device is shown in Fig.3.2.13C-D. By letting cells grow for 3-4 hours after loading them into the device (see sample preparation section in materials and methods) we ensure that growth rate is constant ([14]) and we achieve a well-defined physiological state. Importantly, by changing the composition of the medium flowing in the growth channels and/or the growth temperature, it is possible to fine tune the growth rate. Also, external perturbations can be introduced in a completely controlled fashion by means of a fluidic switch to exchange the medium flowing in the device. These features are desirable for studies on nucleoid spatial organization since cell physiology and in turn nucleoid morphology and dynamics is very sensitive to fluctuations in environmental conditions.

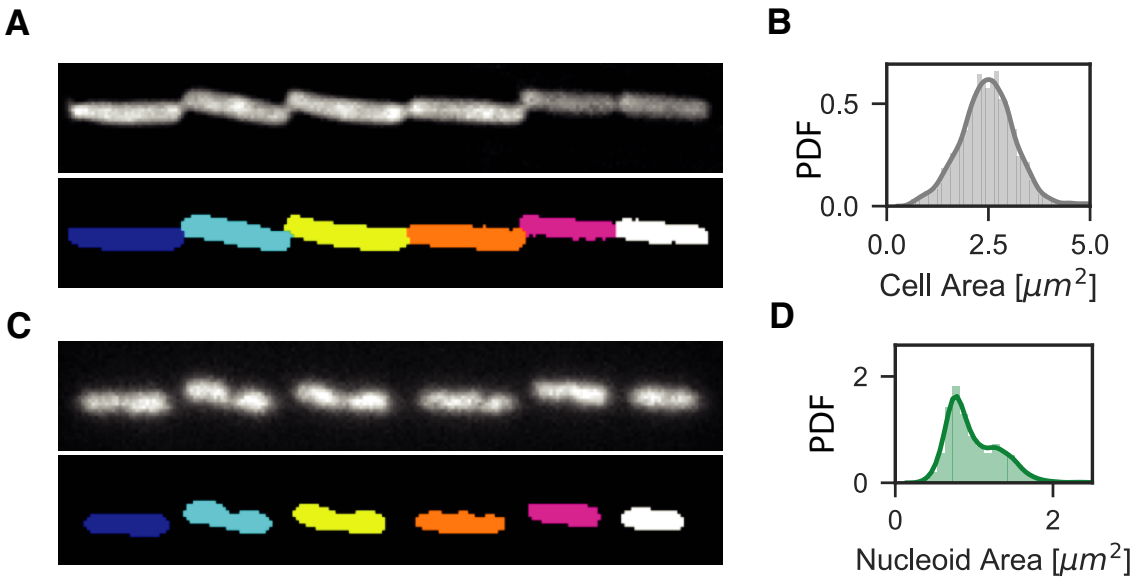


Fig. 3.2.14 **Nucleoid and cell body segmentation and their size distributions.** **(A)** Background subtracted (upper panel) and segmented (lower panel) phase contrast images of a representative growth channel.**(B)** Distribution of cell size from automated image segmentation (N = 3906, images collected across 33 different fields of view). **(C)** Background subtracted (upper panel) and segmented (lower panel) nucleoid (HU::mRuby) images of a representative growth channel. **(D)** Distribution of nucleoid size from automated image segmentation (N = 4255, images collected across 33 different fields of view).

This mother machine implementation was employed in our studies of nucleoid size and dynamics upon crowding perturbation and allowed us to measure cell size, nucleoid size and intracellular crowding over time, under steady exponential growth and during controlled osmotic perturbations (see Chapter 5). We were able to carry out 4-channel

imaging (cytoplasm phase contrast, nucleoid RFP, FRET donor CFP, FRET acceptor YFP) on about 4000 cells with an interframe interval of 2 minutes. The high throughput of the experiment allowed us to efficiently build up statistics of key observables over the course of few hours. Via a custom image analysis software we could analyze about 5GB of data on the same day of the experiment from both phase contrast and fluorescence imaging channels. Fig. 3.2.14 shows an example of cell size and nucleoid size estimation (see materials and methods for details). The segmented cell areas (Fig. 1.2.14A) were subsequently used as masks to compute FRET ratios between the donor (CFP) and acceptor (YFP) fluorophores.

## 3.3 Discussion

We have designed, constructed and developed a set of complementary tools and experimental procedures for fluorescent imaging of bacterial nucleoids in live and fixed cells. The approaches covered by our toolkit span most of the relevant time and length scales for nucleoid transactions throughout the cell cycle. The possibility to combine these diverse imaging tools allows for studying the nucleoid organization and dynamics *in vivo* across a broad range of spatial and temporal scales under physiologically relevant conditions.

#### H-NS-dbd::mEos3.2 is a promising low-perturbation in situ DNA label

Genetically expressing a DNA label endogenously inside living cells overcomes experimental limitations connected to physiological perturbations such as complicated dye incubation protocols or cellular fixation. When employing intercalators like DAPI or nucleic acid stains such as SYTOX/YOYO cells need to be transferred from growth medium to the labeling buffer and then undergo several washing steps before imaging. These protocols can induce undesired cellular responses since cells are very sensitive to a variety of external variables e.g. temperature, pH, osmolarity, cell density and pressure [152–154]. Some labeling techniques require cellular fixation which can introduce structural and imaging artifacts or distort sub-cellular structures by cross-linking [155–158]. Genetic labeling via fluorescent fusions to endogenous DNA-binding proteins such as HU and H-NS circumvents many of these issues, but are not without complications of their own. The relatively large size of protein fluorophores (typically a few nanometers in diameter) means they are more likely to impair the physiological functioning of the native protein being labeled. So when the native copy on the genome is replaced with such fusions, it can lead to unacceptably impaired functionality. Alternatively when the fluorescent fusion is expressed in addition to the native protein, it must be expressed at a sufficiently high level to compete favorably with the native protein in binding DNA to act as an effective chromosome label, but one needs also to be

mindful of possible undesired overexpression phenotypes. Controlling the expression level of the genetically labeled fusions can also present challenges, as plasmid-based expression often leads to high cell-to-cell variability, and chromosome-based expression requires more laborious genetic engineering.

The novel DNA label we developed based on the DNA binding domain of H-NS (H-NS-dbd), due to its lower DNA-binding affinity, it is likely to interfere less with DNA transaction *in vivo* compared to a fluorescent fusion to the endogenous H-NS. We found that this newly designed fusion protein functions well as a chromosomal DNA label in eukaryotic cells (Fig.3.2.2), as well as in bacterial strains where the native H-NS protein is not expressed (Fig.3.2.3). The lower binding affinity than the full-length H-NS makes H-NS-dbd less perturbative to DNA structure but impedes its usability in bacteria expressing the endogenous full version of H-NS, presumably due to binding competition. Our single-particle tracking results suggests that the average time the H-NS-dbd::mEos3.2 spends in association with the nucleoid is lower as compared to the full version of H-NS, which is a desirable feature to minimize perturbations to the endogenous protein functions (Fig. 3.2.1). This can be also qualitatively observed by comparing diffraction limited images of H-NS-dbd::mEos3.2 (Fig.3.2.1) and H-NS::mEos3.2 (Fig.3.2.3) as the cellular background is higher in H-NS-dbd::mEos3.2. For all cell types we tested that do not express a native H-NS protein, the H-NS-dbd::mEos3.2 fusion performed well in labeling chromosomal DNA, and hence is suitable for high spatial resolution imaging e.g. PALM and studies on H-NS mobility via PALM tracking.

**Our toolkit provides complementary imaging approaches at a range of relevant time and length scales**

Having multiple techniques to address the same research question from different angles has many advantages: it allows for validation of results and can give complementary insights into the problem. The techniques in our toolkit can cover a wide range of length scales - 10nm 1um - and time - 10ms 10hrs - within which most relevant cellular processes like replication, transcription, diffusion and cell division take place. Thus, our toolkit provides the possibility of studying nucleoid-associated phenomena across scales via complementary approaches that collectively overcome the limitations associated with each experimental technique.

As an example, we applied localized-photoactivation and PALM tracking to our H-NS photoswitchable fusion in order to study its binding-unbinding dynamics and affinity in living cells. Even if H-NS::mEos2 is known to be prone to aggregation artifacts, the preliminary results of the experiments presented in Fig.3.2.6 suggest that H-NS might be rather mobile

along the nucleoid and perform a "hopping" dynamics jumping across different regions of the chromosome. Combining our H-NS label with localized photo-activation and PALM tracking can thus provide yet another different kind of insight on the global organization of the nucleoid.

Also, we applied both our end-to-end distance estimation algorithm (Fig.3.2.12) and our tracking analysis routine (Fig.3.2.11) to diffraction limited time series of the FROS spots from our functional 6T6L strain. In the future we will use both mobility and end-to-end distance information to study gene compaction *in vivo*, in real time and under different controlled environmental and physiological conditions.

### Future directions and applications

We conclude this chapter with an outlook for future directions in which the presently developed toolkit can be fruitfully applied in the study of nucleoid organization across scales.

At the level of operons and single genes, FROS can be used to label pairs of loci at any distance and to estimate the end-to-end distance between the labels as pioneered by Hensel et al. [145]. Following their work we designed our FROS system with only 6 operator repeats but with the additional feature of placing the insertions only in between terminations of genes, such as to minimize perturbation related to transcriptional activity. We validated the quality of the insertions in one of our designed FROS strain and measured end to end distance between the two FROS insertion in addition to estimating their mobility, proving our system suitable for local gene compaction estimation. Our preliminary results pave the way for more systematic investigations on the relationship between gene compaction and gene regulation: having a quantitative measure of the condensation degree of specific set of genes will allow us in the future to correlate such measure with gene expression patterns of the same genes.

H-NS is involved in the regulation of a large number of physiological processes, including the osmotic shock response via interactions with the proU operon [159–161], and in flagellar biosynthesis via repression of the master operon flhDC [162–164]. Yet, it is not clear what is the molecular mechanism behind these interactions/repressions. The FROS labeling and imaging/analysis protocols we developed are suitable for to studying the nature of NAP-mediated gene regulation in relation to DNA compaction/looping. The methods developed here could be used in the future to study the relationship between local DNA compaction and gene expression. For example by combining FROS with a mother machine device it will be possible to look at the compaction of the proU chromosomal region before and immediately after inducing hyper-osmotic shock and monitor the cellular location time evolution during sustained shocks. The design of experiments investigating the H-NS mediated repression of ProU and its DNA compaction properties has been initiated in our lab. Along these lines, by

covering the motility operon with FROS insertions at different genomic distances, we plan to investigate the chromosomal-organization role of H-NS in the adhesion-motility phenotypical switch, which can be induced again with the mother machine experimental framework by lowering the growth temperature or inducing oxygen starvation [165].

We also plan to employ both H-NS::mEos3.2 and H-NS-dbd::mEos3.2 with a 3D PALM setup to investigate the 3D architecture of the chromosome in bacteria. We note that the fusions to the full-length and the truncated H-NS provide complementary approaches that would be instructive to compare: the full-length fusion has less cellular background (and thus a higher localization precision) as compared to H-NS-dbd as most of the fusion proteins are associated with the nucleoid but on the other hand the dbd is likely to perturb DNA structure and physiology to a minor extent.

As a matter of fact, studies have been carried out both with diffraction-limited imaging and at higher resolution but yet a quantitative study on the 3D architecture of bacterial nucleoids is lacking in the literature. By increasing statistics and imaging cells grown at different rates or uner different growth media or conditions, it will be possible to unveil the details and characterize more in depth the differences in morphologies observed in 2D projected imaging under different growth conditions. As an example, our preliminary 3D PALM images suggest a helical arrangement of the nucleoid in cells grown in minimal medium.

Finally, the analysis software and the imaging protocol of the mother machine framework will be optimized in order to have precise quantitative access to the dynamics of single-cell observables. This will require software-based lineage connection from frame to frame, which is challenging given that image segmentation is prone to errors due to cell proximity in the mother machine channels but needs to be extremely accurate in order to assign cells in different frames to the correct lineage.

In summary, we have developed and tested a toolkit for fluorescence microscopy studies on nucleoid spatial organization under different angles and at a wide range of length and time scales in general with a low degree of perturbation to physiology. We conducted proof-of-principle experiments that will be instructive for future works on the relationship between the spatial organization of the genome and its functional role in the regulation of gene expression.

## 3.4 Materials and Methods

### 3.4.1 Bacterial strains, plasmids and culture conditions

All the strains used in this chapter are summarized in Table 4.1 and Table 4.2
For PALM and diffraction limited imaging of H-NS::mEos and H-NS-dbd::mEos fusions TSS1221, TSS1360, TSS1370 and TSS1510 were inoculated from a glycerol stock in TB tryptone broth (TB; 1% tryptone, 0.5% NaCl, pH 7.0) supplemented with appropriate antibiotics (34 $\mu$g/ml chloramphenicol) and grown overnight at 37C. The morning after cells were inoculated 1:100 into fresh H1 medium ($(NH_4)_2SO_4$ 7.6 mM, $MgSO_4$ 0.5 mM, $Fe_2(SO_4)_3$ 1.25 $\mu$M, Thiamine 0.01%, $NaCl$ 67 mM, $KPO_4$ 50mM) supplemented with aminoacids (1 mM His, 1 mM Leu, 1 mM L-Meth, 1 mM Thr), 0.5% glycerol, appropriate antibiotics, and 0.1% arabinose. Cells were grown at 37C at 250rpm until OD 0.2 (exponential phase).

| **Strain List** | | | | |
|---|---|---|---|---|
| **name** | **genotype** | **plasmid** | **parent** | **source** |
| TSS1221 | *fhuA*2 Δ(*argF- lacZ*)*U*169 *phoA glnV*44 Φ80 Δ(*lacZ*)*M*15 *gyrA*96 *recA*1 *relA*1 *endA*1 *thi*-1 *hsdR*17 | pSJAB76 | Dh5$\alpha$ | [166] |
| TSS1360 | same as above | pSJAB95 | Dh5$\alpha$ | [166] |
| TSS1370 | same as above | pSJAB98 | Dh5$\alpha$ | [166] |
| TSS1510 | same as above | pRD129 | Dh5$\alpha$ | [166] |
| TSS1658 | wild type | pOB2 | MG1655 | [167] |
| TSS1731 | *12tetO* (T1) | pOB2 | MG1655 | [167] |
| TSS1733 | *12tetO* (T2) | pOB2 | MG1655 | [167] |
| TSS1738 | *6etO,6lacO* | pOB2 | MG1655 | [167] |
| TSS1779 | wild type | pSJAB95 | MG1655 | [167] |
| TSS1833 | wild type | pRD129 | MG1655 | [167] |
| TSS1843 | wild type | pSJAB98 | MG1655 | [167] |
| TSS1924 | wild type | pRD129 | MG1655 ΔH-NS | A. S. N. Seshasayee |
| TSS1961 | *hupA-mRuby2* | pSJAB159 | MG1655 | S. Jun |
| TSS2005 | n/a | pRD129 | B. Subtilis | R. Dame |

Table 3.1 Bacterial strains used in this study

| Plasmid List | | | | |
|---|---|---|---|---|
| **name** | **product** | **vector** | **resistance** | **source** |
| pSJAB76 | H-NS::mEos2 | pBAD33 [111] | chloramphenicol | this study |
| pSJAB95 | H-NS::mEos3.2 | pBAD33 [111] | chloramphenicol | this study |
| pSJAB98 | mEos3.2 | pBAD33 [111] | chloramphenicol | this study |
| pSJAB159 | FRET crowding sensor | pTrc [110] | chloramphenicol | this study |
| pOB2 | LacI::mCherry, TetR::EYFP | pBAD24 [111] | chloramphenicol | this study |
| pRD129 | H-NS-dbd::mEos3.2 | pBAD33 [111] | chloramphenicol | R.T. Dame |

Table 3.2 Plasmids used in this study

For the FROS experiments TSS1738 was grown grown overnight in TB supplemented with appropriate antibiotics (100 $\mu$g/ml Ampicillin) at 37C. Cells from the resulting saturated culture were inoculated in the morning into fresh M9 medium ($Na_2HPO_4.7H_2O$ 48 mM, $KH_2PO_4$ 22 mM, $NaCl$ 8,5 mM, $NH_4Cl$ 93 mM, $MgSO_4$ 2 mM, $CaCl_2$ 0,1 mM) supplemented with amino acids (100 $\mu$g/mL Arg, Thr, His, Leu, Pro) with a 1:100 dilution. Cells were grown at 37C until OD 0.2 with no induction. All the cultures were harvested by centrifugation at 5000 rpm for 5 minutes and washed twice in motility medium (PALM and diffraction limited imaging experiments) or in fresh M9 medium (FROS) prior to sample preparation.

### 3.4.2 Microscopy

For PALM experiments the cells were fixed and the sample was prepared as described in chapter 2. DAPI nucleoid staining was achieved by exposing fixed cells to 2ng/ml DAPI solution in motility medium or phosphate buffer sline (PBS) for 15minutes and then wash the cells twice via centrifugation (5000rpm, 5 min) in fresh buffer. For FROS, PALM tracking and diffraction limited imaging experiments 1.5% agarose pads were prepared with a thickness of 1mm. A 1x1cm square was cut from the pad and placed on a microscopy glass. Subsequently, 4$\mu l$ of concentrated cell suspension were sandwiched between the agar pad and a 0.2mm thick coverslip. Both wide field and PALM imaging were performed using the setup described in Chapter 2. For a detailed description of the microscopy methods used in this part, see Chapter 2. For FROS distance measurement experiments we used a double band filter (dichroic: Chroma ZT405/515/561rpc, emission: Chroma EM 59026m)

allowing for imaging EYFP and HU::mRuby2 without moving the filter turret. For the FROS tracking experiment the inter frame interval was 300ms with an exposure time of 30ms and an excitation power of about $400W/cm^2$. PALM tracking experiments were carried out with a 65ms inter frame interval, 15ms exposure time and an excitation power of about $200W/cm^2$ .

### 3.4.3 PALM and SPT data analysis

2D PALM data was analyzed as described in Chapter 2 by means of the Thunderstorm plug-in [79]. An additional module of the plug-in for 3D astigmatism-based PALM was used. The module calibrate the z position of the PSFs by processing an image sequence of immobilized 100nm gold-coated beads during a vertical (z) ramp of our piezo stage. By inputing the step in z corresponding to each frame, the software produces a calibration curve allowing for assigning a z coordinate to any of the deformed PSF in the actual PALM experiment. PALM tracking experiments were analyzed with an adapted version of the tracking software described in Chapter 2. Images from eukaryotic cells were analyzed using ImageJ. For the FROS experiments all the analysis was carried out with Matlab or Python custom written code.

### 3.4.4 FROS data analysis

FROS data is processed with a custom written python or Matlab code for distance and mobility estimation respectively. The analysis pipeline for distance measurements comprises the following steps:

1. Background subtraction
2. Flatf-field correction for excitation laser inhomogenheity
3. FROS spots identification both on YFP and mCherry channel.
4. Filtering of isolated spots and identification of the closest YFP-RFP spot couple
5. Distance computation and plotting

Step 1 requires the construction of both a background image for background subtraction coming from the agar, and a laser profile image for flat-field correction. For the background image we choose a region of the agarose sample without cells and we collect 500 images with both 515nm and 568nm laser illumination under optimized imaging conditions used in the actual experiments. Subsequently we compute an average laser background image to be subtracted from the actual FROS spots images. This step is necessary to increase localization precision and for correct photon counting of FROS YFP and mCherry spots.
To carry out step 2 we follow a similar procedure: we prepare samples of diluted fluorescein

or rodhamin for measuring 515nm and 568nm laser profiles respectively. We collect 500 fluorescence images and we average them to construct a laser profile image. Subsequently, we normalize the averaged profile to its maximum value and rescale the FROS images with that by dividing each data image with the average laser profile. Since lasers in the sample plane exhibit a Gaussian profile, this way we correct for the inhomogeneities of laser illumination near the edges of the field of view.
For step 3 we process the data first by applying a maximum filter. Subsequently we identify the maxima in the image and use their coordinates as guess for fitting the FROS spots with a 2-dimensional Gaussian. In step 4 we discard single localizations of FROS spot inside cells by means of binary mask obtained by image segmentation (see Appendix B). Finally in step 5 we compute, for each segmented cell, the distances between each YFP spot and each mCherry spot in the cell. If a cell happens to have different numbers of spots for the two colors we retain only those couples that happen to have the smallest distance.

For FROS foci tracking on the other hand, we use an adapted version of the tracking software described earlier for tracking of clusters of chemoreceptors allowing for estimation of mobility of each FROS label which allows for single-focus mobility estimation. The adaptations consisted in modifying some of the parameters of the detection and tracking code, namely inter-frame interval, intensity identification threshold for point spread functions, search radius (in nm) for linking subsequents localizations and image dimensions in nm.

### 3.4.5 Mother Machine

#### device preparation

To fabricate the mother machine devices we make use of epoxy molds obtained from PDMS devices which were fabricated from a silicon wafer mold. Fabricating epoxy molds is simpler than fabricating silicon wafers and even though they tend to degrade upon prolonged usage, an epoxy mold can be utilized for several months before renewal. Using epoxy molds instead of wafers also ensures longer duration to the original copy of the device which is stored on wafers and used only a small number of times.

To fabricate the devices we follow the standard PDMS preparation procedure using Sylgard 184 Silicone Elastomer kit, by mixing:

1. 10 parts of PDMS monomers.
2. 1 part of crosslinker.
3. Mix thoroughly

After that, the mixture is deposited on the epoxy mold and baked at 60C for about 8 hours. Devices are then cut from the baked PDMS layer on the epoxy and by means of a 1mm puncher, holes are punched in correspondence of the inlet and outlet.

Freshly made devices need to be cleaned with organic solvents in order to remove the unpolymerized fraction of PDMS and the small impurities and residues of polymerized PDMS that might have ended up in the growth channels. These kind of cleaning procedure has also been proven to remove and cure the PDMS from substances that can otherwise interfere with normal bacterial physiology. Following [14] we do follow the protocol indicated below for device cleaning:

1. Wash the punched devices for two hours by placing the devices in a beaker, submerging them into pentane and placing the filled beaker on a magnetic stirrer.
2. Wash (same procedure as in 1.) for two hours with acetone x2.
3. Dry the device in air at room temperature.

Once the devices have been washed they can be stored for about a month in a dust-protected container.

**Sample preparation and imaging protocol**

Prepared devices have to be firmly attached to the microscopy glass in order for the channels to be seal-proof. For this purpose plasma treatment is required to ensure perfect adhesion of the PDMS to the microscopy glass. We use a 30W Harrick Plasma system where we incubate for one minute in the presence of oxygen both the microscopy glass (Willco-dish glass bottom dish,Willco Wells, product name: GWST-5040 , size 50X7mm, glass thickness 170 μm) and the mother machine device in order to treat both surfaces before sticking them together. After plasma treatment we promptly press the device on the glass surface of the Willco-dish and incubate at 60C for 15minutes to stimulate adhesion.

Subsequently, we need to chemically treat the growth channels with bovine serum albumine (BSA) to avoid unwanted adhesion of the bacterial membrane charged surface to the growth channels. We prepare a 10mg/ml BSA solution in MQ water and inject it in the microfluidic channels via pipetting. After incubation at 37C for about one hour, we flow a concentrated cell suspension from a saturated culture in the mother machine and centrifuge the sample in order to push bacteria into the growth channels. Note that the cells have to be non motile otherwise they will escape the channels. After loading cells via centrifugation, we connect the device to a pump and start flowing fresh growth medium. The cells will be kept

in fresh medium for at least 4 hours in order to be sure that exponential growth is achieved before starting imaging.

The sample preparation procedure is summarized below

1. Prepare BSA solution: add 39.6ml media + 0.4ml 50mg/ml BSA (0.5g into 10ml media and filtered; final 0.5mg/ml)
2. Prepare PDMS devices
   (a) punch holes before cleaning up with pentane
   (b) plasma treatment
   (c) bond to Willco dish and heat at 60C for >5min
3. Add BSA into the mother machine
   (a) add 10ul 50mg/ml BSA solution through 10ul pipette tip
   (b) incubate at 37C for 15 to 45 minutes
4. Add cells
   (a) centrifuge the 2ml culture and remove 1.75ml supernatant (leave 250ul), and dissolve pellet.
   (b) add 10ul of concentrated cell culture (from step (a)) by pipetting
   (c) seal both inlet and outlet with scotch tapes
5. Load cells by centrifugation for 5-10 minutes by means of a custom centrifuge and sample holder based on a fan rotor.
6. Connect tubing to the pump. Tubing was sterilized by running bleach, water, EtOH, and water
7. Use high fresh medium flow rate 8ml/hr to flush cells in main trench for 10min
8. Decrease pumping rate to 1.5ml/hr

Once the cells reach exponential growth phase after 4 to 6 hours of growth in the mother machine (for rich or minimal medium respectively), we can place the sample on the microscope and start imaging.

By means of an emission filter wheel and a motorized excitation filter turret in the microscope, we can rapidly switch from an imaging channel to another. Excitation is carried out by means of LED light at different wavelengths suitable for the fluorophores we employed. By keeping exposure times relatively short (from 30 to 400ms) we achieve low photo-toxicity

and achieve stationary growth rate (data not shown). We control all our equipment with Nikon Elements software which allows to record a set of fields of view to serially perform a given imaging protocol on the recorded stage positions in a completely automated fashion. Details on the equipment and a particular imaging protocol suitable for nucleoid studies under crowding perturbations are detailed in the materials and methods section of Chapter 5.

**Analysis approach and workflow**

We present here a schematic of the analysis work-flow we employed for our investigations on nucleoid spatial organization under crowding perturbations, detailed in Chapter 5. For all our analysis we utilized some Python code that was initially developed in the laboratory of Prof. Suckjoon Jun (UCSD), and then expanded and adapted at AMOLF for the needs of this particular kind of experiments. The code comprises the following modules:

1. Growth channels identification and slicing from phase contrast images
2. Empty channels identification
3. Background subtraction of empty channels from filled channels
4. Phase contrast subtracted image segmentation
5. mRuby2 labeled nucleoids image segmentation
6. FRET ratio computation from CFP and YFP images
7. Cell and nucleoid morphological quantification

When data from an experiment is fed to the whole analysis pipeline, we can obtain the following quantities:

1. Single-cell size distributions over time
2. Single-nucleoid size distributions over time
3. Other morphological parameter distributions (e.g. nucleoid area fraction, length, width, eccentricity, centroid..) over time for both cells and nucleoids
4. FRET ratio distributions from single cells over time

For a more detailed explanation of the analysis code and work-flow see Chapter 5. As an example of the capabilities of our experimental and analysis toolkit, Fig. 3.2.14 shows representative segmented images of nucleoids and cells from phase contrast imaging. From segmented images we compute the cell size and nucleoid size distributions shown in Fig. 3.2.14 (N = 3906, images collected across 33 different fields of view) and D (N = 4255, images collected across 33 different fields of view).

## 3.5 Acknowledgments

The work presented in this chapter has been a collaboration with the laboratory of Prof. Remus Dame (Leiden University). The H-NS-dbd construct was first developed in Dame's laboratory. Experiments on eukaryotic cells (Fig.3.2.2) were performed by Fred Cremazy (from Dame's lab.), who also contributed substantially in the design, cloning (together with Simone Boskamp) and testing of all the H-NS constructs presented in this chapter. The FROS strains were developed by Oskar Bles and Simone Boskamp in our lab.

# Chapter 4

# Sensory stimulation and adaptation affect size and mobility of *E. coli* chemoreceptor clusters

Clustering of bacterial chemoreceptors is important for functional aspects of signaling such as amplification, adaptation, and fold-change detection (FCD), but the stability of these signal processing units *in vivo* has remained an elusive topic, with seemingly conflicting reports in the literature. We have probed the spatial organization and mobility of Escherichia coli chemoreceptor clusters using photoactivation localization microscopy (PALM) and localized photoactivation single-particle tracking (LPA-SPT). Our results reveal that the cluster-size distribution is altered shortly after ligand stimulation. The change in the observed cluster-size distribution is substantial, yet does not drastically affect either the global pattern of localization (studied previously by diffraction-limited imaging), or the nanoscale receptor density within clusters (resolved previously by cryo-EM). Furthermore, we find that CheR/CheB-mediated adaptation restores not only signaling activity but also the spatial organization of receptors upon sustained ligand stimulation. We discuss the possible implications of the dependence of receptor clustering and associated sensory response parameters on the history of experienced stimuli.

## 4.1 Introduction

Cell signaling is dependent on spatial organization across scales, from the positioning and orientation of individual proteins within signaling complexes to the arrangement and movements of organelles at the cellular scale [168]. In *Escherichia coli* and other bacteria, chemosensory

signaling that controls its motile behavior is mediated by clustered chemoreceptors that form extended arrays spanning the plasma membrane (for a recent review, see [169]). The size of these arrays can reach $\sim 100$ nm in diameter, containing thousands of receptor molecules arrayed in a highly ordered lattice together with the output kinase CheA and scaffolding protein CheW, and has been described as a prokaryotic 'proto-organelle' for sensory processing [170].

*E. coli* cells utilize this sensory apparatus to to guide their navigation toward favorable environments, in a process known as chemotaxis [171]. Spatial gradients of attractant or repellent chemoeffectors are sensed by temporal comparisons [172] carried out by a relatively compact signaling network consisting of the chemoreceptor arrays and four additional cytosolic proteins which mediate signal relay to the flagellar motor, and negative feedback for sensory adaptation (for a recent review, see [173]). Ligand binding occurs at the periplasmic domains of the transmembrane chemoreceptors, which transduce the signal from the exterior to the interior of the cell via conformational changes that modulate the activity of the kinase CheA which, in turn, regulates the phosphorylation level of CheY, the cytosolic response regulator of motor activity. Modulation of the phosphorylated CheY (CheY-P) signal is accelerated by a phosphatase CheZ. Two cytosolic enzymes CheR an CheB mediate sensory adaptation via activity-dependent covalent modification [174]. These cytosolic components (CheY, CheZ, CheR, CheB) also spend the majority of time bound to the sensory arrays which are predominantly found at the cell poles [175–177], although large clusters are also found along the lateral region of the cell membrane, albeit at lower frequency [178].

Clustering of chemoreceptor molecules into these signaling arrays is responsible for strong signal amplification, a hallmark of *E. coli* chemotaxis signaling that underlies its exquisite sensitivity to environmental stimuli (e.g. for the attractant L-aspartate, responses to concentrations in the nanomolar range have been reported [179]). Allosteric interactions between clustered receptors have long been hypothesized as responsible for chemotactic signal amplification [180–184], and recent experiments have verified that mutations which interrupt array formation lead to both drastically reduced response cooperativity [185] and attenuated chemotactic performance [186].

While the functional role of receptor clustering in transducing the ligand signal is now well established, whether and how ligand stimuli affect receptor clustering remains an unresolved question. Indeed, there are several reports on the subject with apparently conflicting results. Whereas two studies that imaged clusters by fluorescent fusions of chemotaxis proteins in live *E. coli* cells reported no difference in the visible clustering pattern upon attractant stimulation [187, 188], a series of studies utilizing immunofluorescent labeling in fixed cells (of both *E. coli* and *Bacillus subtilis*) reported that attractant stimulation promotes

diffuse staining of the plasma membrane, interpreted to mean chemoreceptor clusters are destabilized by attractant binding [189–191]. Electron cryomicroscopy (cryo-EM), which has been immensely powerful in resolving the nanoscale arrangement of array components [192, 193], was was used by Briegel *et al.* [194] to address effects of ligand binding in *Caulobacter crescentus* chemoreceptor clusters, but no change was observed upon chemoeffector stimulation in the hexagonal packing with 12 nm spacing. Thus, despite efforts by many groups using a variety of techniques in multiple organisms, a clear view regarding the structural stability of chemoreceptor clusters under sensory stimulation has remained elusive.

At the functional level, experimental evidences have emerged suggesting that the amplification gain of the sensory system can be tuned by environmental conditions. Using cryo-EM, Khursigara *et al.* [195] reported that packing density of chemoreceptors within clusters is higher for cells grown in nutrient-poor media than for those grown in rich media, and *in vivo* FRET measurements on cells grown under these conditions revealed higher degree of cooperativity for those in poor media. Subsequently, Frank *et al.* [196] found by *in vivo* FRET that prolonged stimulation by the non-metabolizable attractant $\alpha$-methylaspartate (MeAsp) leads to attenuated signal amplification, and that this effect is accompanied by an increase in fluorescence anisotropy, interpreted as a reduced receptor packing density. Thus, both growth conditions and the sensory stimulus history appear to affect cooperative amplification, and receptor packing is identified as an important variable that correlates with this sensory performance.

Yet, the notion of 'receptor packing' remains rather abstract, being defined in different ways in different studies. In particular, a change in packing could reflect subtle changes in the position of receptors within intact arrays, or it could reflect more drastic changes, involving also changes in array size. Early immunoelectron [176] and fluorescence [177, 178] microscopy studies suggested that most receptors are present at one or a few clusters per cell. More recently, however, using photoactivation localization microscopy (PALM), a superresolution optical imaging technique [197], Greenfield *et al.* [198] found that the size of chemoreceptor clusters are extremely broadly distributed, with a substantial fraction of detected receptors ($\sim 40$ %) partitioned into many small clusters ($< 100$ receptors) scattered across both lateral and polar regions. Given the overall high density of chemoreceptors on the plasma membrane, changes in the size distribution of such nanoscale clusters could underlie some or all of the changes in packing reported in previous studies.

Here we asked whether and how sensory inputs to chemoreceptors affect their spatial organization and dynamics at lengthscales resolvable by optical superresolution microscopy. Focusing on the MeAsp response of the aspartate receptor Tar, we developed two complementary approaches that utilize photoconvertible fluorescent proteins. First, with a PALM

technique analogous to that of Greenfield *et al.* [198], we asked whether the distribution of chemoreceptor cluster sizes is affected by the stimulus history. Because individual fluorophores are imaged in PALM, it can densely sample not only large arrays of receptors but also the full spatial distribution including small clusters, and allows direct counting of fluorescently labeled molecules [199]. Second, we used localized photoactivation single-particle tracking (LPA-SPT) [200] to efficiently track the movement of Tar clusters within the densely labeled membrane. Our results demonstrate unambiguously that stimulation with the attractant MeAsp alters the spatial organization of chemoreceptors by affecting the cluster-size distribution, and moreover, that on a slower timescale, sensory adaptation serves to counter the effect of ligand to restore the spatial organization toward its pre-stimulus level upon prolonged stimulation.

## 4.2 Results

### 4.2.1 PALM reveals extensive diversity in chemoreceptor spatial organization across cells

To perform PALM imaging of the aspartate receptor Tar, we genetically labeled it with the green-to-red photoconvertible fluorescent protein mEos2 [201] at the receptor's C-terminus. The resulting fusion protein (Tar-mEos2) was expressed in a receptorless genomic background (TSS902) derived from strain RP437 (wildtype for chemotaxis) [202]. After growth in H1 minimal medium (see *Materials and Methods*), cells were harvested and incubated for $\sim$ 60 min in motility medium (MotM; see *Materials and Methods*) at room temperature. As illustrated in Fig. 4.2.1A, cells were then imaged after fixation under three different conditions: (i) in the absence of stimulus, (ii) shortly after exposure to 1 mM MeAsp and (iii) $\sim$1 hr after sustained exposure to 1 mM MeAsp. To achieve (i), a batch of cells was directly fixed without further treatment using 4% para-formaldehyde (PAF) dissolved in MotM for 10 min. Another set of cells (ii) was stimulated with 1 mM MeAsp and immediately fixed with PAF for 10 min. Finally a last set of cells (iii) were incubated after addition of 1 mM MeAsp for $\sim$60 min and fixed for 10 min using PAF. After fixation, cells were imaged by PALM within three hours.

The resulting PALM images revealed a diversity of Tar-mEos2 localization patterns under all three conditions (Fig. 4.2.1 B-D). In agreement with the previous PALM study of Greenfield *et al.* [198], we observed that a significant fraction of receptors reside in small clusters scattered across the length of the cell, in addition to one to a few large

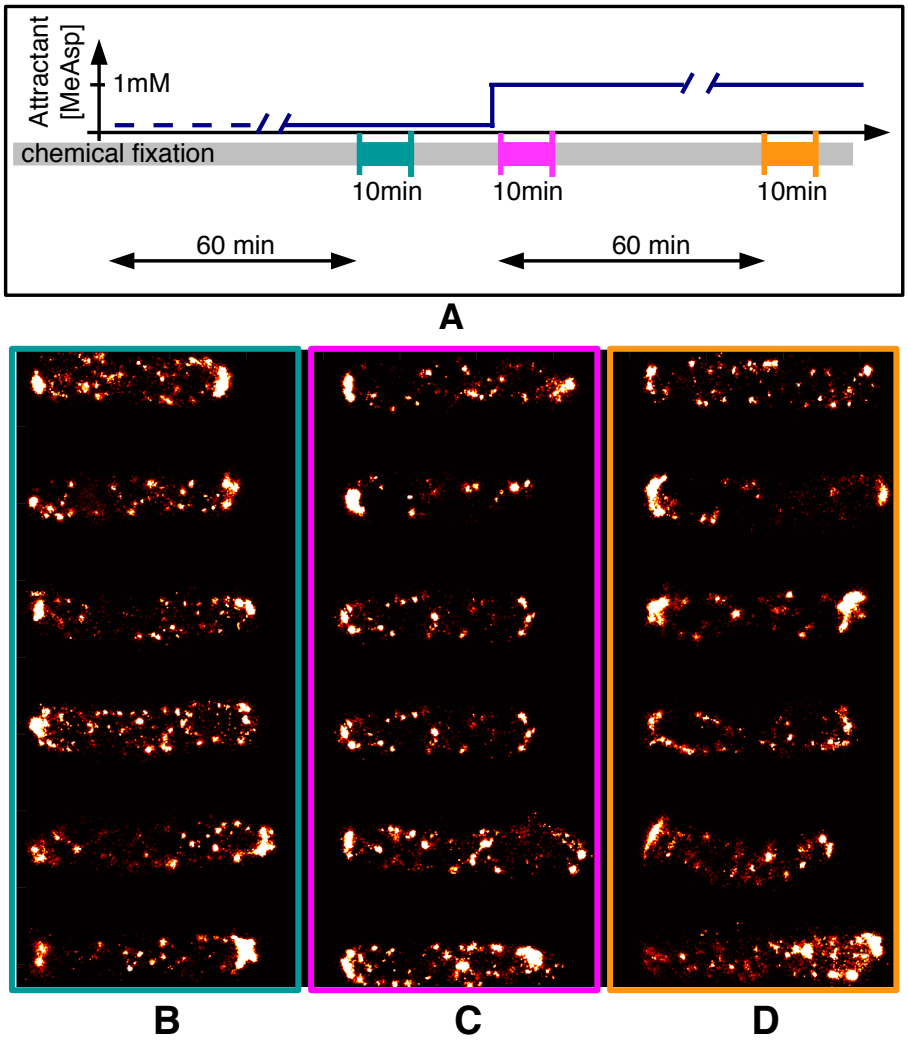


Fig. 4.2.1 **Cell-to-cell variability in receptor spatial distribution.** **(A)** Schematic time course of cell stimulation and fixation protocol prior to PALM imaging. Cells were pre-incubated in the absence of stimulus (MeAsp) for $\sim$ 60 min. Subsequently, a subset of cells were fixed with 4 % PAF without further treatment. Another subset is fixed shortly after 1 mM MeAsp addition, and a final subset is fixed after prolonged exposure ($\sim$ 60 min) to 1 mM MeAsp. Colored segments along the time axis represent fixation time under different stimulation conditions. **(B-D)** Representative PALM images of *E. coli* cells (strain TSS902) expressing Tar-mEos2 and fixed under the three stimulus conditions: unstimulated **(B)**, shortly after stimulation **(C)**, and after prolonged ($\sim$ 60 min) stimulation **(D)** with 1 mM MeAsp.

clusters per cell, usually at the poles [176, 177] but also occasionally in the lateral region [178]. These high-resolution snapshots of Tar-mEos2 spatial distribution across the plasma membrane demonstrate that the pattern of localization varies strongly from cell to cell, even

within isogenic populations grown and prepared under identical conditions. This extensive diversity of localization patterns precludes meaningful comparisons by visual inspection of PALM images alone, and we thus proceeded to develop statistical descriptions of the PALM localization data.

### 4.2.2 Cluster size is reduced upon attractant stimulation, and restored by adaptation

As a basis for quantitatively describing chemoreceptor spatial organization, we took advantage of PALM's inherently discrete imaging protocol, which yields both the exact number of localization events, as well as their spatial coordinates. Previous studies have established how PALM localization coordinates can be used to count the number of photoactivated fluorescent molecules [199], and also perform clustering analyses on coordinates to study spatial organization [198]. A key quantity of interest for bacterial chemoreceptors is the cluster size (defined here as the number of receptors in a cluster), as it places an upper bound on the degree of response cooperativity (which in turn determines signal gain) that can be achieved by allosteric interactions within a cluster [203, 183, 204, 184]. We performed clustering analysis on the set of localized PALM coordinates of receptors under each of the three stimulus conditions (i-iii) (Fig. 4.2.1A). Clusters were defined by a simple algorithm: every localized receptor was assigned membership in one and only one cluster, and two individual receptors were assigned to the same cluster if their localization coordinates were separated by a distance below a threshold $L_{max} = 20nm$ (Fig. 4.2.2A), chosen to be close to the PALM localization precision in our experiment. Once all receptors were assigned to clusters, we computed for each of the stimulus conditions (i-iii) a "cluster-size membership distribution" (CSMD), defined as the probability $P_{\mathrm{CSM}}$ that a randomly chosen receptor is a member of a cluster of size $N$: $P_{\mathrm{CSM}}(N) \equiv Nn_N / \sum_{x=1}^{\infty} xn_x$, where $n_x$ is the number of observed clusters of size $x$. For comparisons across conditions, to avoid binning artefacts we use the cumulative distribution function (CDF) of the CSMD: $CDF(N) = \sum_{x=1}^{N} P_{\mathrm{CSM}}(x)$.

In the absence of stimulus (Fig. 4.2.2B, blue curve), the largest clusters contained thousands of receptors, but a sizeable fraction of receptors ($\sim$ 30-40%) also resided in small clusters ($<$ 100 counts). This very broad distribution of cluster sizes is in agreement with the previous PALM study of ref. [198], which did not address effects of ligand stimulation but reported a similar range of cluster sizes. Interestingly, however, we found that shortly after exposure to 1 mM MeAsp the distribution shifts toward smaller cluster sizes, with the probability for a receptor to be found in a cluster of size $>$ 500 reduced by nearly two-fold (Fig. 4.2.2B, magenta curve). This observation suggests that stimulation by the receptors'

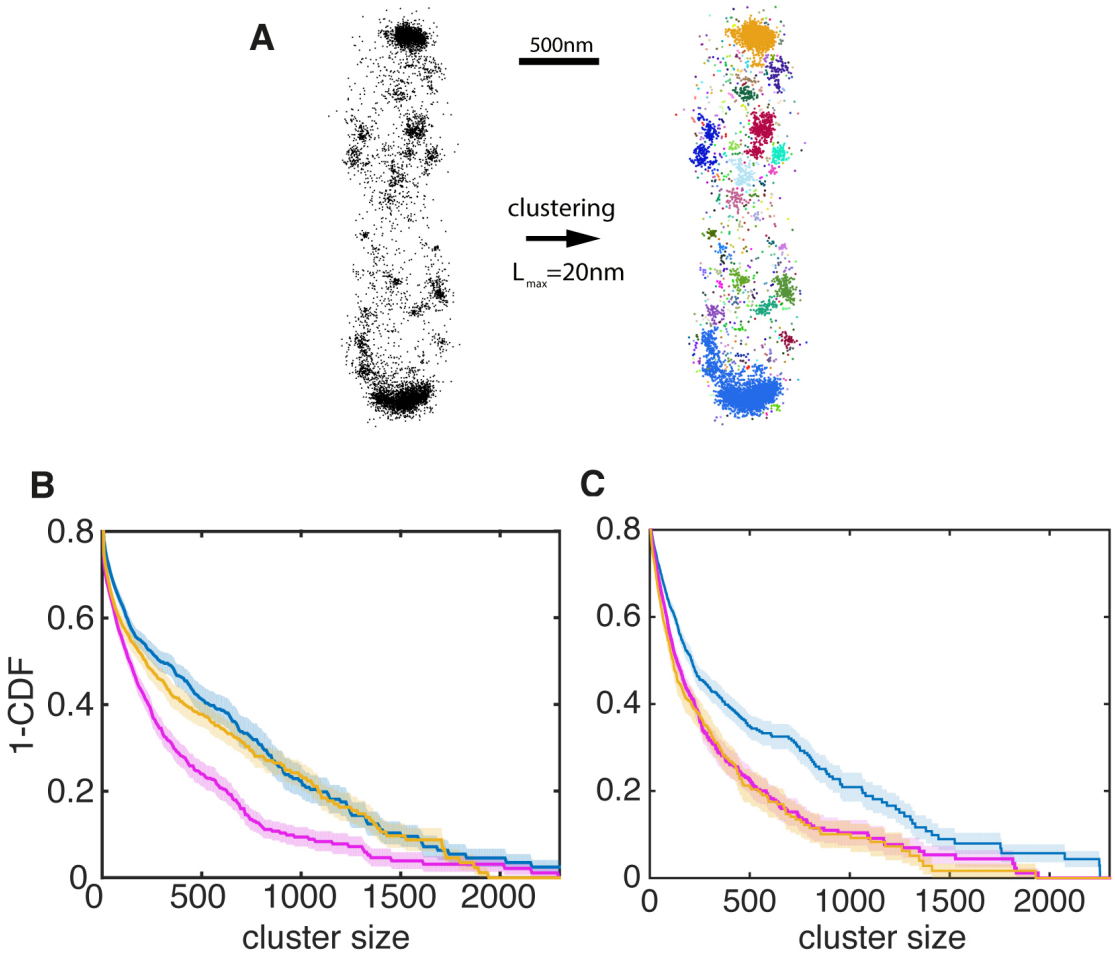


Fig. 4.2.2 **Cluster-size analysis of Tar-mEos2 PALM localizations.** **(A)** Representative output of the spatial clustering of receptor code. Each black dot in the left panel represent individual position of a single Tar-mEos2 receptor. Via the clustering algorithm, two receptors are considered in the same cluster if their pairwise distance is smaller than $L_{max} = 20nm$. In the resulting figure on the right all receptors belonging to the same cluster are represented with the same color. Panels **(B)** and **(C)** show the cluster size membership distribution (CSMD) of adapting (TSS902) **(B)** and non-adapting (TSS1020) cells **(C)** for the following conditions: no stimulus (blue), shortly after 1 mMMeAsp stimulation (magenta) and after prolonged stimulation (yellow). Curves represent complementary cumulative distribution function (1-CDF) which can be interpreted as the probability for a receptor to be found in a cluster of size bigger than a given value on the x-axis. Data in panel (B) were built based on PALM imaging of 86 cells adapted to no stimulus, 64 cells shortly after exposure and 100 cells exposed to prolonged stimulation. For each conditions we counted respectively $2900 \pm 1000$, $3200 \pm 1000$ and $2700 \pm 850$ molecules. Data in panel (C) were built based on PALM imaging of 85 cells exposed to no stimulus, 70 cells exposed to prolonged stimulation, 95 cells imaged shortly after exposure to chemoattractant. For each conditions we counted respectively $2100 \pm 950$, $2000 \pm 800$, $1800 \pm 700$ and $2400 \pm 900$ molecules. Shaded error bars represent the standard deviation obtained via boot strap resampling over cluster size (1000 iterations).

cognate ligand can significantly affect their spatial organization into clusters, which could in turn affect signaling function due to the relationship between cluster size and response cooperativity. The data for prolonged MeAsp stimulation (Fig. 4.2.2B, yellow curve) further demonstrates that this effect of MeAsp stimulation on cluster size is far from stationary. In fact, the distribution at the sampled time ($\sim$ 60 min) is very similar to that of the pre-stimulus condition (Fig. 4.2.2B, yellow curve), suggesting that the ligand effect on cluster size is of a transient nature, with the initial reduction in cluster size followed by a recovery towards the pre-stimulus steady state.

This recovery of receptor spatial organization upon sustained stimulation is reminiscent of the restoration of signaling (CheA kinase) activity due to sensory adaptation, a hallmark of bacterial chemotaxis signaling [205–207, 174]. We thus proceeded to test the possible involvement of the adaptation system, consisting of the methyltransferase/methylesterase enzymes CheR/CheB, by repeating the experiments in a strain that lacks the *cheR* and *cheB* genes (TSS1020). Shortly after stimulation by 1 mM MeAsp, these adaptation-deficient cells demonstrated a downward shift in the CSMD (Fig. 4.2.2C blue and magenta curves), similar to that observed above in adaptation-proficient cells (Fig. 4.2.2B). However, upon prolonged stimulation, no recovery of the CSMD was evident (Fig. 4.2.2C, yellow curve). The lack of cluster-size recovery in the adaptation-deficient (TSS1020) strain was not due to the ligand-induced change being fundamentally irreversible; when these cells were stimulated with 1 mM MeAsp for $\sim$ 60 min and then incubated without attractant for an additional $\sim$ 60 min, the CSMD was restored to its pre-stimulus state *(supporting information Fig.4.5.12 (SI))*.

Taken together, these observations demonstrate that stimulation by the attractant ligand MeAsp leads to a transient reduction in the size of Tar-mEos2 clusters, which recovers towards the pre-stimulus steady state upon prolonged stimulation in a CheR/CheB-dependent manner. Although the experiments presented above were performed in cells expressing Tar-mEos2 as the sole chemoreceptor, we have confirmed a similar (albeit weaker) ligand-dependent reduction in cluster size in a strain (TSS1162) expressing Tar-mEos2 in the presence of other chemoreceptors *(see Supporting Information section 4.5.4, Fig.4.5.9 (SI))*.

### 4.2.3 Global pattern of localization and local density of clusters are conserved under stimulation

As mentioned above (section 4.1), reports in the literature regarding the stability of chemoreceptor clusters upon ligand stimulation present an apparent conflict. On the one hand, studies that utilized diffraction-limited imaging of genetically encoded fluorescent fusion proteins in live cells reported no apparent change in localization [187, 188], and another employing

cryo-EM concluded that there is no change in the nanoscale density of receptors upon attractant stimulation[194]. On the other hand, diffraction-limited imaging studies that used immuno-fluorescence labeling in fixed cells concluded that chemoreceptors re-localize from the poles toward the cell body after attractant stimulation [189–191]. Our PALM observations at first sight might seem more consistent with the latter rather than the former, in that we do observe a stimulus-induced change in receptor spatial organization (Fig. 4.2.2). Upon closer inspection of the data, however, we found that the opposite is actually true.

To compare our PALM data with the global pattern of localization reported in diffraction-limited imaging studies [187–191], we computed the spatial density of PALM localizations along the cell's long axis under the three stimulus conditions (Fig. 4.2.3A). Although there was a mild decrease of PALM localization density at the cell poles shortly after exposure to 1 mM MeAsp, the global density profile was only subtly affected by this attractant stimulus (Fig. 4.2.3A). Similar results were obtained for non-adapting cells (not shown). Thus, no drastic re-localization was observed after attractant stimulation, in agreement with studies that utilized genetically encoded fluorescent fusion proteins [187, 188], but in contrast to those that utilized immuno-fluorescence labeling [189–191]. We note that the spatial density profiles in Fig. 4.2.3A were computed by pooling PALM data from many cells, whereas the analyses in the immuno-fluorescence studies (refs. [189–191]) involved classifying individual cells according to their degree of polar localization (by visual inspection, into classes such as "polar", "lateral" or "diffuse"). The contrasting results we obtained are however not likely explained by the effective ensemble averaging due to pooling of data in Fig. 4.2.3A, as classifying individual cells in a similar manner by their PALM localization pattern did not reveal significant differences across stimulus conditions in the fraction of cells demonstrating polar localization (not shown).

For comparisons with cryo-EM results [194] on the finer-scale arrangement of chemoreceptors within arrays, we computed the spatial density of PALM localizations within identified clusters (Fig. 4.2.3B) by dividing the size (*i.e.* number of detected receptors) of a cluster by the area of the image subregion it spans (*i.e.* its convex hull). This within-cluster density of chemoreceptors detected by PALM remained invariant across stimulus conditions in both adaptation-proficient cells (strain TSS902; Fig. 4.2.3B) as well as adaptation deficient cells (strain TSS1020; not shown). Thus, our PALM data are also compatible with the conclusion of the cryo-EM study of ref. [194], that nanoscale arrangement of array components is invariant under ligand stimulation.

In summary, despite the considerable stimulus-induced changes in the distribution of cluster size resolved by PALM (Fig. 4.2.2), neither the global pattern of cellular localization (Fig. 4.2.3A) nor the within-cluster density (Fig. 4.2.3B) were found to be drastically affected

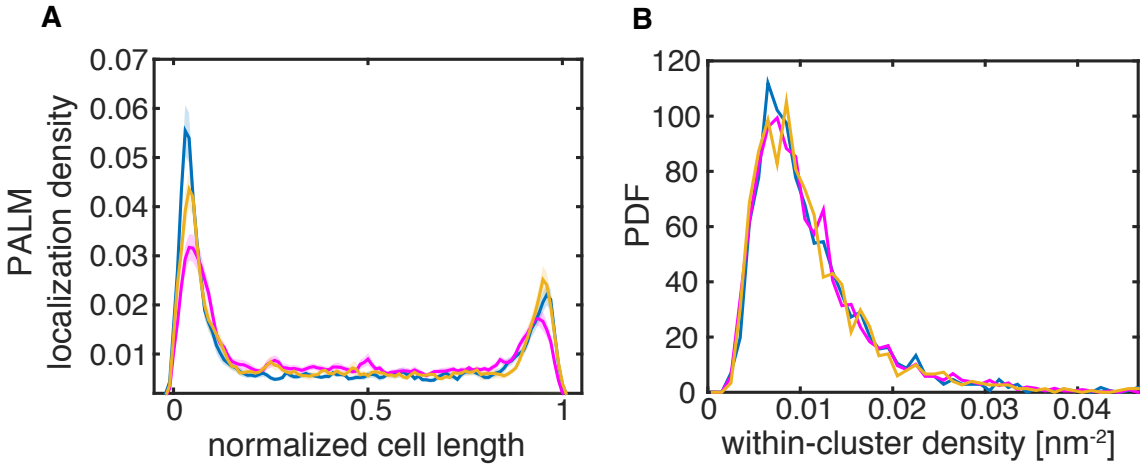


Fig. 4.2.3 **Spatial density of Tar-mEos2 PALM localizations across the cell and within clusters.(A)** Localization density of receptors along the cell body for adaptation-proficient (TSS902) cells. Density profiles were computed from PALM-localized coordinates from experiments similar to those for which PALM images are presented in Fig. 4.2.1. Cells were divided in 100 subregions along the long cell axis. The fraction of receptors in each region was computed and plotted against the normalized cell length. Shaded error bars represent the standard deviation obtained via bootstrap resampling over localizations. **(B)** Distribution of within-cluster density in adaptation-proficient (TSS902) cells. The average density was computed as the number of molecules divided by the area defined by the smallest enclosing perimeter (*i.e.* convex hull) of the cluster. In both **(A)** and **(B)**, data are shown for unstimulated cells (blue), shortly after 1 mM MeAsp addition (magenta) and after prolonged stimulation (yellow) with 1 mM MeAsp.

by ligand stimulation. Our results are thus compatible with previously reported data that showed little or no discernible effect of sensory stimulation on localization patterns by diffraction-limited imaging in live cells [187, 188] and on nanoscale ordering within clusters by cryo-EM [34]. Notably, however, we did not find evidence for the global rearrangement of receptor localization reported in immuno-fluorescence studies that utilized diffraction-limited imaging in fixed cells [189–191].

### 4.2.4 Live-cell PALM confirms stimulus-induced destabilization of receptor clusters without chemical fixation

A plausible explanation for the contrasting conclusions reached by previous studies is that the differences were caused by details of sample preparation protocols prior to imaging. Whereas the studies that reported no change in clustering upon ligand stimulation used either live cells [187, 188] or cryogenic samples [34], those that reported changes in clustering [189–191]

involved chemical fixation of cells that is required for immuno-fluorescence labeling. Our PALM experiments described above also involved chemical fixation of cells prior to imaging. Chemical fixation is standard for PALM imaging, to minimize movement of fluorophores during the relatively long acquisition times (often >1 hr) required for the inherently sequential imaging protocol. However, it is also known that fixation can lead to imaging artefacts, depending on the combination of fixation and labeling methods used, as well as the specific cellular structures being imaged [157, 208].

To rule out the possibility that the changes in clustering we observed (Fig. 4.2.2) are due to fixation artefact(s), we performed PALM imaging within living cells. Live cells of the adaptation-deficient strain TSS1020 were imaged by PALM in the absence of MeAsp and after $\sim$ 60 min exposure to 1 mM MeAsp, and the resulting molecular coordinates were subject to the same clustering analysis to obtain CSMDs (Fig. 4.2.4A). In these live-cell experiments, the shape of the CSMDs are less accurate than those obtained in fixed cells (Fig. 4.2.2B), because in live cells clusters (especially smaller ones) can move by diffusion [178, 209] over distances comparable to or greater than their own spatial extent during the relatively long acquisition times required for PALM imaging (45-60 min under our experimental conditions). Such movement can cause both artefactual splitting of clusters (if movement is sufficiently rapid, receptors belonging to the same cluster can be assigned to different clusters), as well as artefactual merging (if movement transiently brings two clusters into sufficient proximity). Indeed, the shape of the CSMDs obtained by live-cell PALM (Fig. 4.2.4A) were considerably distorted compared to those obtained by PALM in fixed cells (Fig. 4.2.2B). Nevertheless, after stimulation by 1 mM MeAsp, we found that the CSMD is again shifted significantly towards smaller clusters (Fig. 4.2.4A, magenta curve), suggesting that attractant-induced attenuation of cluster size occurs also in live cells that have not been subjected to chemical fixation.

If stimulation by chemoeffector ligands affect cluster size in live cells, we expect that the diffusive mobility of clusters will also be affected. The classic theory by Saffman and Delbrück [210] for Brownian motion of particles in a lipid bilayer predicts that the diffusive mobility $D$ scales as $D \sim \log(1/R)$, where $R$ is the radius of the particle's transmembrane segment. The available experimental evidence on the size dependence of transmembrane protein mobility *in vivo* indicate that the $\sim \log(1/R)$ scaling is sometimes borne out by the data [211] but in other instances it is even steeper [212, 213], presumably due to size-selective diffusion barriers such as membrane-lining cytoskeletal meshes or cell wall components. Nevertheless, the sign of the size dependence is always negative, with mobility decreasing as $R$ (or the number of transmembrane segments) is increased.

We therefore anticipated that the attractant-induced decrease in chemoreceptor cluster size would result in increased mobility. We found that the distribution of live-cell PALM localization spot sizes (*i.e.* the width $s$ of the 2-D Gaussian functions fitted to each photoactivated emitter spot) was significantly altered by MeAsp stimulation in a manner consistent with this expectation (Fig. 4.2.4B). In fixed cells where diffusion is negligible (Fig. 4.2.4B, dashed grey curve), this distribution is peaked at $\sim 120$ nm, close to the width of the point-spread function of the optical system, but is asymmetric with a positive skew due to enlargement of spots above and below the focal plane. In live cells this skew is substantially enhanced (Fig. 4.2.4B, blue curve), because diffusive movement within the finite exposure time ($\Delta t_x = 60$ ms) further enlarges the diffraction-limited spot size $s_{\mathrm{DL}}$ by an increment $\Delta s$ that increases with the diffusion coefficient $D$ of the emitter as $(\Delta s)^2 = s^2 - s_{\mathrm{DL}}^2 = 2D\Delta t_x$ [214–216]. When live cells were stimulated with MeAsp (Fig. 4.2.4B, magenta curve), the weight of the positive tail of the distribution is further augmented by a significant margin, indicating that the fraction of clusters with higher mobility is indeed increased, as expected if cluster size is decreased.

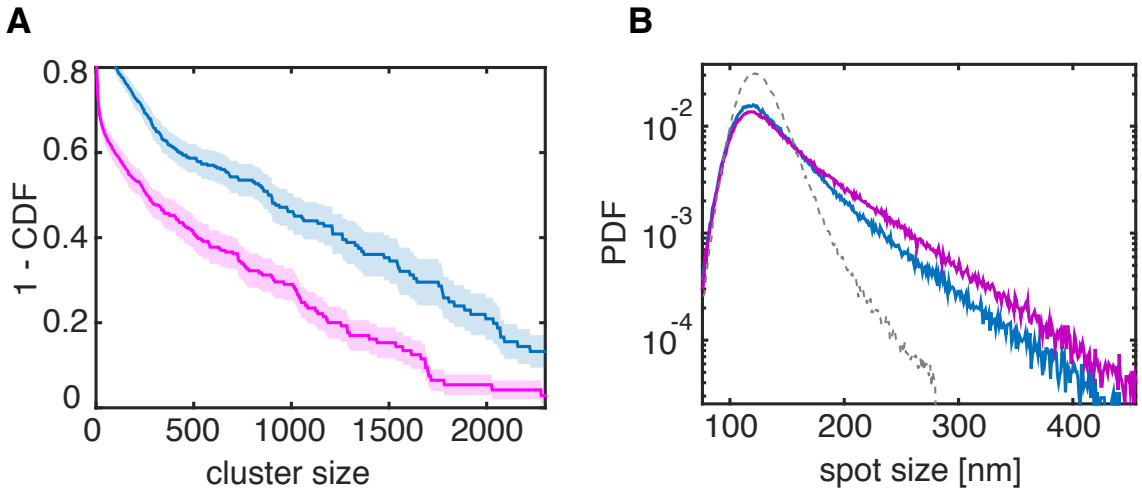


Fig. 4.2.4 **Live-cell PALM confirms MeAsp effect on cluster size and mobility, without chemical fixation.** **(A)** Tar-mEos2 CSMD in live cells (strain TSS1020). Data from unstimulated cells (blue) and cells stimulated with 1 mM MeAsp (magenta). Shaded error bars represent the standard deviation obtained via boot strap resampling over cluster size. **(B)** Distributions of the measured width of the localized spot for single molecules imaged by live-cell PALM. Data are from the same experiment presented in panel **(A)**. The grey dashed curve shows the distribution obtained in fixed cells. Prior to imaging, cells were exposed to MotM without MeAsp (blue) or stimulated for $\sim 60$ min with 1 mM MeAsp in MotM (magenta).

Taken together, these live-cell PALM data provide further support for the conclusion reached above by fixed-cell PALM: stimulation by the attractant MeAsp destabilizes chemoreceptor arrays to increase the fraction of clusters with smaller size (and hence higher mobility) within the population.

### 4.2.5 Direct observation of ligand-induced mobility changes by localized photoactivation single-particle tracking (LPA-SPT)

To more directly test for changes in chemoreceptor mobility upon ligand stimulation, we turned to single-particle tracking (SPT) of chemoreceptor clusters. SPT can be challenging for proteins such as chemoreceptors that are expressed at high spatial density, because both the high fluorescence background and frequent emitter collisions preclude reliable tracking. One strategy to overcome this difficulty is to engineer the expression of the labeled proteins to very low levels, so that single molecules in the emitting state can be tracked against a low fluorescence background until they bleach, and the procedure repeated as new proteins are synthesized by transcription and translation [217, 209, 211]. An alternative approach that utilizes photoconvertible fluorescent labels, known as "PALM tracking" or "sptPALM" [81, 108, 107, 83], allows efficient tracking at high expression levels of the labeled proteins by repeating cycles of stochastic photoactivation, tracking, and bleaching of individual labeled molecules. However, the comparatively low photostability of photoconvertible fluorophores limits achievable track lengths $N_T$ (typically $N_T < 10$ image frames for photoconvertible fluorescent proteins such as mEos2/mEos3.2). The tracklength $N_T$ is a crucial determinant of the precision with which the mobility of tracked emitters can be estimated, as it sets the amount of displacement statistics available for the estimation (to leading order, the uncertainty $\sigma_D$ in the estimate of the mobility $D$ decreases as $\sim N_T^{-1/2}$ [218]).

We therefore developed a modified PALM tracking technique, termed localized photoactivation single particle tracking (LPA-SPT) [200], that exploits the multiplicity of photoconvertible labels present in oligomeric complexes such as chemoreceptor clusters to extend the achievable tracklengths $N_T$. By contrast to standard PALM tracking, in which labels are photoconverted one molecule at a time by weak and uniform irradiation across the sample, in LPA-SPT the photoactivation light pulse is focused to diffraction-limited spots so as to photoactivate multiple labels within clusters that are (by chance) located within these 'hotspots' of photoactivation at the time of the pulse. The typical track length $\langle N_T \rangle$ is the expected number of frames that can be imaged before *all* emitters in a tracked cluster are bleached, so the increased number of emitters per cluster in LPA-SPT leads to longer tracklengths $\langle N_T \rangle$ (see *Materials and Methods*, and also Chapter 2). By use of a microlens

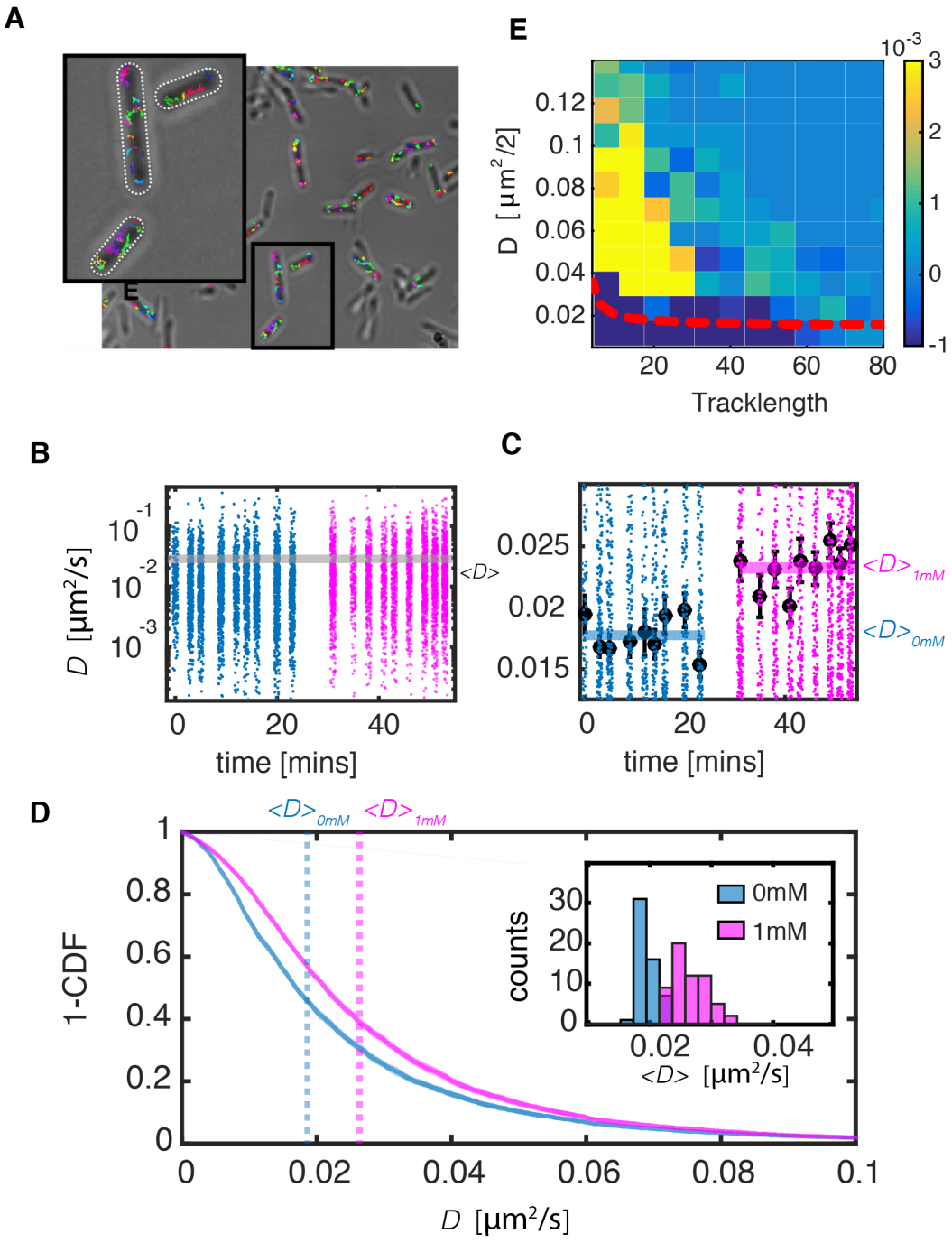


Fig. 4.2.5 **Mobility of receptor clusters under different ligand stimulation states. (A)** Representattive field of view with individual receptor-cluster trajectories obtained by LPA-SPT (each color is a different track) overlaid on bright-field image of cells. (Inset: Enlarged view of boxed region.) **(B)** Diffusion coefficients of all measured tracks as a function of time that were acquired within a $\sim$ 50-minute experiment on non-adapting (TSS1020) cells, either before (blue) or after (magenta) stimulation with 1 mM MeAsp. Each point in the plot correspond to a single track. The position of the gray bar represents the mean diffusivity across the whole experiment, and its width the standard error of the mean (s.e.m.). *(continued on next page)*

Fig. 4.2.5 *(continued from previous page)* **(C)** Zoomed view of the data presented in (B), for values close to the mean value. The mean diffusion coefficient for each field of view (FOV) is marked by a black dot (error bars: s.e.m.). Position of shaded bars correspond to mean, and their width the standard error of the mean across all FOVs for the unstimulated (blue) and stimulated (magenta) conditions. **(D)** Cumulative density function complement (1-CDF) of diffusivities of all tracks for the experiment of panels (B-C). Colors as in panels (B-C) and dashed vertical lines indicate the mean for each condition. Inset: histogram of average diffusivities across many repeats of the same experiment as that of panels (B-C). **(E)** Heat map of the difference between two-dimensional probability massfunctions (2D-PMFs) of unstimulated (0 mM) and stimulated (1 mM) conditions, $\Delta P(N_T, D) = P(N_T, D)_{1\mathrm{mM}} - P(N_T, D)_{0\mathrm{mM}}$. The 2D-PMF $P(N_T, D)$ corresponds the probability of a randomly chosen track in the data set to have a certain tracklength $N_T$ and diffusion coefficient $D$. Approximately 2500 tracks were used to compute $P(N_T, D)$ for both the 0 mM and 1 mM conditions. The red line represent the threshold for $D$ used to discriminate between mobile and immobile fractions of the receptor population *(see next section, Fig.4.5.14 (SI) and Materials and Methods)*.

array to form a lattice of diffraction-limited photoactivation spots at the sample plane (here, a square grid of 25 spots within the field of view), we maintain a high throughput of tracking across many cells simultaneously within the microscope field of view (Fig. 4.2.5A). In a typical experiment with Tar-mEos2, we obtain $\sim 500$ tracks per minute of acquisition time.

The high throughput of LPA-SPT allowed us to study dynamic changes in the mobility of chemoreceptor clusters in live cells undergoing ligand stimulation. Fig. 4.2.5B shows the extracted diffusivity of clusters as a function of the time at which they were acquired, for a typical experiment in which non-adapting (TSS1020) cells experienced a switch in the medium (from buffer to buffer with 1 mM MeAsp, at 25 mins) within a flow cell. Each 'stripe' of points corresponds to a 65 s acquisition ($1000 \times 65$ ms image frames, with 4 photoactivation pulses) within a single filed of view (FOV). The procedure was repeated across 9 FOVs (chosen at approximately equally spaced intervals across the flowcell coverslip on which cells were immobilized) prior to MeAsp addition (blue points), and across another 9 FOVs afterwards (magenta points). Reflecting the very broad distribution of cluster sizes we observed in PALM experiments above, these single-track mobilities were broadly distributed across a broad range both before and after ligand stimulation (Fig. 4.2.5B). However, the mean value of the distribution was significantly different between the two conditions (Fig. 4.2.5C), with the weight of the distribution shifted towards higher mobility after stimulation with 1 mM MeAsp (Fig. 4.2.5D), and this trend was robustly reproduced across many realizations of the same experiment (Fig. 4.2.5D, Inset). The average cluster mobility computed from pooling independent experimental repeats was $\langle D \rangle_{0\mathrm{mM}} = 0.019$

$\mu m^2/s$ without stimulation and increased to $\langle D \rangle_{1\text{mM}} = 0.027\ \mu m^2/s$ under stimulation. As with the PALM experiments above, for simplicity we focus here on genotypes expressing Tar-mEos2 as the sole chemoreceptor species, but we confirmed that a similar increase in mobility is also observed in cells expressing other chemoreceptor species *(see Supporting Information section 4.5.4, Fig. 4.5.10 (SI))*, albeit with a somewhat weaker effect that might be explained by crowding of the local membrane environment (Fig.4.5.11 (SI)). These data unambiguously establish that 1mM MeAsp stimulation significantly increases the mobility of Tar-mEos2 clusters in live cells.

### 4.2.6 Stimulation by cognate ligands trigger an increase in the mobile fraction of chemoreceptors

Could the observed changes in Tar-mEos2 cluster mobility (and size) upon MeAsp addition be triggered by some effect other than binding to its cognate chemoreceptor Tar? Several control experiments ruled out a number of such non-specific mechanisms including osmotic perturbations, effects on the fluorescent protein tag, and any other non-specific effects (e.g. perturbations of the plasma membrane) that could be sensed by a non-cognate chemoreceptor *(see Supporting Information section 4.5.3)*. Furthermore LPA-SPT experiments using an mEos3.2 fusion to the other major chemoreceptor Tsr revealed an analogous mobility change upon stimulation with its cognate ligand serine *(Supporting Information section 4.5.3)*. We thus conclude that a change in mobility (and cluster size) upon stimulation is likely a general feature of chemoreceptor responses to cognate ligands.

To test whether and how the changes in Tar-mEos2 mobility observed above are related to cluster size, we examined further the LPA-SPT data with a particular focus on track length statistics and how they are affected by the multiplicity of photoactivation events within tracked clusters. As noted above, LPA-SPT extends the achievable track length $N_T$ by photoactivating multiple labels in each cluster to the emitting state. Photoactivation can be understood as a stochastic process in which the photoconvertible label attached to each receptor has a probability $p$ of activation upon exposure to the photoactivation pulse. Then, the number of activated labels per cluster $n$ will increase with the cluster size $N$ (as $n \sim Np$), which will in turn extend the expected tracklength $\langle N_T \rangle$. Thus, the LPA-SPT track length $N_T$ bears information about cluster size. Although a precise estimation of the underlying cluster size from track length is complicated by the rather complex bleaching/blinking kinetics of photoconvertible fluorescent proteins (a recent detailed study for mEos2 identified a model with seven states and eleven transition rates [219]), as a general rule, an increase in tracks of

large $N_T$ can be interpreted as an increase in the incidence of large clusters, and vice versa for a decrease in $N_T$ (see also discussion in Materials and Methods, as well as Chapter 2).

We explored how MeAsp stimulation affects both the Tar-mEos2 mobility and track length in LPA-SPT experiments by computing two-dimensional probability mass functions (2D-PMF), $P(N_T, D)$, defined as the probability that a randomly chosen track in the measured set has a given length $N_T$ and diffusivity $D$. The heat map in Fig. 4.2.5E shows the difference $\Delta P(N_T, D) = P(N_T, D)_{1\text{mM}} - P(N_T, D)_{0\text{mM}}$ between the 2D-PMF computed under the stimulated and unstimulated conditions for the experiment of Fig. 4.2.5B-D. Consistently with the CSMD changes observed in PALM experiments (Fig. 4.2.2), Fig. 4.2.5E shows that MeAsp stimulation increases (yellow) the fraction of tracks with characteristics expected for small clusters (low $N_T$ and high $D$) at the expense of decreasing (dark blue) tracks with characteristics expected for large clusters (high $N_T$ and low $D$). As a control we carried out an experiment with the same duration and tracking protocol but with no ligand stimulus, and found no significant difference between 2D-PMFs for tracks in the first and second half of the experiment (data not shown). Thus, the pattern of PMF differences observed upon ligand stimulation further supports the idea that the cluster size distribution shifts towards smaller values upon MeAsp stimulation, and the decreased cluster size underlies the observed increase in mobility. Consistent with this view, in a mutant strain defective in cluster formation (due to the CheW-X3 mutation [220]) we observed no change in Tar-mEos2 mobility upon MeAsp stimulation *(see Fig.4.5.13 (SI))*.

Finally, we note that as in any SPT experiment, the precision $\sigma_D$ with which the mobility $D$ of tracked objects can be estimated using LPA-SPT depends on a number of experimental parameters, the most important of which are the tracklength $N_T$, localization precision $\sigma$, the inter-frame interval $\Delta t$, as well as the mobility $D$ itself. To optimize the tracking protocol, the experimenter can tune (within limits set by relevant constraints) $\sigma$ by controlling the light level, and $\Delta t$ through the camera frame rate, so as to minimize $\sigma_D$ given the expected (or experimentally tested) range of $D$ and $N_T$ values [218, 221]. However, the very broad distribution of chemoreceptor cluster size and mobilities imply that values of $D$ and $N_T$ within the sample span a very broad range. This poses a challenge as it becomes impossible within the same experiment to optimize $\sigma_D$ over the whole range of $D$. We thus computed $\sigma_D$ as a function of $N_T$ for our experimental conditions (Fig. 4.2.5E, red dashed curve) using an estimation method for $\sigma_D$ developed in ref. [218], and used it to classify tracks into two categories. Tracks with estimated mobility $D$ lower than $\sigma_D$ (*i.e.* $D/\sigma_D < 1$) are statistically indistinguishable from a emitter with a fixed position and thus classified as "immobile". The remaining tracks (for which $D/\sigma_D \geq 1$) were classified as "mobile". The data of Fig. 4.2.5E

thus illustrate that upon MeAsp stimulation, the mobile fraction of clusters grows at the expense of the immobile fraction.

### 4.2.7 Dynamics of cluster mobility under sustained stimulation reveals adaptation-dependent recovery

Having confirmed that the mobility of chemoreceptor clusters increase upon attractant stimulation in a manner consistent with the cluster-size decreases observed in PALM experiments, we proceeded to test also the effect of sensory adaptation on cluster mobility using LPA-SPT. We tracked the mobility of Tar-mEos2 in both adapting (TSS902) and non-adapting (TSS1020) cells within a flow cell, before addition of 1 mM MeAsp and at multiple time points thereafter while the stimulus was sustained (Fig. 4.2.6A)). The average mobility $\langle D \rangle$ increased to a maximum at short times ($\sim$ 10 mins after stimulus arrival), as expected, in both adapting cells (Fig. 4.2.6A, blue squares) and non-adapting cells (Fig. 4.2.6A, red circles). Surprisingly, however, upon longer exposure to MeAsp, $\langle D \rangle$ subsequently decreased not only in adapting cells but also in non-adapting cells, and in adapting cells this decay of $\langle D \rangle$ further undershot the pre-stimulus level at the longest time tested ($\sim$ 180 mins after stimulus arrival). By contrast, unstimulated cells maintained an approximately constant level of $\langle D \rangle$ in an identical experiment with no MeAsp addition (Fig. 4.2.6A, gray triangles).

This steady and monotonic decrease in cluster mobility is intriguing, as it occurs in both adapting and non-adapting cells, but only in the presence of the ligand stimulus, and shows no sign of slowing down even at the longest times tested ($\sim$ 180 mins). To gain further insight into the underlying changes in the chemoreceptor population, we examined the 2D-PMF differences between the pre-stimulus condition successive time points after the stimulus (Fig. 4.5.14 (SI)). At short times ($\sim$ 10 mins), the 2D-PMF difference profile was similar between adapting and non-adapting cells (and also to the previous example, Fig. 4.2.5E), with the mobile fraction of tracks (above the red dashed curve in Fig. 4.5.14 (SI), where $D/\sigma_D \geq 1$) increasing at the expense of the immobile fraction. At longer times, however, the positive (yellow) peak that appeared in the mobile fraction gradually dissipated in adapting cells and had vanished by the final time point ($\sim$ 180 mins), whereas in non-adapting cells the peak appeared more stable, and was still present (albeit at a somewhat diminished profile) at $\sim$ 180 mins. Strikingly, the immobile fraction of tracks (below the red dashed curve in Fig. 4.5.14 (SI), where $D/\sigma_D < 1$) slowly, but steadily increased at long times in both adapting and non-adapting cells (Fig. 4.2.6B). Interestingly, this increase in the immobile fraction was not observed in the experiment with no MeAsp stimulus.

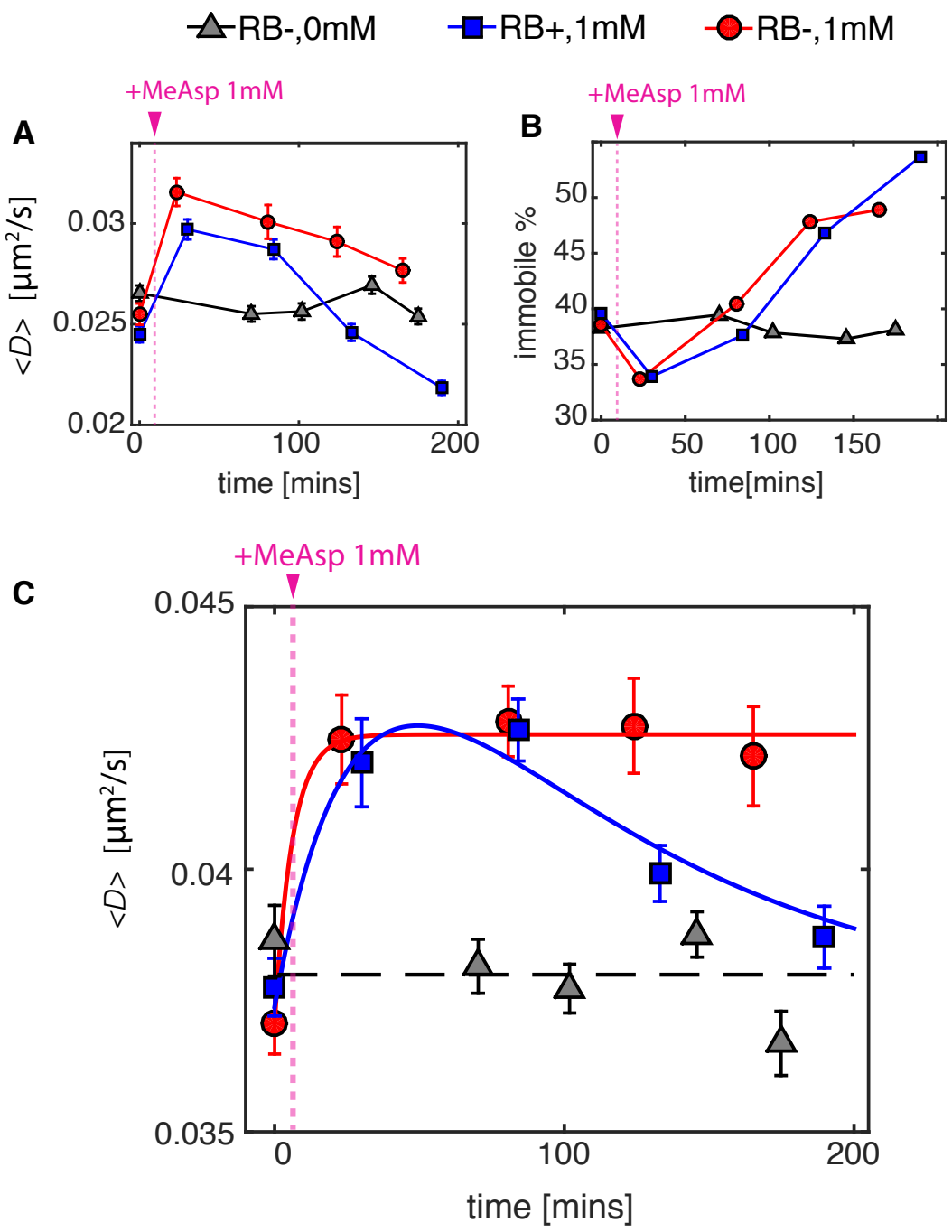


Fig. 4.2.6 **Time evolution of Tar-mEos2 cluster mobility upon prolonged MeAsp stimulation.** **(A)** Time evolution of the average diffusion coefficient $\langle D \rangle$ for non-adapting cells (TSS1020, red circles) and adapting cells (TSS902, blue squares) exposed to sustained 1 mM MeAsp stimulation. Time of MeAsp addition indicated by the the magenta arrow. Unstimulated cells are also shown for comparison (TSS1020, gray triangles). **(B)** Time evolution of the fraction of clusters classified as immobile according to the criterion $D/\sigma_D < 1$ (see text). Colors and symbols as in (A). **(C)** Same as (A) but recomputed after excluding immobile clusters. Data for non-adapting cells (TSS1020, red) were fit with $f(x) = p_1\ [1 - e^{-x/p_2}]$, giving $p1 = 0.038 \mu m^2/s$, $p2 = 5.8$ mins. Data for adapting cells (TSS902, blue) were fit with $f(x) = p_1\ (1 - e^{-x/p_2})\ e^{-x/p_3}$ giving $p1 = 0.01 \mu m^2/s$, $p2 = 10.2$ mins, $p3 = 109.7$ mins.

The immobile fraction's slow and monotonic dynamics, its presence in both adapting and non-adapting cells, and dependence on the presence of the MeAsp stimulus (Fig. 4.2.6B) suggested that it might be responsible for the slow and monotonic decay in the average mobility $\langle D \rangle$ (Fig. 4.2.6A). We thus recomputed the time evolution of $\langle D \rangle$ after excluding the immobile fraction (Fig. 4.2.6C). This revealed a striking contrast between adapting and non-adapting cells in their long-time $\langle D \rangle$ dynamics under sustained MeAsp stimulation. Whereas $\langle D \rangle$ in adaptation-deficient cells remained approximately constant after the initial stimulus-induced increase, $\langle D \rangle$ in adapting cells gradually recovered towards the pre-stimulus level of mobility.

Taken together, the observations above suggest that MeAsp stimulation triggers three distinct processes that play out on different timescales: (i) at short times, stimulation of the cognate chemoreceptor Tar rapidly reduces its cluster size and increases its mobile fraction; (ii) at long times, slow but steady (and CheR/CheB-independent) growth of the immobile fraction dominates; (iii) at intermediate times, the initial increase in mobility is counteracted by the adaptation system which reduces the mobility of the mobile fraction in a CheR/CheB-dependent manner.

## 4.3 Discussion

Chemoreceptor clusters are the central hub for signal processing in the control of bacterial chemotaxis behavior. They are observed ubiquitously across the diverse range of prokaryotic species that possess chemoreceptors [222, 223], and the highly ordered arrangement of molecules within their nanoscale array structure [28, 193] appears to be universally conserved [224]. Functionally, they provide the structural basis for signal amplification [225, 203, 226, 220], precise adaptation [227, 228], integration of multiple chemical and physical stimuli [183, 204], and play a central role in determining the response to time-varying inputs [229–231] in a manner that enhances migratory responses to environmental gradients [115]. Although a large body of work over decades has succeeded in detailed characterization of both structural and functional properties of chemoreceptor clusters, the stability of their spatial organization under environmental signal perturbations has remained an elusive topic, with multiple prior studies [36, 32, 31, 33, 224, 35] drawing contrasting conclusions.

Our results unambiguously demonstrate that *E. coli* chemoreceptor clusters undergo changes in their spatial organization in response to sensory stimuli. Given the importance of clustering in chemoreceptor function, dynamic and stimulus-dependent modulation of clustering could have far-reaching consequences for chemotactic signal processing. We discuss

here the implications of our observations in the context of prior works, and highlight the new questions they raise regarding both underlying mechanisms and functional consequences.

**Both ligand stimulation and adaptation affect chemoreceptor clustering**

Although our observation that attractant stimulation significantly reduces chemoreceptor cluster size (Fig. 4.2.2) seems at first to contradict previous diffraction-limited imaging studies that reported no change under similar perturbations in clusters labeled by GFP variants [36, 32], further analysis of our PALM data revealed that the global pattern of PALM localizations at the cellular scale was only subtly affected, with no drastic relocalization upon stimulation (Fig. 4.2.3A). Such subtle changes in the receptor density profile would likely have been missed in those previous studies, which reported results of visual inspection rather than detailed quantitative analysis of the diffraction-limited images. Similarly, our results are also compatible with the cryo-EM study that reported no change in the nanoscale arrangement upon stimulation [34], as in our PALM data we found no change in the within-cluster density of labeled chemoreceptors upon stimulation (Fig. 4.2.3B). Conversely, previous diffraction-limited imaging studies that utilized immuno-fluorescence labeling of chemoreceptors [31, 33, 35] reported a global redistribution of chemoreceptors, from polar localization in the absence of stimulus, to a nearly uniform "diffuse" staining of the plasma membrane upon attractant stimulation. Our PALM experiments did not recapitulate this pattern of drastic relocalization either in live or fixed cells. The reason for this discrepancy is presently unknown, but it is known that immuno-labeling can produce imaging artefacts that depend on details of fixation/permeabilization methods [157], and it has been speculated [34] that subtle conformational changes that result from ligand binding might affect binding of the conjugated antibody labels. Our experiments combining PALM in both fixed and live cells, and LPA-SPT in live cells reveal a consistent picture in which attractant stimulation significantly reduces the cluster size distribution without strong effects on either the global pattern of localization or the nanoscale ordering of molecules within clusters.

From a functional point of view, stability of chemoreceptor clusters has strong implications for logarithmic sensing of chemoeffector concentration, which allow cells to respond to relative, rather than absolute, changes in inputs (also known as Weber's law [232] or fold-change detection [233]). The quantitative theory of chemoreceptor cluster function based on allosteric MWC models [183, 204, 184, 234] that successfully reproduces nearly all of the reported dose-response data, predicts that the observed logarithmic sensing in bacterial chemotaxis [232, 235, 231] requires the effective cluster size $N$ (i.e. the number of strongly coupled ligand-binding units; also called the "signaling team" size by some authors) to be invariant upon adaptation to different background levels of stimuli [229, 231]. The significant

ligand-induced changes we observed by PALM in the cluster size distribution (CSMD) would thus seem detrimental to logarithmic sensing and at odds with multiple studies that have demonstrated it over a broad range of background stimulus levels [232, 235, 231]. Our observation that CheR and CheB act to restore the cluster size distribution upon prolonged stimulation suggests that these adaptation enzymes provide recovery of not only signaling activity, but also the spatial organization of chemoreceptor clusters upon prolonged stimulations, to maintain the invariance in effective cluster size ($N$) required for logarithmic sensing upon adapting to changes in ambient stimulus levels.

**Relation to slow dynamics in chemoreceptor signaling**

Previous experiments by Frank et al. [236] combining *in vivo* FRET with fluorescence anisotropy measurements revealed gradual changes in the signaling activity of receptors under prolonged stimulation by MeAsp lasting $\sim$ 10 mins, much slower than the initial receptor-kinase response upon ligand binding, which occurs within 1 s [237, 238]. These slow changes were interpreted to be the result of changes in the packing density of receptors. Consistent with the idea that such slow changes reflect alterations in clustering state, these slow dynamics were absent in mutant cells unable to form large clusters [220]. It seems plausible that such changes in signaling activity and 'receptor packing' result from the stimulus-induced changes in the cluster size distribution we observed our PALM and LPA-SPT experiments. The change in fluorescence anisotropy upon sustained MeAsp stimulation observed by Frank et al. [236] was due to a decrease in homo-FRET between YFP-labeled chemoreceptors, the efficiency of which falls sharply to zero on a $\sim$ 10 nm length scale. In our PALM data analysis, clusters were defined by a distance threshold of 20 nm (matched to the approximate localization precision), so the MeAsp-induced repartitioning of the receptor population into smaller clusters we observed should be detectable as a reduced 'packing density' in fluorescence anisotropy measurements of the type reported in refs. [236, 220]. Furthermore the sign of the slow changes in signaling activity observed by Frank et al. using (hetero-)FRET between CheY and CheZ [236] was negative, that is, receptor-kinase activity slowly *decreased* under prolonged MeAsp stimulation. Furthermore, they found that the same prolonged MeAsp stimulus also caused a reduction in the response cooperativity of receptors. These observations are consistent with expectations if the cluster size were gradually decreasing during the same interval, as cluster size is known to correlate positively with response cooperativity and inversely with the stimulus concentration that elicits a half-maximal receptor-kinase response [183, 204, 184], *i.e.* smaller clusters respond more strongly to the same sub-saturating concentration of ligand. Thus, although it remains possible that the slow changes in 'receptor packing' observed by Frank et al. [236] is caused

by more subtle rearrangement of receptor spacing within intact clusters, ligand-induced destabilization of chemoreceptor clusters of type we observed here by PALM/LPA-SPT may provide a sufficient explanation.

More recently, two studies that applied CheY-CheZ FRET at the single-cell level [239, 240] discovered large fluctuations in receptor-kinase activity in the absence of changes in ligand concentration. In adapting (CheRB+) cells, timescale of such fluctuations matched the $\sim$ 10 s timescale expected for the stochastic kinetics of the the adaptation enzymes CheR/CheB, but fluctuations were still present in non-adapting (CheRB-) cells on a slower ($\sim$ 100 s) timescale. The origin of such adaptation-independent fluctuations remain to be determined conclusively, but given that they occur in the absence of stimulation or adaptation, most likely represent intrinsic dynamics of chemoreceptor clusters. Our observations with PALM/LPA-SPT that both ligand stimulation and adaptation cause changes in cluster size clearly indicate that chemoreceptor clusters *in vivo* are more dynamic than previously envisaged [241], and thus may undergo size fluctuations even in the absence of external perturbations. Given that the changes in clustering due to prolonged stimulation are observable as changes in signaling activity [236], it seems plausible that fluctuations in the cluster-size distribution could underlie the observed adaptation-independent signal fluctuations at the single-cell level [239, 240]. Given that the amplitude and timescale of chemotactic signal fluctuations can affect both search and gradient-climbing behaviors of swimming bacteria [242–244], it will be of interest to study further the role of cluster-size dynamics in generating these steady-state signal fluctuations.

### Open questions and future directions

One aspect we have not addressed extensively in this study is the diversity of possible chemoreceptor cluster stoichiometries and expression levels of components. Functional chemoreceptor clusters are ternary complexes between chemoreceptors, the scaffolding protein CheW, and the kinase CheA. Their assembly *in vivo* is expected to be a stochastic process [5] and thus at steady state we expect a finite fraction of subunits to be diffusing freely or in intermediate complexes that might involve e.g. only receptor-receptor or receptor-CheW contacts. Furthermore, although for simplicity we have concentrated here mainly on genotypes that express only a single receptor species, we have shown that the magnitude of ligand-induced changes can clearly depend also on the presence of other receptor species (Figs. 4.5.9 (SI),4.5.10 (SI)) as well as the chemoreceptor expression level (Fig. 4.5.11 (SI)). It is known that the total level of chemotaxis protein expression depends on the growth medium [245] and relative stoichiometries of chemoreceptors change with the cell density in batch cultures [246, 247, 239]. Thus, it will be of interest to extend our PALM/LPA-SPT

experiments to probe the dependence of cluster-size dynamics on cluster stoichiometry. To address also possible heterogeneity in cluster composition under fixed expression levels of components, it would be informative to perform such experiments with fluorescent labeling of multiple chemoreceptor species, as well as cytosolic subunits such as CheA.

One surprising finding in the LPA-SPT experiments was that in addition to the initial increase in mobility (decrease in cluster size) upon MeAsp stimulation and slower adaptation-dependent recovery (Fig. 4.2.6A), MeAsp stimulation also triggered a very slow, but steady, growth of the large clusters at very long times (Fig. 4.2.6B). Although the origin of these very slow stimulus-dependent dynamics is not clear at present, it is interesting to note that a recent study that applied diffraction-limited imaging in growing cells over multiple generations [248] revealed that polar and lateral regions of the cell appear to present different diffusion barriers for chemoreceptor clusters, and weak disruptions of chemoreceptor cluster stability (by expressing the array-formation-deficient scaffolding mutant CheW-X3 in addition to wt CheW) appear to facilitate the "escape" of smaller clusters from the lateral region to preferentially join the larger clusters at the pole. It is plausible that in our LPA-SPT experiments, the ligand-induced destabilization of clusters also facilitates the escape of smaller clusters from lateral regions to eventually join larger clusters at the pole. It will be of interests to explore this possibility in future LPA-SPT experiments, by following the cellular loci of tracked clusters and determining whether the stimulus-induced slow growth of large clusters occurs at the cell poles.

In conclusion, our PALM/LPA-SPT results reveal that the *E. coli* chemoreceptor clusters are more dynamic than previously appreciated. The cluster-size distribution is affected by both ligand stimulation and sensory adaptation, and we in addition discovered a very slow increase in the chemoreceptor fraction belonging to very large clusters. Although we have focused here mainly on cells expressing a single chemoreceptor species (Tar or Tsr), our observation that these stimulus-dependent changes in cluster size are specific to cognate stimuli for each receptor species raise the possibility that the stimulus history can affect how multiple chemoreceptor species are partitioned into clusters, and hence how signals are different sensory stimuli are integrated by the cell.

## 4.4 Materials and methods

### 4.4.1 Bacterial strains and plasmids

All strains used in this study are derivatives of RP437 [202], a widely used *E. coli* K-12 strain for studies of chemotaxis signaling and behavior, and are listed in Table 4.1. UU1250

is a receptorless strain lacking genomic copies of all chemoreceptors, originally constructed in the laboratory of Prof. J.S. Parkinson (U. Utah), but obtained through Prof. H.C. Berg's laboratory (Harvard U.). VH1, a gift of Prof. V. Sourjik (MPI, Marburg, Germany), is also receptorless, but in addition lacks the *cheR* and *cheB* genes and is hence deficient in sensory adaptation.

The coding sequence of the photoconvertible fluorescent protein mEos2 was genetically fused to that of Tar receptors to yield a fusion protein Tar-mEos2, which was placed under the control of an IPTG-inducible promotor in a pTrc99A plasmid expression vector [110] (ampicillin resistance). Tar was fused to mEos2 via a GSGGGG flexible linker. The plasmid was transformed in both strains, UU1250 and VH1, which were named TSS902 and TSS1020, respectively. Functionality of the constructs was checked using a cell swarming assay and by measuring the activity of CheA kinase using a FRET sensor [249, 250], *(see Fig.4.5.5 (SI))*.

| **Strain** | **Background** | **Source** | **Relevant genotype** | **Plasmid** |
|---|---|---|---|---|
| TSS902 | UU1250 | [113] | $\Delta tsr, \Delta tar\text{-}tap, \Delta trg, \Delta aer$ | pSJAB4 |
| TSS1020 | VH1 | [114] | $\Delta tsr, \Delta tar\text{-}tap, \Delta trg, \Delta aer$ $\Delta cheRBYZ$ | pSJAB4 |
| TSS1045 | UU1250 | [113] | $\Delta tsr, \Delta tar\text{-}tap, \Delta trg, \Delta aer$ | pSJAB35 |
| TSS1162 | VS172 | [249] | $\Delta tar\text{-}tap$ $\Delta cheRBYZ$ | pSJAB4 |
| TSS1907 | VH1 | [114] | $\Delta tsr, \Delta tar\text{-}tap, \Delta trg, \Delta aer$ $\Delta cheRBYZ$ | pSJAB156 |
| TSS1961 | UU2869 | Sandy Parkinson | $\Delta tsr, \Delta tar\text{-}tap, \Delta trg, \Delta aer$, *cheW-X3* $\Delta cheRBYZ$ | pSJAB4 |

Table 4.1 Bacterial strains used in this study

| Plasmid | Product | System | Inducer | Resistance | Source |
|---|---|---|---|---|---|
| pSJAB4 | Tar-mEos2 | pTrc99A | IPTG | ampicillin | this work |
| pSJAB35 | Tar-mEos3.2 | pTrc99A | IPTG | ampicillin | this work |
| pSJAB156 | Tsr::mEos3.2 | pRR48 | IPTG | ampicillin | this work |

Table 4.2 Plasmids used in this study

### 4.4.2 Media and buffer

For overnight cultures, we used TB medium (10 g/L Bactotryptone, 5 g/L NaCl, pH 7). Day cultures were prepared in H1 minimal medium (50 mM $KPO_4$, 7.6 mM $(NH_2)_4SO_4$, 0.5 mM $MgSO_4$, 1.25 $\mu M$ $Fe_2(SO_4)_3$, 0.01% thiamine, 67 mM NaCl, 1 mM histidine,1 mM leucine, 1 mM L-methionine, 1 mM threonine, pH 7.4). For experiments, cells were washed with and resuspended in motility medium (MotM: 10 mM $KPO_4$, 10 mM lactic acid, 1 $\mu M$ L-methionine, 0.1 mM EDTA, pH 7.4 for PALM and pH 7.0 for single particle tracking).

### 4.4.3 Cell culture

Cells were inoculated from a glycerol stock into rich liquid culture medium (TB) and grown overnight until saturation. The morning after, the saturated culture was inoculated 1:100 into fresh H1 medium (100 $\mu L$ in 10 mL) supplemented with 0.5% glycerol as carbon source, 100 $\mu g/mL$ ampicillin and 20 $\mu M$ IPTG. After 6 h and 15 min growth in a shaker incubator (180rpm) in the dark at 33.5 °C, cells were harvested by centrifugation (Eppendorf Centrifuge 5810) at 5000 rpm for 5 minutes at room temperature and kept at room temperature for the following steps. Supernatant was discarded and the cells were resuspended in 20 mL MotM. This washing step (centrifugation and resuspension) was repeated twice. For PALM imaging, after the last centrifugation step, cells were finally resuspended in 1.5 mL MotM (the culture was thus concentrated of a factor of $\sim$7) and incubated for 60 minutes at room temperature before further treatment. For single particle tracking, after the last centrifugation step, cells were resuspended in a final volume of 1 mL (the culture was thus concentrated of a factor of $\sim$10) and incubated at least 30 minutes at room temperature.

### 4.4.4 Sample preparation

#### PALM experiments

#### Preparation of fixative solution

Fixative solutions of 4% paraformaldehyde were prepared freshly before each experiment according to the following protocol: 18 mL of 0.01 M NaOH solution were prepared and heated to ∼50°C. 0.8 g of para-formaldehyde powder (PFA, Sigma Aldrich, product number: P6148) were dissolved in the warm solution by shaking for ∼30 min. The solution was cooled down to room temperature and 2 mL of 10x MotM were added. pH was adjusted to 7.4 using ∼140 µL HCl (5 M). For fixation of stimulated cells, fixative solutions were prepared in the presence of the non-metabolizable attractant α-methyl-[DL]-aspartic acid (MeAsp, Sigma Aldrich, product number: M6001). 10 µL of 1 M MeAsp solution (in MotM) were added to 10 mL of PFA solution ∼30 s prior to cell fixation.

**Cleaning and coating of coverslips and glass slides** Coverslips (24x60 $mm^2$, thickness 0.17mm) and glass slides (26x76 $mm^2$) were cleaned as follows: glass slides were positioned in teflon holders and washed with Milli-Q (MQ) water. They were rinsed successively with acetone, MQ water, ethanol and MQ water, and incubated in 1% Hellmanex (Sigma Aldrich, product number: Z805939) solution overnight. After thorough rinsing with MQ, coverslips were further incubated in 50% $H_2O_2$ (Sigma Aldrich, product number: 516813) at 80°C overnight. $H_2O_2$ was removed by thorough washing with MQ water. Coverslips were dried with filtered $N_2$. After drying, coverslips were stored not longer than 1 month in air in a sealed beaker for later use.

For immobilizing bacterial cells, a drop of 0.05% Poly-L-Lysine solution (Sigma Aldrich, product number: P8920) was deposited at the center of a clean coverslip for ∼15 min, which was then carefully rinsed with MQ water by use of a micropipette. Then a 3-5 µL drop from a 100–fold diluted stock solution of fiducial markers (100 nm diameter gold particles, Cytodiagnostic, purchased from Sigma Aldrich, product number: 742031), that was shortly treated in a sonification bath before use, was added. After ∼15 min, the coated spot on the coverslip was carefully rinsed three times with MQ water and three times with MotM. Cells were finally deposited on the drop for 15 min in the dark and non attached cells were removed by gently rinsing three times with MotM. The final cell density on the coverslip was ∼1 cell per $\mu m^2$. Note that only ∼20% of the cells were attached properly for imaging.

**Stimulation and fixation of cells** Clustering of Tar receptors was investigated under three different conditions: *(i)* no stimulation, *(ii)* short stimulation with MeAsp and *(iii)* prolonged

exposure to MeAsp. In general, after incubation for one hour at room temperature in MotM, cells were centrifuged at 10.000 rpm for 5 min. In case of *(i)*, cells were resuspended in fresh 4% PFA solution. For condition *(ii)*, the challenge lies in limiting the time between stimulation and exposure to PFA. For stimulation, cells were resuspended in 0.75 mL MotM containing 1 mM MeAsp. We then added 0.75 mL of 8% PFA solution containing 1 mM MeAsp as well. Time between resuspension and addition of fixative solution was as short as possible ($\sim$10 s). As before, the final PFA concentration was 4%. To realize condition *(iii)*, cells were resuspended in 1 mL MotM containing 1 mM MeAsp and incubated for 60 min. Afterwards, cells were centrifuged again at 10.000 rpm for 5 min and then resuspended in 4% PFA solution containing 1 mM MeAsp. Always, cells were fixed for $\sim$10 min in the respective PFA solutions, then washed three times in MotM and kept in the dark prior to imaging.

**Sample chamber assembly** A silicone spacer with a round aperture (Grace biolabs, CoverWell imaging chambers) was sticked on a clean microscope slide and the resulting chamber was filled with MotM. The coverslip coated with cells and fiducial markers was placed on top of the spacer with the cells facing toward the fluid. The chamber was quickly and carefully sealed by gently pressing the boundaries. The sample was imaged not later than $\sim$3 hours after fixation. Waiting a longer time between PFA fixation and imaging leads to detection of false positive localizations what might impair further analysis.

**Live-cell PALM** For live-cell PALM imaging, cells were cultured following the same protocol as in the fixed-cell experiments (see above). Here, two conditions were studied: *(i)* unstimulated (in MotM buffer) and *(ii)* prolonged exposure to 1 mM MeAsp. After incubation for one hour in MotM at room temperature, cells were centrifuged and resuspended in either *(i)* MotM or *(ii)* 1 mM MeAsp solution in MotM for $\sim$60 min. Imaging chambers containing either *(i)* MotM or *(ii)* 1 mM MeAsp in MotM were prepared in the same way as in the PALM experiments (see above).

### Localized photoactivation single-particle tracking (LPA-SPT)

**Flow cell assembly** For flow cell experiments, we used round coverslips (ø 12 mm, bioWORLD, thickness=0.17mm) that were cleaned in the same manner as the PALM experiments (see above). 15 µL of concentrated cell suspension were deposited on a cleaned coverslip where a circular pattern of vacuum grease had been deposited for later sealing to the flowcell. 1 to 2 µL of anti-FliC antibodies solution ($\sim$2 ng/ml, a gift of H.C. Berg) were added onto the coverslip followed by incubation for 20 minutes.

During this incubation time, the stainless flow-cell was cleaned with acetone and ethanol by injecting the solvents in the inlet and outlet with a syringe. After that, the flowcell was connected to the pump, sealed with an empty coverslip whose rim was coated with a ring of vacuum grease and rinsed with MQ water for 5 minutes and MotM for 1 minute (for a more detailed description of the flowcell setup see Chapter 2).

After incubation time had elapsed, the empty coverslip used to seal the flowcell during the washing step was replaced with the one on which bacteria had been immobilized. MotM flow was initiated, the flowcell was placed on the microscope stage and bacteria were focused using bright field imaging. By means of a fluidic switch, we could change the medium and that is flowing in the flow chamber. That allowed us to modulate the stimulation state of the immobilized cells, and we could perform LPA-SPT under the different conditions described in the results section.

### 4.4.5 Microscopy

All PALM and LPA-SPT experiments were carried out on an inverted Nikon Eclipse Ti-E equipped with a high numerical aperture objective (CFI Apo TIRF 100X Oil, NA = 1.49, Nikon), chromatic filters (SemRock, for green state of mEos: EX R405/491/561/635 multi-edge, EM FF01- 525/45-25. For red state of mEos2: EX R405/491/561/635 multi-edge, EM NF02 405S-25/NF03 561E-25/FF01-607/70-25) and an EMCCD camera (Andor iXon Ultra 897, 512x512 pixels) with a 150x magnification (pixelsize = 106 nm). The camera was used in electron multiplying mode with a gain of 100. Bright field cell images were recorded with a dia-illumination lamp and condenser (from the Nikon Eclipse Ti-E microscope ). For photoactivation of mEos2 a 405 nm laser (Coherent, CUBE 405-100C maximum power: 100mW) and for excitation of photoactivated mEos2/mEos3.2 a 568 nm laser (Coherent, Sapphire 568 CW, maximum power: 200mW) were used. For PALM imaging, both beams were focused on the back focal plane of the microscope objective. In this configuration, the sample is illuminated with approximately collimated beams. For LPA-SPT, the 405 nm laser was focused on the objective focal plane via a microlens array (Edmund Optics, focal length at 405 nm F $\simeq$ 25 mm, pitch = 1500 $\mu$m, array of 6 × 6 = 36 microlenses, custom product) to locally switch our receptor fusions to the red-fluorescent state. Both lasers were controlled by an acusto-optical tunable filter (AA Opto Electronic, model: MCQ110-A2-VIS) that allowed for precise stroboscopic illumination. The 405 nm laser was also blocked by a mechanical shutter to avoid mEos2/mEos3.2 photoactivation outside the localized photoactivation pulse window. In order to minimize background light from out-of-focus fluorescence we used highly inclined illumination ($\theta \sim 60^o$) [251]. A mirror inserted in a L-shaped, 1x telescope allowed us to incline the beam illuminating the sample. The mirror is installed on a translation

mount with micrometer sensitivity (Thorlabs, PT1) allowing for fine tuning of the beam inclination. Sample position and focus were controlled with a motorized piezo stage and the microscope's built-in Perfect Focus System (PFS; Nikon).

### PALM imaging protocol

The imaging procedure for PALM have been extensively described in a general context by Betzig et al. [197] and more specifically for *E. coli* chemoreceptor imaging by Greenfield et al. [198]. Briefly, mEos2/mEos3.2 fluorophores, initially in their green fluorescent state, are stochastically photo-switched to their red fluorescent state by means of 405 nm laser irradiation at low light density. The photoactivation rate is kept sufficiently low compared to the bleaching rate to enable successive imaging and bleaching of randomly photoactivated individual fluorescent proteins which allows precise localization of the fluorescent reporter [197, 252]. The 405 nm laser power was increased exponentially over time from $\sim$1.6 mW/cm$^2$ to $\sim$395 mW/cm$^2$ in order to compensate for depletion of the pool of unbleached proteins and keep the activation rate approximately constant. Both the pulse duration of the 568 nm laser for red-state excitation as well as the camera exposure time were set to 60 ms and a delay of 5 ms was kept between consecutive frames, to achieve an acquisition rate of 1/(65 ms)$\approx$15 image frames per second. The excitation intensity per unit area at the sample plane was $\sim 500 W.cm^{-2}$.

Before starting the acquisition, samples were first exposed to 568 nm irradiation in order to bleach undesired auto-fluorescence and enable subsequent low-background imaging. Focus was maintained actively with the microscope's PFS system. For all samples, great care was taken to adjust focus on the fiducial markers attached to the coverglass surface. This ensured that the bottom part of the cells (proximal to the glass surface) is imaged with a depth of field of approximately $\sim$400 nm. This depth of field corresponds to the distance at which the size of a diffraction limited spot is increased by two fold [253].

### LPA-SPT imaging protocol

By tuning the amount of antibodies added to the bacterial solution on the slide relative to the optical density of the bacterial solution, we could obtain a convenient (avoiding overlapping of bacteria but also providing enough cells in the field of view to overlap with the LPA 405nm spots) density of well attached bacteria, suitable for LPA-SPT analysis. Care was taken to avoid bacteria overlapping and to avoid sparse bacterial profiles leading to low tracking throughput. The stage was translated so that the 25 focused 405-nm spots overlapped as much as possible with immobilized bacteria. Tracks were collected from dozens of fields

of view (FOVs) per experiment, sampled following a grid spatial pattern to avoid repeated measurements of the same sample area. For each FOV, a sequence of 1000 images was collected. First, a short pulse of 405 nm activation laser produced 25 photoactivation spots. Photoactivation was repeated 3 times every 250 images during acquisition. Each localized photoactivation pulse lasted 4 to 10 ms and each localized photoactivation spot carried 0.04 mW on average. Photoactivated mEos2/mEos3.2 molecules were excited with the 568 nm laser at a light density of $\sim$1500 W/cm$^2$. Frame rate was 15 Hz, but excitation lasted only half of the frame duration to minimize localization error due to PSF motion blur. For each different stimulation condition, tracking was repeated for a typical number of 8 different FOVs contributing around 500 tracks each, leading to a total of around 4000 tracks per condition in a typical experiment.

### 4.4.6 Data analysis

#### Localization and reconstruction in PALM images

Localization and data reconstruction were all performed using custom code written in MATLAB (MathWorks) with procedures commonly used in localization microscopy [254]. First, fluorophores were detected using an image segmentation algorithm based on wavelet transform [255]. Second, for each detected fluorophore subpixel localization was achieved by fitting the point spread function (PSF) to a Gaussian function [256, 257] using a maximum likelihood estimator [258]. The average standard error on the position of molecules was estimated [258] to $\sim$20 nm in our experimental conditions. Then, gold particles localized with $\sim$2 nm precision were used for microscope stage drift correction. In a next step, diffraction limited spots that were detected in consecutive images and separated by less than the localization error were considered as images of the same molecule. The localization was thus performed again using the sum of the raw images to increase localization precision. Finally, for each cell all coordinates of receptors were assembled to form a super-resolution image.

As fluorophores are detected and then irreversibly bleached during the PALM experiment, one expects a saturation of the total number of detected molecules when all the molecules in the field of view are imaged. We found that not all cells imaged with PALM demonstrated this characteristic saturation of detected fluorophores. Because the lack of saturation could reflect the presence of a large number of background fluorophores (*i.e.* a high incidence of false-positive counts inside the imaged cells, which were found to increase with time after fixation), we discarded cells that do not demonstrate saturation of detected fluorophores from further analysis see *(Supporting information)*.

### Clustering and molecular counting

Because PALM imaging is based on localization of single-molecules, one obtains information not only about the spatial density of the labeled molecules but also their absolute abundance. In principle, obtaining the absolute number of molecules present in a sample could be as simple as keeping count of the PALM localizations during the imaging protocol until complete bleaching is achieved. However, there are multiple sources sources of error can confound molecular counting by PALM, and careful consideration and correction of these errors, using appropriate control data is essential to minimize errors in PALM counting. Here, we provide a brief overview of the corrections we have applied to minimize errors in our counting of Tar-mEos2 localizations (for a more detailed discussion of these factors and our corrections, see *Supporting Information*.

In principle, PALM allows molecular counting. However, blinking of the fluorophore might lead to several localizations of the same receptor. Several attempts have been made to overcome this issue [259, 260, 199]. Lee *et al.* proposed an iterative algorithm which, via careful calibration of the blinking kinetics, allows precise counting [199]. But this method is applicable only for structures the size of the PSF which are separated by more than the localization precision. It was thus difficult to employ on our data. Instead, we used an estimator for the number of molecules *(see [199] and supporting information)*. Calibrating mEos2 blinking, we found an average of 1.25 localization per molecule (0.25 blinking events) in our experimental conditions. The number of proteins per cluster was thus rescaled by this number. Calibration of mEos2 blinking is described in the *Supplementary information*.

In case of cells with Tar-mEos2 expression levels much higher than the average, probability increases that two molecules separated by less than the size of the PSF are activated at the same time and cannot be distinguished. This is a problem for super-resolution as well as molecular counting. We thus want to select for those cells that do not exhibit successive activations at a time distance $< t_{off}$, the average time between two blinking events, to avoid PSF to appear in the same diffraction limited region at a given time. Since in our PALM experiments the rate of mEos2 activation is approximately constant during the first 4500 seconds of imaging *(see Fig.4.5.4A,B (SI))*,

Even in our low 405nm irradiation regime, for cells where the Tar-mEos2 expression level is much higher than the average, there is an increased probability that two molecules are activated at the same time in the same Diffraction Limited (DL) region, and thus cannot be distinguished. It is evident that this is a problem for super-resolution as well as molecular counting. We thus want to select for those cells where two successive localizations happen at a time distance minor than $t_{off}$, the average time between two blinking events, to avoid PSF from different mEos molecules to appear in close proximity a given time. In fact, via

post-processing of PALM data is possible to identify blinking events and filter out unwanted localizations of the same fluorophore, but only if no other fluorophores are activated in the same DL region between blinking bursts. Given that under our imaging conditions mEos2 molecules blink less than once on average before bleaching, (*see Supporting Information*) excluding cells with a measured localization rate major than $1/t_{off}$ will reduce the total number of localizations duplicates in our data. In our PALM experiments the localization rate per cell is approximately constant during the first 4500 seconds of imaging *(see Fig.4.5.4B (SI))* and in that time window the localization rate scales with the total number of fluorophores in the cell. Thus, to select cells in which we localize at most one fluorophore during a time interval $t_{off}$, we can impose a threshold $N^*$ on the total number of localized fluorophores per cell in the experiment. Given the assumptions above, $N^*$ is given by

$$\frac{N}{2T} = k^* < 1/t_{off} \tag{4.1}$$

$$N < \frac{2T}{t_{off}} \equiv N^* \tag{4.2}$$

where $k_{th} = 1/t_{off} s^{-1}$ and $t_{tot}$ is the total duration of the experiment.
From our PALM data we find that 40% of the receptors are associated in the biggest cluster of the cell (data not shown), and the biggest cluster is the cellular location where the probability of activating two proximal fluorophores at the same time is highest. In addition, cells usually exhibit two large clusters, found at each cellular pole (see Fig. 4.2.1B,C and D). We thus rescale $N_{th}$ by this factors to obtain

$$N_{th} < 0.4\, k_{th}\, t_{tot} \times 2 \tag{4.3}$$

where the factor of 2 takes accounts the presence of two big polar clusters. From our calibration of the photophysics of mEos2 we find $\langle t_{off} \rangle = 1.8s$. Plugging the values of $\langle t_{off} \rangle$ and $t_{tot} = 10000s$ in Eq. 4.3 we obtain

$$N_{th} < 0.4 \times 1/1.8 \times 10000 \times 2 = 4777 \tag{4.4}$$

Clustering was performed using a custom algorithm written in MATLAB. Two localizations were considered as clustered if their pairwise distance was smaller than a threshold $L_{max}$ = 20 nm. For each cluster, the algorithm validated if one localization from the contour of this cluster was at a distance lower than $L_{max}$ from one molecule at the contour of another cluster, and would merge these clusters in this case. This procedure was repeated for all clusters

iteratively until the number of clusters per cell reached a steady-state. A cluster was defined by *(i)* a list of localizations within the cluster and *(ii)* a list of localizations at its contour.

### Spatial distribution of Tar receptors

Analysis of the spatial distribution of receptors along the cell axis was performed in a semi-automated fashion. The major axis was defined manually for each cell and the axis for each individual cell was divided into 100 equal segments. For each segment the fraction all localization events that project onto that segment was computed. Pooled data from all cells were then averaged separately for each condition.

Polar regions were defined as the regions between the cell boundary at the cell pole and a point at a distance along the cell axis smaller than 15% of cell length from this boundary. Polar clusters were defined as a peak located in a polar region having a density above the mean density of cell body plus three times the standard deviation of the mean. For the data presented in Fig. 3A, we first projected the pixel values of PALM reconstructed images of single cells (separately for all the conditions presented in Fig3) along the (normalized) long axis of the cell, we then re-oriented all the projected line profiles thus obtained such as to have the bigger polar cluster (peak) on the same side and then averaged all the re-oriented projections.

### LPA-SPT tracks analysis for mobility estimation

Localization and tracking (i.e. subsequent localizations linking) of localized activation data was performed via a custom made script which based on the 'u-track' tracking software from G. Danuser's laboratory [119]. All the subsequent analyses were carried out via a custom written MATLAB or Python code. To reduce the error on our estimates of diffusion coefficients, tracks were filtered according to length ($L > 5$ frames) and position in the sample, retaining only tracks that overlapped completely with bacteria. To filter out tracks that did not overlap with cells, bright field images of bacterial cells in the FOV were segmented via a custom written Python code that employs the Skimage package and makes use of adaptive thresholding to cope with inhomogeneous illumination. Only the tracks that fell onto the segmentation mask were retained. This way we discarded unwanted localizations from emitters outside the cells. From the segmented bright field image we also retrieved the subcellular position of the tracks (polar or middle cell), such that we could monitor mobility in the polar and middle-cell regions separately (as in Fig.4.5.10 (SI)). After aligning the long cell axis of each segmented cell with the abscissa, cell poles were defined as the set of pixels whose projection on the x axis was falling between 0 and 15% or 85% and 100% of the cell's

long axis length. Tracks where classified as "polar" if at least 85% of the localizations in each track were found inside a polar region (similarly for middle-cell tracks). If a track spanned both polar and middle cell regions in similar proportion it was classified as "spurious" and discarded form the polar-middle analysis.

The following quantities were computed at the single-track level: *(i)* mean-squared displacement as a function of time lags ($MSD(t)$), *(ii)* unbiased covariance-based estimator (CVE) for the mobility $D$ (Eq. (14) or (16) of ref. [218], see below), *(iii)* sub-cellular position, *(iv)* track length in frames. These quantities were pooled together to build distributions for each condition of these measured and estimated parameters as described in the text.

### Using tracklength from LPA-SPT experiments as a proxy for cluster size

As discussed in Chapter 2, our LPA-SPT analysis revealed a correlation between track-length and diffusivity: receptor clusters that are tracked for longer, tend to have a lower diffusivity. The standard Safman-Delbruck theory for the diffusivity of a membrane protein predicts that the mobility $D$ is a monotonically decreasing function of size (of the transmembrane segment). We thus employ track-length as a proxy of cluster size in our analysis. As mentioned in section 4.2.6, a fully quantitative understanding of this correlation would require treatment of the rather complex photophysics of mEos fluorophores, as recently detailed in ref. [219] involving seven states and 11 rates, not all of which have been measured/estimated. Nevertheless, we expect the tracklength to increase monotonically with the tracked cluster size due to the following simple line of reasoning.

The number $n$ of activated fluorophores follows a binomial distribution with a mean $\langle n \rangle = Np$ that increases with the cluster size $N$ and the probability $p$ that each of the single $N$ fluorophores is switched on by the photoactivation pulse. The number of frames a cluster can be tracked after localized photoactivation is determined by the first passage time $t^*$ at which the number of emitting molecules drops to zero (we note that our system has sensitivity down to the single-molecule regime). The distribution of $t^*$ is of course dependent on the bleaching/blinking statistics of mEos fluorophores, but a generic feature of first-passage times is that the expectation value $E[t^*]$ is an increasing function of the initial value $n$. Thus, the average tracking time $E[t^*]$ must increase with $\langle n \rangle = Np$. Thus, the track length $t^*/\Delta t$ (where $\Delta t$ is the inter-frame interval) can be used as a proxy for cluster size $N$.

### Unbiased estimator for D and mobile/immobile classification of tracked clusters

To estimate clusters' diffusion coefficient from LPA-SPT tracks we employed the covariance-based estimator (CVE) method introduced by Vestrgaard et al. [218], which obtains unbiased

estimates of the mobility $D$ directly from the statistics of displacements, rather than those of mean-squared displacements (MSD). The estimator presented in that work, is superior to traditional methods based on MSD [261] for diffusion coefficient estimation, since it does not require fitting and does not suffer from the correlation between squared displacements at different times. This estimator has been shown to be bias-free also for short noisy time series, as opposed to other estimators based on maximum likelihood and MSD [218]. Thus, it is well suited for tracks coming from protein based fluorophores (like mEos) which have a relatively low photostability compared to organic dyes. Computation of the CVE takes into account the finite localization precision of experimental detection systems, motion blur during camera exposure, as well as the non-zero (anti-)correlation between successive displacements, which would otherwise generate biases and large uncertainties on diffusion coefficient estimation from short noisy tracks.

The treatment given in [218] stems from including stochastic errors caused by finite localization precision and motion blur due to particle motion during camera exposure in the estimation of diffusion coefficients. Here we outline the essential line of reasoning and method of calculation.

We first define the experimentally measured position of the tracked particle in the $n$-th image frame as

$$x_n = \int_{t_n-\Delta t}^{t_n} x_{true}(t_n - t)c(t)dt + \sigma\xi_n \tag{4.5}$$

where $x_{true}(t)$ represent the actual position of the particle, $\sigma$ is the localization error (which is possible to estimate by performing multiple localizations of the same immobile emitter with a given imaging system and by taking the square root of the variance of the outcomes), $\xi_n$ represents Gaussian noise with zero mean, unit variance and zero autocovariance while the function $c(t)$ describes the state of the camera shutter during a time lapse $\Delta t$: $c(t) = 0$ means closed shutter, while $c(t)$>0 means open shutter. We note two important features of Eq. 4.5; (i) the time integral of the product of the true position of the particle and the function $c(t)$ accounts for motion blur during camera exposure (ii) the additive term $\sigma\xi_n$ accounts for stochastic errors in localization with variance $\sigma^2$.

Starting from Eq. 4.5, Berglund [262] derived an analytic expression for the covariance of displacements ($\Delta x_n = x_n - x_{n-1}$)

$$\langle \Delta x_n \Delta x_m \rangle = \begin{cases} 2D\Delta t + 2(\sigma^2 - 2DR\Delta t) & \text{for n = m} \\ -(\sigma^2 - 2DR\Delta t) & \text{for m = n + 1} \\ 0 & \text{for |n-m|>1} \end{cases} \tag{4.6}$$

where $R \equiv (\Delta t)^{-1} \int_0^{\Delta t} \left[\int_0^t c(t')dt'\right] \left[1 - \int_0^t c(t')dt'\right] dt$ is a 'motion blur coefficient' that depends only on the shutter function $c(t)$ and for most experiments takes a constant value between zero (perfect strobe, *i.e.* no motion blur) and 1/4 (fully open shutter). From Eqs. 4.6 it is clear that the mean squared displacement of experimental trajectories suffers from correlations between observed displacements (second term in the first row of Eq. 4.6) induced by motion blur and static localization noise in tracking experiments even though free Brownian particles actually move with uncorrelated displacements. Importantly, the first row of Eqs. 4.6 reduce to $2D\Delta t$ if we have exact knowledge of the position of the tracked particle. The CVE for $D$ and $\sigma^2$ is obtained by substituting the expected values $\langle \cdots \rangle$ in Eqs. 4.6 with averages $\overline{\cdots}$ computed from experimentally measured trajectories and solving Eqs. 4.6 for $D$ and $\sigma^2$. These estimators are easy to compute, take into account motion blur and localization errors and thus are superior to classic MSD-based estimators that, as we have seen, ignore the correlation of displacements present in experimentally measured trajectories and assume $MSD = \langle (\Delta x_n)^2 \rangle = 2D\Delta t$.

To compute the data in Fig. 4.2.5C,D and E showing diffusivity of clusters under different attractant stimulation conditions, we analyzed our tracks (time series of cluster positions) with Eq. (14) from ref. [218] which provides an unbiased estimator for $D$:

$$D = \frac{\overline{(\Delta x_n)^2}}{2\Delta t} + \frac{\overline{\Delta x_n \Delta x_{n+1}}}{\Delta t}. \tag{4.7}$$

On the other hand, the diffusion coefficients plotted in Fig. 4.2.6 and for classifying clusters as mobile or immobile (see red line in Fig. 4.2.5B and Fig. 4.5.14 (SI)) we computed D using instead Eq. (16) from ref. [218]:

$$D = \frac{\overline{(\Delta x_n)^2} - 2\sigma^2}{2(1-2R)\Delta t} \tag{4.8}$$

The difference between Eq. 4.7 and Eq. 4.8 is in the way the localization error $\sigma^2$ comes into play: in Eq. 4.7 it is implicitly taken into account by the second term which makes use of the positional data at the single track level, while Eq. 4.8 requires a prior estimation of such parameter (when we employed Eq. 4.8, instead of using $\sigma^2$ computed for each single track we evaluated its average $\overline{\sigma^2}$, by averaging the values of $\sigma^2$ obtained for single tracks, see below). This difference between the two equations, is the reason why values for D presented in Fig.4.2.5 and Fig.4.2.6 differ slightly for the same condition (we used eq 4.7 and 4.8 respectively) while the temporal trends under attractant stimulation were conserved.

Subsequently, we wanted to estimate the error on our estimate of $D$ to compare it to the value of $D$ itself in search of a criterion for classifying mobile and immobile clusters, when tracked with our imaging system. We used Eq. (18) from Vestergaard et al. to estimate $\sigma_D^2$

$$\sigma_D^2 = [\frac{D^2(2+4\varepsilon+3\varepsilon^2)}{N_T(1-2R)^2} + \frac{\mathrm{var}(\sigma^2)}{(1-2R)^2(\Delta t)^2}] \tag{4.9}$$

where $N_T$ is the track length and

$$\varepsilon \equiv \frac{\sigma^2}{D\Delta t} - 2R \tag{4.10}$$

To evaluate $\varepsilon$ we used again the average value of the squared localization error $\overline{\sigma^2}$ from all tracks. To compute the average, we computed the localization error $\sigma^2$ for each single track using eq (15) of [218])

$$\sigma^2 = R\overline{(\Delta x_n)^2} + (2R-1)\overline{\Delta x_n \Delta x_{n+1}} \tag{4.11}$$

We then used $\overline{\sigma^2}$ in order to compute $\varepsilon$. We found $\overline{\sigma^2} = 5.29 \times 10^{-4} \mu m^2$. The numerator in the second term in the right hand side of Eq. 4.9 accounts for stochastic error on the estimate of $\langle \sigma^2 \rangle$ (*i.e.* it is the uncertainty on the estimate of $\sigma^2$), and is computed as the variance of the localization error $\mathrm{var}(\sigma^2)$ across all (independent) tracks in the experiment. We found $\mathrm{var}(\sigma^2) = 9.43 \times 10^{-7} \mu m^4$.

We then used Eq. 4.9 with $\varepsilon$ and $\sigma$ estimated in this manner to classify each tracked clusters as immobile or mobile. Specifically, tracks were classified as immobile if

$$\frac{D}{\sigma_D} < 1 \tag{4.12}$$

and they were classified as mobile otherwise.

## 4.5 Supporting Information

### 4.5.1 Molecular Counting with PALM

Performing molecular counting via PALM imaging is challenging due to the complicated photo physics of photo-activatable or photo-convertible fluorophores (PCFP, like mEos). For instance, due to blinking (see Fig. 4.5.1A (SI)) or incomplete bleaching during the imaging frame time, a single molecule can be localized over subsequent imaging frames and counted multiple times. In addition to irreversible bleaching PCFP can indeed decay to intermediate energy dark state via heat release. These dark states are long lived triplet state with life time ranging from milliseconds to seconds. PCFP will then further loose energy to return into the red state. In practice, this leads to blinking of single emitters. As shown in Fig.4.5.1A

(SI), alternate periods of emission of the PCFP of duration $t_{on}$ and dark periods of duration $t_{off}$ can be observed when imaging PCFP. If ignored, such blinking would lead to multiple detection of the same PCFP and over-counting as the number of time a single emitter is detected $N_{burst}$ can be greater than one.

A trivial way to cure the blinking issue would be to reduce drastically the 405 nm activation rate so that the delay between activation of two PCFP in a diffraction limited region would be much greater that the average $t_{off}$. In theory, this would allow to temporally resolve a series of bursts from another series arising from different emitters. In practice, it would increase the experiment duration drastically thus introducing other issues related to sample aging. We opted instead for a mathematical analysis of the average number of blinking events per mEos2 molecule in order to estimate a correction factor with which rescale the number of single molecule localizations in each cluster. Lee et al. [199] provided a method to quantify the impact of PCFP blinking on molecular counting, which we successfully employed. They have shown that the number of blinking events is well described by a geometric distribution:

$$p(N_{blink}) = (1-q)\, q^{N_{blink}} \tag{4.13}$$

where $q$ depends of the bleaching rate $k_b$ and the rate at which mEos2 is converted into the dark state D $k_d$ :

$$q = \frac{k_d}{k_d + k_b} \tag{4.14}$$

They have shown that by calibrating mEos2 blinking one can provide an unbiased estimate of the true number of molecules, $N_{moc}$:

$$N_{moc} = \frac{N_{burst}}{1 + < N_{blink} >} \tag{4.15}$$

Where $N_{burst}$ is the total number of PALM localizations. We have thus used equation 4.15 to rescale the number of molecules in each cluster by $1 + < N_{blink} >$. In the next section we describe the methodology we adopted to estimate $< N_{blink} >$ from our PALM data.

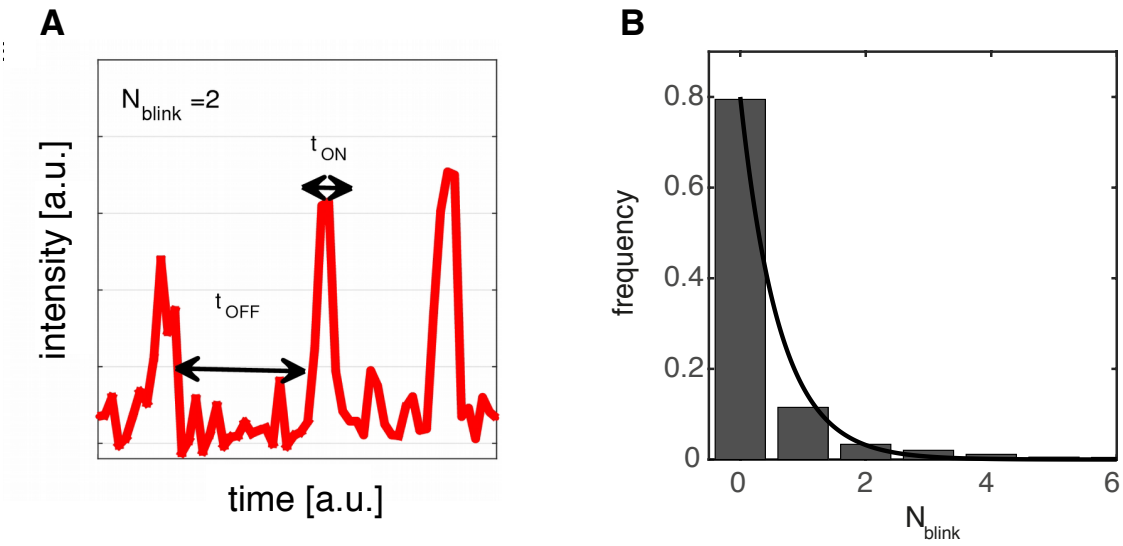


Fig. 4.5.1 (SI) **Blinking of single emitter.** (**A**) The figure shows an example time series of a single mEos2 molecule emission during a PALM imaging experiment in TSS902. The integrated intensity from a single emitter is plotted as a function of frame number (frame rate $\sim 15$ Hz). In this particular example, one can observe three burst ($N_{blink} = 2$). We define $t_{off}$ as the time delay between two burst and $t_{on}$ as the burst duration. (**B**) Distribution of number of blinking events per molecule in cells expressing mEos2 alone (TSS1002, parent: UU1250 $\Delta tsr, \Delta tar\text{-}tap, \Delta trg, \Delta aer$, plasmid: pRSETA expressing mEos2). Bars are the experimental data and black line show the best fit to a geometric distribution : $p(N_{blink}) = (1-q)q^{N_{blink}}$. We found $q = k_d(k_d + k_b)^{-1} = 0.2$ and thus $< N_{burst} >= 1 + < N_{blink} >= 1.25$.

### Calibration of mEos2 photo-physical properties

As discussed in the previous section, for estimating the true number of molecules in our PALM based counting experiments we needed to measure $< N_{blink} >$, the average number of blinking events per molecule. In this context we also compared mEos2 photo-physics in the presence and absence of MeAsp in order to confirm that the blinking statistics was similar in the two different buffers ($0mM$ MeAsp and $1mM$ MeAsp in Mot. Med.).

We first estimated the average number of bursts per mEos2 molecule (not fused to any chemoreceptor) for cells in the imaging buffer (Mot. Med.), expressing mEos2 alone. mEos2 was expressed from a plasmid in a cell lacking genomic copies of all receptors (TSS1002, parent: UU1250 $\Delta tsr, \Delta tar\text{-}tap, \Delta trg, \Delta aer$, plasmid: pRSETA expressing mEos2). Cells were grown and fixed with para-formaldehyde following the exact same protocol as the one followed for the data in the main text. The imaging laser power density at $568nm$, exposure and inter frame interval were the same as for the PALM experiments presented in the main text.

However the activation laser power 405*nm* was kept much lower (100 fold lower) and was not exponentially increased. This allowed us to image single FP with a sufficient time interval between different activations, in order to completely avoid overlapping of burst time series from different molecules. The distribution of measured $N_{blink}$ is presented on Fig.4.5.1B (SI). We estimated the average number of burst per molecule to be $1+ < N_{blink} >= 1.25 \pm 0.5$ (see Fig.4.5.1B (SI)). We thus used this number to re-scale our molecular counting outcomes. For each cluster the number of burst detected is divided by 1.25 to estimate the true number of molecules.

We then repeated the procedure above for Tar-mEos2, in the absence of MeAsp. For these experiments cells were grown and fixed with para-formaldehyde and imaged following the same protocol as for the experiments presented in the main text. Again, the activation power was maintained 100 fold lower compared to the PALM counting experiments. As shown on Fig. 4.5.2A and B we found $< N_{blink} >= 1.38 \pm 0.5$ in the absence of MeAsp and $< N_{blink} >= 1.29 \pm 0.5$ in the presence of MeAsp. Such a small difference can not produce nor affect the shift in CSMD we observed (Fig. 2A and B of the main text) and we attribute it to experimental variability. As shown in Fig. 4.5.2C,D (SI) the distribution of $t_{on}$ and $t_{off}$ nicely overlap for Tar-mEos2 in the presence or absence of 1 mM MeAsp (Fig.4.5.2C,D (SI)). We conclude that MeAsp do not influence the blinking kinetics of mEos under our experimental conditions.

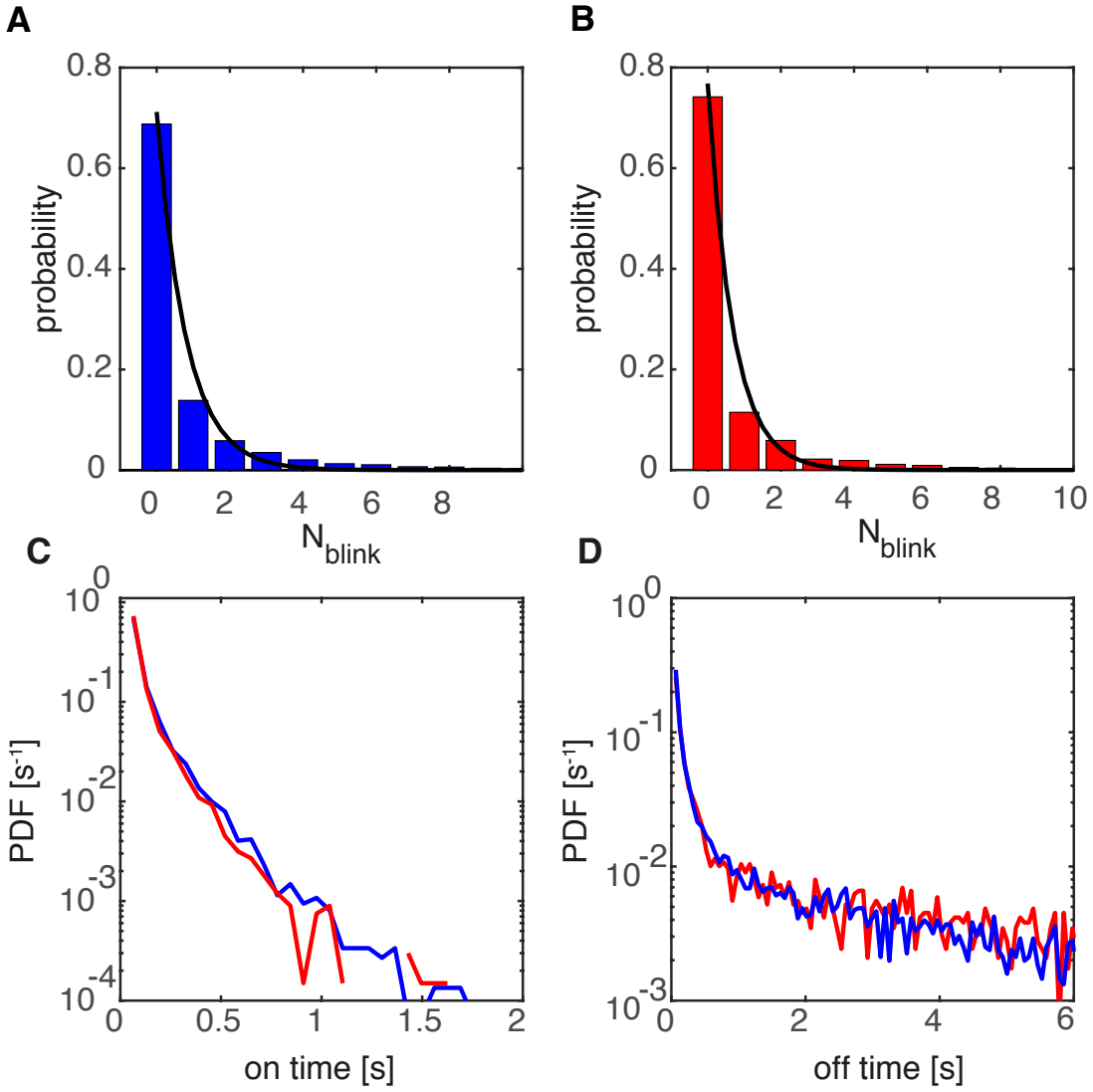


Fig. 4.5.2 (SI) **Comparison of mEos2 photo-physical parameters in the presence and absence of 1 mM MeAsp.** Data for unstimulated cells are presented in blue and data for cells stimulated with 1 mM MeAsp are presented in red. - (**A**) Distribution of number of blinking events per molecule for Tar-mEos2 in unstimulated cells ($0mM$ MeAsp). Blue bars are the experimental data and black line show the best fit to a geometric distribution. $p(N_{blink}) = (1-q)q^{N_{blink}}$. We found $q = k_d(k_d+k_b)^{-1} = 0.28$ and thus $< N_{burst} >= 1 + < N_{blink} >= 1.38$. - (**B**) Distribution of number of blinking events per molecule for Tar-mEos2 in stimulated cells (1 mM MeAsp). Red bars are the experimental data and black line show the best fit to a geometric distribution. $p(N_{blink}) = (1-q)q^{N_{blink}}$. We found $q = k_d(k_d+k_b)^{-1} = 0.23$ and thus $< N_{burst} >= 1 + < N_{blink} >= 1.29$. - Distribution of off time (**C**) and on time (**D**) for stimulated (red) and unstimulated cells (blue). There is no difference in mEos2 photo-physical parameters in the absence or the presence of 1 mM MeAsp.

### Estimation of the fraction of non-detected molecules

Some molecules may prematurely bleach before emitting enough photons to be detected by our system. In order to estimate the number of molecules that are not detected in our experimental conditions we analyzed the distribution of the number of photons for each detected point spread function generated by single mEos2. As shown in Fig.4.5.3 (SI) the distribution exhibits a bell shape with a long tail. The long tail follow a nearly exponential decay.

The extinction rate of a molecule is constant and is given by $k_e = k_b + k_d$ where $k_b$ is the bleaching rate and $k_d$ is the rate of conversion to the dark state (causing blinking) since bleaching and blinking are the only two processes that can impede a fluorescent molecule to emit under continuous excitation.

The conversion to the bleached or dark state are both first order processes, we expect an exponential distribution for $\Delta t_{ext}$ which is the time elapsed prior to FP extinction. Moreover, assuming that the rate of photon emission by the FP is constant, the number $N$ of photons detected by the camera prior to FP extinction is proportional to $\Delta t_{ext}$. We write the expected distribution of measured $N$ as :

$$p(N) = \lambda \; e^{-\lambda N} \tag{4.16}$$

where $\lambda$ is a parameter that depends on $k_e$ and the experimental apparatus. Finally the histogram of measured $N$ can be written

$$H(N) = N_{moc} \; p(N) = N_{moc} \; \lambda \; e^{-\lambda N} \tag{4.17}$$

where $N_{moc}$ is the true number of molecules.

As shown in Fig.4.5.3 (SI) our experimental histogram of emitted photons per mEos2 deviate from such distribution: for low values of $N$ we hit the detection limit of our system since FP prematurely bleached are not detected. However, to estimate the fraction of molecule that are missed in our experimental conditions we can estimate $N_{moc}$ by fitting only the a subset of our data (for N larger than our detection limit) to the theoretical exponential function. We fit only the part of our histogram corresponding to $N > 150$, that appeared to be well described by an exponential distribution.

We found $N_{moc} = 412870$ while we detected 250015 events. We conclude that we were able to detect $\sim 60\%$ of the mEos2 molecules in our experimental conditions. Note that because the maturation time of mEos2 is fast we neglect this process in our analysis. However this number is in reasonable agreement with some more refined estimation of the fraction of detected fluorophores in PALM [263].

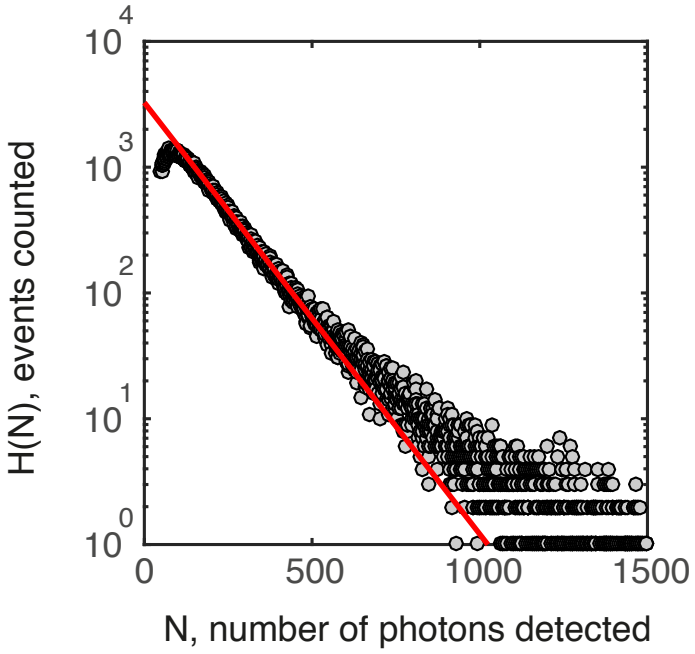


Fig. 4.5.3 (SI) **Histogram of the detected number of photons per localization event.** Black dots the estimated number of collected photons per mEos2 molecule, obtained by pooling data from all PALM experiments on TSS902 presented in the main text. The red line show the best fit to exponential distribution (equation 4.17).

### False positive localizations are negligible in our PALM experiment conditions

Similarly to most fluorescence based imaging techniques, auto-fluorescence of the sample is an issue in PALM imaging and detection of non-specific emitters could impair or bias molecular counting by generating false-positive localizations. In addition, para-formaldehyde is known to increase cellular auto-fluorescence [264], and small particles in the sample can also lead to false positive detection via light scattering. A general rule to treat these issues in PALM imaging is to reduce the false positive detection rate to a value much lower than the fluorophore activation rate. To do so, sample preparation (coverslip cleaning and buffer preparation) is important in order to reduce the number of false positive caused by scattering of spurious particles in the sample. To reduce autofluorescence, we used H1 minimal medium (in lieu of undefined rich media) which has the advantage of having a defined chemical composition as opposed to the undefined nutrient solutions (i.e. yeast extract) often found in rich media. Medium composition, buffer preparation and coverslip cleaning are described in the method section of the main text.

To test for the presence of false positives in our reconstructed PALM images we examined the time evolution of the total number of localization events as a function of time (Fig.4.5.4 (SI)). We expect the cumulated number of localizations to reach a plateau (saturation) at the end of the experiment as the total number of labeled receptor per cell is finite. The data presented in Fig.4.5.4A (SI) is computed out of multiple PALM imaging data of TSS902 with no stimulation. Similar results is obtained for the other strains studied in this work.

The saturation of the cumulated number of localization as a function of time clearly indicate that false positive can be neglected in our experimental conditions. This is true if cells are imaged shortly after fixation. We found that waiting more than three hours after cell fixation leads to higher false positive fraction.

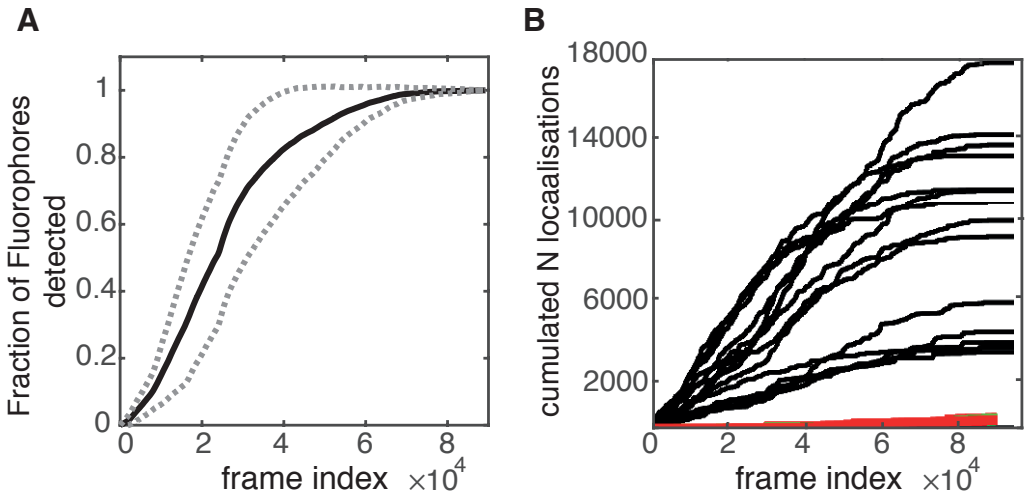


Fig. 4.5.4 (SI) **Analysis of total number of localization over a course of a PALM experiment.** (**A**) Fraction of total molecule detected as a function of PALM acquisition series under our experimental conditions. The black line shows the average over the whole dataset of PALM experiments on TSS1020. The dashed gray lines show the standard deviation to the mean. Note that the standard deviation converge to nearly zero after frame 70000. (**B**) Time evolution of the cumulated number localizations as a function of acquisition time. Data were recorded under the imaging conditions described in the main text. The black lines show representative time evolution of cumulated number of localizations for cells expressing Tar-mEos2 (TSS1020). The red line show the cumulated number of localizations for cells expressing no fluorophore (TSS903).

As a control we also performed similar experiments in cells that were not expressing any fluorophore (TSS903 alias for UU1250, $\Delta tsr, \Delta tar\text{-}tap, \Delta trg, \Delta aer$). Fig.4.5.4B (SI) shows a comparison of the cumulated number of localizations as a function of time for TSS903

(red curves) and a typical imaging experiment of cells expressing Tar-mEos2 (TSS902, black curves).

### 4.5.2 Functionality of the Tar-mEos2 fusion

Results presented in the main text suggest that cluster size distribution and mobility of the Tar-mEos2 receptor cluster under ligand stimulation, depend on the signaling activity of the receptor complexes. Here we present experimental controls demonstrating that our Tar-mEos2 fusion is at least partially functional.

#### Motility plate experiments

Motility plate experiments were performed in 9mm petri dishes containing 25 mL of 0.26% w/v bacterial agar (Sigma) in H1 minimal media, supplemented with 0.5% glycerol, 1mM aspartate, appropriate antibiotics, inducers and essential amino acids (see Mat. Met. section). Petri dishes were inoculated with $5\mu L$ of bacterial solution from saturated cultures in TB of different strains. Dark-field images were obtained in a custom-build dark-field imager with a digital camera (Canon) inside an incubator maintaining constant temperature of 33.5 C. Colony diameters were obtained by hand fitting a disk to the colonies in each image frame, using the imageJ open source software (Fig.4.5.5A,B (SI)). We compared motility of a strain lacking receptors but expressing our Tar-mEos2 fusion from a plasmid with the wild type strain and a strain lacking receptors and expressing Tar from a plasmid. These experiment clearly shows that our fusion strain is motile and capable of chemotaxis despite to a slightly lower extent when compared to the unfused receptor expressed from the same plasmid in the same background strain.

#### Tar-mEos2 fusion allows activation and de-activation of the CheA kinase and adaptation via CheR and CheB

We performed a FRET experiment monitoring the activity of CheA on TSS902 to test the functionality of our receptor fusion within the chemotaxis network. This well established assay was described originally here [226] and previously employed in our group. In brief, measuring non-radiative energy transfer between CheY-YFP and CheZ-CFP allows to monitor CheY phosphorylation rate and thus CheA activity. We expressed the FRET pair CheY-YFP and CheZ-CFP in cells expressing Tar-mEos2. Cells were grown in minimal H1 medium with appropriate inducers and antibiotics.

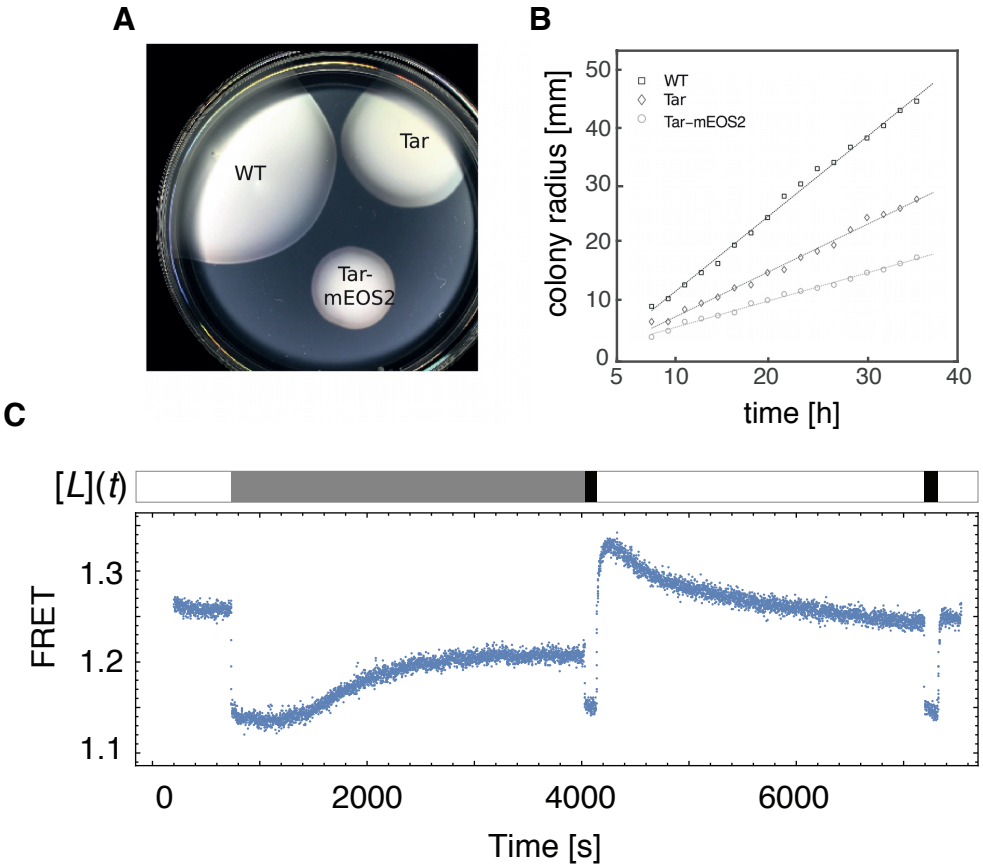


Fig. 4.5.5 (SI) **The Tar-mEos2 fusion mediates both ligand response and adaptation**. **The Tar-mEos2 fusion supports chemotactic migration on semi-solid agar plates. (A)** Dark-field image of colonies after 36 h of growth in soft agar plates based on H1 minimal media at 33.5C. Strains: wild type (RP437 with empty pTrc99A), Tar (Tar on pTrc99A in UU1250), and Tar-mEos2 (TSS902, Tar-mEos2 on pTrc99A in UU1250). Agar percentage 0.26%, with $100\mu g/mL$ ampicillin and $20\mu M$ IPTG. (**B**) Colony expansion as a function of time, co-plotted with a linear fit to the data points to obtain a motility rate. Motility rates for the different strains were 1.48 $\pm$ 0.09 (WT); 0.81 $\pm$ 0.03 (Tar); and 0.48 $\pm$ 0.01 mm/h (Tar-mEos2). Average and standard deviation were obtained from three different colonies measured on the same day. The FRET ratio of YFP over CFP fluorescence coming from a population of cells is plotted as a function of time. First cells were exposed to neutral buffer (white). Then a $100\mu M$ MeAsp saturating stimulus was added (grey) and sustained for about one hour. The stimulus was then increased to 1mM (black) for about 2 minutes and removed. Cells were stimulated once more long after removal (about one hour) with a stimulus of 1mM MeAsp. The curve show changes upon each stimulus/removal we applied, indicating that our mEos2 fusion does not completely impair the normal activity of Tar.

Fig.4.5.5C (SI) shows the population averaged FRET signal from cells exposed to the following stimulation protocol:

1. no stimulus
2. sustained $100\mu M$ over the course of about one hour.
3. short ($\sim$ 2 minutes) exposure to 1mM MeAsp
4. removal of stimulus
5. no stimulation for about one hour
6. short ($\sim$ 2 minutes) exposure to 1mM MeAsp
7. removal of stimulus

We observed a partial recovery of kinase activity during step 2 (sustained $100\mu m$ stimulation). When we switched to 1mM we measured a FRET response, demonstrating that cells adapted to some extent to the previous $100\mu m$ stimulus. If cells would not have adapted at all, we would not observe any response to 1mM, since a stimulus of $100\mu m$ MeAsp is saturating. We also measured an overshoot after removal of the ligand, indicating that methylation of the receptors did occur. Cells were also able to respond to an additional 1mM stimulus, demonstrating cell viability at the end of the experiment.

These results clearly show that even though adaptation is not perfect for TSS902 (it is known that cells where Tar is the sole receptor are not capable of perfect adaptation [265]), methylation/de-methylation via CheR and CheB occurs also for this Tar-mEos2 receptor fusion. We thus exclude any major impairment of Tar physiological function caused by the fusion to mEos2.

### 4.5.3 Evidence that cognate ligand binding triggers changes in chemoreceptor cluster mobility

The LPA-SPT experiments presented in the main text clearly established that Tar-mEos2 mobility increases upon stimulation by 1mM MeAsp. To address whether this MeAsp-induced change in mobility can be triggered by some non-specific effect of MeAsp addition (other than binding to its cognate chemoreceptor Tar), we performed several control experiments to rule out specific alternative mechanisms.

#### Tests for osmotic effects

Osmotic shock is known to mechanically perturb chemoreceptors in a manner that can affect their signaling activity [266]. Although such effects have been reported only for changes in

osmolyte concentration exceeding 10 mM, we tested whether osmotic effects contribute at all to the observed changes in cluster mobility by tracking Tar-mEos2 clusters before and after addition of 1 mM sucrose, an osmolyte that does not bind Tar and is impermeable to the inner membrane of *E. coli*. No significant mobility change was observed upon this weak sucrose shock *(see Fig.4.5.6 (SI))*, thus ruling out that the change in mobility upon 1 mM MeAsp stimulation we observed is due to an osmotic perturbation.

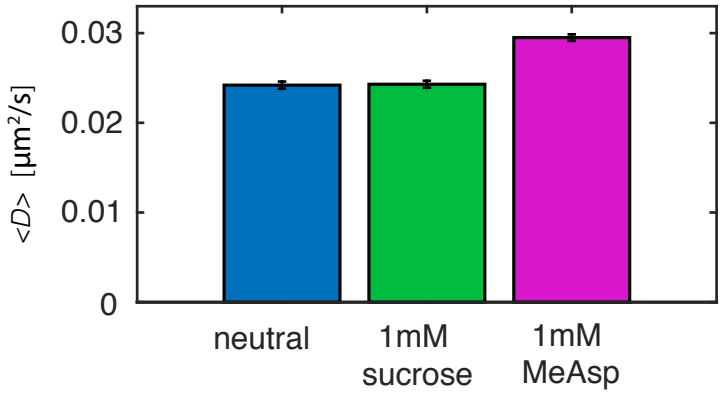


Fig. 4.5.6 (SI) **Sucrose as a control for non-specific effect on cluster mobility.** Results from LPA-SPT in the absence of any perturbation (blue), after addition of 1*mM* sucrose(green) and after adding 1*mM* MeAsp (magenta). The plot is showing average diffusion coefficient of clusters for the three conditions. Error bars represent standard error of the mean.

### Fluorescent protein label

Fluorescent protein tags can affect clustering/aggregation of the proteins to which they are fused [267]. The mEos2 protein we have used here is also known to mediate such potential artefacts [268, 269], so it is of interest to test whether the observed MeAsp-induced increase in mobility is robust to changing the fluorophore label. We thus tracked clusters for Tar fused to another fluorescent probe mEos3.2 [268], which mEos3.2 is known to be less prone to aggregation as compared to mEos2 [269]. With this fusion we also found a significant increase of cluster mobility under MeAsp stimulation (Fig. 4.5.7 (SI)).

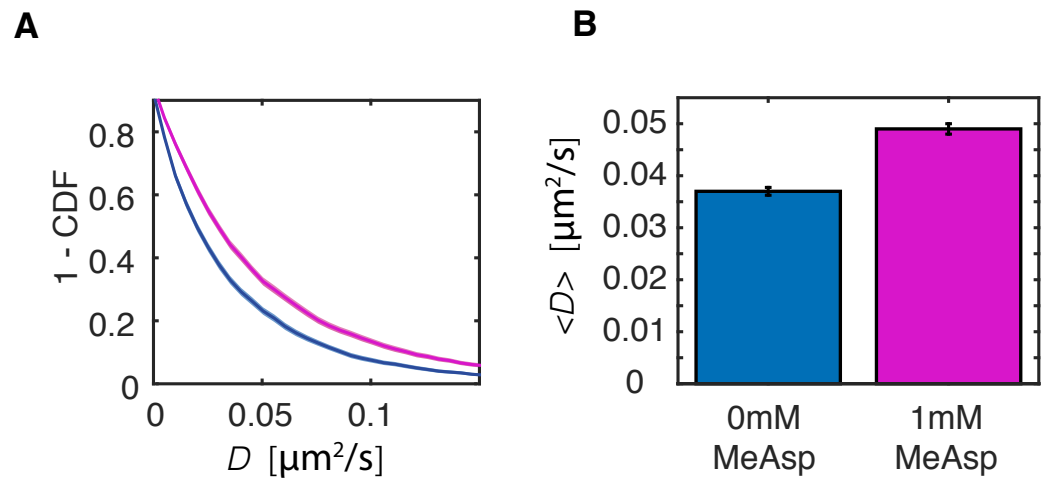


Fig. 4.5.7 (SI) **Mobility of labeled Tar-mEos3.2 receptor clusters**. We expressed Tar-mEos3.2 in cells lacking the genomic copy of all the receptors and lacking the enzymes CheR and CheB (TSS1045). Data before stimulation are shown in blue and data after adding 1mM methyl-D-aspartate addition are shown in magenta. (**A**) CDF, where haded error bars represent the standard deviation obtained via boot strap resampling over D (1000 iterations), (**B**) average diffusion coefficient. Error bars represent standard error of the mean. We found : $< D_{0mM} >= 0.037 \pm 0.002 \mu m^2/s$ and $< D_{1mM} >= 0.049 \pm 0.002 \mu m^2/s$

### Additional tests with the Tsr chemoreceptor

To test whether the stimulus-induced increase in mobility is specific to MeAsp/Tar or whether it is a more general effect of attractants on chemoreceptors, we performed similar tracking experiments on clusters formed by the other major chemoreceptor Tsr (which together with Tar makes up $\sim 90$ per cent of the receptor population). As shown in the supporting information (*Fig.4.5.8 (SI)*) Tsr-mEos3.2 clusters exhibit a similar mobility increase when stimulated with 1 mM serine, the cognate ligand for Tsr. Conversely, stimulation of Tsr-mEos3.2 by 1 mM MeAsp, a non-cognate ligand that does not bind significantly to Tsr at this concentration [249], did not significantly affect Tsr-mEos3.2 mobility. Thus, an increase of mobility upon stimulation is not specific to MeAsp/Tar, and may be a general feature of chemoreceptor responses to their cognate attractant stimuli.

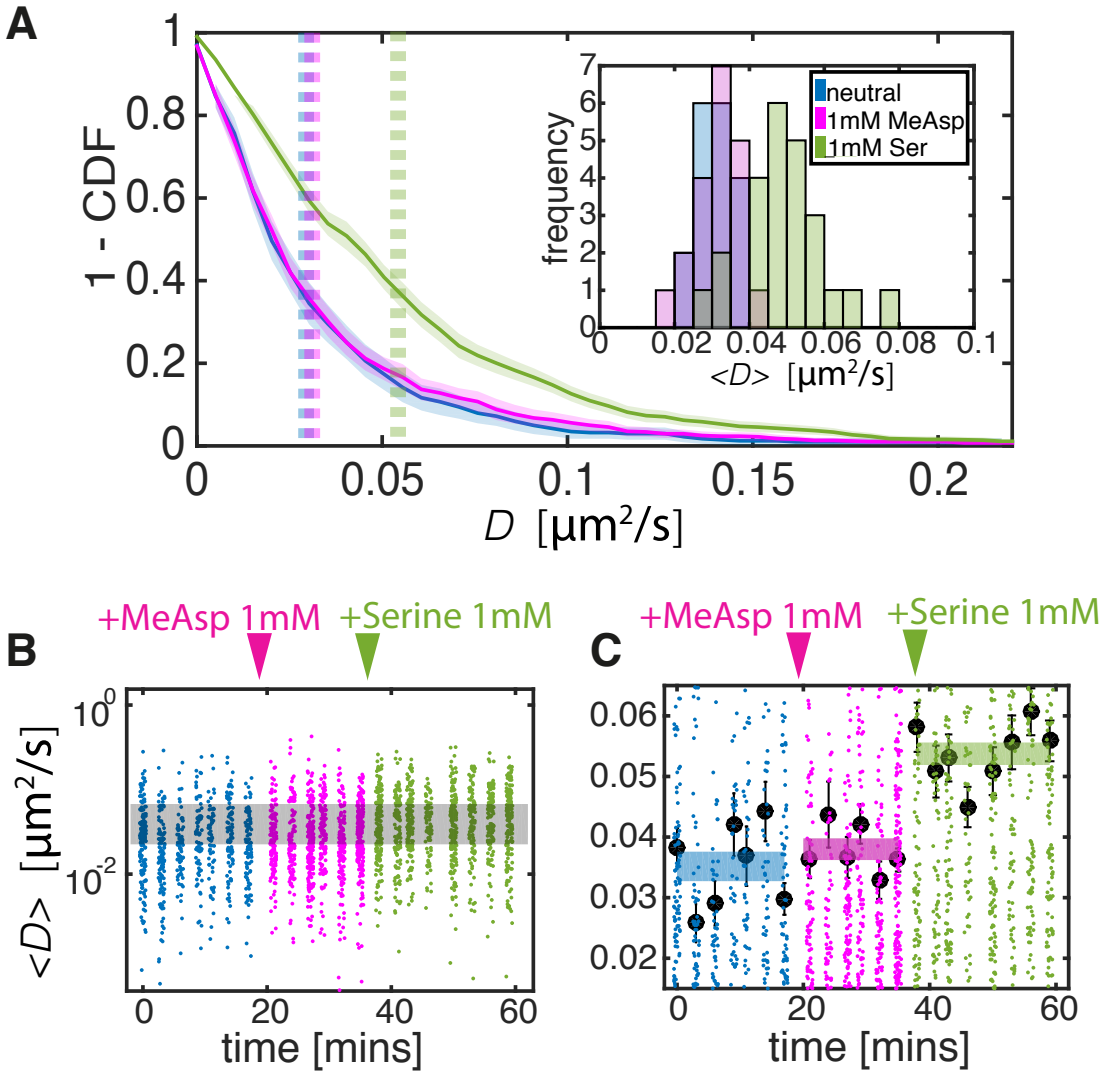


Fig. 4.5.8 (SI) **Mobility of Tsr-mEos3.2 receptor clusters**. Tsr-mEos3.2 was expressed in cells lacking all receptors and enzymes CheR and CheB (TSS1907). Data for unstimulated cells are shown in blue. Data for cells stimulated with 1 mM MeAsp are shown in magenta and data for cells exposed to 1 mM serine are shown in green. **(A)** Cumulative density function complement (1-CDF) of the Tsr-mEos3.2 diffusion coefficient. Dashed lines are in correspondence of average values of $D$, the thickness indicating the uncertainty on our estimate (shaded regions in panel (C)). Shaded error bars represent the standard deviation obtained via boot strap resampling over D (1000 iterations). Inset shows histograms of average diffusion coefficients across different experimental repeats for the three conditions. **(B)** Single track diffusion coefficient over time. Each point represent the diffusion coefficient of a single cluster estimated from its trajectory as explained in the main text. Each line of points correspond to a round of LPA-SPT over a field of view (FOV). Grey line represent our confidence interval given by $\sigma_D$. **(C)** Zoomed in version of panel (B), black dots indicate average diffusion coefficient per single FOV, error indicate standard error of the mean across all the tracks in that FOV. We found the average mobility of Tsr-mEos3.2 clusters to be $\langle D \rangle_{0\text{mM}} \approx 0.035 \mu m^2/s$ in the absence of stimulus and to be $\langle D \rangle_{1\text{mM}} \approx 0.052 \mu m^2/s$ in the presence of its cognate ligand. Although MeAsp is believed to bind Tsr it does so with much lower affinity than to serine [226]. We did not find a significant change of Tsr cluster mobility upon exposure to 1 mM MeAsp.

### 4.5.4 Dependence of the ligand-effect on chemoreceptor expression levels

Both PALM and LPA-SPT data presented in the main text were collected in strains expressing Tar-mEos2 as the sole chemoreceptor. Here we show that the Tar-mEos2 cluster size and mobility are similarly perturbed when other chemoreceptors are present, albeit more weakly. We conducted both PALM and LPA-SPT experiments in an adaptation-deficient strain (TSS1162) that expresses Tar-mEos2 in a genetic background ($\Delta tartapcheRcheBcheYcheZ$) that retains the native chromosomal alleles of genes encoding the Tsr, Trg, and Aer chemoreceptors. The PALM data Fig. 4.5.9 (SI) reveal that cluster size is attenuated also in this strain, although the shift in the CSMD is smaller than that observed in the non-adapting (TSS1020) and adapting (TSS902) strains expressing Tar-mEos2 as the sole chemoreceptor.

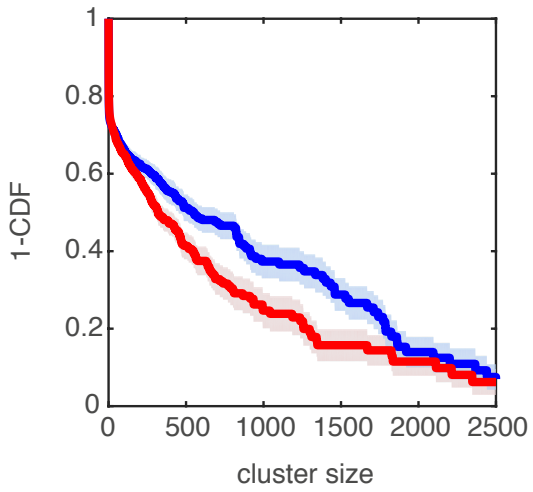


Fig. 4.5.9 (SI) **CSMD of Tar-mEos2 in the presence of other receptors.** Cluster size distribution of Tar-mEos2 in cells lacking the genomic copy of Tar but expressing endogenously other receptors types. This strain (TSS1162) do not express CheR nor CheB. Cells were fixed and then imaged with PALM as described in the main text. The complementary cumulative CSMD of Tar-mEos2 in stimulated cells is given in blue. The red curve shows the same data for cells stimulated for $1h$ with 1 mM MeAsp. In the presence of other receptors we measured that the probability for Tar-mEos2 to be found a cluster of size bigger than 500 is decreased by 20% upon addition of 1 mM MeAsp. In both panels, haded error bars represent the standard deviation obtained via boot strap resampling over cluster size.

The LPA-SPT data for TSS1162 (Fig. 4.5.10 (SI)) also showed a weaker change in mobility upon stimulation, but interestingly, mobility was significantly altered only in clusters

located in the lateral regions of the cell (*i.e. the cylindrical region excluding the hemispherical caps*).

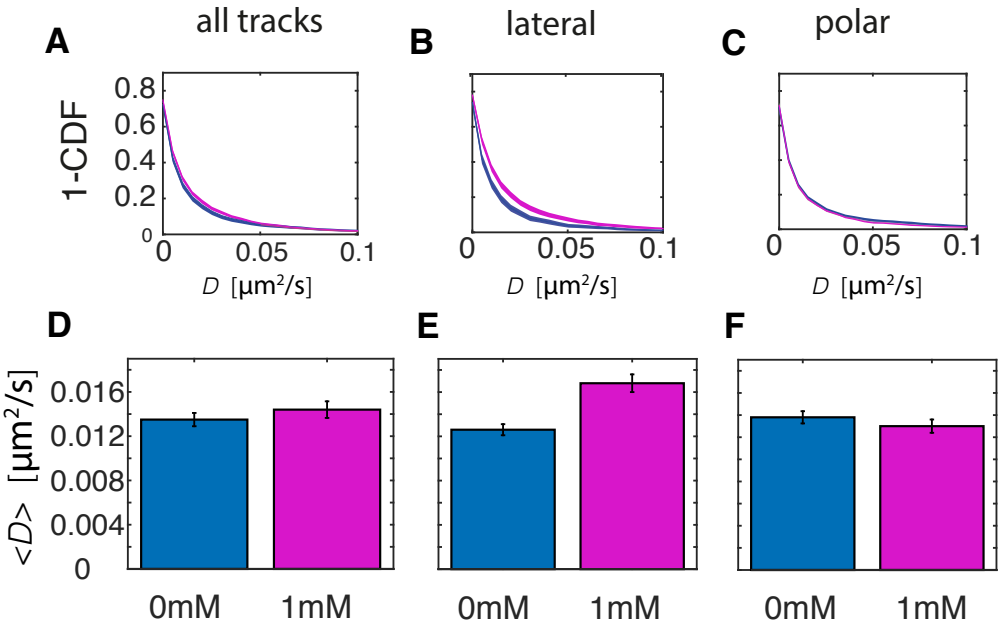


Fig. 4.5.10 (SI) **Effect of ligand stimulation on cluster mobility in cells expressing Tar-mEos2 as well as all the receptor species.** Tar-mEos2 was expressed in cells lacking the genomic copy of Tar but otherwise expressing all other receptors. This strain (TSS1162) do not express CheR neither CheB and is thus unable to adapt. Blue: data for non-stimulated cells; magenta data for stimulated cells (1 mM MeAsp). (**A**) CDF of estimated diffusion coefficient for all tracks. (**B and C**) CDF of diffusion coefficient sorted by cellular location (polar clusters (C) and lateral clusters (B). Shaded error bars represent the standard deviation obtained via boot strap resampling over D (1000 iterations). (**D**)) average diffusion coefficient for all tracks. ((**E**) and (**F**)) average diffusion coefficient sorted by cellular localization (polar versus non-polar clusters).

The reason why the presence of other receptors attenuates ligand-induced changes remains an open question, but one possibility is that the total expression level of all chemoreceptor species plays a role. For example, the increased spatial density of receptors due to high expression might lead to crowding of the local membrane environment, which could in turn limit cluster mobilities and inter-cluster distances. Consistently with this line of reasoning, by performing LPA-SPT in Tar only cells (TSS1020) with Tar-mEos2 over-expressed (3-fold higher induction level), we also found a weaker effect of ligand on cluster diffusion coefficient under overexpression conditions *(Fig.4.5.11 (SI))*.

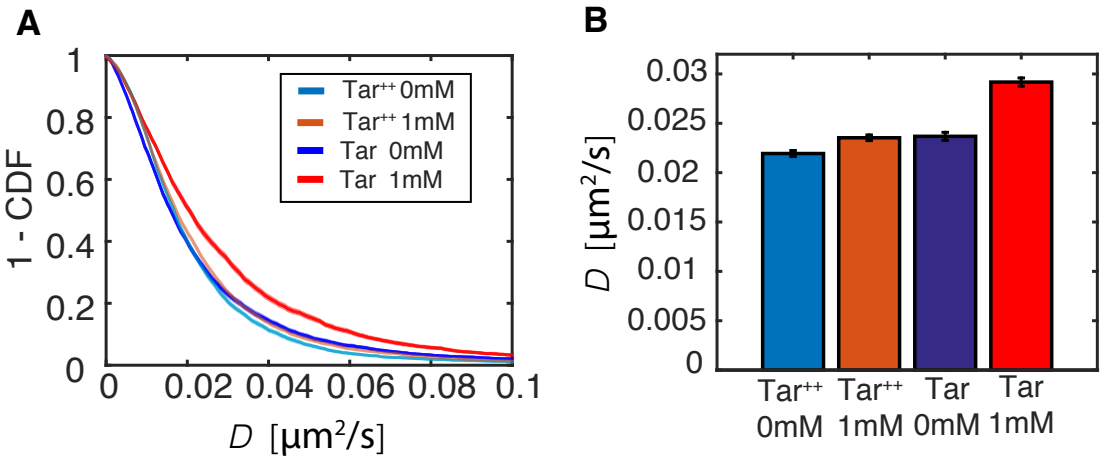


Fig. 4.5.11 (SI) **Effect of ligand stimulation on cluster mobility in cells over-expressing Tar-mEos2.** Results comparison from LPA-SPT on TSS902 expressing Tar at the same level as in the main text (Tar, [IPTG]=20$\mu M$) and over expressed by three- fold higher induction (Tar$^{++}$, inducer concentration: [IPTG]=60$\mu M$). (**A**) CDF of cluster mobility of Tar under normal and over expression conditions for 0$mM$ and 1 mM MeAsp stimulation. Blue: Tar $^{++}$, 0$mM$ MeAsp; orange: Tar $^{++}$, 1 mM MeAsp; dark blue: Tar, 0$mM$ MeAsp; red: Tar , 1 mM MeAsp; Shaded error bars represent the standard deviation obtained via boot strap resampling over D (1000 iterations). (**B**) Average cluster mobility for the four conditions. Same color scheme as panel (A).

### 4.5.5 Additional Supporting Figures

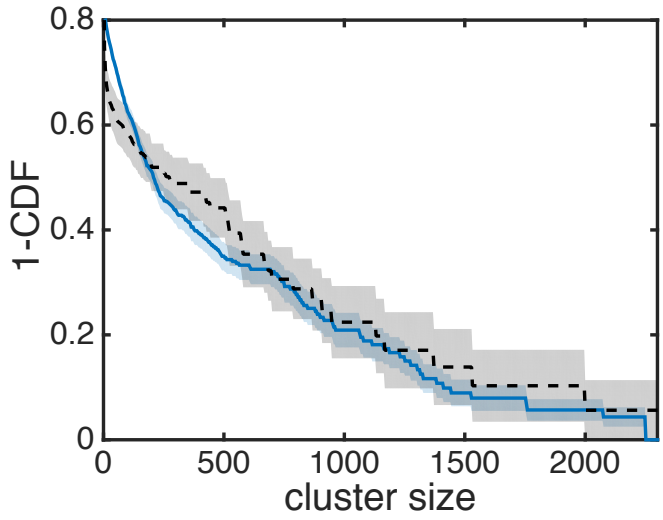


Fig. 4.5.12 (SI) **Effect of addition and removal of MeAsp on Tar-mEos2 CSMD in non-adapting cells.** Cells (TSS1020, Δ*cheRB*) were exposed for 60*min* to 1 mM MeAsp and then washed with Mot. Med. thus removing the MeAsp stimulus for 60*min*. Cells were fixed and then imaged with PALM as described in the main text. The complementary cumulative CSMD of Tar-mEos2 after removal of stimulus is shown grey. Data (already presented in the main text) for cells exposed to no stimulus (blue) are shown for comparison. Shaded error bars represent the standard deviation obtained via boot strap resampling over cluster size.

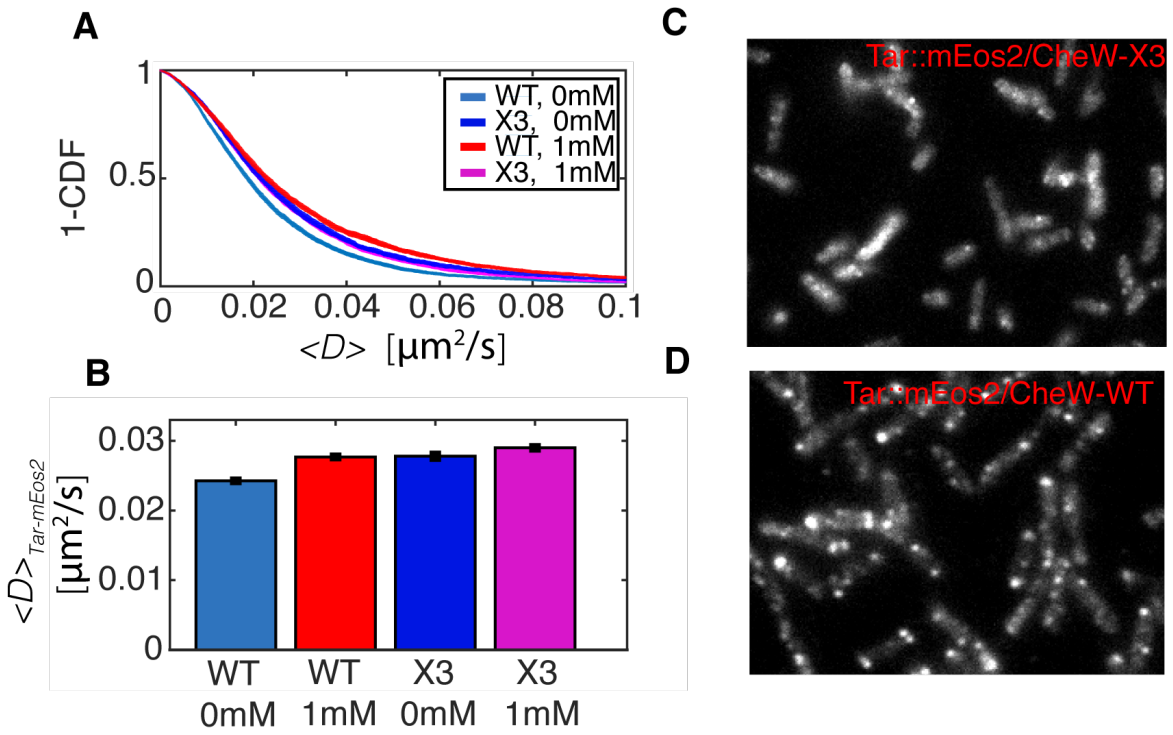


Fig. 4.5.13 (SI) **Mobility of Tar-mEos2 receptor clusters in CheWX3 mutants (TSS1961).** We performed tracking experiments in cells with mutated CheW (X3 residue). This mutation was shown to drastically reduce cluster formation [220]. **(A)** CDF of diffusion coefficient in TSS1961 (X3) compared that of TSS1020 (Tar) before and after MeAsp stimulation. Blue: Tar, 0*mM*; red: Tar, 1 mM; dark blue: X3, 0*mM*; purple: X3, 1 mM. Shaded error bars represent the standard deviation obtained via boot strap resampling (1000 iterations). **(B)** Average mobility for the same conditions of panel (A). **(C)** diffraction-limited image of Tar-mEos2 in cells with wild type CheW and **(D)** diffraction-limited image of Tar-mEos2 in CheW-X3 mutants.

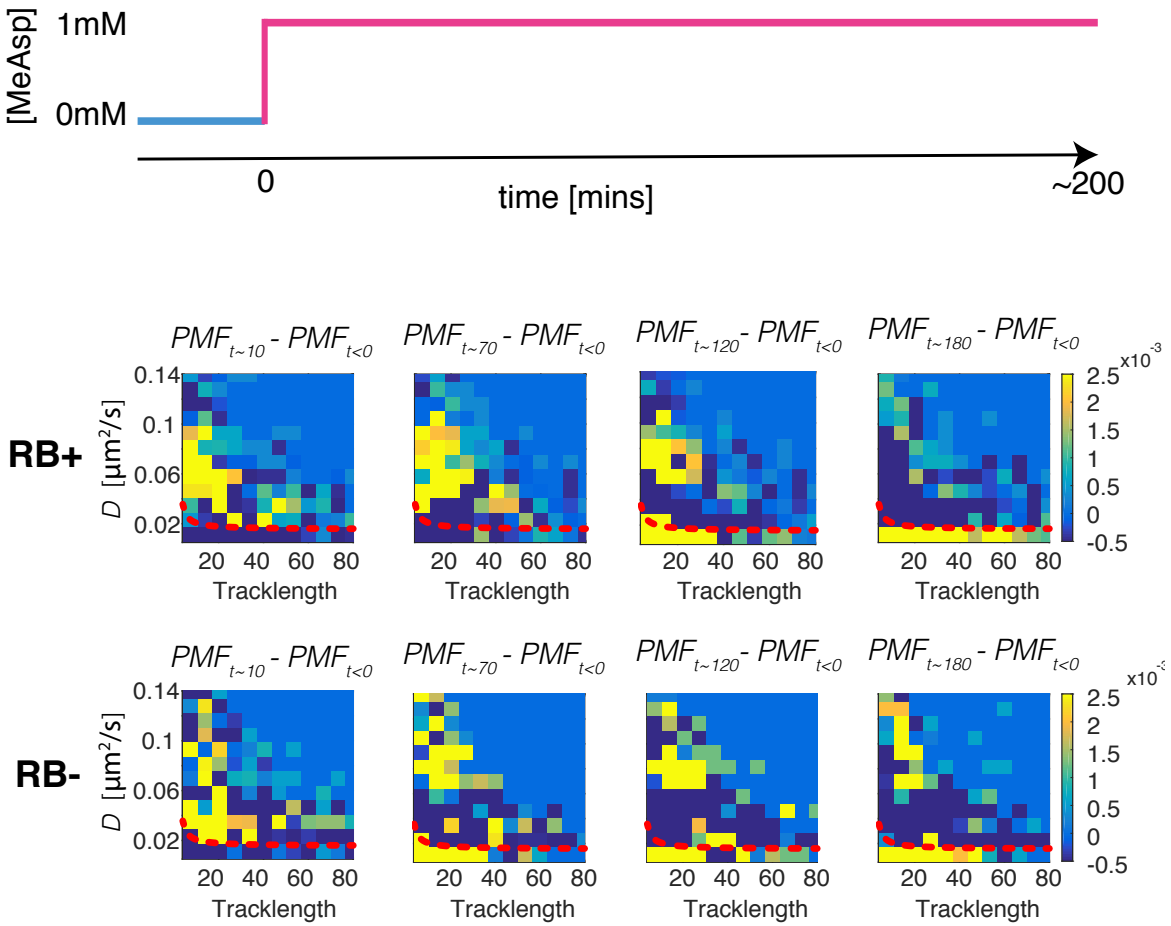


Fig. 4.5.14 (SI) **Immobile Cluster fraction increase upon MeAsp stimulation.** Schematics of the stimulation protocol in the experiment (top), time evolution of 2D-PMF differences ($P(L,D)_{t2} - P(L,D)_{t1}$, where $L$ is the track length) following 1 mM MeAsp addition in adapting cells (RB+, TSS902, middle) and non-adapting cells (RB-, TSS1020 bottom). In each of the two experiments we performed LPA-SPT before adding 1 mM MeAsp ($t < 0$), and at different times after adding the stimulus: t≃10mins, t≃70mins, t≃120mins and t≃180mins. We then subtracted the PMF obtained in the absence of from those obtained at increasing times , as indicated on top of each PMF difference panel. Red line shows our mobile-immobile cluster classification criterion based on diffusion coefficient $D$. The number of tracks for each sampling time for RB+ cells were 2588 for $t < 0$, 2820 for t≃10mins, 3102 for t≃70mins, 2935 for t≃120mins and 2945 for t≃180mins. For RB- cells the number of tracks were were 2140 for $t < 0$, 2795 for t≃10mins, 2363 for t≃70mins, 2295 for t≃120mins and 2632 for t≃180mins. These data show that the decrease in mobility observed in Fig. 4.2.6A, is accompanied by an increase in cluster size, as indicated by the yellow (positive) region at the bottom of the PMF differences plot for increasing time after stimulation. Such regions indicate that the fraction of clusters with slow diffusivity and long tracklength (big, immobile clusters) is increasing over time.

# Chapter 5

# Nucleoid organization under increased crowding and confinement *in vivo*

Macromolecular crowding is important for many cellular processes such as cytoplasmic transport and metabolic reactions, but its effects on essential DNA transactions *in vivo* remains largely unexplored. Here we ask whether and to what extent crowding of the cytoplasm affects the spatial organization of the *E. coli* nucleoid. Although crowding has been shown to drive compaction of isolated nucleoids in vitro, demonstrating its role *in vivo* has been challenging, in part because numerous other specific factors influence nucleoid configuration, but more fundamentally because tools for directly quantifying crowding in live cells has been lacking. Here we present experiments in which a recently developed Förster resonance energy transfer (FRET) sensor of cytoplasmic crowding was combined with high-throughput live-cell imaging to dissect the role of crowding on nucleoid spatial organization *in vivo*. We followed the temporal evolution of both crowding and nucleoid morphology simultaneously in thousands of exponentially growing cells. To probe the response of the nucleoid to crowding perturbations, we subjected cells to osmotic shocks. Nucleoids collapsed in size upon increased crowding and expanded upon decreased crowding, suggesting that crowding plays an important role in determining nucleoid size during steady growth. In agreement with previous observations, we find that nucleoids adopt different sizes and morphologies at different growth rates, but the relationship between nucleoid size and crowding was highly stereotyped, suggesting that physical parameters relevant to crowding are largely invariant. Our data also provide clear evidence that nucleoid size and morphology is not determined by crowding alone. Changes in both crowding and nucleoid size demonstrated hysteresis, likely reflecting the role of active processes during osmoadaptation. Treatment with the drug 2,4-dinitrophenol (DNP), which inhibits active processes in the cell, led to dramatic nucleoid expansion while crowding remained invariant, suggesting that the net force exerted on the

nucleoid by active processes during steady growth is compressive. Taken together our data confirm the importance of crowding in the compaction of chromosomal DNA *in vivo*, and provide new insights on the role of active processes in the homeostatic regulation of nucleoid size in bacteria.

## 5.1 Introduction

In its native cellular environment, the bacterial chromosome is a highly compacted polymer, a DNA molecule of length $\sim 1\,\mathrm{mm}$ confined within a cytoplasmic volume of $\sim 1\,\mu\mathrm{m}^3$. Unlike eukaryotic chromosomes, which reside in a membrane-bound nuclear compartment, it resides within the cytosol but its density nevertheless occupies a distinct subvolume known as the nucleoid. Recent advances in optical microscopy and sequencing-based technologies have revealed that chromosomal DNA in the nucleoid are by no means random polymers but possess a complex multi-scale spatio-temporal organization ([126, 129, 83, 270–272, 69, 273]). Despite very high degrees of compaction, nucleoids are visibly dynamic, demonstrating a rich repertoire of morphologies depending on growth conditions [84], cell cycle [129], and various physiological perturbations [274, 275]. The demand for sophisticated spatial organization of the nucleoid is tangible if one considers the degree of compaction on the one hand, and the plethora of vital functions that require access to chromosomal DNA on the other. Such essential DNA transactions include chromosome replication, segregation and gene expression in response to external stimuli [276, 277, 21], and to support these functions the nucleoid volume includes, in addition to chromosomal DNA, polymerases, nascent messenger RNAs, transcription factors, as well as a variety of other DNA-associated proteins. Yet, how bacterial cells achieve, maintain, and dynamically modulate the spatial organization of their genetic material in the crowded cytoplasmic environment remain largely open questions, and the underlying mechanisms and design principles have become subjects of an increasingly active area of research.

A variety of specific biochemical processes have been proposed to modulate nucleoid configuration *in vivo*, with varying degrees of experimental and theoretical support. These processes include transcription by RNA polymerases (RNAPs) [69, 83], cotranscriptional translation and bilayer insertion of membrane proteins (transertion) [278], DNA supercoiling [279], nucleoid associated proteins (NAPs) and structural maintenance of chromosome proteins (SMCs) [58, 273]. Indeed, the panel of proposed mechanisms are nearly as diverse as the repertoire of chromosomal DNA transactions, and although some proposed effects have been studied/confirmed in more detail than others, most proposals are not mutually exclusive, and it is likely that in reality a combination of many (if not all) of these specific

mechanisms play some role in the complex overall organization of bacterial nucleoids across diverse environmental and physiological conditions.

In this chapter, we focus on the effects of macromolecular crowding, an ubiquitous physical phenomenon in living cells, on the spatial organization of the *E. coli*| nucleoid *in vivo*. Unlike the specific biochemical processes postulated to affect nucleoid size and morphology discussed above, macromolecular crowding does not depend on the activity of specific molecular species, but rather reflects generic features of the physical environment such as the cell's volume and the size distribution of its molecular constituents. In recent years, the effects of crowding have gained increased attention not only in mechanistic studies of nucleoid compaction but also in those focused on the relationship between gene expression and DNA spatial organization [39, 52, 280, 281]. By slowing diffusion, affecting spatial proximity of interaction partners and rates in biochemical reactions, crowding appears indeed to be relevant for many important cellular processes like metabolic activity, initiation of DNA replication, and transcription [52, 282, 283].

Recent *in vitro* experiments on nucleoids isolated by cell lysis have unambiguously demonstrated that the addition of artificial crowding agents can compact the *E. coli* nucleoid, with the compaction degree increasing with the magnitude of the crowding perturbation (change in volume fraction of synthetic polymers) [43, 44]. Other *in vitro* experiments and theoretical works have shown that isolated nucleoids can be compacted by increased protein or polymer concentrations (e.g. lysozyme and polyethylene glycol), that crowding could account for the formation of the two-arms chromosome configuration, and that the nucleoid can undergo a continuous collapse mediated by depletion interactions [60, 44, 284, 285, 66, 45]. All of these results point towards a fundamental role of crowding in shaping the chromosome's configuration in live bacteria, but in lieu of direct experimental test *in vivo*, exactly how and to what extent crowding impacts nucleoid morphology in its native cellular environment remains a subject of active debate.

We have developed a novel live-cell imaging approach that allows parallel measurement of nucleoid morphology and the crowding state of the cell across time as bacteria experience environmental changes that affect cytoplasmic crowding and other physiological parameters. We made use of a genetically encoded protein FRET sensor developed by Boersma and coworkers [54] to quantify crowding in growing *E. coli* cells, and perturb crowding by osmotic challenges under different growth and metabolic conditions. By employing microfluidic growth chambers of the 'mother machine' type ' [98], we achieve continuous imaging at single-cell resolution and high throughput during exponential growth, with rapid medium exchange to implement step-like environmental changes. Imaging through multiple spectral

channels allowed us to follow changes in the nucleoid and cell morphologies together with the crowding level of the cytoplasm upon applied osmotic shocks of varying magnitude.

Our ability to simultaneously follow nucleoid and crowding dynamics in a large number of cells ($\sim$ 2000 cells per experiment) enables data-rich inquiries of crowding effects on the nucleoid *in vivo*. Here, we exploited this capability to address the following questions:

- *What is the role of crowding in setting the nucleoid size in living cells?* Given the variety of important cellular processes that require a certain degree of crowding and the scaling of cell size with growth rate, the idea that crowding might be actively controlled by the cell has recently introduced [52]. We sought to determine whether and to what extent crowding shapes the steady state chromosome configuration by perturbing the steady-state level of crowding by osmotic shocks.

- *Does crowding play a role in the distinct nucleoid sizes observed at different growth rates?* The shape and size of the nucleoid is different under fast and slow growth [84] but the underlying causes of such differences remain unknown. It is well established that cytoplasmic composition varies when cells are growing at different rates and in particular ribosomal protein fraction of the proteome increases linearly with growth rate [286, 287]. Thus crowding might act differently in cells growing at different rates, and we sought to compare the response of the nucleoid to crowding perturbations in cells under contrasting growth conditions.

- *What is the relative importance of active and passive processes in determining the state of the nucleoid?* It has been shown that shutting down metabolism with 2,4-dinitrophenol (DNP) can drastically affect the physical state of the cytoplasm, as evidenced by a strong attenuation in the mobility of large particles [70]. We reasoned that monitoring the state of the nucleoid and cytoplasmic crowding upon metabolic shutdown could provide new insights regarding the balance between active and passive forces acting on the nucleoid.

By simultaneous monitoring of cell size and morphology, in addition to the state of the nucleoid and crowding, our approach also allowed us to further dissect the expected causal chain of events upon osmotic shock, namely the change in crowding upon osmotic perturbations to the cell volume, and the change in the nucleoid state in response to crowding.

## 5.2 Results

### 5.2.1 Hyperosmotic shock in growing cells leads to transient crowding increase and nucleoid compaction

To achieve parallel measurement of nucleoid and cell morphologies as well as intracellular crowding at high throughput, we developed a multi-channel imaging system based on a microfluidic device of the 'mother machine' type [98] (Fig. 5.2.1). This device consists of two linear arrays of parallel slit-like growth chambers, of width comparable to that of the cells and of length several times that of cells. These growth-chamber arrays flank a larger central channel which provides a constant nutrient feed by steady flow of growth medium (Fig. 5.2.1A). Because of the short length of the slit-like growth chambers ($\sim 10\,\mu m$), the cells experience a rapid change in their environment upon a switch in the incubation medium, controlled by a fluidic valve near the device's inlet. Throughout the experiment, 30 fields of view (FOV), each containing 100-200 cells are imaged in rapid succession at regular intervals in four spectral channels to monitor three observables (Fig. 5.2.1B): (i) phase contrast channel for cell morphology, (ii) FRET donor (CFP) and acceptor (YFP) fluorescence channels for intracellular crowding, and (iii) red (mRuby2) fluorescence channel for nucleoid morphology.

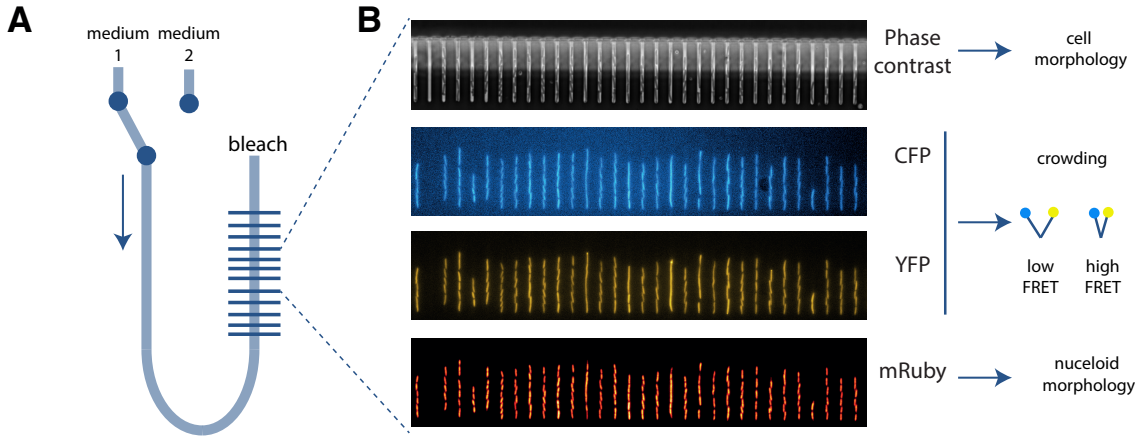


Fig. 5.2.1 **Mother machine setup, experimental approach and observables (A)** Schematic of the "mother machine" PDMS device used in this study. The fluidic switch valve at the inlet is used to rapidly exchange the medium to apply osmotic shocks and other perturbations to cellular physiology. **(B)** Representative images of one field of view within the mother machine device, in the four spectral channels used for parallel monitoring of three observables: (i) phase contrast channel for cell morphology, (ii) FRET donor (CFP) and acceptor (YFP) fluorescence channels for intracellular crowding, and (iii) red (mRuby2) fluorescence channel for nucleoid morphology.

To test the effect of osmotic upshifts on cell size, nucleoid size, and crowding, we exchanged the nutrient medium during exponential growth with an identical one supplemented with an osmotic agent (sucrose) and followed the state of the cell and nucleoid in the four imaging channels of our setup. Fig. 5.2.2 shows images and extracted observables from a typical experiment in which cells were challenged with a 0.6M osmotic upshift during fast growth (in a chemically defined rich medium; see Methods). Both the cytoplasm and nucleoid were visibly attenuated in size just after addition of sucrose (Fig. 5.2.2A), which permeates *E. coli*'s outer membrane but not the inner membrane [288]. Volume reduction of the cytoplasm was often accompanied by noticeable deformations due to plasmolysis (indicated by red arrow in Fig. 5.2.2A), at a frequency that increased with the magnitude of applied osmotic upshifts. Nucleoid compaction was also far from isometric, with initially elongated density profiles often collapsing into globular density peaks.

The average cell area and nucleoid area, as well as the acceptor/donor fluorescence ratio (YFP/CFP) of the FRET crowding sensor (hereafter referred to as "FRET ratio") were stationary during exponential growth in the mother machine, but upon the application of hyper-osmotic shock, all of these observables were significantly perturbed (Fig. 5.2.2B). The fractional change $\Delta A_c/A_{c_0} = (A_c - A_{c_0})/A_{c_0}$ of the cytoplasmic area $A_c$ from its steady-state value $A_{c_0}$ peaked immediately after the 0.6M sucrose stimulus with an average magnitude $|\Delta A_c/A_{c_0}| \approx 15\%$, in good agreement with the higher time-resolution measurements of Pilizota and Shaevitz [288] who found that cytoplasmic volume change reaches a maximum amplitude $\Delta V_c/V_{c_0}$ $(= (1 + \Delta A_c/A_{c_0})^{3/2} - 1)$ of $|\Delta V_c/V_{c_0}| \approx 20\%$ within seconds after a sucrose stimulus of comparable magnitude for cells grown in another rich medium (LB).

Strikingly, initial changes in nucleoid size and crowding following the shock were antiparallel, with the change in the FRET ratio indicating an increase in crowding concomitant with osmotic compression of the cytoplasm, while nucleoid area decreased during the same interval, as expected if increased crowding were driving the observed nucleoid collapse. By contrast, changes in cell and nucleoid areas were approximately parallel, both decreasing rapidly just after osmotic upshift, followed by a slower recovery. Interestingly, however, the overall degree of compression/compaction was greater for the nucleoid than that for the cell, as could be seen in the clear decrease of the nucleoid area fraction (defined as nucleoid area divided by cell area) just after the osmotic shock Fig. 5.2.2B). The fact that the nucleoid is compacted by a factor greater than that for the cytoplasmic volume strongly suggests that the observed nucleoid compaction is not due to increased confinement of the nucleoid polymer by the cytoplasmic membrane.

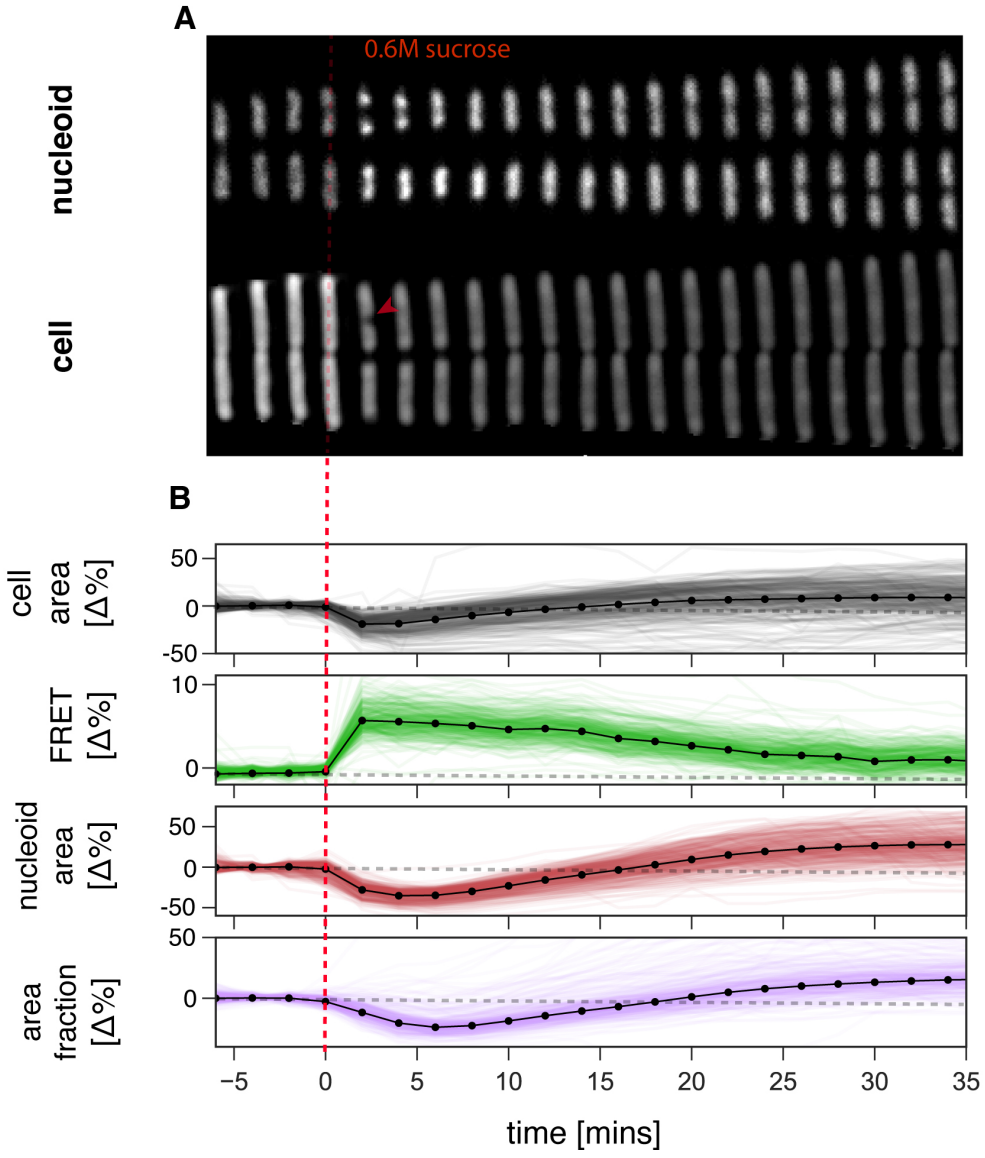


Fig. 5.2.2 **Image sequences and time series of extracted observables in a typical hyperosmotic shock experiment (A)** Image sequences of mRuby (top) and phase contrast (bottom) channels showing the time evolution of the nucleoid and cytoplasm morphologies upon hyperosmotic shock (addition of 0.6M sucrose) during fast growth, for a representative cell lineage (image sequence aligned at the midpoint of progenitor cell). Red arrow indicates visible plasmolysis event. Time scale is as indicated in panel B. **(B)** Time traces from a 0.6M sucrose osmotic upshift experiment, from top to bottom: cell area from phase contrast image segmentation, FRET signal form crowding sensor, nucleoid area from mRuby2 fluorescence images segmentation, nucleoid area fraction defined as the ratio of nucleoid area to cell area. For all observables per cent changes with respect to steady state values, normalized to the steady state, are shown (for an observable $x$, traces represent $\frac{\langle \Delta x \rangle}{\langle x \rangle_0} \times 100$). Red dashed line indicates the time points at which the sucrose-growth medium solution arrived in the microscope field of view, grey dashed lines indicate the steady-state average level prior to shock. Colored curves represent averages over single growth chambers, and black curve and points represents the ensemble average over all growth channels.

Taken together, the decrease in nucleoid area fraction combined with the antiparallel trajectories of the nucleoid area and FRET crowding signal implicate increased crowding, and not confinement, as the driver of nucleoid compaction upon osmotic upshift.

Over longer times after osmotic upshift, the initial rapid compression is followed by a slower recovery of both the nucleoid and cytoplasm, with their respective sizes slowly increasing, while the crowding FRET signal concomitantly decreased, toward pre-shock values. Interestingly, recovery of both the nucleoid and cytoplasm eventually overshoots the pre-shock level, but the overshoot amplitude is greater for the nucleoid which thus occupies a larger fraction of the cytoplasm at long times after osmotic upshift (Fig. 5.2.2B, lower two panels).

In summary, we showed that the nucleoid in fast-growing *E. coli* cells can be further compacted by osmotic shock, that the collapse upon shock is likely not caused by increased cellular confinement, and that increased crowding correlates with compaction.

### 5.2.2 Hypoosmotic shock reduces crowding and increases nucleoid size

The results of the previous section suggested that crowding might play a significant role in determining the steady-state size of the nucleoid within growing cells. We reasoned if that were true, decreasing intracellular crowding could also affect nucleoid size. We thus tested whether an opposite osmotic stimulus (a hypoosmotic shock) could induce a crowding perturbation of the opposite sign by challenging growing cells with a sudden downshift in environmental osmolarity.

By contrast to the hyperosmotic shock response, upon a hypoosmotic shock applied by rapid exchange of the growth medium with distilled water ($dH_2O$), no rapid changes in the observables were detected (Fig 5.2.3). We note that these data are not inconsistent with previous work [289] in which the *E. coli* cytoplasm was found to transiently expand upon hypoosmotic shock, because the duration of the volume peaks reported in that study were shorter than the image acquisition interval of our experiment (2 min).

Over longer times, our data indicate a mild decrease in the cytoplasmic volume while the FRET crowding signal slowly decreased over the same interval (Fig 5.2.3A). A decrease in crowding implies a reduction of the macromolecular volume fraction $\phi = V_m/V$, which could result from a change in the cytoplasmic volume, $V$, the volume occupied by macromolecules $V_m$, or both. Given that the population averaged cytoplasmic volume $\langle V \rangle$ is decreasing, $\langle V_m \rangle$ must also be decreasing and at a faster relative rate, *i.e.* $d\ln\langle V_m \rangle/dt < d\ln\langle V \rangle/dt < 0$. During steady exponential growth, the net rate of cytoplasmic volume production $\alpha$ is balanced by the rate of cell division $\mu$, so that the average cytoplasmic volume is stationary, $d\ln\langle V \rangle/dt = \alpha - \mu\ln 2 = 0$. The net rate of macromolecular volume production $\alpha_m$ must also

balance the cell division rate, so that $d\ln\langle V_m\rangle/dt = \alpha_m - \mu\ln 2 = 0$. Thus, $\alpha_m = \alpha = \mu\ln 2$ during steady growth, and the decrease in both cytoplasmic volume ($d\langle V\rangle/dt < 0$) and FRET crowding signal ($d\langle\phi\rangle/dt < 0$) in our data implies a hierarchy among the rates $\alpha_m < \alpha < \mu\ln 2$ during the prolonged hypoosmotic challenge.

Visual inspection of the image sequences indeed confirmed an altered balance between cell elongation and division under the hypoosmotic condition in our experiment. After exchange of the growth medium with $dH_20$, both cell elongation and division gradually slowed and eventually halted. But decay of the elongation rate (which is proportional to $\alpha$) proceeded more rapidly than that of the division rate ($\mu$), resulting in a reduction of the average cell size (*i.e.*, $\alpha < \mu\ln 2$). Changes in the cytoplasmic growth rate $\alpha$ could in principle reflect in addition to *bona fide* changes in growth, also the inflation/deflation of the cell upon the osmotic shock and subsequent osmo-adaptation. In fact, it has been shown that certain hypoosmotic stimuli can trigger a transient decrease of the cytoplasmic volume (after the aforementioned transient increase immediately following the shock) that can last for tens of minutes [289]. However such osmo-adaptive volume reductions typically play out much more rapidly (within a few minutes after the shock) compared to the gradual decay of cytoplasmic volume we observed here (Fig 5.2.3A). We therefore think it more likely that the decrease in cell volume observed here is due to cumulative effects of the $dH_2O$ environment on biosynthetic processes that support growth. Our experiment does not provide a direct means of monitoring the net rate of macromolecular volume production $\alpha_m$, but the hierarchy noted above suggests that it slows down even more rapidly than the production rate of cytoplasmic volume, such that $\alpha_m < \alpha$ under the sustained hypoosmotic stimulus.

Interestingly, the decrease in the FRET crowding signal was accompanied by a concomitant enlargement of the nucleoid (Fig 5.2.3A). The nucleoid area increased by $\sim 10$ per cent over $\sim 50$ mins, despite the $\sim 10$ per cent reduction in the cytoplasmic volume during the same interval. As a result, the fraction of the cytoplasmic area occupied by the nucleoid increased substantially (by $\sim 20$ per cent; Fig 5.2.3A), as could also be confirmed by visual inspection (Fig 5.2.3B).

In summary, under sustained hypoosmotic conditions we observed a gradual decrease of cytoplasmic crowding, and a concomitant expansion of the nucleoid. The changes in the observables were smaller in amplitude and slower compared to those upon hyperosmotic shock, but nevertheless are statistically significant (Fig. 5.2.3A). The decrease in crowding occurs despite a reduction in cytoplasmic volume during the same interval, and likely reflects a shift in the balance between growth of the cytoplasm and that of macromolecules that act as crowders.

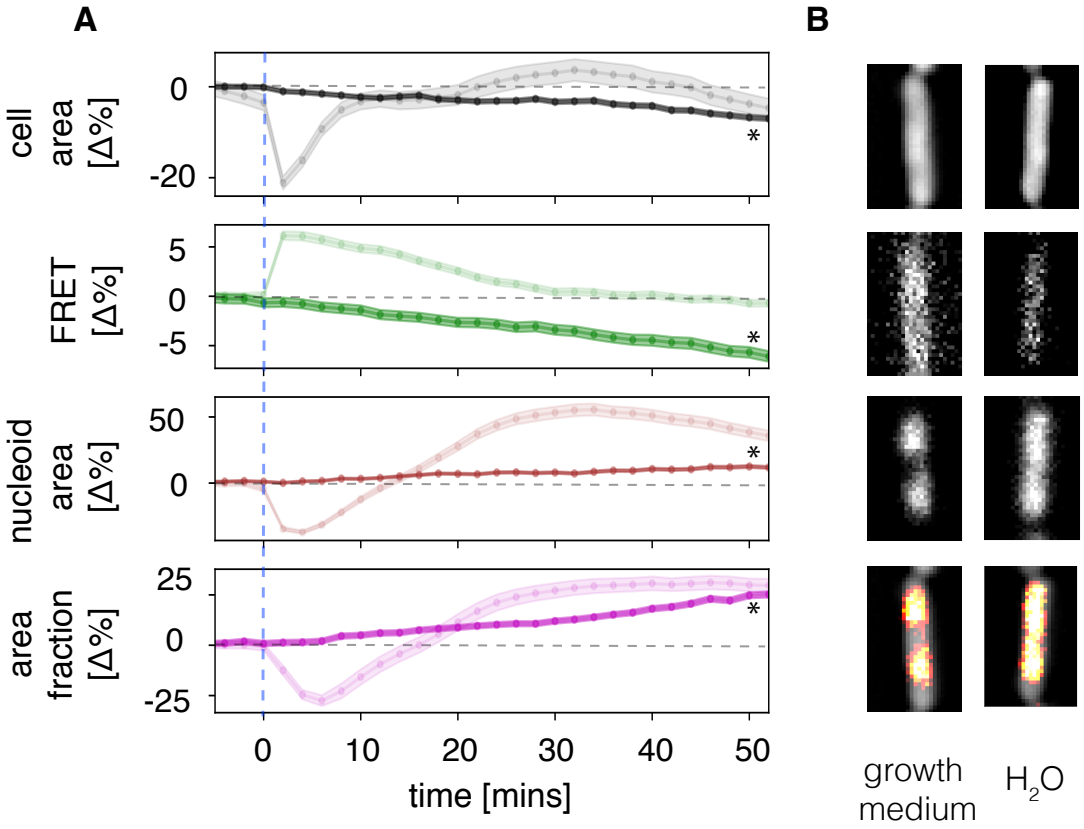


Fig. 5.2.3 **Response of the cell and nucleoid to hypoosmotic shock.**. **(A)** Time series of average cell area, FRET, nucleoid area and area fraction (nucleoid area divided by cell area) upon a sustained hypo-osmotic stimulus (exchange of growth medium by $dH_2O$). The shock arrives at time 0 (red dashed vertical line). Shaded regions correspond to mean $\pm$ s.e.m. For comparison, the average single-cell time series for the hypoosmotic shock experiment of Fig. 5.2.2 are also shown (in lighter shades of the same color). For all observables changes with respect to steady state mean, normalized by the steady state mean, are shown (*i.e.* we plot $\frac{\langle \Delta x \rangle}{\langle x \rangle_0}$ for an observable $x$ with steady-state mean $\langle x \rangle_0$). Asterisks indicate time points from which the values for Figure 5.2.4B were taken. **(B)** Images of representative cells before and after sustained hypo-osmotic stimulation showing (from top to bottom) background-subtracted phase contrast, YFP channel from the FRET sensor, HU::mRuby2 signal from the nucleoid and the latter overlaid to the cell body image at the top.

### 5.2.3 Crowding plays an important role in setting the steady-state nucleoid size *in vivo*

We summarize in Figure 5.2.4 our observations on the relationship between crowding and nucleoid size in the hyper- and hypo-osmotic shock experiments of Figs. 5.2.2 and 5.2.3, using data from time points at which we observed the maximum change relative to the pre-stimulus steady state (the time of the peak response in Fig. 5.2.2 and the time indicated by asterisks in 5.2.3). Although both hyper- and hypo-osmotic shocks induced a reduction in the cytoplasmic volume (Fig. 5.2.4A, upper left panel), the fraction of that volume occupied by the nucleoid decreases upon hyperosmotic shock and increases during sustained hypoosmotic stimulation (Fig. 5.2.4A, lower right panel). Furthermore, hyper- and hypo-osmotic stimulation exerted opposite effects on crowding (Fig. 5.2.4A, upper right panel) and nucleoid size (Fig. 5.2.4A, lower left panel).

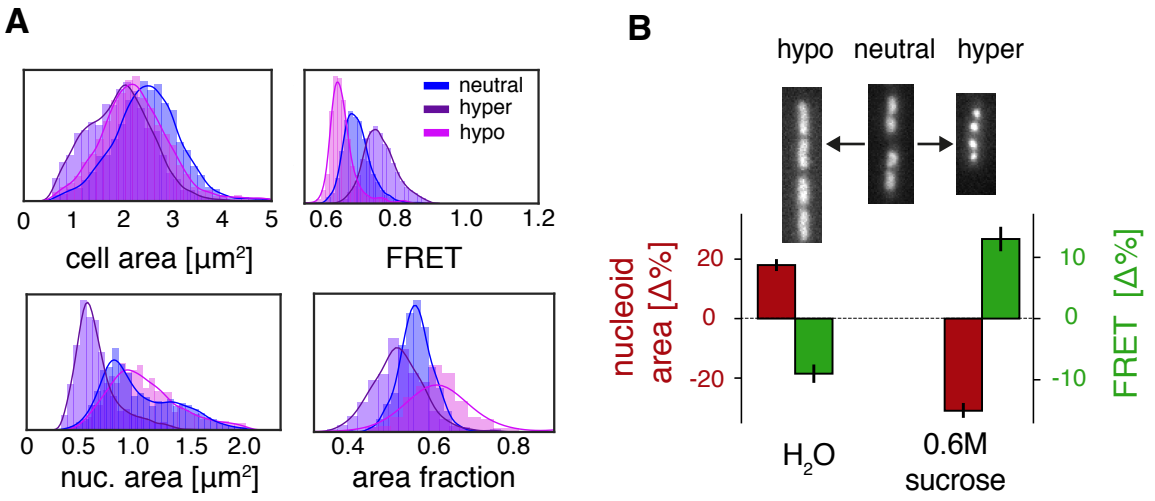


Fig. 5.2.4 **Crowding and nucleoid size can be modulated by both hyper- and hypo-osmotic shock**. **(A)** Distributions of cell area, FRET ratio, nucleoid area and nucleoid area fraction are shown for different osmotic conditions: unperturbed (blue) peak response after the 0.6 M sucrose hyper-osmotic shock of the experiment of Fig. 5.2.2 (purple) and at under sustained hypo-osmotic shock (magenta). Data for the hypo-osmotic case correspond to the time point marked by the asterisks in Fig. 5.2.3A. For cell area, FRET ratio and nucleoid area, single-cell statistics were used. For nucleoid area fraction, growth-channel-level averages were used. **(B)** Average changes in FRET (green) and nucleoid area (dark red) for hyper- and hypo-osmotic shock, normalized to the unperturbed values ($\frac{\langle \Delta x \rangle}{\langle x \rangle_0}$). Upper panel: representative images show typical cells in each condition over which the average was performed to compute the values reported in the plot. Lower panel: Error bars represent standard error of the mean computed over the single-cell statistics.

Although these histograms demonstrate that there exists considerable variability in each of these observables at the single-cell level, the changes of opposing sign in both nucleoid size and crowding upon hypo- and hyper-osmotic stimulation are clearly statistically significant (Fig. 5.2.4B).

The fact that the cytoplasmic volume fraction occupied by the nucleoid can increase or decrease while the cytoplasmic volume itself decreases indicates that changes in confinement by the cytoplasmic membrane are not the primary driver of nucleoid size changes upon osmotic shocks. By contrast, nucleoid size is clearly anticorrelated with the crowding FRET signal, upon both hyperosmotic and hypoosmotic shock. The fact that both upward and downward perturbations to crowding affect nucleoid size supports the idea that crowding plays a significant role in shaping nucleoid configuration in living cells during steady-state growth.

### 5.2.4 Magnitude of nucleoid-size responses to hyperosmotic shock are comparable at different growth rates

The morphology and cellular volume fraction of the *E. coli* nucleoid are known to depend on growth conditions [84]. To examine the role of crowding in the contrasting nucleoid organization under different growth conditions, we measured the response of the cell and nucleoid to osmotic shocks of varying magnitude in under fast- and slow-growth conditions (with doubling time $\sim 20$ min and $\sim 45$ min, respectively; see Methods for media composition).

Prior to osmotic stimulation, the cytoplasmic area was significantly larger under fast growth compared to the slow growth condition (mean$\pm$s.e.m. = 2.47$\pm$0.01 vs. 1.93$\pm$0.01 $\mu m^2$; Fig. 5.2.5A). The nucleoid area, however, was very similar (1.01$\pm$0.003 vs. 1.03$\pm$0.01 $\mu m^2$; Fig. 5.2.5B), thus yielding a similar fold-difference in the nucleoid area fraction but of opposing sign (0.55$\pm$0.002 vs. 0.62$\pm$0.002; Fig. 5.2.5C) comparable to that of the cytoplasm alone. The observed distributions of the FRET crowding signal (Fig. 5.2.5C) indicates an apparent difference between the two growth conditions, but interpreting this absolute difference between growth conditions requires care as a rigorous comparison would require additional calibration of the FRET sensor within our experimental setup to make the absolute level of the signal interpretable. We thus focus hereafter on the relative change in FRET signal within each growth condition, and defer discussion of this apparent difference in the steady-state FRET level to the Discussion section.

We tested responses to osmotic shocks of varying magnitude under both fast and slow growth conditions, applying the same protocol as that of the experiment in Fig. 5.2.2,

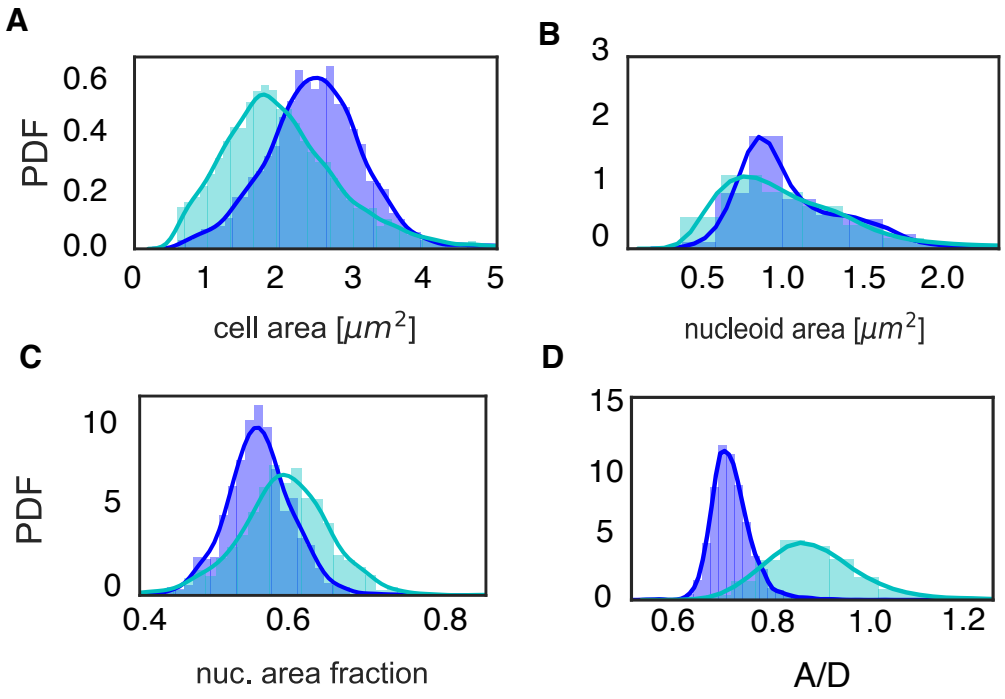


Fig. 5.2.5 **Steady-state distribution of observables under fast and slow growth conditions.** Distributions of **(A)** cell area, **(B)** nucleoid area, and **(C)** the fraction of cell area occupied by the nucleoid, and **(D)** the crowding FRET signal (YFP/CFP fluorescence ratio). In all panels, blue corresponds to the fast growth condition, and light blue to the slow growth condition.

but with varying sucrose concentrations. The qualitative features of the time series were similar across all tested shock magnitudes (Fig.5.2.6A), with the cell and nucleoid areas initially decreasing while the crowding FRET signal increased, before reaching a peak value from which each observable recovered towards its steady-state value. The magnitude of fractional response at the response peak, which is likely determined by the balance between the passive response to the shock and the active processes that account for the subsequent recovery, increased monotonically with the applied shock magnitude, and the dependence on the shock magnitude was nearly linear in all three observables (Fig.5.2.6B), indicating that the shocks we applied are far from saturating the response.

Interestingly, the peak fractional change in nucleoid size at each tested sucrose shock magnitude (Fig.5.2.6B, lower panel) was very similar between the two growth conditions, despite the steady-state differences in cell size and nucleoid fraction noted above.The dependence of the peak change in crowding FRET (Fig.5.2.6B, middle panel) on the shock magnitude was also similar within experimental error, although as noted above, quantitative comparisons of the FRET signal across different growth conditions requires caution.

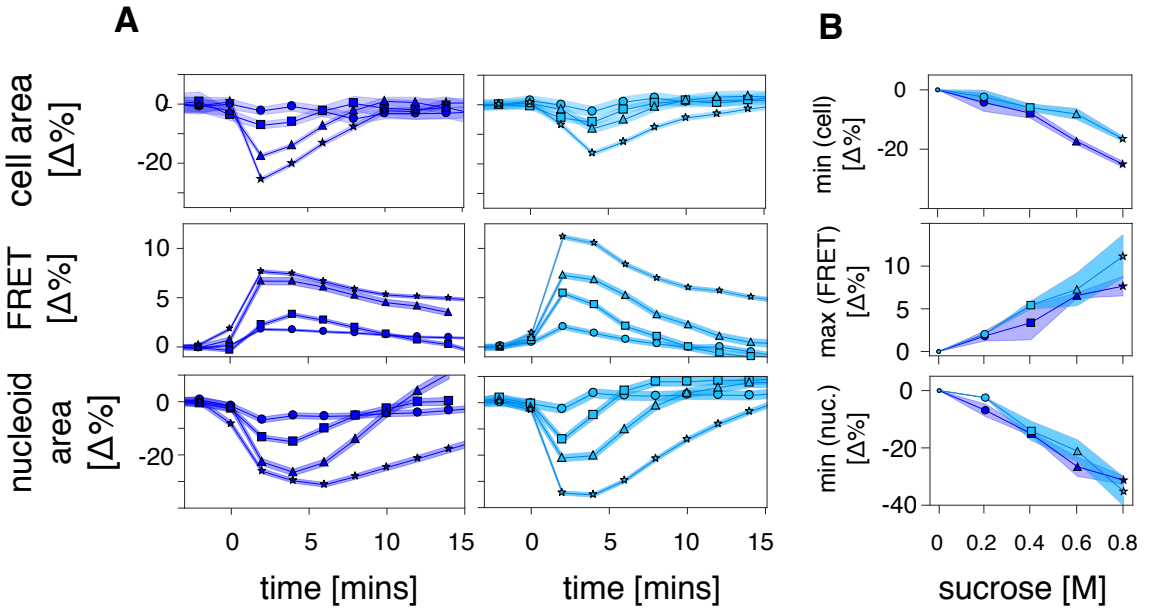


Fig. 5.2.6 **Response to hyperosmotic shocks of varying magnitude under fast and slow growth conditions.** **(A)** Time traces for sustained osmotic shock magnitudes averaged over experimental repeats for fast (blue) and slow (light blue) growth conditions. From top to bottom: cell area, crowding FRET ratio, nucleoid area. Magnitudes of sucrose shocks (M) were 0.2 (circles), 0.4 (squares), 0.6 (triangles) and 0.8 (stars). Shaded regions represent s.e.m. from single-cell data at each time obtained by pooling two independent experimental repeats **(B)** Dose-response curves for increasing magnitudes of osmotic shock for cell area, crowding FRET signal, and nucleoid area. Response magnitudes correspond to per cent fractional changes relative to the pre-shock steady-state ($\langle \Delta x \rangle / \langle x_0 \rangle$ for observable $x$), at the time of the peak response. Shaded regions represent s.e.m. from the two independent repeats when available.

By contrast, the peak cytoplasmic volume response demonstrated significant differences in magnitude between the two growth conditions, with the fast-growing cells demonstrating a greater change in size compared to slow-growing cells.

### 5.2.5 Both crowding and nucleoid dynamics demonstrate hysteresis across hyperosmotic shock response and recovery

Another notable feature of the time series data of Fig. 5.2.6 is that the times at which the change in the observables reach their peak value generally do not coincide. In particular, at larger shock magnitudes, the peak time of the nucleoid-size response tends to be delayed relative to those for the cytoplasmic volume and the crowding FRET signal. The fact that the nucleoid can continue to decrease in size even after cytoplasmic volume in crowding begin

their recovery indicates that the nucleoid, though affected by it, is not in equilibrium with the crowding state of the cell.

To investigate further this disequilibrium between crowding and nucleoid size, we examined the time series of Fig.5.2.6 as trajectories in the phase space of observables. Projections of these trajectories in the nucleoid size-crowding plane (Fig.5.2.7, upper two rows) demonstrate considerable hysteresis; within each trajectory, segments corresponding to the response phase (orange curve) and recovery phase (gray curve) do not overlap. Furthermore, characteristic loops were observed around the response peak for experiments with the largest shock magnitudes (0.6 and 0.8 M sucrose). This looped profile reflects both the delay in the onset of recovery for the nucleoid relative to crowding at early times, as well as the faster recovery of the nucleoid at later times.

By contrast, projections in the cytoplasmic volume-crowding plane (Fig.5.2.7, lower two rows) demonstrate that the peak response of these two observables do coincide in time across all tested shock magnitudes. Nevertheless, hysteresis was observed in the the relationship between cytoplasmic volume and crowding at larger shock magnitudes (0.6 and 0.8 M sucrose), with the crowding FRET signal recovering more slowly than the cytoplasmic volume. The trajectories in this plane did not form loops, however, reflecting that the recovery of the FRET signal remains slower than that of the cytoplasmic volume throughout the recovery trajectory. We mention in passing that this threshold for hysteresis in the cytoplasmic volume-crowding relationship (between 0.4 and 0.6 M sucrose) approximately coincides with that above which plasmolysis events become noticeable. Although we have not undertaken a systematic analysis of plasmolysis frequency here, one can speculate that the recovery from plasmolysis could involve additional active mechanisms not deployed upon the recovery from milder osmotic shocks and hence contribute to the observed disequilibrium at large osmotic shocks.

Finally, cytoplasmic volume-crowding trajectories (Fig.5.2.7, lower two rows) also indicate that the cytoplasmic volume typically did not overshoot its initial level by large margins, if at all, and their endpoints tended to coincide with their origin. A notable exception is the experiment with 0.8M sucrose under fast growth (Fig.5.2.7, third row, rightmost panel), where the trajectory does give the impression of a significant overshoot. However, inspection of the time series revealed that this could be due to incomplete relaxation at the end of the finite duration of the experiment (see Discussion). By contrast, nucleoid size-crowding trajectories (Fig.5.2.7, upper two rows) typically overshoot by a considerable margin, and in most cases did not recover to their origin. Thus, changes in cytoplasmic volume alone can not explain the dynamics of crowding, and changes in crowding alone can not explain the dynamics of the nucleoid. These apparently irreversible/hysteretic trajectories demonstrate

that both the nucleoid and cytoplasmic volume are not rapidly equilibrated with the crowding state of the cell, and indicate that their dynamics involve active processes.

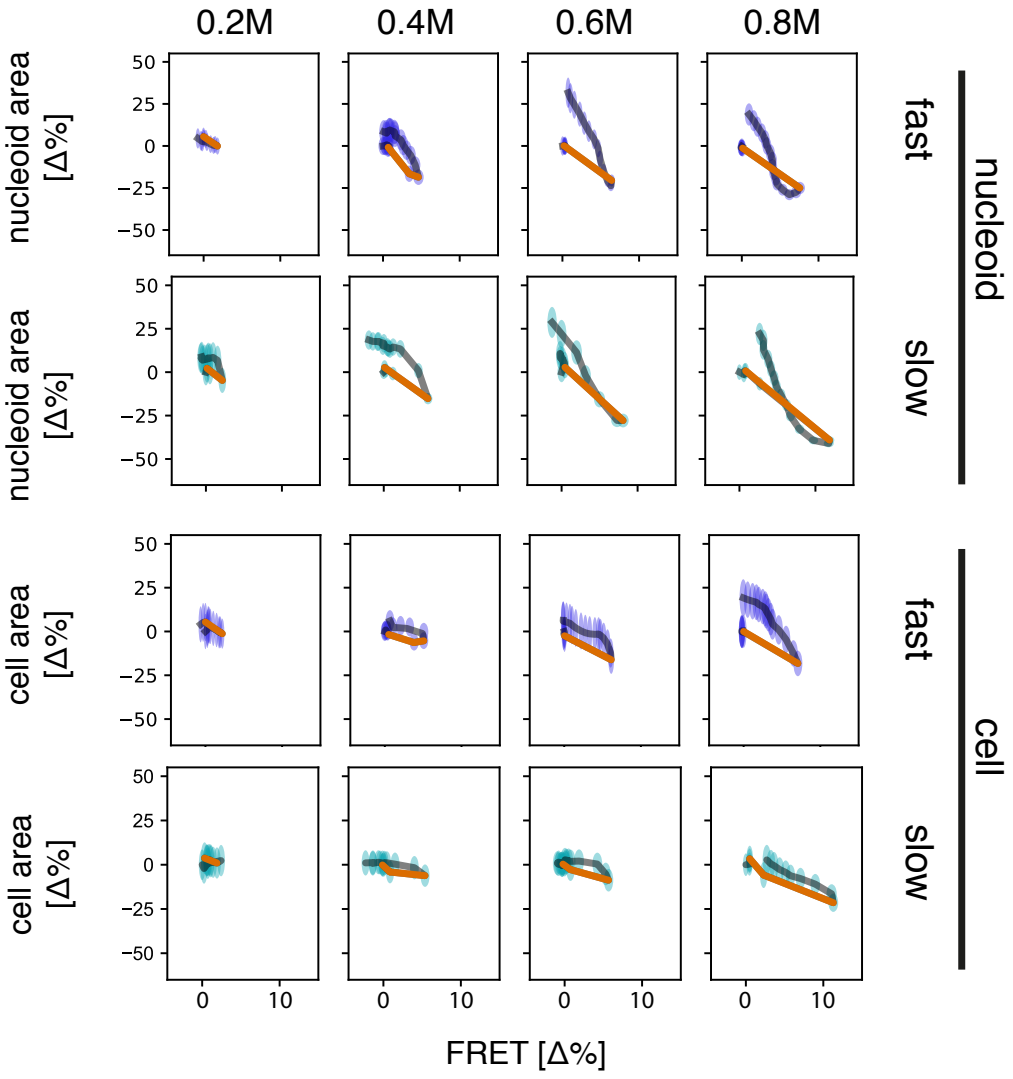


Fig. 5.2.7 **Phase-space trajectories following hyperosmotic shock reveal disequilibrium between cytoplasmic volume, crowding, and nucleoid size.** Projections of the phase space trajectories on to the nucleoid area-crowding plane (upper two rows) and cytoplasmic area-crowding plane (lower two rows). Each panel corresponds to a representative experiment for the indicated shock size (columns) and growth condition (rows). The coordinates correspond to fractional changes from the pre-shock steady-state mean. Segments of the trajectory preceding the crowding (FRET) response peak (collapse phase) are indicated by orange curves, and segments thereafter (recovery phase) by gray curves. Shaded regions indicate the 70% contours of single-cell distributions, in orange for the collapse phase, and blue (fast growth) or light blue (slow growth) for the recovery phase.

### 5.2.6 Nucleoid collapse, but not recovery, upon hyperosmotic shock follows a stereotyped trajectory

Overlaying the phase space trajectories of Fig.5.2.7 in the nucleoid size-crowding plane revealed that trajectory segments corresponding to the initial collapse phase (orange), but not the subsequent recovery phase (gray), follow a simple pattern (Fig. 5.2.8). The collapse-phase paths for all shock magnitudes fall on top of one another, and are well approximated by a straight line. This is consistent with the approximate linearity of the dose-response relations of both the FRET crowding signal and nucleoid size against osmotic stimuli observed in Fig. 5.2.6B. Because those dose response relations address the peak response at the onset of osmo-adaptive recovery, the (approximate) proportionality of their amplitude with respect to the applied shock size indicates that recovery begins within the linear regime of the initial collapse response upon hyperosmotic shock.

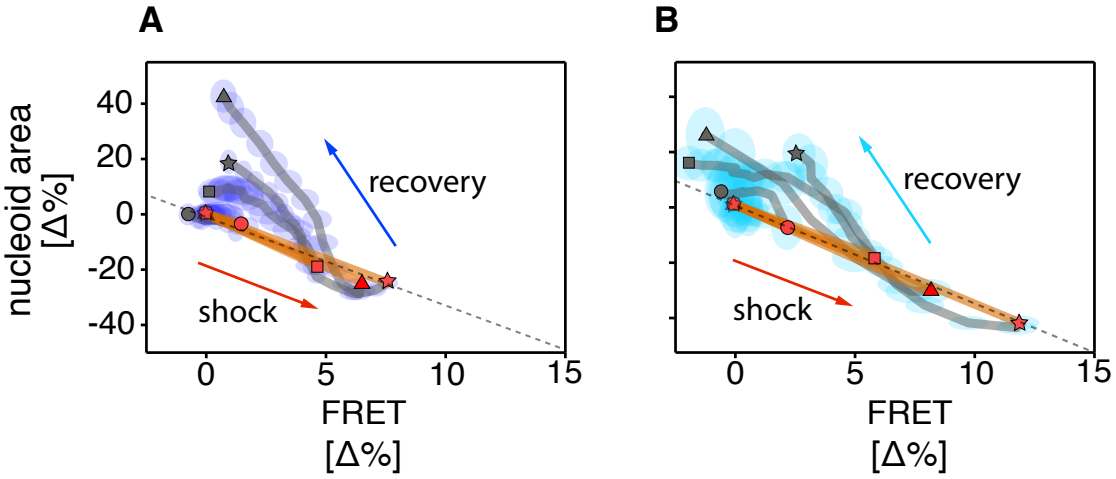


Fig. 5.2.8 **Relationship between crowding and nucleoid area following hyperosmotic shock is stereotyped during the collapse phase, but not during recovery phase.** Overlays of the nucleoid area-crowding trajectories (Fig. 5.2.7) for all shock magnitudes under fast **(A)** and slow **(B)** growth conditions. Color scheme of curves and shaded regions are as in Fig. 5.2.7. Symbols mark the beginning and of the collapse phase (red) and the final time point of the experiment (gray). Shape of symbols indicate the shock magnitude of the experiment, as in Fig. 5.2.9.

Remarkably, the slopes of these linear trajectory segments in the nucleoid size-crowding plane (Fig. 5.2.8, orange) are very similar not only across all tested shock magnitudes, but also between the fast and slow growth conditions (-3.75 $\pm$ 1.79 and -3.78 $\pm$ 0.97 for the fast and slow growth conditions, respectively). A parsimonious explanation for this stereotypy is

that crowding drives nucleoid collapse, and the manner in which it does so is similar under these contrasting growth conditions.

By contrast, trajectory segments corresponding to the recovery phase are far more diverse, following tortuous nonlinear paths that vary with both the applied shock magnitude and the growth conditions under which the cells experience the shock. The stark contrast between the recovery- and collapse-phase trajectories suggest that the mechanisms driving nucleoid compaction and recovery are different from one another.

### 5.2.7 Metabolic shutdown dilates the nucleoid independently of crowding and inhibits recovery from collapse

Whereas the highly stereotyped relationship between nucleoid size and crowding during the collapse phase upon hyperosmotic shock (Fig. 5.2.8) suggests that crowding is a key determinant of the the compaction magnitude during the collapse phase, the distinct phase space trajectories during osmoadaptive recovery indicate the involvement of additional mechanisms other than crowding in regulating nucleoid size. Furthermore, given the hysteretic nature of the collapse-recovery cycle, one or more active process must be involved in either the collapse phase, the recovery phase, or both. To directly test the role of active processes in nucleoid organization, we subjected cells to the drug 2,4-dinitrophenol (DNP), a membrane permeable protonophore that de-energizes cellular metabolism by uncoupling oxidative phosphorylation.

Treatment of fast-growing cells with DNP led to a dramatic decondensation of the nucleoid, which expanded by $\sim 35$ per cent in $\sim 10$ mins while cytoplasmic growth was arrested more rapidly, within $\sim 5$ mins (Fig. 5.2.9 A). Interestingly, the FRET crowding signal and the average cytoplasmic volume, remained nearly invariant throughout the course of this nucleoid dilation (Fig. 5.2.9 B), during which the fraction of cytoplasmic area occupied by the nucleoid increased from $\sim 51$ per cent to $\sim 67$ per cent. This observation confirms that crowding, despite playing an important role in determining the steady-state nucleoid organization (Fig. 5.2.4), is not the sole player in determining nucleoid configuration in living cells.

Subsequent application of a hyperosmotic shock (0.6 M sucrose) led to a large decrease in both the cytoplasmic volume and the nucleoid size, with a concomitant large increase in the FRET crowding signal. Given the shutdown of metabolic activity by DNP, these changes in cytoplasmic volume and nucleoid size represent a response to osmotic shock in the absence of active processes that require dissipation of metabolic energy.

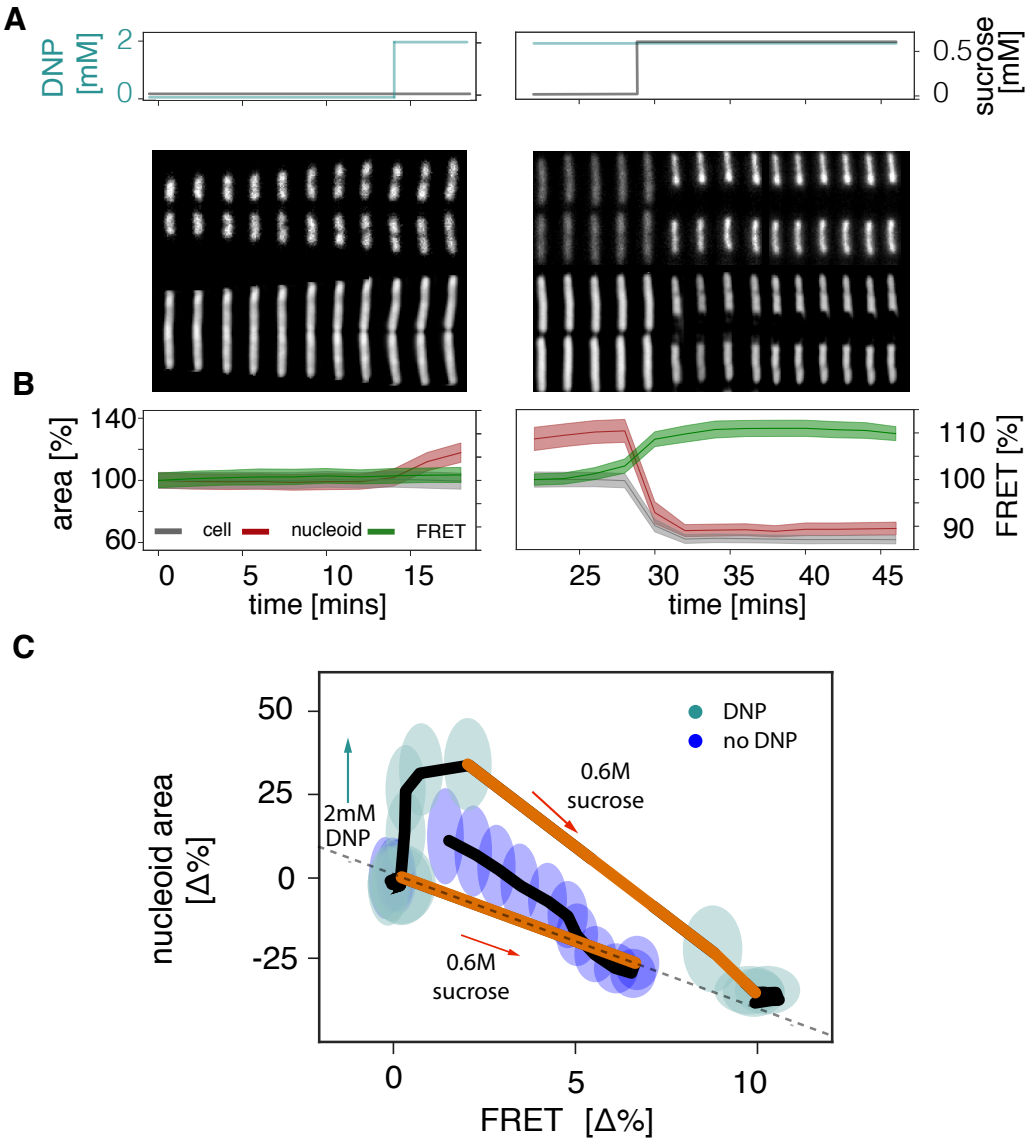


Fig. 5.2.9 **Effect of metabolic shutdown on nucleoid size and hyperosmotic shock response. (A)** Image sequences of the nucleoid (upper row, mRuby channel) and cytoplasm (lower row, phase-contrast channel) across time during DNP treatment and subsequent hyperosmotic shock. Top panel shows the medium exchange protocol of the experiment, in which 2mM DNP and 0.6mM sucrose were added at the indicated times. Time axis is shared with panel B. **(B)** FRET, normalized nucleoid and cell area time traces. Color code is indicated in legend. Shaded areas represent mean ± s.e.m. **(C)** Comparison of trajectories in the nucleoid size-crowding phase space for the same osmotic shock magnitude (0.6M sucrose) in the presence (dark green) and absence (blue) of 2mM DNP. Color code and shaded regions are as in Figs. 5.2.7 and 5.2.8, except for the color of shaded regions for DNP experiment, which is given in legend. Orange curves indicate the collapse phase of the shock, black curves indicate the recovery phase. Green curve corresponds to the expansion phase of nucleoid under the effect of 2mM DNP, prior to shock. The dashed line is a fit to the collapse phase of the no-DNP experiment, showing that the collapsed phase in the presence of DNP lies very close to the extension of the collapse-phase dynamics in the absence of DNP.

These passive responses in the cytoplasmic and nucleoid areas led to decreases of $\sim 34$ per cent and $\sim 84$ per cent, respectively, corresponding to a $\sim 15$ per cent decrease in the area fraction occupied by the nucleoid. Upon sustained shock, we did not observe recovery of any of our observables (cytoplasm area, FRET crowding signal, and nucleoid size), confirming that recovery from osmotic shock is an active process.

Net fractional changes in the nucleoid size and crowding level reached upon sustained shock in the presence of DNP exceeded the peak changes observed upon the same 0.6M shock applied in the absence of DNP (Fig. 5.2.9C), with the nucleoid area decreasing by $\sim 35$ percent and the crowding FRET signal increasing by $\sim 10$ per cent. Interestingly, this terminal phase-space coordinate of the passive response of DNP-treated cells lies very close to the extension of the phase-space trajectory of the collapse phase of DNP-untreated cells (Fig. 5.2.9C, dashed line). This observation lends further support to the idea that nucleoid dynamics during the collapse phase of hyperosmotic responses (Figs. 5.2.7, 5.2.8) largely reflect the passive response to changes in crowding.

In summary, examining nucleoid dynamics upon DNP-induced metabolic shutdown provided clear evidence that not only crowding, but also additional active processes determine the steady-state nucleoid size in growing *E. coli* cells. Furthermore, neither cytoplasmic volume nor nucleoid size recovered following hyperosmotic compression/condensation in these metabolically arrested cells, thus demonstrating that osmoadaptive recovery requires dissipation of metabolic energy. The observed extent of nucleoid size and crowding changes are compatible with the hypothesis that nucleoid collapse upon hyperosmotic shock is dominated by the passive response to crowding changes in the cytoplasm.

## 5.3 Discussion

By combining fluorescence imaging, microfluidics, and a FRET sensor of macromolecular crowding, we have carried out a quantitative experimental investigation of the effect of crowding on nucleoid spatial organization within growing *E. coli* cells. Although the effects of crowding on nucleoid organization has been studied both theoretically and through *in vitro* experiments, to our knowledge this is the first systematic investigation of crowding effects on the bacterial nucleoid *in vivo*.

#### Crowding plays a significant role in nucleoid spatial organization *in vivo*

From a polymer physics point of view, it is non-trivial that the nucleoid occupies only a fraction of the available cellular volume. The most entropically favorable configuration of an ideal confined polymer with a radius of gyration larger than the confining region is one that

fills the available volume, and based on *in vitro* experiments, it has been estimated that the *in vivo* compacted state of the *E. coli* nucleoid stores about $10^5$ $k_BT$ of mechanical energy [43]. Theoretical and experimental results of previous studies have identified four main classes of mechanisms that could contribute to this remarkable degree of compaction within living cells: (1) confinement by the plasma membrane [290, 291, 43], (2) macromolecular crowding in the cytoplasm [44, 292, 43], (3) the activity of DNA associated proteins (RNA polymerase, ribosomes, NAPs and SMCs) [69, 293–295, 273], and (4) supercoiling of chromosomal DNA [44, 292].

Confinement was suggested to be an important factor for nucleoid organization, by limiting the number of possible configurations the chromosomal DNA polymer can assume. It has been proposed by means of theoretical arguments and numerical simulations that confinement could promote segregation and that a confined polymer can assume a nucleoid-like configuration with appropriate choice of parameters [290, 296]. We found that during nucleoid collapse, both confinement and crowding increase but that the ratio of nucleoid size over cell size decreases significantly. This suggests that it is crowding rather than confinement that induces the collapse of the nucleoid. The possibility that crowding can induce nucleoid collapse is also supported by previous *in vitro* results [44, 43, 295] where the size of isolated nucleoids were found to be modulated by tuning the concentration of artificial crowders.

Our results show a clear negative correlation between the crowding FRET signal and nucleoid size, both when crowding is increased rapidly by hyperosmotic shock, and when it is decreased more gradually under sustained hypoosmotic conditions. For the case of hyperosmotic shock, the causal relationships connecting the osmotic upshift and the increase in the crowding FRET signal is straightforward: the cell volume $V$ decreases as water flows out to balance the increased extracellular osmolarity, leading to an increase in the macromolecular volume fraction $\phi = V_m/V$ which in turn reduces the average distance between the donor and acceptor domains of the FRET sensor (and hence increases FRET [54]). The causal sequence of events is less obvious for the hypoosmotic perturbation, as we observed a slow decrease, rather than increase, in the average cell size upon the reduction in extracellular osmolarity, yet still observed a decrease in the crowding FRET signal. These hypoosmotic results are counterintuitive at first, but could be explained by considering the net balance between the rates of cytoplasmic growth, cell division, and macromolecule production. The decrease in the crowding FRET signal under the hypoosmotic ($dH_2O$) environment implies a decrease in the average macromolecular volume fraction ($d\langle\phi\rangle/dt = d\langle V_m/V\rangle/dt < 0$). Given that the cytoplasmic volume also decreased during the same interval ($d\ln\langle V\rangle/dt < 0$), the average volume occupied by macromolecules must also have decreased, and at a faster rate than that of the cytoplasmic volume ($d\ln\langle V_m\rangle/dt < d\ln\langle V\rangle/dt < 0$). Thus, the negative

correlation between crowding and nucleoid size holds both for the hypo- and hyper-osmotic conditions, strongly suggesting the importance of crowding in the steady-state compaction of the nucleoid *in vivo*.

**The role of active processes in maintaining the nucleoid's steady state and osmoadaptive recovery**

In addition to macromolecular crowding — a set of passive (equilibrium) effects that manifest at high macromolecular volume fraction $\phi$ — our data also demonstrate the importance of active (non-equilibrium) processes in shaping nucleoid spatial organization and dynamics *in vivo*. Depression of metabolic activity in fast-growing cells via the membrane potential uncoupler DNP led to a dramatic increase in the nucleoid volume while the cytoplasmic volume and crowding FRET signal remained invariant (Fig. 5.2.9). These observations clearly demonstrate that active processes dependent on the availability of metabolic energy contribute to the steady-state nucleoid compaction in growing cells. The fact that the crowding FRET signal remained invariant during this shutdown-induced nucleoid expansion further suggests that the manner in which these active processes contribute to the steady-state nucleoid compaction is orthogonal to that of crowding. Interestingly, Joyner et al. recently reported a small, but significant volume reduction in *E. coli* cells treated with DNP[297] and speculated that crowding might thus be affected by metabolic shutdown. This contrasts with our our observation (Fig. 5.2.9B) that the cell size remains invariant under DNP treatment. The reason for this apparent discrapancy remains unclear at this time, but we note that the experiment of Joyner et al. differs in many ways from our own (strain, growth conditions, measurement techinques), including the duration of the DNP exposure (30 minutes), which in that work was more than twice as long as that in our experiment. Thus, it remains possible that a similar reduction would be observable under our experimental setup upon longer exposure to DNP, but the results presented here nevertheless indicate that a change in nucleoid size can be induced by DNP treatment in the absence of changes in cell size or crowding. Decondensation of the nucleoid upon DNP treatment had been noted in a previous study [151], in which the authors' focus was the effects of metabolic shutdown not on the nucleoid but rather the physical state of the cytoplasm — the mobility of large particles (protein aggregates of length $\sim 900$ nm) diffusing in the cytoplasm was found to be strongly diminished upon DNP treatment. The invariance of the FRET signal in our experiments upon DNP treatment suggests that the DNP-induced changes in the cytoplasm reported in ref. [151] do not affect macromolecular crowding effects felt by molecules of more moderate size (the FRET sensor used here measures $< 10$ nm in length).

Active cellular processes reported to affect the nucleoid configuration include transcription by RNA polymerase (RNAP) [298, 69, 83], cotranscriptional translation and membrane insertion of transmembrane proteins (transertion) [293, 278], as well as ATP-hydrolyzing structural maintenance of chromosome (SMC) proteins, such as the MukBEF complex [63, 273]. Interestingly, while some of these active processes (RNAPs and SMC proteins) contribute to compaction of the nucleoid, others (transertion) contribute to its expansion. The increased nucleoid volume we observed upon DNP treatment during fast growth (Fig. 5.2.9) thus indicates that the net balance among forces exerted by these active processes during steady growth favors nucleoid compaction, at least under the experimental conditions tested here.

Effects of active processes were also apparent in the nucleoid dynamics following hyperosmotic shock (Figs. 5.2.7, 5.2.8). The relationship between the crowding FRET signal and nucleoid size contrasted strongly between the initial collapse phase of the response and the subsequent recovery phase, demonstrating considerable hysteresis (Fig. 5.2.7). Although hysteresis could in principle arise from the involvement of active processes in the collapse phase, recovery phase, or both, the highly stereotyped trajectories of the collapse dynamics (Fig. 5.2.8), and the absence of the recovery phase upon metabolic shutdown (Fig. 5.2.9) motivate the interpretation that active processes contribute primarily to osmoadaptive recovery, and not to the initial collapse response.

What cellular processes could be responsible for this active osmoadaptation of nucleoid size? Osmoadaptation of the cytoplasmic volume involves both passive and active processes, with an initial rapid volume recovery triggered by passive potassium ion ($K^+$) influx through constitutively expressed potassium channels, and subsequent recovery requiring active synthesis of additional transporters and biosynthetic enzymes that eventually replace the increased $K^+$ with organic osmoprotectants such as glycine betaine, proline, and trehalose [299–301]. More specifically for the nucleoid, Cagliero et al. [69] found by imaging cells chemically fixed at various times after osmotic shock that the initial collapse of the nucleoid upon hyperosmotic shock is accompanied by dissociation of RNAPs from the nucleoid (possibly as a result of the transient increase in cytoplasmic $K^+$ concentration), and that the dissociated RNAPs return to the nucleoid during the osmoadaptive recovery phase. Although RNAP activity is generally considered to contribute to nucleoid condensation [69, 83], it is also involved in transertion, and thus could contribute to nucleoid expansion [293, 278], especially if expression of transmembrane proteins were augmented during the recovery phase. In the future, it will be interesting to further dissect the interplay between these active processes and crowding effects on nucleoid compaction, by extending the experiments presented here to include perturbations to the osmoadaptation pathways (e.g. by removing environmental

$K^+$, or deleting genes involved in the transport/synthesis of organic osmoprotectants), as well as other active processes such as transcription and translation using drugs that specifically target each process (e.g. rifampicin for transcription, chloramphenicol for translation).

**The dependence of crowding and nucleoid configuration on growth conditions**

In agreement with previous reports [84], we found that the fraction of cytoplasmic space occupied by the nucleoid differs between cells growing at fast and slow rates, with fast growing cells exhibiting a lower area fraction occupied by the nucleoid (Fig. 5.2.5C). The absolute area occupied by the nucleoid was remarkably similar between the two growth conditions (Fig. 5.2.5B), but considering also that faster growing cells contain more chromosomal DNA [302], we conclude that the degree of nucleoid compaction is higher in fast growing cells. The mechanistic determinants of this difference remain unknown, but likely involve the activity of both active (RNAPs, ribosomes, SMCs) and passive (NAPs, crowding) molecular machinery. Interestingly, we observed a higher level of the crowding FRET signal in slow-growing cells (Fig. 5.2.5D); the mean ($\pm$s.e.m.) values for this ratiometric signal (YFP/CFP) were $0.70\pm0.001$ and. $0.88\pm0.002$ for the fast and slow growth conditions, respectively. As noted in Results, interpretation of the absolute level of the FRET signal in our experiments requires caution as the sensor has not been calibrated within our experimental setup. It will be of interest to confirm with future experiments with calibration (using appropriate controls of cellular background fluorescence and purified FRET sensor) whether this represents a true difference in the degree of cytoplasmic crowding, but we note here that the trends we observe in the fractional changes to the various observables upon osmotic shock (Fig. 5.2.6B) could in principle be explained by a higher level of crowding in slow growing cells (though other interpretations are also possible).

Consider a bacterium immersed in a medium of osmotic pressure $p$. The cytoplasm is turgid, that is, the internal osmotic pressure of the cytoplasm $p^*$ is greater than that of the environment ($p^* > p$), leading to a positive turgor pressure $\Delta p = p^* - p$. When the external osmotic pressure exceeds that of the cell interior ($p > p^*$), the cell loses turgidity ($\Delta p \to 0$) and the cytoplasmic volume $V$ decreases according to a conservation law for osmotic work $p(V - V_m) = p^*(V^* - V_m)$. Here the difference $V - V_m$ is the osmotically active volume. Rearranging, and writing in terms of the macromolecular volume fraction $\phi = V_m/V$, we have

$$V/V^* = (1-\phi^*)p^*/p + \phi^*, \tag{5.1}$$

where $V^*$ and $\phi^*$ are the cytoplasmic volume and the macromolecular volume fraction, respectively, at the isoosmotic point $p = p^*$. Eq. 5.1 (or close variants thereof) has been

found to fit well the cytoplasmic volume response to osmotic shock for $p > p^*$ in a number of previous studies [303, 304], and implies that the dependence of cytoplasmic volume on external osmotic pressure

$$\left.\frac{\partial \ln V}{\partial p}\right|_{p=p*} = -(1-\phi^*)/p^* \tag{5.2}$$

will become steeper if either the initial level of crowding $\phi^*$, the initial internal osmotic pressure $p^*$, or both are reduced. The data of (Fig. 5.2.6B, upper panel) does indeed indicate a steeper dependence of the fractional change in cytoplasmic volume on the change in external osmolarity ($(\Delta V/V)/\Delta p \approx \partial \ln V/\partial p$) for the fast growth condition, for which the data of Fig. 5.2.5D indicate a lower degree of crowding. Thus, the observed difference in the slope of the cytoplasmic volume response $(\Delta V/V)/\Delta p$ is at least qualitatively consistent with a difference in the crowding parameter $\phi$ although we can not exclude the possibility that it is instead due to differences in the internal osmotic pressure $p^*$.

On the other hand, the observed response in nucleoid size to jumps in external osmolarity (Fig. 5.2.6B, lower panel) was very similar between the fast and slow growth conditions. Combined with the observation that the cytoplasmic volume decreases more rapidly with external osmolarity for the fast growth condition (Fig. 5.2.6B, upper panel), this implies a greater fractional change in nucleoid size per fractional change in cytoplasmic volume for the slow growth condition. The latter trend could also be explained, in principle, by a higher steady-state level of crowding $\phi$ for the slow growth condition, because the strength $f_{\mathrm{dep}}$ of the depletion interaction driving nucleoid compaction is, to leading order, proportional to the crowder volume fraction $\phi = V_m/V$: $f_{\mathrm{dep}}/k_BT \approx (V_{\mathrm{excl}}/v_m)(V_m/V)$ where $V_{\mathrm{excl}}$ is the excluded volume around the DNA (modeled as a cylinder) and $v_m$ is the volume of individual crowder molecules [37, 292]. This means the dependence of the depletion interaction on fractional changes to the cytoplasmic volume,

$$\left.\frac{\partial f_{\mathrm{dep}}}{\partial \ln V}\right|_{V=V^*} \approx -\phi^* V_{\mathrm{excl}}/v_m, \tag{5.3}$$

is proportional to the steady-state crowder volume fraction $\phi^*$. Thus, the slow-growth condition's steeper nucleoid-size response to changes in cytoplasmic volume (Fig. 5.2.6B, upper panel) is again compatible with its higher crowding FRET signal level (Fig. 5.2.5D), although we can not rule out the possibility that the steeper response rather reflects a difference in the typical size of crowder molecules $v_m$ between the two growth conditions, which could arise from differences in proteome composition at different growth rates.

### Outlook and future directions

By high-throughput imaging at the single-cell level under a variety of environmental perturbations, we investigated the role of macromolecular crowding in nucleoid spatial organization *in vivo*. Our results strongly suggest a significant role of crowding in determining the steady-state level of nucleoid compaction under steady growth conditions, and open the way to a variety of future studies on the complex interplay between nucleoid spatial organization and cellular physiology. In the future, it will be exciting to extend the experimental approach presented here to further dissect both the causes and consequences of nucleoid spatial organization. We conclude by highlighting a few particularly promising directions for future work.

NAPs are expected to drastically affect nucleoid spatial organization through multiple effects. On the one hand, they can enhance the response to crowding changes by increasing the effective cross-sectional area of the DNA polymer. On the other hand, NAPs can also counter crowding effects by crosslinking chromosomal DNA segments at multiple sites. Although we used a fluorescently labeled NAP (HU::mRuby2) to image the nucleoid, our experiments did not address the role of NAPs in determining the *in vivo* configuration of the nucleoid. By carrying out experiments similar to those presented here in mutants of specific NAPs, such as H-NS, HU or Fis. By comparing steady-state and osmotically perturbed values of nucleoid size and measuring the spatial distribution of such proteins in mutant and wild type strains, future experiments could clarify whether and how NAPs contribute to nucleoid organization under both physiological and perturbed conditions.

Similarly, extending the approach of our experiment to mutants of active proteins that contribute to nucleoid organization, such as SMCs, RNAPs and ribosomes, would be both exciting and informative in dissecting the role of active processes in steady-state nucleoid compaction, as well as in the adaptation following osmotic shocks.

Another important set of experiments that could be carried out in this context are osmotic upshifts delivered in a potassium-free medium. It is well established that potassium ($K^+$) ]import is, together with the slower timescale glycine import, the main process responsible for the initial cell size recovery upon sustained osmotic shocks [288, 299, 304, 305]. When osmotic shock is applied through a potassium-free medium, cells are not able to recover from plasmolysis, and a previous study has indicated that the absence of potassium in the medium also reduces of the effects of osmotic shock on the nucleoid [305]. By comparing the degree of nucleoid compression after osmotic shock between potassium-free and potassium-containing media, one could quantify the effects of the transient $K^+$ influx at the onset of osmoadaptation. This would help disentangle the effect of the crowding perturbation from

those associated with the active nucleoid expansion during sustained osmotic upshifts in metabolically active cells.

To better understand the dependence of nucleoid organization on growth physiology, it will be instrumental to calibrate within our experimental setup the FRET sensor against *in vitro* measurements of crowding (using e.g. Ficoll) and taking into account the growth-rate dependent cellular background fluorescence. This will allow more meaningful comparisons of the absolute level of the crowding FRET signal between different growth conditions, and help resolve whether growth-condition dependent differences in cytoplasmic and nucleoid osmotic responses are due to crowding or other factors (see discussion in above).

Finally, simply expanding the range of osmotic shock magnitudes tested in the experiment will be highly informative. Due to the relatively mild osmotic shocks applied here, the nucleoid responses observed in the present study appear to be within (or at least not far from) the linear regime of the response (Fig. 5.2.6B). The full dynamics of disordered polymers are nearly always characterized by nonlinear functions (often power laws) [68], and in the case of the nucleoid, it remains an open question whether the collapse we observed *in vivo* upon osmotic shock represents a continuous [44] or discontinuous [43, 306] transition. Testing the osmotic response over a broader range of shock magnitudes would also help estimate the steady-state osmotic pressure of the cytoplasm (by fitting Eq. 5.1 to changes in the cytoplasmic volume, $V$). Future studies that combine a larger range of osmotic shock magnitudes with FRET calibration and the expanded repertoire of mutant strains described above would undoubtedly help to dissect further the roles of the multiple factors (passive and active DNA-binding proteins, osmoadaptation, growth physiology, and crowding) in shaping nucleoid spatial organization and dynamics *in vivo*.

## 5.4 Materials and methods

### 5.4.1 Bacterial strains and plasmids.

The strains and plasmids used in this study are listed in Table 5.1 and 5.2.

| Plasmids | | | | | |
|---|---|---|---|---|---|
| **name** | **Vector** | **Gene(s)** | **Resistance** | **Induction** | **Source** |
| n/a | pRSET-A | FRET crowding sensor | Amp | IPTG | B. Poolman [54] |
| pSJAB159 | pTrc99Aα* | FRET crowding sensor | Amp | IPTG | This study |

Table 5.1 Plasmids used in this study

**pTrc99Aα is a modified version of pTrc99A. In this version the plasmid-borne start codon is deliberately mutated to ATG for cloning the native RBS of the protein of interest. This way no unintended translation occurs from the RBS that comes with the vector.*

| Bacterial strains | | | | |
|---|---|---|---|---|
| **Strain Name** | **Genotype** | **Parent** | **Source** | **Plasmid** |
| SJ540 | *hupA::mRuby2,* (native promoter), | MG1655 | Suckjoon Jun | - |
| TSS1961 | SJ540 transformed with crowding sensor plasmid | MG1655 | this study | pSJAB159 |

Table 5.2 Strains used in this study

### 5.4.2 Growth conditions

In this study we used two types of growth media which were both based on the AB medium described for the first time in [307] (solution A: 2.0 g $(NH_4)_2SO_4$, 6.0 g $Na_2HPO_4$, 3.0 g $KH_2PO$ 4, 3.0 g $NaCl$, 0.011 g $Na_2SO_4$, dissolved in 200 ml. of water. Solution B: 0.2 g

$MgCl$, 0.010 g $CaCl_2$ and 0.0005 g $FeCl_3, 7H_20$ dissolved in 800 mL water. A and B are mixed after autoclaving by pouring A into B. No precipitate is formed). To achieve fast growth conditions with a doubling time of about 25 minutes at 37C, we supplemented the AB medium with EZ (teknova 5X Supplement EZ), all 4 nucleotides (10X ACGU solution, teknova) to a final concentration of 0.02mM and 0.5% glycerol (which does not interfere with our IPTG inducing system). For achieving slow growth with an average doubling time of 45 minutes we supplemented AB with 0.5% glycerol and 6 amino acids (methionine, histidine, arginine, proline, threonine and tryptophan, final concentration is 0.5mg/ml for each amino acid).

For both slow and fast conditions, cells were grown overnight in the respective medium. The morning after, the saturated culture was diluted 1:10 into fresh medium and cultured for about 4hrs. Cells were then harvested and concentrated $\sim$10 times via centrifugation at 10000rpm for 1 minute (Eppendorf Centrifuge 5424) prior to loading them in a mother machine device (see Sample Preparation section below).

### 5.4.3 Overview of experimental setup and measurement strategy.

Our study required simultaneous monitoring of nucleoid size, intracellular crowding and cell size and a means to perturb intracellular crowding in growing *E. coli* cells. To implement step-like perturbations in time, we also needed a way to rapidly exchange the medium in the environment of growing cells. To meet these requirements, we made use of a PDMS-based "mother machine" microfluidic device, which enables microscopic imaging of thousands of individual cells during steady-state growth [98].

For nucleoid-size readout we employed an *in situ* DNA label based on the nucleoid associated protein HU, which has been used widely for nucleoid labeling purposes and has been shown to colocalize with DNA-intercalating dyes such as DAPI [130, 129, 43, 60]. We made use of an MG1655 derivative strain bearing a genomic mRuby2 fusion to *hupA* (SJ540, see materials and methods section). In this strain the nucleoid is labeled with good contrast by the HU::mRuby2 fusion upon imaging live cells growing within the mother machine, as shown in Fig. 5.2.1.

To measure intracellular crowding, we made use of a FRET sensor recently developed by Boersma et al. [54]. The sensor consists of a clamp-like protein composed by two arms with a donor CFP (mCerulean) and acceptor YFP (mCitrine) fluorescent protein respectively on the tip of each of its arms. CFP acts as the donor for FRET while YFP is the acceptor. Under constant environments, the FRET signal (acceptor-to-donor fluorescence ratio; $I_{\mathrm{YFP}}/I_{\mathrm{CFP}}$) is stationary and its amplitude determined by the average distance between the CFP and the YFP domain. Increased crowding forces the two domains into closer spatial proximity,

resulting in an increased FRET signal. The sensor has been shown to robustly measure crowding changes *in vitro* under variation of of different environmental conditions relevant for *in vivo* measurements (temperature, pH, NaCl and DNA) for a number of different crowders (Ficoll, PEG, sucrose), crowder sizes and sensor concentrations. The FRET signal increase is nearly proportional to the volume fraction of crowders ($\phi = V_m/V$) across the physiologically relevant range ($0 < \phi < 0.3$) and the sensor has been shown to be insensitive to osmoprotectants such as potassium glutamate and glycine betaine. Tests *in vivo* on bacterial cells under osmotic shock induced by increasing concentrations of sucrose, showed that the FRET signal increases nearly proportionally with the magnitude of the shock (for details see ref. [54]).

To monitor in parallel the size of the cells' cytoplasm, the nucleoid as well as crowding, we developed a multichannel imaging system capable of phase contrast imaging in addition to fluorescence imaging in the relevant wavelength bands for mRuby2, CFP and YFP fluorophores. Excitation filters and dichroic mirrors were mounted on the motorized turret of an inverted fluorescence microscope (Nikon Ti-E), and emission filters on a motorized filter wheel (Nikon TI-FLBW-E) attached at the microscope's emission output port. The motorized turret and filter wheel enable rapid switching between imaging channels, so that each field of view (FOV) could be imaged in all four channels (phase contrast, mRuby2, CFP and YFP) in $< 2$ s.

The microscope was placed in a temperature-controlled room (37C) and a fast-switching ($< 200$ ms) emission filter wheel was positioned just before the camera for spectral separation of our imaging channels. Actual imaging time of our four channels sum up to about 0.7 s (fluorescence excitation is carried out with a multi-wavelength LED, Lumencor Spectra X) but switching both the excitation filter turret and the emission filter wheel takes on average about 0.2s per imaging channel so the time needed to image a field of view is about 1.5s. Image acquisition (including excitation light pulses, filter switching, and translation of the motorized microscope stage) was automated using custom-written scripts in NIS-Elements software (Nikon Instruments, NIS-Elements Advanced Research). The script repeats the 4-channel imaging across a set of FOVs pre-selected by the user (in a typical experiment, $\sim 30$ FOVs) at regular time intervals. We observed minimal sample drift under these conditions when a time series are constructed from image sequences of each FOV. Since we image around 30 FOVs er experiment, our frame rate is limited by acquisition time. Moving the stage from one FOV to another takes about 1.5s which added to the acquisition time sum up to about 3 seconds per FOV. Thus to acquire images at one time point for 30 FOVs requires at minimum $3. \times 30$ s = 90 s. To leave some margin and prevent errors in the timing of the image acquisition, we set our inter-frame interval to 120 s.

We chose to implement perturbations to crowding via sucrose hyper-osmotic shock which has been shown to perturb crowding in live *E. coli* cells [54]. As discussed in Chapter 3, the mother machine microfluidic device enables continuous imaging during steady state exponential growth at high-throughput (here 3000 cells per experiment), as well as rapid exchange of media for step-like environmental perturbations [98, 43].

A typical experiment comprises the following steps: (i) load cells in mother machine and incubate under constant temperature and nutrient flow to achieve steady exponential growth, (ii) image cell body morphology in phase contrast channel, (iii) image nucleoid morphology in red fluorescence emission channel, (iv) image FRET donor (cyan) and acceptor (yellow) fluorescence emission channels for crowding analysis, (v) repeat steps (ii)-(iv) to obtain statistics of observables during steady-state growth, (vi) exchange medium to apply osmotic shock or other perturbations to cellular parameters, (vii) repeat steps (ii)-(iv) to obtain statistics of dynamical response to the perturbation applied in (vi).

### 5.4.4 Microfluidic experiments in the mother machine

PDMS (SYLGARD 184, 10 g clip-pack) was mixed with cross-linker to a 10:1 ratio in weight for a total weight of 70g. The solution was stirred for about 5 minutes and poured onto the epoxy mold (SJ110 model from Prof. Suckjoon Jun's lab) where the devices (12 per mold) were impressed. The mold with the PDMS was then baked for 8 hours at 60C. After that, the PDMS, which has a thickness of about 0.8cm at this stage, was detached from the mold via a metal cutter, single devices cut apart and holes were punched to create inlet and outlet ports at the two ends of the main channel (see Fig. 5.2.1). Single devices were then immersed in pure pentane and stirred continuously for 4 hours with a magnetic stirrer. After that, the devices were transfered into pure acetone and washed twice for 2 hours with continuous stirring. Subsequently the devices were left to dry in air and stored in plastic containers. We used the devices within two weeks after drying.

After devices were washed and dried, they were plasma treated (30W Harrick Plasma system) for 1 minute together with the Willco dish (WillcoWells, GWST-5040, 50X7mm, glass thickness 170 μm), promptly sticked to the dish and incubated at 60C for about 15 minutes to stimulate adhesion. To prepare the sample for microscopy, a concentrated bacterial solution (O.D.$\sim$ 2) from a day culture (see Growth Conditions section) was injected into the main channel by pipetting. When the bacterial suspension had filled the main channel, the Willco dish was secured by means of a custom holder into a custom centrifuge (based on a commercial fan rotor) taking care to place it such as to make the main microfluidic channel and the radius of the centrifuge perpendicular to each other. This way bacteria were pushed into the growth channels upon centrifugation. The centrifuge was run for 10 minutes at about

800rpm and in the meanwhile a microfluidic tubing (PTFE 24AWG .55mmID .30mm Wall 100ft, Zeus, SC, USA of about 50cm length was filled with fresh medium via a syringe with needle. After centrifugation, one of the holes punched earlier on the device was connected to the tubing filled with fresh medium (inlet) and the other to a piece ($\sim$ 20 cm) for the waste (outlet). The inlet was then connected to a syringe driven by a pump (PHD ULTRA, Harvard Apparatus, MA, USA), which was loaded with fresh growth medium. The pump was turned on, set to a flow rate of 1.5ml/h and the bacteria were left to grow at 37C while fresh medium was flowing in the main channel. When exponential growth was achieved (4 hours for fast growth condition and 6 for slow growth condition) about 10 frames for each imaging channel were acquired at 2-minutes interval under unperturbed conditions. After that the medium flowing in the mother machine was switched to apply the environmental perturbation (hyper-/hypo-osmotic shock, and/or DNP) by connecting the pump to a different syringe filled with the relevant medium. Phase contrast, YFP, CFP and mRuby images were then recorded at 2 minute s inter-frame interval in the presence of the environmental perturbation.

### 5.4.5 Microscopy

For our experiments with the mother machine, which were mainly carried out in San Diego at UCSD, we make use of a Nikon Ti-E inverted microscope, a 60X objective suitable for phase contrast imaging (Nikon CFI Plan Apochromat DM60x oil), a sCMOS camera (Andor Neo sCMOS 5.5), a LED (Lumencor Spectra X) for fluorescence excitation, multiband dichroic (Chroma 69008bs), multiband excitation filters (Chroma 69008x) and multiband emission filter (Chroma 69008m). LED illumination was coupled into the microscope via a fluorescence illumination attachment (Nikon Ti built-in LED or lamp coupling arm) to produce a homogeneous illumination pattern on the sample plane. Emission filters were mounted on a motorized filter wheel (Nikon TI-FLBW-E) placed in the emission path just before the camera while excitation filters and dichroics were mounted into standard filter cubes for Nikon Ti microscopes. The sample holder is mounted on a motorized stage (Nikon Ti built-in motorized stage). The exposure times for imaging in each imaging channel were 30ms for phase contrast, 50ms for YFP, 400ms for CFP and 200ms for mRuby. Camera exposure and LED illumination times were the same for all imaging channels and the LED power was kept to its maximum value. For achieving high throughput, the 4-channel image sequences were acquired in about 30 FOVs in each experiment. With the specifications of the current setup, each cycle of 30-FOV acquisitions could be completed within 2 minutes (see above).

### 5.4.6 Quantitative data analysis and image processing.

As discussed briefly in chapter 3, for all analyses described in this chapter we utilized Python code that was initially developed in the laboratory of Prof. Suckjoon Jun (UCSD), but expanded and adapted here for the specific needs of the present study. The code was already optimized for channel identification, channel slicing, empty channel averaging and background subtraction while we added the module that compute FRET ratios of CFP and YFP images, the nucleoid segmentation and the morphological quantification modules. The code comprises the following modules (explained more in detail in Chapter 3):

1. Growth-channel identification and slicing from phase contrast images:
   Starting from time series of images similar to those presented in Fig. 5.2.1, we compute the projection of phase contrast images on the horizontal axis. We thus obtain a peaked profile where peaks correspond to the middle axes of single growth channels. The position of the peak is used for channel identification and slicing. Each growth channel in each FOV is sliced and stacked at each time point.
2. Empty-channel identification:
   This module of the analysis involves a manual selection of identified channels that are empty, as well as channels that are to be discarded from the analysis because of imperfections in the PDMS or other defects. Via a GUI it is possible to select which channels to discard and mark empty channels for background subtraction.
3. Background subtraction of empty channels from filled channels:
   Here images of empty sliced channels are first averaged together to obtain a more general estimate of the background spatial profile. The averaged empty channel image is aligned with images of filled channels by means of cross correlation maximization between two images. After alignment the empty channel image is subtracted from the filled one.
4. Phase contrast subtracted image segmentation:
   The resulted growth channel subtracted images are passed through a segmentation algorithm based on watershed transform [308]. To identify seeds for the watershed we cast a straight Otsu algorithm to threshold the subtracted image. The thresholded image is then passed through a distance transform and the transformed image is thresholded to retain only those parts of binary regions that have a distance greater than 1.5 pixels (159nm) from the edge of the segmented region(s). The resulting image is used as the seed image for watershed transform. After watershed, the final image is filtered to remove segmented cells touching the boundary of an image (most likely coming from a segmentation artifact), cells smaller than $0.75\mu m^2$ in area and cells exceeding $8\mu m^2$.

A challenge of mother machine image segmentation is indeed to properly separate cells with automatic segmentation as they often are found in very close spatial proximity and sometimes segmentation identifies multiple cells as a single binary region. Each resulting image from each segmented growth channel time series in each FOV is stacked together.

5. mRuby-labeled nucleoid image segmentation:
   A very similar approach is used for segmenting nucleoid images. Here the challenge deriving from cells being close to each other is less drastic but it can be present when segmenting nucleoids in slow growing cells where nucleoid area fraction is higher. As before, the seeds are identified by distance thresholding a rough binary mask obtained via Otsu's algorithm mRuby from which the (fluorescence) background was also subtracted employing empty channels images as described above for phase contrast images. For slow growth the threshold value obtained from Otsu's algorithm is rescaled by a factor of 1.25 to attenuate the aforementioned proximity issue. Since upon collapse a replicating nucleoid can split into two distinct blobs for some osmotic shock magnitudes, our segmentation algorithm could assign two different binary regions to the two blobs even though before shock they were part of the same nucleoid in the segmented image. As a consequence our measured nucleoid size change would be biased at the time point of sucrose arrival since the number of identified nucleoids would increase due to nucleoid splitting upon osmotic shock and we would thus underestimate the average nucleoid size at the time of the shock. To resolve this issue, we always force segmented nucleoids whose centroids are closer than 250nm to belong to the same binary region. Filtering is applied as for segmented phase contrast images but we set the size threshold to $4\mu m$ this time.

6. FRET ratio computation from CFP and YFP images:
   To measure crowding levels using the crowding sensor from [54] we need to compute the ratio of the acceptor fluorophore (YFP) to the donor (CFP) from the two different images. We use the segmented phase contrast image to identify rectangular boxes around each segmented cell from phase contrast. We then crop regions corresponding to the boxes from both the YFP and the CFP images, and take the sum of the cropped YFP image and divide it by the sum of the corresponding cropped CFP image. We note that we used the same phase contrast image to define the boxes, such as the YFP and CFP images are clipped with an identical box. We repeat this procedure for each cropped image of single growth channels and store Acceptor/Donor values at each time point.

7. Cell and nucleoid morphological quantification:
   All the morphological parameters in this work are extracted from segmented images. Each segmented image is assigned a unique label. We make use of the function "regionprops" of the morphology module of the scikit-image python package (freely available online http://scikit-image.org/). The function returns (among other properties) area, centroid position, major and minor axes of an input binary region. As input, we pass to the function segmented images of isolated single cells which are possible to isolate thanks to our segmented images being labeled: each region (cell) identified by the watershed segmentation has a different numerical label.

## 5.5 Acknowledgments

The work in this chapter has been a collaboration with the laboratory of Prof. Suckjoon Jun (UCSD). All the experiments described in this chapter here were performed by the author during a 3-month visit (Jan-Apr 2017) to Prof. Jun's laboratory at UCSD. The image analysis code was partly developed by John T. Sauls from Prof. Jun's laboratory. The crowding sensor, a kind gift of Prof. Bert Polman (U. Groningen) was cloned into the pTrc99A$\alpha$vector by Simone Boskamp from Tom Shimizu's laboratory at AMOLF.

# Appendix A

# Absorpion profile imaging of silicon nano-wires via adsorbtion activated localization microscopy

# Abstract

Nanophotonics is becoming invaluable for an expanding range of applications, from controlling the spontaneous emission rate and the directionality of quantum emitters, to reducing material requirements of solar cells by an order of magnitude. These effects are highly dependent on the near field of the nanostructure, which constitutes the evanescent fields from propagating and resonant localized modes. Although the interactions between quantum emitters and nanophotonic structures are increasingly well understood theoretically, directly imaging these interactions experimentally remains challenging. Here we demonstrate a photoactivated localization microscopy-based technique to image emitter-nanostructure interactions. For a 75 nm diameter silicon nanowire, we directly observe a confluence of emission rate enhancement, directivity modification and guided mode excitation, with strong interaction at scales up to 13 times the nanowire diameter. Furthermore, through analytical modelling we distinguish the relative contribution of these effects, as well as their dependence on emitter orientation.


# Introduction

The near-field interactions of a quantum emitter with a nanostructure can be summarized largely by three pheonomena: first, the excitation of guided and resonant modes within the structure, second, the directing of emission through interference with scattering from the nanostructure, and third, the modification of the total emission rate of the quantum emitter.

Nanowires have proven to be an ideal model system for nanophotonic exploration as they are both geometrically simple enough to be amenable to analytical analysis, while also expressing strong coupling to all three of these channels, as depicted by the inset in Fig. A.0.1a. They support both localized resonances [1] and guided modes [2], which modify the local density of optical states (LDOS) at the location of the emitter (allowing for emission rate and efficiency enhancements) as well as its radiation pattern (allowing for improved directional emission)[3].

This ability to control both the emission and absorption of light has led to a huge number of applications throughout the fields of light-emitting diodes[4], nanoscale lasers[5], photovoltaic[6–8] and photodetection devices[9], single-photon sources[3, 10], and enhanced biological imaging[11]. Despite this wide interest, imaging these phenomena within the near field of such structures has proven quite challenging.

Super-resolution fluorescence measurements provide the intriguing possibility of directly imaging near-field optical interactions while eliminating the need for either external probes[12–14] (which can perturb the local environment) or electron-beam excitation[15–18] present in other methods. Previous measurements have generally examined plasmonic properties using dye functionalized onto the surface of metallic nanostructures[101, 20–22], diffusing at low densities around a hotspot[309] or immobilized in a plasmonic lattice[24]. These studies, however, do not map the near-field interactions away from the surface of a single structure. Furthermore, these techniques have not been demonstrated for semiconductor structures, likely because the lower interaction strength and higher absorption necessitates large sampling ensembles, higher signal-to-noise ratios or both.

Here we demonstrate a super-resolution technique utilizing photo-activated localization microscopy (PALM) of fluorophore molecules in a liquid-phase medium to allow mapping of point-emitter–nanostruture interactions with an approximately 25 nm resolution over large (hundreds of square microns) areas. While traditional PALM measurements determine solely the location of molecules on an unknown structure to probe the physical geometry of the sample[25, 310, 74], herein we use a solution of fluorophore dye, providing local measurements at all positions. This is similar to the point accumulation for imaging in nanoscale topography (PAINT) technique [28]. By measuring the modulation of the observable brightness as well as location, we interrogate the near-field optical interactions between quantum emitters and nanostructures, providing direct imaging of the strong, extended coupling between dipole-like sources and nanoscale antennas.

# Results

## Dipole-nanowire interactions

We begin by computationally exploring the interaction of 648 nm wavelength emitters with a 75 nm diameter silicon nanowire, as shown in Fig. A.0.1a-c. These interactions can be calculated using commercial software packages (FEM, FDTD) or, as in this case, solved analytically using a Green's function approach [29]. For this size and wavelength, absorption in the nanowire is minimal and can be neglected (Supplementary Note 1), such that we

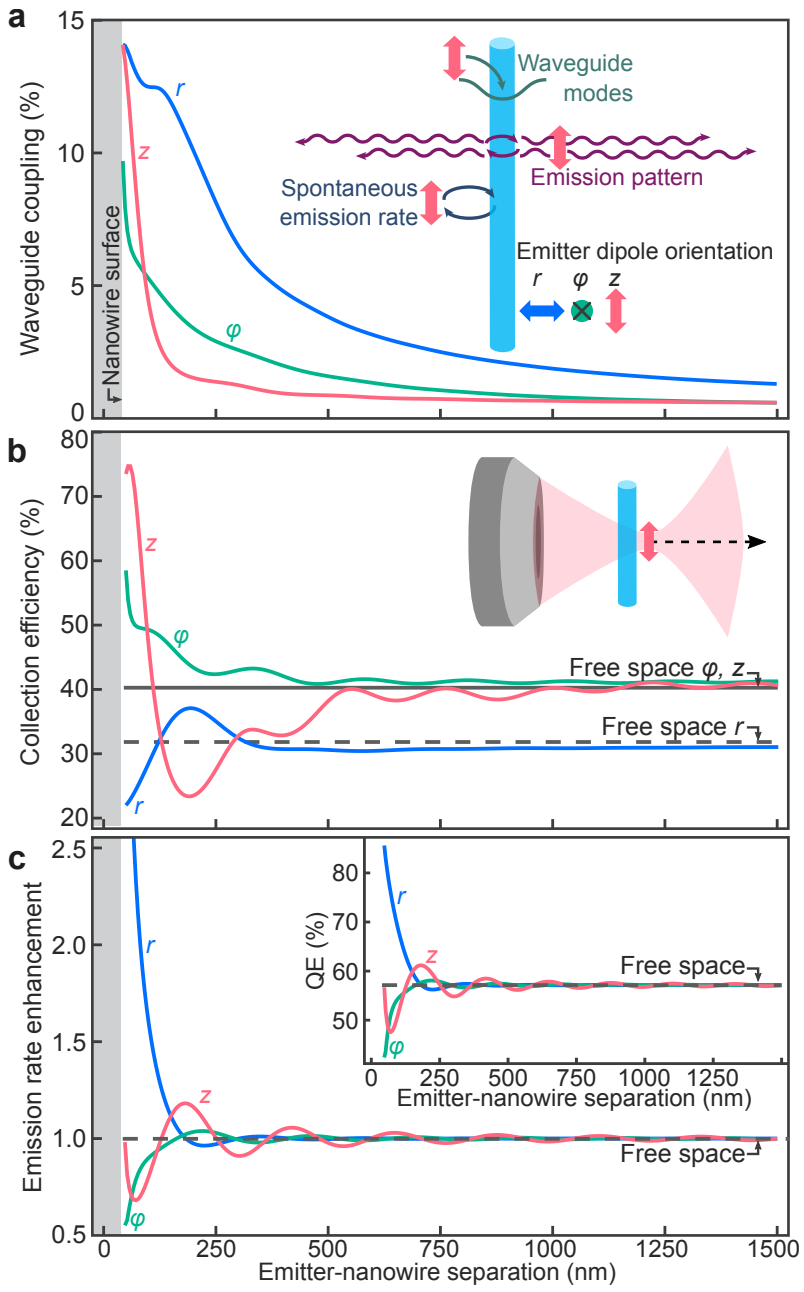


Fig. A.0.1 **Simulations of nanowire–dipole optical interactions.** a, Fraction of light coupling to nanowire waveguide modes, with colors representing the three cardinal dipole orientations. Inset, schematic summarizing dipole-nanowire optical interactions, of coupling to waveguide modes, interference modifying the emission pattern, emission rate modification, and the cylindrical coordinate dipole orientations. b, Collection efficiency, measured as the fraction of light emitted in an $\sim 75^\circ$ half-angle cone relative to the full sphere, corresponding to the collection of a 0.97 numerical aperture objective lens, compared to free space dipole emission (solid and dashed black lines). Inset, diagram depicting the simulation. c, Emission rate enhancement relative to the emitter in free space. Inset, quantum efficiency modification for emitters with a free-space quantum efficiency $\eta_0 = 0.57$. All plots are taken for 648 nm wavelength dipoles with respect to the distance to the centre of a 75 nm diameter silicon nanowire (grey shaded regions), beginning at 5 nm from the surface.

only have to consider the scattering and excitation of waveguide modes. First, Fig. A.0.1a demonstrates the coupling into the $HE_{11}$ waveguide mode of the wire via the extended evanescent field, even for dipoles 1500 nm (40 times the radius) away from the surface of the nanowire. This extended evanescent field is also responsible for the exceptionally large absorption cross sections observed in vertically oriented nanowires, even though those nanowires typically have larger diameters with higher confinement of the guided modes [7, 30]. This extended interaction has been essential particularly for the development of high efficiency photovoltaic and photodetection devices [6–9].

The nanowire also supports localized resonances which strongly scatter[1], leading to interference with the emitter and thus modification of the emission pattern, as visualized in Fig. A.0.1b. Radiation pattern shaping (directivity modification) is of great interest for applications where high yields are required, such as single-photon sources[3, 10]. Fig. A.0.1b shows the fraction of emitted photons collected by a 0.97 numerical aperture (NA) objective, as dipoles move further behind the nanowire (depicted in the inset diagram). We see that contrary to a simple ray-optics view, the collection of emission at small distances behind the nanowire is greatly enhanced, reaching 75%, or almost twice the collection efficiency without the nanowire (dashed and solid grey lines).

Finally, Fig. A.0.1c shows the modification to the total emission enhancement of a dipole emitter by the nanowire acting as a nanoscale antenna. This arises from the nanowire modifying the LDOS in the emitter environment, thereby affecting both the quantum efficiency (QE) of emitters (inset) [31] and the output rate when emitters are excited at saturation. We show herein that all three of these effects influence measurements of the near field of nanowire optical interactions.

## Experimental imaging of interactions

The experimental setup used to image these interactions is summarized in Fig. A.0.2a – silicon nanowires are cast onto a glass substrate, along with gold nanoparticles used for drift correction and orientation (Fig. A.0.2b-d). The fluorophore solution is then cast onto the substrate, and a top glass coverslip is placed to aid focus stabilization and slow solvent evapouration. Caged fluorophores, which are only luminescent after optical activation at higher energies than excitation[32], are used to allow for high total dye concentrations while maintaining a low active density within a single frame required for super-resolution localization. A polarisation filter is inserted in the collection pathway to selectively collect emission from fluorophores oriented either perpendicular (TE) or parallel (TM) to the nanowire axis. PAINT-intensity maps are computed as the average photons per emission event detected, averaged in 25 nm square bins (Supplementary Note 2). Additionally, control

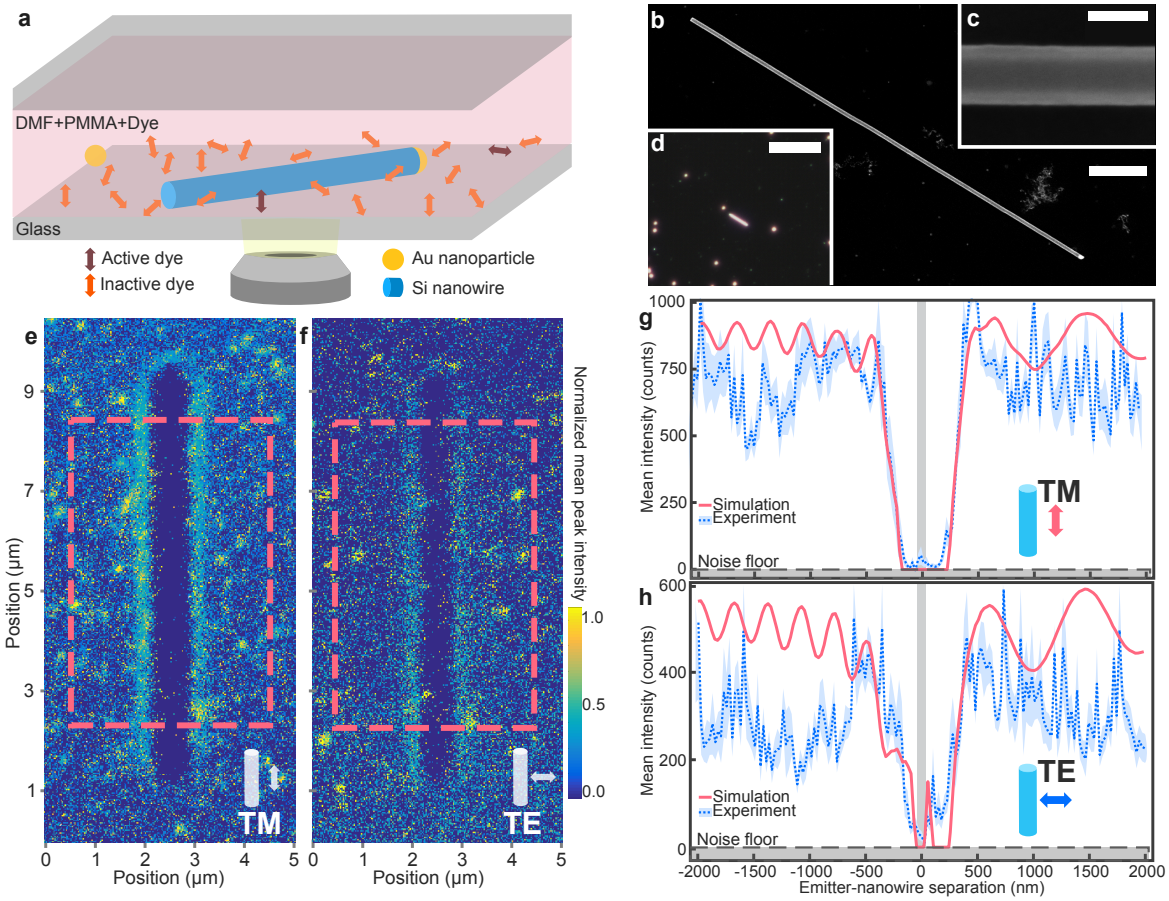


Fig. A.0.2 **Super-resolution-intensity nanowire measurements.** a, Schematic representation of experimental setup, showing nanowire surrounded by fluorophore dye in a solution of poly(methyl methacrylate) (PMMA) and dimethylformamide (DMF), on an inverted microscope. b, Scanning electron micrograph of the investigated silicon nanowire (scale bar = 1 μm), with c, inset high resolution image of the smooth wire surface, and ∼75 nm diameter (scale bar = 70 nm), and d, dark field optical image of the investigated wire, with surrounding gold nanoparticles visible (scale bar = 20 μm). e, f, 2-dimensional super-resolution fluorescence intensity plots of TM and TE fluorescence polarisation, respectively, with a 25 nm square bin averaging. g, h, Corresponding line traces of regions denoted by the dashed red boxes in e & f, showing the mean intensity in counts of the fluorescence measured until bleached. Simulated traces are overlaid, combining analytical calculations of waveguide coupling, emission rate enactment, directivity modification, point spread function distortion and laser non-uniformity. The vertical grey shaded region depicts the physical nanowire diameter, while the horizontal dashed line corresponds to the noise floor fit in our simulations. The emitter-nanowire separation is measured from the centre of the nanowire. The blue shaded region corresponds to standard error of the mean of the integrated rows.

measurements on silicon oxide nanowires are performed to ensure the measured effects are purely optical and not due to spatial variations in dye concentration from the presence of the structure (Supplementary Note 3).

In the 2D plots in Fig. A.0.2e,f (showing TM and TE collection polarisations, respectively), we show the obtained PAINT-intensity maps of our nanowire-fluorophore interactions. The large dark regions surrounding the nanowire location make it immediately apparent that the interactions exist at scales far exceeding the nanowire diameter. Bright spots are also visible in these plots, likely due to fluorphore clustering – while we remove the most extreme clustering events during the data processing, the cut-off is somewhat arbitrary and so only events far outside the mean (four standard deviations; Supplementary Note 2) are removed. The influence of this clustering is negligible when averaged between rows, and so to better visualize the responses we show line scans integrated over the indicated dashed regions.

The line scans in Fig. A.0.2g,h clarify the large trough of reduced intensity around the wire location, spanning $\sim 13\times$ the nanowire diameter (shown as the grey vertical shaded region), providing a direct visualization of the nanowire antenna effect. We observe an asymmetric recovery from the extended trough, with the negative positional values expressing a reduced slope relative to the positive positions. Additionally, there is a marked difference between the two polarisations, particularly in the existence of a peak within the trough in the TE polarisation. While it may be tempting to immediately attribute the presence of the substantial decrease in fluorescence intensity to excitation of waveguide and resonant modes in the nanowire, the multitude of possible phenomena discussed in Fig. A.0.1 suggests that the true interactions are more complex.

## Modeling of interactions

In addition to the three main interactions discussed in Fig. A.0.1, we incorporate a calculation of the dependence of the field from the laser excitation on the location relative to the nanowire – this occurs from interference of the excitation laser with the field scattered by the nanowire. Additionally, the laser enters the experimental setup at an $\sim 30^{\circ}$ angle to limit back reflections, concomitantly producing an asymmetric response on the left and right sides of the wire. Furthermore, the directivity modifications shown in Fig. A.0.1b influence our experimental measurements not only as a modification of the observable peak brightness, but also as a distortion of the point spread function (PSF), shifting the peak location from the true fluorophore position away from the wire when close to the wire surface. These effects are also calculated and included in our simulations (Supplementary Note 4).

By first comparing our simulated and experimentally measured trends in detected brightness as a function of the emitter position relative to the nanowire centre, as shown in Fig.

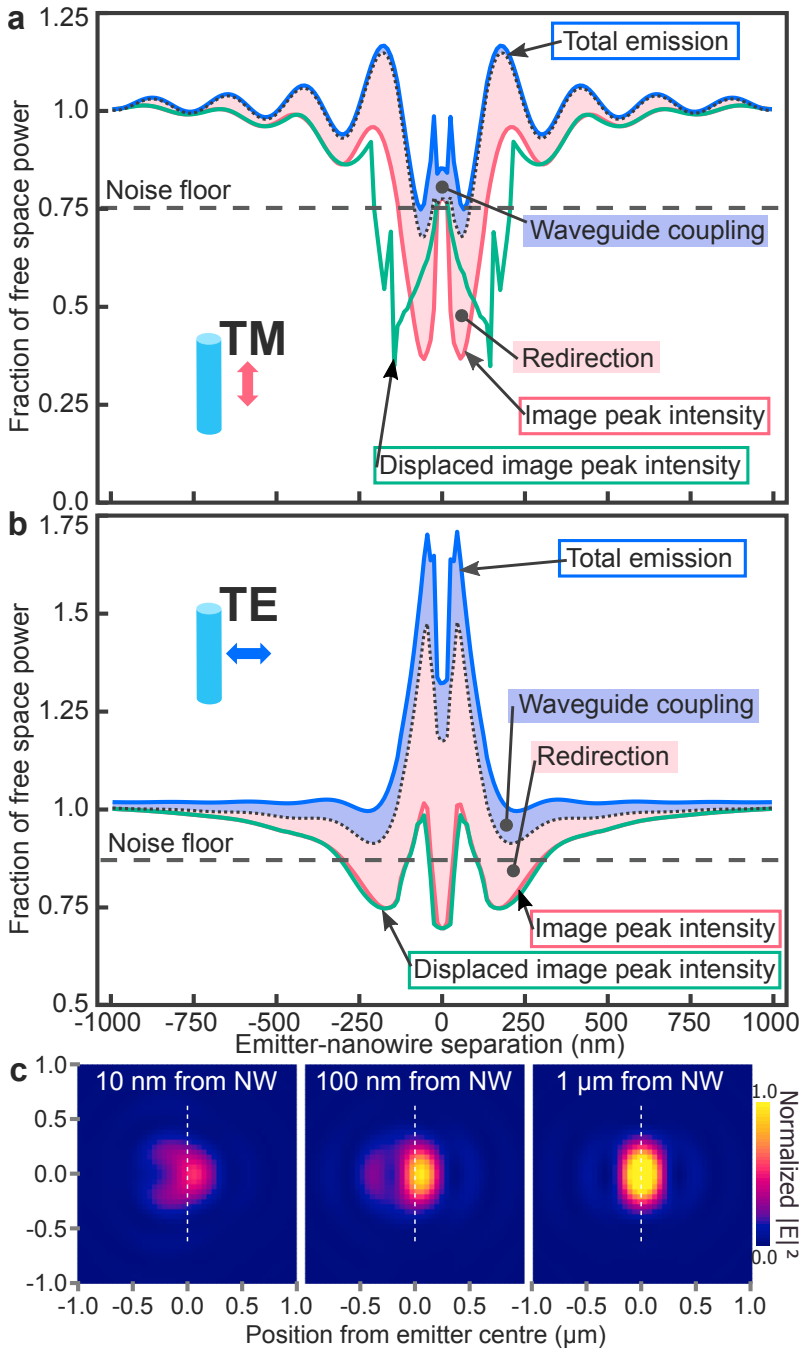


Fig. A.0.3 **Deconvolved power distributions.** Simulated power distributions for TM, a, and TE, b, polarisations. Neglecting the excitation laser influence for clarity, fluorophore total emission due to enhancement (or quenching) by the wire (blue line) and the observable peak intensity of a Gaussian fit to the point spread function (PSF) image (pink line) are shown. The power difference between these two traces is shown divided between the coupling to waveguide modes and the redirection of emission by scattering (blue and pink shaded regions, respectively). The above are taken with respect to the true dipole positions, with the final bottom green trace showing the locations when the PSF displacements are included. c, Image plane simulations of PSF modification by interaction of a $z$ dipole with the nanowire, showing peak displacement from the true dipole position (white line) as well as geometric distortions (which also decrease the peak intensity).

A.0.2g & h, we can establish the validity and completeness of our theoretical models. In Fig. A.0.2g,h, we incorporate a single fitting parameter between our model and experimental data, equivalent to a noise floor – this is necessary as sufficiently dim fluorescence events calculated by our model would not be possible to localize in an experiment. After the determination of the centre position and noise floor fit between the TM polarisation model and experimental data, these parameters are used (not re-fit) for running the simulation of the TE polarisation. This ensures that the only difference between the two simulations is indeed the polarisation being simulated. Doing so, we observe good agreement between main features of the dim regions – the width, asymmetric steepness of the trough sides, and the periods of the oscillations on negative-valued side of the wire (327 nm & 359 nm experimental for TM and TE, respectively, versus 320 nm in the simulation, as determined through Fourier analysis; Supplementary Fig. 3a). We additionally recover the observed peak within the trough in this polarisation, and observe evidence of the flat region at approximately -200 nm in the TE polarisation, further supporting the validity of the simulations to capture the rich interactions present in the experimental traces. The confirmation of such features also demonstrates the necessity of super-resolution measurements – the absence of such features (as in a diffraction-limited measurement, Supplementary Note 5) would preclude any assurance of the agreement with theory.

## Deconvolution of interactions

The observed agreement between the simulations and experiments furthermore allows for the extraction of parameters not directly measurable experimentally (for example, waveguide mode excitation) with a reasonable level of confidence. To this end we compute the power distribution into the various channels (emission modification, waveguide mode excitation and collected emission) present in our measurements.

In Fig. A.0.3, we show the relative contribution of the modelled optical phenomena to our PAINT-intensity traces. In these calculations we begin with the total emission from a dipole as modified by the proximity to the nanowire (top blue trace). We then remove the power coupled into waveguide modes (blue shaded region) followed by the power not collected due to redirection (pink shaded region), resulting in the red trace. The influence of the image distortion causing displacement of the PSF from the true dipole location is finally included in the bottom green trace. For clarity we discount the influence of the laser excitation non-uniformity in the analysis here.

We first note that the emission of the dipole due to the LDOS enhancement from the wire (modifying the quantum efficiency and rate of emission) is substantially different between the two polarisations – the TM polarisation shows an oscillating behaviour from the vertically-

oriented ($z$) dipoles expressing a Drexhage-like effect in emission[13], as is also observed in Fig. A.0.1c. The TE polarisation, however, shows a strong enhancement of emission, largely due to the substantial LDOS enhancement of radially-oriented ($r$) dipoles near the wire.

While it is observable that waveguide coupling of the dipole emission (displayed as the dark blue shaded region in Fig. A.0.3a & b) is not the dominant influence in the observed interactions, the contribution is still important; the TM polarised collected emission (corresponding to $z$-oriented dipoles in Fig. A.0.1a) shows strong coupling immediately adjacent to the wire, with the contribution falling off rapidly beyond $\sim$100 nm. Conversely, for the TE polarised collected emission (largely $r$-oriented dipoles in Fig. A.0.1a), the waveguide coupling is notable even beyond 1000 nm. The excitation of Mie resonances (responsible for both broadening and distorting/displacing the PSF of the image) contributes more notably to the reduction in the peak intensity (pink shaded area in Fig. A.0.3a & b).

Additionally, while large displacements influence the green trace in the TM polarisation quite significantly, they play almost no role in the final trace of the TE polarisation, indicating that polarisation control can be useful in limiting the observation of PSF distortions (depicted in Fig. A.0.3c) in such measurements where this influence is not of interest. Recent work has also shown metasurfaces to have promising applications for the limitation of PSF shape influences [33]. Alternatively, techniques could be employed to simultaneously measure the position and orientation of the imaged dipoles as demonstrated previously [34], thereby allowing additional control over the imaged field components and orientations.

# Discussion

These measurements provide new experimental evidence of the nature of the long range interactions present between dipole-like emitters and dielectric nanostructures, and offer a novel characterization method to quantify these interactions at high resolution, without the need for external near-field probes.

Here, we measure the ensemble of interactions between fluorophores and nanostructures. Further improvements to the method, particularly those discussed in limiting PSF distortions as well as combinations with lifetime measurements[13, 24]. Combined, these methods could permit detailed mapping of individual optical components, providing a valuable new tool in understanding the near-field environments of nanophotonic objects.

# Methods

## Sample preparation

The silicon nanowires are grown epitaxially on a silicon substrate by a vapour-liquid-solid growth mechanism using an atmospheric-pressure chemical vapour deposition system. 100 nm gold colloids (BBI Solutions) were used as catalysts. The growth was conducted at 850°C for 20 minutes with silicon tetrachloride ($SiCl_4$) as the precursor. The carrier-gas flows during growth are Ar=95 sccm and $H_2$=30 sccm, while 19 sccm Ar gas flows directly through the silicon tetrachloride precursor bubbler (held at 0°C in a temperature-controlled bath).

The clean coverslips are prepared by soaking overnight in Hellmanex detergent, sonicating for 15 min in each acetone and ethanol, and soaking in 50% hydrogen peroxide overnight, with rinsing in Milli-Q purified water after each step, and finally drying in nitrogen. Wires are exfoliated in isopropanol and cast on the clean glass coverslips. Fiducial marks are scribed into the sample for rough wire position determination, and additional gold nanoparticles are cast as well for drift correction and to aid in fine positional wire location, between super-resolution and SEM measurements.

## Fluorophore solution preparation

Solutions of 0.01 g $L^{-1}$ CAGE 635 fluorophore (Abberior) in dimethylformamide (DMF) with a 5 %wt poly(methyl methacrylate) (PMMA) 395,000 molecular weight polymer (Sigma-Aldrich) are mixed immediately prior to imaging, to limit dye clustering. PMMA is used to increase solution viscosity, limiting dye desorption and (rotational) diffusion, and ensuring collection during full dye bleaching. The solution dye concentration is calibrated to remain low enough to ensure only single localizations within a diffraction limited spot, but high enough to allow for dense sampling over the area of interest within a reasonable timeframe ($\sim$30 minute measurements) before clustering or solvent evapouration become overly problematic.

25 µL of the dye solution is sandwiched between two clean glass coverslips to limit evapouration of the DMF solvent and improve stability of the instrument's active focus stabilization system. The dye forms a layer approximately 1 µm in thickness, as measured by the calibrated focus system in the microscope, far larger than the depth of field of the employed objective, and thus has no influence on the localization.

## Super-resolution measurements

The measurement setup consists of a Nikon Ti Eclipse inverted microscope with an oil (n=1.515) immersion objective of NA=1.49 (although the usable NA is likely closer to 1.46)[35], and an electron-multiplying charge-coupled device (EMCCD) camera (Andor iXon Ultra 897). A custom-made polarisation filter can be optionally inserted to limit collection polarisation to a particular orientation with respect to the wire.

Dye molecules are activated by a 405 nm wavelength activation laser, at a power of $\sim$40 W $cm^{-2}$, and pumped until bleached with a 640 nm excitation laser, at a power of $\sim$400 W $cm^{-2}$. Laser powers are chosen to allow a small number of dye molecules (much fewer than 1 per square micron) to be activated in any given frame, while pumping most active dye molecules until bleached within the single frame integration time of 95 ms. Emissions lasting multiple frames are merged to measure total brightness. Band pass filters are placed in the collection path to limit detection of the activation and excitation lasers, while still collecting the 648 nm peak activated dye emission.

The low localization uncertainty (50 $nm^2$ mean squared error) yet high mean-square displacement when free in solution (10 $\mu m^2$ in a 95 ms frame), implies that events are localized only when stochastically adsorbed onto a surface (Supplementary Note 6).

Measurements consist of $\sim$30,000 frames, corresponding to $\sim$300,000 localization events within an $\sim$15x15 $\mu m^2$ area of interest around a nanowire. After collection of the image frames, the PSF localization is performed using the ThunderSTORM v1.3 package [79]. After all optical measurements are complete (to prevent carbon contamination), samples are imaged in a scanning-electron microscope to determine the precise geometry of the interrogated structure. These measurements are used in the analytical modelling of the system.

For additional details on the data processing and analysis see Supplementary Note 2.

## Analytical model

In order to determine the contributions of the optical effects in our system we create a semi-empirical Monte-Carlo simulation of imaging conditions: A 1D array of 300,000 virtual fluorophores is established, with their position uniformly distributed along the surface of the substrate and nanowire (in agreement with the larger number of localizations around the wire observed in control measurements; see following section). For each fluorophore a random dipole orientation is assigned.

Analytical Green's function and Lorenz-Mie theory calculations are used to deconvolve the possible interactions. Specifically, we incorporate the excitation power of the laser (and its interference with the nanowire), the quantum efficiency and local density of optical states (LDOS) enhancement of the fluorophore by the nanowire, the absorption in the wire, the scattering/collection modification, and the distortion of the PSF allowing possible displacements in the imaged *vs.* true location of the fluorophore. All calculations are implemented in the Julia language [37].

For additional details on the simulations and calculation methods, see Supplementary Note 4.

## Data availability

The data that support the findings of this study are available from the corresponding author upon reasonable request.

# References


[1] Bohren, C. F. & Huffman, D. R. *Absorption and Scattering of Light by Small Particles* (Wiley-VCH Verlag GmbH, 1998).

[2] Snyder, A. W. & Love, J. *Optical Waveguide Theory*. Science paperbacks (Springer, 1983).

[3] Claudon, J. *et al.* A highly efficient single-photon source based on a quantum dot in a photonic nanowire. *Nat. Photonics* **4**, 174–177 (2010).

[4] Bao, J., Zimmler, M. A., Capasso, F., Wang, X. & Ren, Z. F. Broadband ZnO single-nanowire light-emitting diode. *Nano Lett.* **6**, 1719–1722 (2006).

[5] Duan, X., Huang, Y., Agarwal, R., Lieber, C. M. C. & Fast, C. G. Single-nanowire electrically driven lasers. *Nature* **421**, 241–245 (2003).

[6] Garnett, E. & Yang, P. Light trapping in silicon nanowire solar cells. *Nano Lett.* **10**, 1082–1087 (2010).

[7] Krogstrup, P. *et al.* Single-nanowire solar cells beyond the Shockley–Queisser limit. *Nat. Photonics* **7**, 306–310 (2013).

[8] Wallentin, J. *et al.* InP Nanowire Array Solar Cells Achieving 13.8% Efficiency by Exceeding the Ray Optics Limit. *Science* **339**, 1057–1060 (2013).

[9] Hayden, O., Agarwal, R. & Lieber, C. M. Nanoscale avalanche photodiodes for highly sensitive and spatially resolved photon detection. *Nat. Mater.* **5**, 352–356 (2006).

[10] Babinec, T. M. *et al.* A diamond nanowire single-photon source. *Nat. Nanotechnol.* **5**, 195–199 (2010).

[11] Shalek, A. K. *et al.* Vertical silicon nanowires as a universal platform for delivering biomolecules into living cells. *Proc. Natl. Acad. Sci. U. S. A.* **107**, 1870–5 (2010).

[12] Ditlbacher, H. *et al.* Silver nanowires as surface plasmon resonators. *Phys. Rev. Lett.* **95**, 1–4 (2005).

[13] Frimmer, M., Chen, Y. & Koenderink, a. F. Scanning emitter lifetime imaging microscopy for spontaneous emission control. *Phys. Rev. Lett.* **107**, 123602 (2011).

[14] le Feber, B., Rotenberg, N. & Kuipers, L. Nanophotonic control of circular dipole emission. *Nat. Commun.* **6**, 6695 (2015).

[15] Vesseur, E. J. R., De Waele, R., Kuttge, M. & Polman, A. Direct observation of plasmonic modes in Au nanowires using high-resolution cathodoluminescence spectroscopy. *Nano Lett.* **7**, 2843–2846 (2007).

[16] Xue, H. *et al.* Probing the strain effect on near band edge emission of a curved ZnO nanowire via spatially resolved cathodoluminescence. *Nanotechnology* **21**, 215701 (2010).

[17] Brenny, B. J. M. *et al.* Directional Emission from Leaky and Guided Modes in GaAs Nanowires Measured by Cathodoluminescence. *ACS Photonics* **3**, 677–684 (2016).

[18] Coenen, T. *et al.* Nanoscale Spatial Coherent Control over the Modal Excitation of a Coupled Plasmonic Resonator System. *Nano Lett.* **15**, 7666–7670 (2015).

[19] Zhou, X. *et al.* Quantitative super-resolution imaging uncovers reactivity patterns on single nanocatalysts. *Nat. Nanotechnol.* **7**, 237–41 (2012).

[20] Lin, H. *et al.* Mapping of surface-enhanced fluorescence on metal nanoparticles using super-resolution photoactivation localization microscopy. *ChemPhysChem* **13**, 973–981 (2012).

[21] Blythe, K. L., Mayer, K. M., Weber, M. L. & Willets, K. Ground state depletion microscopy for imaging interactions between gold nanowires and fluorophore-labeled ligands. *Phys. Chem. Chem. Phys.* **15**, 4136–4145 (2013).

[22] Wertz, E., Isaacoff, B. P., Flynn, J. D. & Biteen, J. S. Single-Molecule Super-Resolution Microscopy Reveals How Light Couples to a Plasmonic Nanoantenna on the Nanometer Scale. *Nano Lett.* **15**, 2662–2670 (2015).

[23] Cang, H. *et al.* Probing the electromagnetic field of a 15-nanometre hotspot by single molecule imaging. *Nature* **469**, 385–388 (2011).

[24] Guo, K., Verschuuren, M. A. & Koenderink, A. F. Superresolution imaging of the local density of states in plasmon lattices. *Optica* **3**, 289 (2016).

[25] Hess, S. T., Girirajan, T. P. K. & Mason, M. D. Ultra-high resolution imaging by fluorescence photoactivation localization microscopy. *Biophys. J.* **91**, 4258–4272 (2006).

[26] Rust, M. J., Bates, M. & Zhuang, X. W. Sub-diffraction-limit imaging by stochastic optical reconstruction microscopy (STORM). *Nat. Methods* **3**, 793–795 (2006).

[27] Betzig, E. *et al.* Imaging intracellular fluorescent proteins at nanometer resolution. *Science* **313**, 1642–1645 (2006).

[28] Sharonov, A. & Hochstrasser, R. M. Wide-field subdiffraction imaging by accumulated binding of diffusing probes. *Proc. Natl. Acad. Sci. U. S. A.* **103**, 18911–18916 (2006).

[29] Tai, C.-T. *Dyadic Green functions in electromagnetic theory* (IEEE Press, 1994).

[30] Snyder, a. W. Surface Waveguide Modes Along a Semi-Infinite Dielectric Fiber Excited by a Plane Wave. *J. Opt. Soc. Am.* **56**, 601–606 (1966).

[31] Novotny, L. & Hecht, B. *Principles of Nano-Optics* (Cambridge University Press, 2006).

[32] Politz, J. C. Use of caged fluorochromes to track macromolecular movement in living cells. *Trends Cell Biol.* **9**, 284–287 (1999).

[33] Backlund, M. P. *et al.* Removing orientation-induced localization biases in single-molecule microscopy using a broadband metasurface mask. *Nat. Photonics* (2016).

[34] Gould, T. J. *et al.* Nanoscale imaging of molecular positions and anisotropies. *Nat. Methods* **5**, 1027–1030 (2008).

[35] Kurvits, J. A., Jiang, M. & Zia, R. Comparative analysis of imaging configurations and objectives for Fourier microscopy. *J. Opt. Soc. Am. A* **32**, 2082 (2015).

[36] Ovesny, M., Krizek, P., Borkovec, J., Svindrych, Z. & Hagen, G. M. ThunderSTORM: A comprehensive ImageJ plug-in for PALM and STORM data analysis and super-resolution imaging. *Bioinformatics* **30**, 2389–2390 (2014).

[37] Bezanson, J., Karpinski, S., Shah, V. B. & Edelman, A. Julia: A fast dynamic language for technical computing. *Preprint at http://arxiv.org/abs/1209.5145* (2012).

# Acknowledgments

The authors thank M. Kamp and A.F. Koenderink (AMOLF) for helpful discussions. This work is part of the research program of the Foundation for Fundamental Research on Matter (FOM), which is part of The Netherlands Organization for Scientific Research (NWO). The authors acknowledge financial support from the European Research Council under the European Union's Seventh Framework Programme (FP/2007-2013)/ERC Grant Agreement No. 337328, "NanoEnabledPV", and by a TKI instrumentation grant together with FEI.


# Author contributions

E.C.G., E.J., J.S. and T.S.S. designed the experiments. E.J. and J.S. carried out the experiments. J.W. provided the nanowire materials. E.J. and S.A.M. designed and carried out the simulations. E.J. processed, analyzed, and interpreted the data. All authors contributed to the writing of the manuscript.

# Competing financial interests

The authors declare no competing financial interests.

# Summary

Bacteria are amongst the smallest known living organisms and yet they carry out an incredible variety of different functions and are able to respond to a large variety of different external stimuli. Growing evidence is suggesting that specific proteins and sub-cellular components (e.g. the nucleoid) need to be highly organized both on the membrane and inside the cellular volume in order to carry out vital tasks like cell replication or chemotaxis and to respond to external changes in the environment. In this thesis I investigated experimentally the spatial organization of different sub-cellular components (nucleoid) and protein species (NAPs and chemoreceptors) and its importance for physiological processes inside living bacterial cells. Most of the experiments presented here are carried out in living cells, and our results thus provide insights also into the spatio-temporal organization and the dynamics of the response to controlled perturbations.

The work introduced in Chapter 4 presents novel results on the dynamic organization of membrane chemoreceptor clusters in response ligand stimulation. Opposing results are found in the literature about cluster stability upon stimulation: experiments employing fluorescent fusion and cryo-EM reported no change in the global and local arrangement of chemoreceptors upon sensory stimulation while independent results exploiting immunofluorescent labeling showed a diffuse staining of the plasma membrane upon ligand stimulation, interpreted to mean chemoreceptor clusters are destabilized by attractant binding. In this section we utilized two orthogonal approaches (PALM imaging and particle tracking) to show that the stability of chemoreceptor clusters can actually be altered by cognate ligand stimulation (e.g. Tar clusters are destabilized by methyl-aspartate stimulation and Tsr clusters by serine) without changing the local arrangement of the receptor lattice. I discuss the implications of such destabilization in relation to signal amplification, chemotactic adaptation, membrane diffusion and crowding: we found that both the cluster size and the mobility of chemoreceptor clusters are modulated shortly after and upon prolonged ligand stimulation in an adaptation dependent fashion.

In Chapter 5 I focused on nucleoid morphology and size in relation to intracellular crowding, investigating the dynamic response of the nucleoid under intracellular crowding

perturbations. Crowding modulations have been shown to modulate in turn the size of isolated nucleoids and to compress nucleoid inside cells imaged after fixation but the importance of crowding in the dynamic spatio-temporal organization of the nucleoid remain elusive. I present a set of pioneering experiments where thousands of fluorescently labeled nucleoids were imaged in living *E. coli* under osmotic perturbations of different magnitudes (which have been shown to perturb intracellular crowding), showing that nucleoid size anticorrelates with crowding levels measured by a FRET crowding sensor expressed in living cells. I discuss the importance of intracellular crowding in nucleoid spatio-temporal organization suggesting that nucleoid size and morphology is determined by the concerted action of passive (e.g. crowding) and active processes.

To produce the data discussed in chapter 4, I developed a novel tracking technique that we named "Localized-Photo-Activation Single-Particle Tracking" (LPA-SPT). LPA-SPT makes use of photoswitchable fluorophores and a focused activation beam to allow for tracking of chemoreceptor clusters in the crowded membrane environment. This technique together with the extended PALM setup and protocol for chemoreceptor imaging at high spatial resolution, are described in Chapter 2. The data presented in Chapter 5 was acquired via an adapted "mother machine" setup, allowing 4-channel imaging and rapid medium switching. Our mother machine setup is described in Chapter 3, together with a novel DNA label (H-NS-dbd) based on the nucleoid-associated protein H-NS, that can be expressed inside living cell. Chapter 3 also presents a set of pioneering nucleoid imaging experiments utilizing a non-perturbative Fluorescent-Repressor-Operator-System (FROS) and PALM (both 3D and 2D). Appendix A is the result of a collaboration with Eric Garnett's group at AMOLF where I designed and executed the experimental part (extended PALM protocol by means of caged fluorophores) together with E. Johlin.

Taken together, the results presented in this thesis resolve a long-standing controversy in the chemotaxis field about stability of clusters of chemoreceptors: ligand binding can destabilize clusters not at the level of the receptor lattice structure but more at the cluster size level. Also, this work gives new insights into the role of intracellular crowding inside living cells, suggesting that crowding is an important but not the sole determinant in shaping nucleoid morphology, size and dynamics. We thus provide more experimental evidences for the importance of spatio-temporal organization of proteins and sub-cellular components inside living bacteria. In addition, a set of novel techniques and extensions/additions to state of the art microscopy techniques are presented. This imaging toolkit will be used in the future to investigate further the dynamics of receptor clusters under ligand stimulation as well as the relationship between crowding, nucleoid morphology, growth conditions and gene expression patterns.

# Acknowledgements

First of all I would like to thank my Family.

Family is fundamental for most Italian people and I am no exception. Thanks a lot Mamma, Babbo e Duccio for all your support and presence and help in all difficult, boring and challenging passages of these past 5 years: my moving to the Netherlands, my health, my PhD. Thanks for being so great, open and understanding. It feels so good to have you at the deepest core of my Family. Thanks a lot to Zia and Mauro, always present as well, always great and stimulating, always interested in my adventures abroad and always ready to prepare mushrooms or fish delicacies (e.g. "zuppa di femminelle") whenever I was back home. Thanks also to Gabriella who became with time another great older sister.

Most people when thinking about their family they only include relatives with whom they have a blood binding. But I think that sometimes binding between people that are not related by lineage can be even stronger than binding with (some) relatives. I personally mean "Family" as a more extended concept, including all the persons that I feel really close, that I can trust and with whom I happily journeyed through segments of life. So big thanks to my extended family that supported me, made me laugh, taught me things and with whom I had good times in Amsterdam, starting of course from the Levantkade crew: Pepe, Oreste and Michele co-founders of Levantkade 2.0, Titta and Tark that really "take at good", and last but not least Shantiliga with her fluffy R and her exploding positive energy. Together we built an amazing reality in that crazy flat. We will never foget these years <3 nor the last few months with Mae (Fabien). Very important members of the Family are Steven, that helped me so many times and from whom I learned so many things e.g. how to be a social-party animal, Jenny with her explosive laughter, her never ending inner fire that keeps the positiveness burning and her honesty and her true and empathic soul. Special thanks to Bertus companion of music and music technology, Ben one of the most stylish and beautiful soul I had the luck to meet in Amsterdam, Adythia my table-tennis guru that introduced me to mother India via his incredible wedding, Andrea "compagno di sventure, avventure, di ping-pong e di bevute", Giacometto with whom I rapidly developed a deep soul binding in at least three distant parts of the world, Paul who made me laugh so hard but also proved himself a trustful man of word

and honor. Thanks also to all the girls that lived in my heart during these years, in particular Flaminia, Sunny, Kate and now.. Taraneh. You (cucciola) are filling and fulfilling my mind, body and soul.

Some really special thanks to all the special colleagues and people I met through my PhD. Starting from people that were and are at AMOLF I want to thank colonel Agata and her super funny humor, Parisa and her amazing smile, energy and positiveness, Giulia for sharing music, "cannette" and a little piece of our hearts, Chetan for all the deep conversations and for being the best student I could possibly hope to supervise, Wiebe for being my smoking buddy even under the worse Dutch weather and for his stories, Clyde for being so happy all the time and for letting me know amazing places and people outside AMOLF, Jasmijne, Maga, Jeanette, Giorgio, Marco, Nicola and Federica. You made AMOLF a much more enjoyable place for me and helped going through hard times by chatting and venting at the coffee corner and outside AMOLF. Thanks also to Yuval, Marijolein, Martijn, Vanda, Bart, David, George and all the people I shared long hours in the wet lab. Last but not least a big thanks to Francois who without any doubt is the person who taught me and from whom I learned the most about how to do Science. Thanks also to the ARCNL crew, in particular to Cristina and Alessandro and to the VU crew, in particular Luca, Felix and Fabio. Was so nice to share retreats and conferences with you guys.A very special thank to all the support staff at AMOLF in particular Marko, Marco, Carl, Wiebe, Erik, Wouter, and all the other people without whom I would have never be able to accomplish my PhD.

Thanks Tom for supervising and guiding my work as a PhD, thanks to Remus and Fred for collaborating together (it was really fun and I learned a lot of biology form you), thanks to Suckjoon for the really inspirational and instructive period at UCSD, and thanks to all the great Suckjoon's lab member: J.T., Fangwei, Dongyang, Sarah and Guilleaume (thanks for all your help inside and outside the lab). A very special thanks to Bela for kicking off together the Python team at AMOLF and for all the great support.

Last but not least, thanks to all the past and present lab members: first of all Johannes (my brother in Science) we have grown a lot together at AMOLF from the time we were duckling Francois, Sebastian with his eccentric humor, Katja one of the smartest and toughest of us, Keita the kindest and most determined person I know, Stephen, Ercag, Mathijs the runner, Steffen, Victor and his amazing fungi and Simone for all the help and support in the wet lab.

# References


[1] Ron Milo. What is the total number of protein molecules per cell volume? A call to rethink some published values. *BioEssays*, 35(12):1050–1055, 2013.

[2] Howard Gest. The discovery of microorganisms by Robert Hooke and Antoni van Leeuwenhoek, Fellows of The Royal Society. *Notes Rec. R. Soc.*, 58(2):187–201, 2004.

[3] Malathy Krishnamurthy, Richard T Moore, Sathish Rajamani, and Rekha G Panchal. Bacterial genome engineering and synthetic biology: combating pathogens. *BMC Microbiol.*, 16(1):258, 2016.

[4] Ben N G Giepmans, Stephen R Adams, Mark H Ellisman, and Roger Y Tsien. The fluorescent toolbox for assessing protein location and function. *Science*, 312(5771):217–24, apr 2006.

[5] Derek Greenfield, Ann L McEvoy, Hari Shroff, Gavin E Crooks, Ned S Wingreen, Eric Betzig, and Jan Liphardt. Self-organization of the Escherichia coli chemotaxis network imaged with super-resolution light microscopy. *PLoS Biol.*, 7(6):e1000137, jun 2009.

[6] Edgar Huitema, Sean Pritchard, David Matteson, Sunish Kumar Radhakrishnan, and Patrick H. Viollier. Bacterial birth scar proteins mark future flagellum assembly site. *Cell*, 124(5):1025–1037, 2006.

[7] Hubert Lam, Whitman B. Schofield, and Christine Jacobs-Wagner. A landmark protein essential for establishing and perpetuating the polarity of a bacterial cell. *Cell*, 124(5):1011–1023, 2006.

[8] Anuradha Janakiraman and Marcia B Goldberg. From the Cover: Evidence for polar positional information independent of cell division and nucleoid occlusion. *Pnas*, 101(3):835–840, 2004.

[9] David H. Edwards and Jeffery Errington. The Bacillus subtilis DivIVA protein targets to the division septum and controls the site specificity of cell division. *Mol. Microbiol.*, 24(5):905–915, 1997.

[10] David Z. Rudner and Richard Losick. Protein subcellular localization in bacteria. *Cold Spring Harb. Perspect. Biol.*, 2(4):1–14, 2010.

[11] Achillefs N. Kapanidis, Stephan Uphoff, and Mathew Stracy. Understanding Protein Mobility in Bacteria by Tracking Single Molecules. *J. Mol. Biol.*, 2018.

[12] Susan M. Sullivan and Janine R. Maddock. Bacterial division: Finding the dividing line. *Curr. Biol.*, 10(6):249–252, 2000.

[13] Sonja Schulmeister, Michaela Ruttorf, Sebastian Thiem, David Kentner, Dirk Lebiedz, and Victor Sourjik. Protein exchange dynamics at chemoreceptor clusters in Escherichia coli. *Proc. Natl. Acad. Sci. U. S. A.*, 105(17):6403–6408, 2008.

[14] Sattar Taheri-Araghi, Serena Bradde, John T. Sauls, Norbert S. Hill, Petra Anne Levin, Johan Paulsson, Massimo Vergassola, and Suckjoon Jun. Cell-size control and homeostasis in bacteria. *Curr. Biol.*, 25(3):385–391, 2015.

[15] Jacques Monod. a Certain Number. *Annu. Rev. M*, 3(Xl):371–394, 1949.

[16] Margolin W. Ftsz and the division of prokaryotics cells and organelles. *Nature reviews Molecular cell biology.*, 6:862–871, 2005.

[17] C A Hale, H Meinhardt, and P A de Boer. Dynamic localization cycle of the cell division regulator MinE in Escherichia coli. *EMBO J.*, 20(7):1563–72, 2001.

[18] Barbara Di Ventura and Victor Sourjik. Self-organized partitioning of dynamically localized proteins in bacterial cell division. *Mol. Syst. Biol.*, 7(457):457, jan 2011.

[19] Victor Sourjik and Judith P Armitage. Spatial organization in bacterial chemotaxis. *EMBO J.*, 29(16):2724–2733, 2010.

[20] P. Hammar, P. Leroy, a. Mahmutovic, E. G. Marklund, O. G. Berg, and J. Elf. The lac Repressor Displays Facilitated Diffusion in Living Cells. *Science (80-. ).*, 336(6088):1595–1598, 2012.

[21] Remus T Dame, Olga J Kalmykowa, and David C Grainger. Chromosomal macrodomains and associated proteins: implications for DNA organization and replication in gram negative bacteria. *PLoS Genet.*, 7(6):e1002123, jun 2011.

[22] Joanna Hołówka, Damian Trojanowski, Katarzyna Ginda, Bartosz Wojtaś, Bartłomiej Gielniewski, Dagmara Jakimowicz, and Jolanta Zakrzewska-Czerwińska. HupB Is a Bacterial Nucleoid-Associated Protein with an Indispensable Eukaryotic-Like Tail. *MBio*, 8(6):e01272–17, 2017.

[23] R. Carballido-Lopez. The Bacterial Actin-Like Cytoskeleton. *Microbiol. Mol. Biol. Rev.*, 70(4):888–909, 2006.

[24] Henrik Strahl, Frank Bürmann, and Leendert W Hamoen. The actin homologue MreB organizes the bacterial cell membrane. *Nat. Commun.*, 5:3442, 2014.

[25] George H. Wadhams and Judith P. Armitage. Making Sense of it All: Bacterial Chemotaxis. *Nat. Rev. Mol. Cell Biol.*, 5(December):1024–1037, 2004.

[26] Howard C. Berg and Richard M. Berry. *E. Coli in motion*, volume 58. 2005.

[27] J Adler. A method for measuring chemotaxis and use of the method to determine optimum conditions for chemotaxis by Escherichia coli. *J. Gen. Microbiol.*, 74(1):77–91, 1973.

[28] a. Briegel, X. Li, a. M. Bilwes, K. T. Hughes, G. J. Jensen, and B. R. Crane. Bacterial chemoreceptor arrays are hexagonally packed trimers of receptor dimers networked by rings of kinase and coupling proteins. *Proc. Natl. Acad. Sci.*, 109(10):3766–3771, 2012.

[29] David Kentner, Sebastian Thiem, Markus Hildenbeutel, and Victor Sourjik. Determinants of chemoreceptor cluster formation in Escherichia coli. *Mol. Microbiol.*, 61(2):407–417, 2006.

[30] Victor Sourjik and Howard C Berg. Functional interactions between receptors in bacterial chemotaxis. *Nature*, 428(March):1–4, 2004.

[31] Allison C. Lamanna, George W. Ordal, and Laura L. Kiessling. Large increases in attractant concentration disrupt the polar localization of bacterial chemoreceptors. *Mol. Microbiol.*, 57(3):774–785, 2005.

[32] Motohiro Homma, Daisuke Shiomi, Michio Homma, and Ikuro Kawagishi. Attractant binding alters arrangement of chemoreceptor dimers within its cluster at a cell pole. *Proc. Natl. Acad. Sci. U. S. A.*, 101(10):3462–7, 2004.

[33] M. Jack Borrok, Erin M. Koionko, and Laura L. Kiessling. Chemical probes of bacterial signal transduction reveal that repellents stabilize and attractants destabilize the chemoreceptor array. *ACS Chem. Biol.*, 3(2):101–109, 2008.

[34] Ariane Briegel, Morgan Beeby, Martin Thanbichler, and Grant J. Jensen. Activated chemoreceptor arrays remain intact and hexagonally packed. *Mol. Microbiol.*, 82(3):748–757, 2011.

[35] Kang Wu, Hanna E. Walukiewicz, George D. Glekas, George W. Ordal, and Christopher V. Rao. Attractant binding induces distinct structural changes to the polar and lateral signaling clusters in Bacillus subtilis chemotaxis. *J. Biol. Chem.*, 286(4):2587–2595, 2011.

[36] Louisa Liberman, Howard C. Berg, and Victor Sourjik. Effect of chemoreceptor modification on assembly and activity of the receptor-kinase complex in Escherichia coli. *J. Bacteriol.*, 186(19):6643–6646, 2004.

[37] Sho Asakura and Fumio Oosawa. Interaction between particles suspended in solutions of macromolecules. *J. Polym. Sci.*, 33(126):183–192, 1958.

[38] Kim A. Sharp. Analysis of the size dependence of macromolecular crowding shows that smaller is better. *Proc. Natl. Acad. Sci.*, 112(26):7990–7995, 2015.

[39] R. John Ellis. Macromolecular crowding: Obvious but underappreciated. *Trends Biochem. Sci.*, 26(10):597–604, 2001.

[40] Anja Nenninger, Giulia Mastroianni, and Conrad W. Mullineaux. Size dependence of protein diffusion in the cytoplasm of Escherichia coli. *J. Bacteriol.*, 192(18):4535–4540, 2010.

[41] Geert Van Den Bogaart, Nicolaas Hermans, Victor Krasnikov, and Bert Poolman. Protein mobility and diffusive barriers in Escherichia coli: Consequences of osmotic stress. *Mol. Microbiol.*, 64(3):858–871, 2007.

[42] Steven B Zimmerman and Allen P Minton. MACROMOLECULAR CROWDING: Biochemical, Biophysical and Physiological Consequences. *Annu. Rev. Biophys.*, 22:27–65, 1993.

[43] J. Pelletier, K. Halvorsen, B.-Y. Ha, R. Paparcone, S. J. Sandler, C. L. Woldringh, W. P. Wong, and S. Jun. Physical manipulation of the Escherichia coli chromosome reveals its soft nature. *Proc. Natl. Acad. Sci.*, 109(40):E2649–E2656, 2012.

[44] Sónia Cunha, Conrad L Woldringh, and Theo Odijk. Polymer-Mediated Compaction and Internal Dynamics of Isolated Escherichia coli Nucleoids. *J. Struct. Biol.*, 136(1):53–66, 2001.

[45] Suckjoon Jun. Chromosome, cell cycle, and entropy. *Biophys. J.*, 108(4):785–786, 2015.

[46] Gernot Guigas and Matthias Weiss. Effects of protein crowding on membrane systems. *Biochim. Biophys. Acta - Biomembr.*, 1858(10):2441–2450, 2016.

[47] Joseph E. Goose and Mark S P Sansom. Reduced Lateral Mobility of Lipids and Proteins in Crowded Membranes. *PLoS Comput. Biol.*, 9(4), 2013.

[48] Martin Lindén, Pierre Sens, and Rob Phillips. Entropic tension in crowded membranes. *PLoS Comput. Biol.*, 8(3):1–10, 2012.

[49] Felix Höfling and Thomas Franosch. Anomalous transport in the crowded world of biological cells. *Reports Prog. Phys.*, 76(4), 2013.

[50] Grzegorz Wieczorek and Piotr Zielenkiewicz. Influence of Macromolecular Crowding on Protein-Protein Association Rates—a Brownian Dynamics Study. *Biophys. J.*, 95(11):5030–5036, dec 2008.

[51] Jay R. Wenner and Victor A. Bloomfield. Crowding effects on EcoRV kinetics and binding. *Biophys. J.*, 77(6):3234–3241, 1999.

[52] Jonas van den Berg, Arnold J. Boersma, and Bert Poolman. Microorganisms maintain crowding homeostasis. *Nat. Rev. Microbiol.*, 15(5):309–318, 2017.

[53] Germán Rivas and Allen P. Minton. Macromolecular Crowding In Vitro, In Vivo, and In Between. *Trends Biochem. Sci.*, 41(11):970–981, 2016.

[54] Arnold J Boersma, Inge S Zuhorn, and Bert Poolman. A sensor for quantification of macromolecular crowding in living cells. *Nat. Methods*, 12(3):227–9, 1 p following 229, 2015.

[55] IVAR LOSSIUS KJELL KLEPPE, STEINAR VREB. The Bacterial Nucleoid. 1624(2):1–13, 2017.

[56] Remus T. Dame. The role of nucleoid-associated proteins in the organization and compaction of bacterial chromatin. *Mol. Microbiol.*, 56(4):858–870, 2005.

[57] Remus T Dame, Maarten C Noom, and Gijs J L Wuite. Bacterial chromatin organization by H-NS protein unravelled using dual DNA manipulation. *Nature*, 444(7117):387–390, 2006.

[58] Shane C Dillon and Charles J Dorman. Bacterial nucleoid-associated proteins, nucleoid structure and gene expression. *Nat. Rev. Microbiol.*, 8(3):185–95, 2010.

[59] Steven F Lee, Michael A Thompson, Monica A Schwartz, Lucy Shapiro, and W E Moerner. Super-resolution imaging of the nucleoid-associated protein HU in Caulobacter crescentus. *Biophys. J.*, 100(7):L31–3, apr 2011.

[60] Anna S. Wegner, Svetlana Alexeeva, Theo Odijk, and Conrad L. Woldringh. Characterization of Escherichia coli nucleoids released by osmotic shock. *J. Struct. Biol.*, 178(3):260–269, 2012.

[61] Paul a Wiggins, Keith C Cheveralls, Joshua S Martin, Robert Lintner, and Jané Kondev. Strong intranucleoid interactions organize the Escherichia coli chromosome into a nucleoid filament. *Proc. Natl. Acad. Sci. U. S. A.*, 107(11):4991–4995, 2010.

[62] Anjana Badrinarayanan, Christian Lesterlin, Rodrigo Reyes-Lamothe, and David Sherratt. The escherichia coli SMC complex, MukBEF, shapes nucleoid organization independently of DNA replication. *J. Bacteriol.*, 194(17):4669–4676, 2012.

[63] Anjana Badrinarayanan, Rodrigo Reyes-Lamothe, Stephan Uphoff, Mark C Leake, and David J Sherratt. In vivo architecture and action of bacterial structural maintenance of chromosome proteins. *Sci. New York NY*, 338(6106):528–531, 2012.

[64] Tung B K Le, Maxim V Imakaev, Leonid a Mirny, Michael T Laub, and High-resolution Mapping. High-Resolution Mapping of the Spatial Organization of a Bacterial Chromosome. *Science*, 731(October), oct 2013.

[65] Sun-Hae Hong, Esteban Toro, Kim I Mortensen, Mario a Díaz de la Rosa, Sebastian Doniach, Lucy Shapiro, Andrew J Spakowitz, and Harley H McAdams. Caulobacter chromosome in vivo configuration matches model predictions for a supercoiled polymer in a cell-like confinement. *Proc. Natl. Acad. Sci. U. S. A.*, 110(5):1674–9, jan 2013.

[66] Juin Kim, Chanil Jeon, Hawoong Jeong, Youngkyun Jung, and Bae-Yeun Ha. A polymer in a crowded and confined space: effects of crowder size and poly-dispersity. *Soft Matter*, 11(10):1877–1888, 2015.

[67] F.C. Neidhardt and R. Curtiss. *Escherichia Coli and Salmonella: Cellular and Molecular Biology*. Number v. 1 in Escherichia Coli and Salmonella: Cellular and Molecular Biology. ASM Press, 1996.

[68] Pierre-Gilles De Gennes and Pierre-Gilles Gennes. *Scaling concepts in polymer physics*. Cornell university press, 1979.

[69] Cedric Cagliero, Ralph S Grand, M Beatrix Jones, Ding J Jin, and Justin M O'Sullivan. Genome conformation capture reveals that the Escherichia coli chromosome is organized by replication and transcription. *Nucleic Acids Res.*, (16):1–14, apr 2013.

[70] Bradley R Parry, Ivan V Surovtsev, Matthew T Cabeen, Corey S O,Äôhern, Eric R Dufresne, and Christine Jacobs-Wagner. The Bacterial Cytoplasm Has Glass-like Properties and Is Fluidized by Metabolic Activity. *Cell*, pages 1–12, 2013.

[71] C Robinow and E Kellenberger. The bacterial nucleoid revisited. *Microbiol. Rev.*, 58(2):211–32, 1994.

[72] Sviatlana Shashkova and Mark C Leake. Single-molecule fluorescence microscopy review: shedding new light on old problems. *Biosci. Rep.*, 0(July):BSR20170031, 2017.

[73] Christian Combs. Fluorescence Microscopy: A Concise Guide to Current Imaging Methods. *Curr. Protoc. Neurosci.*, pages 1–19, 2010.

[74] Eric Betzig, George H Patterson, Rachid Sougrat, O Wolf Lindwasser, Scott Olenych, Juan S Bonifacino, Michael W Davidson, Jennifer Lippincott-Schwartz, and Harald F Hess. Imaging intracellular fluorescent proteins at nanometer resolution. *Science (80-. ).*, 313(5793):1642–1645, 2006.

[75] Mats G L Gustafsson. Nonlinear structured-illumination microscopy: Wide-field fluorescence imaging with theoretically unlimited resolution. *Proc. Natl. Acad. Sci. U. S. A.*, 102(37):13081–13086, 2005.

[76] Xiaowei Zhuang. Nano-imaging with Storm. *Nat. Photonics*, 3(7):365–367, 2009.

[77] Ulrike Endesfelder, Sebastian Malkusch, Benjamin Flottmann, Justine Mondry, Piotr Liguzinski, Peter J Verveer, and Mike Heilemann. Chemically induced photoswitching of fluorescent probes–a general concept for super-resolution microscopy. *Molecules*, 16(4):3106–18, jan 2011.

[78] Russell E Thompson, Daniel R Larson, and Watt W Webb. Precise nanometer localization analysis for individual fluorescent probes. *Biophys. J.*, 82(5):2775–2783, may 2002.

[79] M. Ovesny, P. K i ek, J. Borkovec, Z. vindrych, and G. M. Hagen. ThunderSTORM: a comprehensive ImageJ plug-in for PALM and STORM data analysis and super-resolution imaging. *Bioinformatics*, 30(16):2389–2390, 2014.

[80] Hari Shroff, Catherine G Galbraith, James a Galbraith, and Eric Betzig. Live-cell photoactivated localization microscopy of nanoscale adhesion dynamics. *Nat. Methods*, 5(5):417–23, may 2008.

[81] Suliana Manley, Jennifer M Gillette, George H Patterson, Hari Shroff, Harald F Hess, Eric Betzig, and Jennifer Lippincott-Schwartz. High-density mapping of single-molecule trajectories with photoactivated localization microscopy. *Nat. Methods*, 5(2):155–157, feb 2008.

[82] Zhen Liu, Dong Xing, Qian Peter Su, Yun Zhu, Jiamei Zhang, Xinyu Kong, Boxin Xue, Sheng Wang, Hao Sun, Yile Tao, and Yujie Sun. Super-resolution imaging and tracking of protein-protein interactions in sub-diffraction cellular space. *Nat. Commun.*, 5:4443, 2014.

[83] Mathew Stracy, Christian Lesterlin, Federico Garza de Leon, Stephan Uphoff, Pawel Zawadzki, and Achillefs N Kapanidis. Live-cell superresolution microscopy reveals the organization of RNA polymerase in the bacterial nucleoid. *Proc. Natl. Acad. Sci. U. S. A.*, 112(32):E4390–9, 2015.

[84] Nastaran Hadizadeh Yazdi, Calin C. Guet, Reid C. Johnson, and John F. Marko. Variation of the folding and dynamics of the Escherichia coli chromosome with growth conditions. *Mol. Microbiol.*, 86(6):1318–1333, 2012.

[85] Preeti Srivastava, Gäelle Demarre, Tatiana S. Karpova, James McNally, and Dhruba K. Chattoraj. Changes in nucleoid morphology and origin localization upon inhibition or alteration of the actin homolog, MreB, of Vibrio cholerae. *J. Bacteriol.*, 189(20):7450–7463, 2007.

[86] Stephen A Sciochetti, Garry W Blakely, and J Patrick. Growth Phase Variation in Cell and Nucleoid Morphology in a Bacillus subtilis recA Mutant Growth Phase Variation in Cell and Nucleoid Morphology in a Bacillus subtilis recA Mutant. 183(9):2963–2968, 2001.

[87] Daphna Frenkiel-Krispin, Irit Ben-Avraham, Joseph Englander, Eyal Shimoni, Sharon G. Wolf, and Abraham Minsky. Nucleoid restructuring in stationary-state bacteria. *Mol. Microbiol.*, 51(2):395–405, 2004.

[88] Ali Azam Talukder and Akira Ishihama. Growth phase dependent changes in the structure and protein composition of nucleoid in Escherichia coli. *Sci. China Life Sci.*, 58(9):902–911, 2015.

[89] Philippe Nghe, Sarah Boulineau, Sebastian Gude, Pierre Recouvreux, Jeroen S. van Zon, and Sander J. Tans. Microfabricated Polyacrylamide Devices for the Controlled Culture of Growing Cells and Developing Organisms. *PLoS One*, 8(9):1–11, 2013.

[90] Avelino Javer, Nathan J. Kuwada, Zhicheng Long, Vincenzo G. Benza, Kevin D. Dorfman, Paul a. Wiggins, Pietro Cicuta, and Marco Cosentino Lagomarsino. Persistent super-diffusive motion of Escherichia coli chromosomal loci. *Nat. Commun.*, 5(May):1–8, 2014.

[91] H.C. Berg. A miniature flow cell designed for rapid exchange of media under high-power microscope objectives. *Microbiology*, 130(11):2915–2920, 1984.

[92] T Katsu, T Tsuchiya, and Y Fujita. Dissipation of membrane potential of Escherichia coli cells induced by macromolecular polylysine. *Biochem. Biophys. Res. Commun.*, 122(1):401–406, 1984.

[93] Ping Wang, Lydia Robert, James Pelletier, Wei Lien Dang, Francois Taddei, Andrew Wright, and Suckjoon Jun. Robust growth of Escherichia coli. *Curr. Biol.*, 20(12):1099–1103, 2011.

[94] Douglas B Weibel, Willow R Diluzio, and George M Whitesides. Microfabrication meets microbiology. *Nat. Rev. Microbiol.*, 5(3):209–18, 2007.

[95] Yu Tanouchi, Anand Pai, Heungwon Park, Shuqiang Huang, Rumen Stamatov, Nicolas E Buchler, and Lingchong You. A noisy linear map underlies oscillations in cell size and gene expression in bacteria. *Nature*, 523(7560):357–360, jun 2015.

[96] Yu Tanouchi, Anand Pai, Heungwon Park, Shuqiang Huang, Nicolas E. Buchler, and Lingchong You. Long-term growth data of Escherichia coli at a single-cell level. *Sci. Data*, 4:1–5, 2017.

[97] Brenda Youngren, Henrik Jörk Nielsen, Suckjoon Jun, and Stuart Austin. The multi-fork Escherichia coli chromosome is a self-duplicating and self-segregating thermodynamic ring polymer. *Genes Dev.*, 28(1):71–84, 2014.

[98] Ping Wang, Lydia Robert, James Pelletier, Wei Lien Dang, Francois Taddei, Andrew Wright, and Suckjoon Jun. Robust growth of escherichia coli. *Current biology*, 20(12):1099–1103, 2010.

[99] Esther Wertz, Benjamin P. Isaacoff, Jessica D. Flynn, and Julie S. Biteen. Single-Molecule Super-Resolution Microscopy Reveals How Light Couples to a Plasmonic Nanoantenna on the Nanometer Scale. *Nano Lett.*, 15(4):2662–2670, 2015.

[100] Hongzhen Lin, Silvia P. Centeno, Liang Su, Bart Kenens, Susana Rocha, Michel Sliwa, Johan Hofkens, and Hiroshi Uji-I. Mapping of surface-enhanced fluorescence on metal nanoparticles using super-resolution photoactivation localization microscopy. *ChemPhysChem*, 13(4):973–981, 2012.

[101] Xiaochun Zhou, Nesha May Andoy, Guokun Liu, Eric Choudhary, Kyu Sung Han, Hao Shen, and Peng Chen. Quantitative super-resolution imaging uncovers reactivity patterns on single nanocatalysts. *Nat. Nanotechnol.*, 7(4):237–241, 2012.

[102] Eric Johlin, Jacopo Solari, Sander A. Mann, Jia Wang, Thomas S. Shimizu, and Erik C. Garnett. Super-resolution imaging of light-matter interactions near single semiconductor nanowires. *Nat. Commun.*, 7:1–6, 2016.

[103] Eric Betzig. Single Molecules, Cells, and Super-Resolution Optics (Nobel Lecture). *Angew. Chemie - Int. Ed.*, 54(28):8034–8053, 2015.

[104] SW Hell. Far-field optical nanoscopy. *Science (80-. ).*, 316(2007):246–9, 2007.

[105] Bo Huang, Mark Bates, and Xiaowei Zhuang. Super-Resolution Fluorescence Microscopy. *Ann. Rev. Biochem.*, 78(1):993–1016, 2009.

[106] Eric Betzig. Proposed method for molecular optical imaging. *Opt. Lett.*, 20(3):237–9, 1995.

[107] Brian P English, Vasili Hauryliuk, Arash Sanamrad, Stoyan Tankov, Nynke H Dekker, and Johan Elf. Single-molecule investigations of the stringent response machinery in living bacterial cells. *Proc. Natl. Acad. Sci. U. S. A.*, 108(31):E365–E373, 2011.

[108] L Niu and J Yu. Investigating intracellular dynamics of FtsZ cytoskeleton with photoactivation single-molecule tracking. *Biophys. J.*, 95(4):2009–2016, 2008.

[109] Victor Sourjik, Ady Vaknin, Thomas S. Shimizu, and Howard C. Berg. In Vivo Measurement by FRET of Pathway Activity in Bacterial Chemotaxis. In *Methods Enzymol.*, volume 423, pages 365–391. 2007.

[110] Egon Amann, Birgit Ochs, and K.J. Abel. Tightly regulated tac promoter vectors useful for the expression of unfused and fused proteins in escherichia coli. 69:301–15, 10 1988.

[111] L. M. Guzman, D. Belin, M. J. Carson, and J. Beckwith. Tight regulation, modulation, and high-level expression by vectors containing the arabinose P(BAD) promoter. *J. Bacteriol.*, 177(14):4121–4130, 1995.

[112] Leonard Guarente. Yeast promoters and lacz fusions designed to study expression of cloned genes in yeast. 101:181–91, 02 1983.

[113] Peter Ames, Claudia a Studdert, Rebecca H Reiser, and John S Parkinson. Collaborative signaling by mixed chemoreceptor teams in Escherichia coli. *Proc. Natl. Acad. Sci. U. S. A.*, 99(10):7060–7065, 2002.

[114] Robert G Endres, Olga Oleksiuk, Clinton H Hansen, Yigal Meir, Victor Sourjik, and Ned S Wingreen. Variable sizes of Escherichia coli chemoreceptor signaling teams. *Mol. Syst. Biol.*, 4(211):211, jan 2008.

[115] Vered Frank, Germán E Piñas, Harel Cohen, John S Parkinson, and Ady Vaknin. Networked Chemoreceptors Benefit Bacterial Chemotaxis Performance. *MBio*, 7(6):1–9, dec 2016.

[116] Rajalakshmi Srinivasan, Vittore Ferdinando Scolari, Marco Cosentino Lagomarsino, Aswin Sai Narain, and Aswin Sai Narain Seshasayee. The genome-scale interplay amongst xenogene silencing, stress response and chromosome architecture in Escherichia coli. *Nucleic Acids Res.*, 43(1):295–308, 2015.

[117] M. Daszykowski and B. Walczak. Density-Based Clustering Methods. In *Compr. Chemom.*, volume 70, pages 635–654. Elsevier, mar 2009.

[118] Keegan Colville, Nicolas Tompkins, Andrew D. Rutenberg, and Manfred H. Jericho. Effects of poly(L-lysine) substrates on attached escherichia coli bacteria. *Langmuir*, 26(4):2639–2644, 2010.

[119] Khuloud Jaqaman, Dinah Loerke, Marcel Mettlen, Hirotaka Kuwata, Sergio Grinstein, Sandra L Schmid, and Gaudenz Danuser. Robust single-particle tracking in live-cell time-lapse sequences. *Nat. Methods*, 5(8):695–702, aug 2008.

[120] Sebastian Thiem, David Kentner, and Victor Sourjik. Positioning of chemosensory clusters in E. coli and its relation to cell division. *EMBO J.*, 26(6):1615–23, mar 2007.

[121] Hironori Niki, Yoshiharu Yamaichi, and Sota Hiraga. Dynamic organization of chromosomal DNA in Escherichia coli Dynamic organization of chromosomal DNA in Escherichia coli. pages 212–223, 2000.

[122] Michèle Valens, Stéphanie Penaud, Michèle Rossignol, François Cornet, and Frédéric Boccard. Macrodomain organization of the Escherichia coli chromosome. *EMBO J.*, 23(21):4330–4341, 2004.

[123] Olivier Espeli, Romain Mercier, and Frédéric Boccard. DNA dynamics vary according to macrodomain topography in the E. coli chromosome. *Mol. Microbiol.*, 68(6):1418–27, jun 2008.

[124] Douglas F. Browning, Jeffrey A. Cole, and Stephen J W Busby. Regulation by nucleoid-associated proteins at the Escherichia coli nir operon promoter. *J. Bacteriol.*, 190(21):7258–7267, 2008.

[125] Sophie Nolivos and David Sherratt. The bacterial chromosome: Architecture and action of bacterial SMC and SMC-like complexes. *FEMS Microbiol. Rev.*, 38(3):380–392, 2014.

[126] Christoph Spahn, Ulrike Endesfelder, and Mike Heilemann. Super-resolution imaging of Escherichia coli nucleoids reveals highly structured and asymmetric segregation during fast growth. *J. Struct. Biol.*, pages 1–7, jan 2014.

[127] Esteban Toro and Lucy Shapiro. Bacterial chromosome organization and segregation. *Cold Spring Harb. Perspect. Biol.*, 2(2):a000349, feb 2010.

[128] Rodrigo Reyes-Lamothe, Emilien Nicolas, and David J. Sherratt. Chromosome Replication and Segregation in Bacteria. *Annu. Rev. Genet.*, 46(1):121–143, 2012.

[129] Jay K Fisher, Aude Bourniquel, Guillaume Witz, Beth Weiner, Mara Prentiss, and Nancy Kleckner. Four-Dimensional Imaging of E. coli Nucleoid Organization and Dynamics in Living Cells. *Cell*, 153(4):882–95, may 2013.

[130] Muriel Wery, Conrad L. Woldringh, and Josette Rouviere-Yaniv. HU-GFP and DAPI co-localize on the Escherichia coli nucleoid. *Biochimie*, 83(2):193–200, 2001.

[131] Somenath Bakshi, Heejun Choi, Nambirajan Rangarajan, Kenneth J. Barns, Benjamin P. Bratton, and James C. Weisshaar. Nonperturbative imaging of nucleoid morphology in live bacterial cells during an antimicrobial peptide attack. *Appl. Environ. Microbiol.*, 80(16):4977–4986, 2014.

[132] Optical Setup, S. Wang, J. R. Moffitt, G. T. Dempsey, X. S. Xie, and X. Zhuang. Characterization and development of photoactivatable fluorescent proteins for single-molecule-based superresolution imaging. *Proc. Natl. Acad. Sci.*, 111(23):1–9, may 2014.

[133] Diana Di Paolo, Oshri Afanzar, Judith P. Armitage, and Richard M. Berry. Single-molecule imaging of electroporated dye-labelled CheY in live Escherichia coli. *Philos. Trans. R. Soc. B Biol. Sci.*, 371(1707):20150492, 2016.

[134] T Atlung and H Ingmer. H-NS: a modulator of environmentally regulated gene expression. *Mol. Microbiol.*, 24(1):7–17, 1997.

[135] Bo Huang, Wenqin Wang, Mark Bates, and Xiaowei Zhuang. Three-dimensional super-resolution imaging by stochastic optical reconstruction microscopy. *Science*, 319(5864):810–3, feb 2008.

[136] Idit Anna Berlatzky, Alex Rouvinski, and Sigal Ben-Yehuda. Spatial organization of a replicating bacterial chromosome. *Proc. Natl. Acad. Sci. U. S. A.*, 105(37):14136–40, sep 2008.

[137] Wenquin Wang, Gene-Wei Li, Chongyi Chen, Sunny X. Xie, and Xiaowei Zhuang. Live Bacteria. *Science (80-. ).*, 333(6048):1445–1449, 2012.

[138] Rotem Gura Sadovsky, Shlomi Brielle, Daniel Kaganovich, and Jeremy L. England. Measurement of Rapid Protein Diffusion in the Cytoplasm by Photo-Converted Intensity Profile Expansion. *Cell Rep.*, 18(11):2795–2806, 2017.

[139] Sun-Hae Hong and Harley H McAdams. Compaction and transport properties of newly replicated Caulobacter crescentus DNA. *Mol. Microbiol.*, 82(6):1–10, dec 2011.

[140] C Robinett, a Straight, G Li, C Willhelm, G Sudlow, a Murray, and a S Belmont. In vivo loclization of DNA sequences and visualization of large-scale chromatin organizacion using lac operator/represor recognition. *J. Cell Biol.*, 135(6- part 2):1685–1700, 1996.

[141] MC Joshi and Aude Bourniquel. Escherichia coli sister chromosome separation includes an abrupt global transition with concomitant release of late-splitting intersister snaps. *Proc. . . .*, 108(7):2765–2770, feb 2011.

[142] Xindan Wang, Xun Liu, Christophe Possoz, and David J Sherratt. The two Escherichia coli chromosome arms locate to separate cell halves. *Genes Dev.*, 20(13):1727–31, jul 2006.

[143] Paul a Wiggins, Keith C Cheveralls, Joshua S Martin, Robert Lintner, and Jané Kondev. Strong intranucleoid interactions organize the Escherichia coli chromosome into a nucleoid filament. *Proc. Natl. Acad. Sci. U. S. A.*, 107(11):4991–5, mar 2010.

[144] Patrick H Viollier, Martin Thanbichler, Patrick T McGrath, Lisandra West, Maliwan Meewan, Harley H McAdams, and Lucy Shapiro. Rapid and sequential movement of individual chromosomal loci to specific subcellular locations during bacterial DNA replication. *Proc. Natl. Acad. Sci. U. S. A.*, 101(25):9257–62, jun 2004.

[145] Zach Hensel, Xiaoli Weng, Arvin Cesar Lagda, and Jie Xiao. Transcription-factor-mediated DNA looping probed by high-resolution, single-molecule imaging in live E. coli cells. *PLoS Biol.*, 11(6):e1001591, jan 2013.

[146] R M Dickson, a B Cubitt, R Y Tsien, and W E Moerner. On/off blinking and switching behaviour of single molecules of green fluorescent protein. *Nature*, 388(6640):355–8, jul 1997.

[147] Mark C Leake, Nicholas P Greene, Rachel M Godun, Thierry Granjon, Grant Buchanan, Shuyun Chen, Richard M Berry, Tracy Palmer, and Ben C Berks. Variable stoichiometry of the TatA component of the twin-arginine protein transport system observed by in vivo single-molecule imaging. *Proc. Natl. Acad. Sci. U. S. A.*, 105(40):15376–81, oct 2008.

[148] Avelino Javer, Zhicheng Long, Eileen Nugent, Marco Grisi, Kamin Siriwatwetchakul, Kevin D. Dorfman, Pietro Cicuta, and Marco Cosentino Lagomarsino. Short-time movement of E. coli chromosomal loci depends on coordinate and subcellular localization. *Nat. Commun.*, 4(May):1–8, 2013.

[149] B. Alberts, D. Bray, J. Lewis, M. Raff, K. Roberts, and J.D. Watson. *Molecular Biology of the Cell*. Garland, 4th edition, 2002.

[150] Sin Yi Lee, Ci Ji Lim, Peter Dröge, and Jie Yan. Regulation of Bacterial DNA Packaging in Early Stationary Phase by Competitive DNA Binding of Dps and IHF. *Sci. Rep.*, 5(December):1–10, 2015.

[151] Bradley R. Parry, Ivan V. Surovtsev, Matthew T. Cabeen, Corey S. O'Hern, Eric R. Dufresne, and Christine Jacobs-Wagner. The bacterial cytoplasm has glass-like properties and is fluidized by metabolic activity. *Cell*, 156(1-2):183–194, 2014.

[152] Akshay K. Harapanahalli, Jessica A. Younes, Elaine Allan, Henny C. van der Mei, and Henk J. Busscher. Chemical Signals and Mechanosensing in Bacterial Responses to Their Environment. *PLoS Pathog.*, 11(8):1–6, 2015.

[153] Melissa B Miller and Bonnie L Bassler. Ensing in. *Annu. Rev. Microbiol.*, 55:165–99, 2001.

[154] Anna Maria Giuliodori, Claudio O. Gualerzi, Sara Soto, Jordi Vila, and María M. Tavío. Review on bacterial stress topics. *Ann. N. Y. Acad. Sci.*, 1113:95–104, 2007.

[155] Donna R Whelan and Toby D M Bell. Image artifacts in Single Molecule Localization Microscopy: why optimization of sample preparation protocols matters. *Sci. Rep.*, 5:7924, 2015.

[156] Zhe Liu, Luke D. Lavis, and Eric Betzig. Imaging Live-Cell Dynamics and Structure at the Single-Molecule Level. *Mol. Cell*, 58(4):644, 2015.

[157] Ulrike Schnell, Freark Dijk, Klaas A. Sjollema, and Ben N.G. Giepmans. Immunolabeling artifacts and the need for live-cell imaging. *Nat. Methods*, 9(2):152–158, 2012.

[158] Yuanqing Chao and Tong Zhang. Optimization of fixation methods for observation of bacterial cell morphology and surface ultrastructures by atomic force microscopy. *Appl. Microbiol. Biotechnol.*, 92(2):381–392, 2011.

[159] Thomas A. Owen-Hughes, Graham D. Pavitt, Diogenes S. Santos, Julie M. Sidebotham, Christopher S J Hulton, Jay C D Hinton, and Christopher F. Higgins. The chromatin-associated protein H-NS interacts with curved DNA to influence DNA topology and gene expression. *Cell*, 71(2):255–265, 1992.

[160] Minsang Shin, Arvin Cesar Lagda, Jae Woong Lee, Abhay Bhat, Joon Haeng Rhee, Jeong Sun Kim, Kunio Takeyasu, and Hyon E. Choy. Gene silencing by H-NS from distal DNA site. *Mol. Microbiol.*, 86(3):707–719, 2012.

[161] Bart J.A.M. Jordi, Anne E. Fielder, Christopher M. Burns, Jay C.D. Hinton, Nir Dover, David W. Ussery, and Christopher F. Higgins. DNA binding is not sufficient for H-NS-mediated repression of proU expression. *J. Biol. Chem.*, 272(18):12083–12090, 1997.

[162] P Bertin, E Terao, E H Lee, P Lejeune, C Colson, a Danchin, and E Collatz. The H-NS protein is involved in the biogenesis of flagella in Escherichia coli. *J. Bacteriol.*, 176(17):5537–40, sep 1994.

[163] M Ko and C Park. Two novel flagellar components and H-NS are involved in the motor function of Escherichia coli. *J. Mol. Biol.*, 303(3):371–82, oct 2000.

[164] Eun A Kim and David F. Blair. Function of the Histone-Like Protein H-NS in Motility of Escherichia coli: Multiple Regulatory Roles Rather than Direct Action at the Flagellar Motor. *J. Bacteriol.*, 197(19):3110–3120, 2015.

[165] Michelle M Barnhart and Matthew R Chapman. NIH Public Access. pages 131–147, 2010.

[166] Douglas Hanahan. Studies on transformation of Escherichia coli with plasmids. *J. Mol. Biol.*, 166(4):557–580, 1983.

[167] F. R. Blattner. The Complete Genome Sequence of Escherichia coli K-12. *Science (80-. ).*, 277(5331):1453–1462, 1997.

[168] B Alberts, A Johnson, J Lewis, M Raff, K Roberts, and P Walter. *Molecular Biology of the cell, 6th Ed.* Springer, 2015.

[169] Ariane Briegel and Grant Jensen. Progress and potential of electron cryotomography as illustrated by its application to bacterial chemoreceptor arrays. *Annual review of biophysics*, 46:1–21, 2017.

[170] Joseph J Falke and Kene N Piasta. Architecture and signal transduction mechanism of the bacterial chemosensory array: Progress, controversies, and challenges. *Current opinion in structural biology*, 29:85–94, 2014.

[171] Howard C Berg. *E. coli in Motion*. Springer, 2004.

[172] Jeffrey E Segall, Steven M Block, and Howard C Berg. Temporal comparisons in bacterial chemotaxis. *Proceedings of the National Academy of Sciences*, 83(23):8987–8991, 1986.

[173] Shuangyu Bi and Victor Sourjik. Stimulus sensing and signal processing in bacterial chemotaxis. *Current opinion in microbiology*, 45:22–29, 2018.

[174] Naama Barkai and Stan Leibler. Robustness in simple biochemical networks. *Nature*, 387(6636):913, 1997.

[175] MR Alley, Janine R Maddock, and Lucille Shapiro. Polar localization of a bacterial chemoreceptor. *Genes & development*, 6(5):825–836, 1992.

[176] Janine R Maddock and Lucille Shapiro. Polar location of the chemoreceptor complex in the escherichia coli cell. *Science*, 259(5102):1717–1723, 1993.

[177] Victor Sourjik and Howard C Berg. Localization of components of the chemotaxis machinery of escherichia coli using fluorescent protein fusions. *Molecular microbiology*, 37(4):740–751, 2000.

[178] Sebastian Thiem, David Kentner, and Victor Sourjik. Positioning of chemosensory clusters in e. coli and its relation to cell division. *The EMBO journal*, 26(6):1615–1623, 2007.

[179] Hanbin Mao, Paul S Cremer, and Michael D Manson. A sensitive, versatile microfluidic assay for bacterial chemotaxis. *Proceedings of the National Academy of Sciences*, 100(9):5449–5454, 2003.

[180] Dennis Bray, Matthew D Levin, and Carl J Morton-Firth. Receptor clustering as a cellular mechanism to control sensitivity. *Nature*, 393(6680):85–88, 1998.

[181] TAJ Duke and D Bray. Heightened sensitivity of a lattice of membrane receptors. *Proceedings of the National Academy of Sciences*, 96(18):10104–10108, 1999.

[182] Bernardo A Mello and Yuhai Tu. Quantitative modeling of sensitivity in bacterial chemotaxis: the role of coupling among different chemoreceptor species. *Proceedings of the National Academy of Sciences*, 100(14):8223–8228, 2003.

[183] Victor Sourjik. Receptor clustering and signal processing in E. coli chemotaxis. *Trends Microbiol.*, 12(12):569–76, dec 2004.

[184] Juan E Keymer, Robert G Endres, Monica Skoge, Yigal Meir, and Ned S Wingreen. Chemosensing in escherichia coli: two regimes of two-state receptors. *Proceedings of the National Academy of Sciences*, 103(6):1786–1791, 2006.

[185] Germán E Piñas, Vered Frank, Ady Vaknin, and John S Parkinson. The source of high signal cooperativity in bacterial chemosensory arrays. *Proceedings of the National Academy of Sciences*, 113(12):3335–3340, 2016.

[186] Vered Frank, Germán E Piñas, Harel Cohen, John S Parkinson, and Ady Vaknin. Networked chemoreceptors benefit bacterial chemotaxis performance. *MBio*, 7(6):e01824–16, 2016.

[187] Louisa Liberman, Howard C Berg, and Victor Sourjik. Effect of chemoreceptor modification on assembly and activity of the receptor-kinase complex in escherichia coli. *Journal of bacteriology*, 186(19):6643–6646, 2004.

[188] Motohiro Homma, Daisuke Shiomi, Michio Homma, and Ikuro Kawagishi. Attractant binding alters arrangement of chemoreceptor dimers within its cluster at a cell pole. *Proceedings of the National Academy of Sciences of the United States of America*, 101(10):3462–3467, 2004.

[189] Allison C Lamanna, George W Ordal, and Laura L Kiessling. Large increases in attractant concentration disrupt the polar localization of bacterial chemoreceptors. *Molecular microbiology*, 57(3):774–785, 2005.

[190] M Jack Borrok, Erin M Kolonko, and Laura L Kiessling. Chemical probes of bacterial signal transduction reveal that repellents stabilize and attractants destabilize the chemoreceptor array. *ACS chemical biology*, 3(2):101–109, 2008.

[191] Kang Wu, Hanna E Walukiewicz, George D Glekas, George W Ordal, and Christopher V Rao. Attractant binding induces distinct structural changes to the polar and lateral signaling clusters in bacillus subtilis chemotaxis. *Journal of Biological Chemistry*, 286(4):2587–2595, 2011.

[192] Ariane Briegel, Xiaoxiao Li, Alexandrine M Bilwes, Kelly T Hughes, Grant J Jensen, and Brian R Crane. Bacterial chemoreceptor arrays are hexagonally packed trimers of receptor dimers networked by rings of kinase and coupling proteins. *Proceedings of the National Academy of Sciences*, 109(10):3766–3771, 2012.

[193] J Liu, B Hu, D R Morado, S Jani, M D Manson, and W Margolin. PNAS Plus: Molecular architecture of chemoreceptor arrays revealed by cryoelectron tomography of Escherichia coli minicells. *Proc. Natl. Acad. Sci. U. S. A.*, 109(3):E1481—-E1488, 2012.

[194] Ariane Briegel, Morgan Beeby, Martin Thanbichler, and Grant J Jensen. Activated chemoreceptor arrays remain intact and hexagonally packed. *Molecular microbiology*, 82(3):748–757, 2011.

[195] Cezar M Khursigara, Ganhui Lan, Silke Neumann, Xiongwu Wu, Suchie Ravindran, Mario J Borgnia, Victor Sourjik, Jacqueline Milne, Yuhai Tu, and Sriram Subramaniam. Lateral density of receptor arrays in the membrane plane influences sensitivity of the e. coli chemotaxis response. *The EMBO journal*, 30(9):1719–1729, 2011.

[196] Vered Frank and Ady Vaknin. Prolonged stimuli alter the bacterial chemosensory clusters. *Molecular microbiology*, 88(3):634–644, 2013.

[197] Eric Betzig, George H Patterson, Rachid Sougrat, O Wolf Lindwasser, Scott Olenych, Juan S Bonifacino, Michael W Davidson, Jennifer Lippincott-Schwartz, and Harald F Hess. Imaging intracellular fluorescent proteins at nanometer resolution. *Science*, 313(5793):1642–1645, 2006.

[198] Derek Greenfield, Ann L McEvoy, Hari Shroff, Gavin E Crooks, Ned S Wingreen, Eric Betzig, and Jan Liphardt. Self-organization of the escherichia coli chemotaxis network imaged with super-resolution light microscopy. *PLoS biology*, 7(6):e1000137, 2009.

[199] Sang-Hyuk Lee, Jae Yen Shin, Antony Lee, and Carlos Bustamante. Counting single photoactivatable fluorescent molecules by photoactivated localization microscopy (palm). *Proceedings of the National Academy of Sciences*, 109(43):17436–17441, 2012.

[200] J Solari, F Anquez, KM Scherer, and TS Shimizu. Bacterial chemoreceptor imaging at high spatiotemporal resolution using photoconvertible fluorescent proteins. *Meth Mol Biol*, 1729:203–231, 2018.

[201] Sean A McKinney, Christopher S Murphy, Kristin L Hazelwood, Michael W Davidson, and Loren L Looger. A bright and photostable photoconvertible fluorescent protein for fusion tags. *Nature methods*, 6(2):131, 2009.

[202] JOHN S Parkinson and SUSAN E Houts. Isolation and behavior of escherichia coli deletion mutants lacking chemotaxis functions. *Journal of bacteriology*, 151(1):106–113, 1982.

[203] Thomas S Shimizu, Sergej V Aksenov, and Dennis Bray. A spatially extended stochastic model of the bacterial chemotaxis signalling pathway. *Journal of molecular biology*, 329(2):291–309, 2003.

[204] Bernardo A Mello and Yuhai Tu. An allosteric model for heterogeneous receptor complexes: understanding bacterial chemotaxis responses to multiple stimuli. *Proceedings of the National Academy of Sciences of the United States of America*, 102(48):17354–17359, 2005.

[205] Robert M Macnab and DE Koshland. The gradient-sensing mechanism in bacterial chemotaxis. *Proceedings of the National Academy of Sciences*, 69(9):2509–2512, 1972.

[206] J. Adler. Chemotaxis in Bacteria. *Science (80-. ).*, 153(3737):708–716, aug 1966.

[207] Steven M Block, Jeffery E Segall, and Howard C Berg. Adaptation kinetics in bacterial chemotaxis. *Journal of bacteriology*, 154(1):312–323, 1983.

[208] Yue Li, Luay M Almassalha, John E Chandler, Xiang Zhou, Yolanda E Stypula-Cyrus, Karl A Hujsak, Eric W Roth, Reiner Bleher, Hariharan Subramanian, Igal Szleifer, et al. The effects of chemical fixation on the cellular nanostructure. *Experimental cell research*, 358(2):253–259, 2017.

[209] Dongmyung Oh, Yang Yu, Hochan Lee, Barry L. Wanner, and Ken Ritchie. Dynamics of the serine chemoreceptor in the escherichia coli inner membrane: A high-speed single-molecule tracking study. *Biophys. J.*, 106(1):145–153, 2014.

[210] P. G. Saffman and M Delbruck. Brownian motion in biological membranes. *Proc Natl Acad Sci USA*, 72(8):3111–3113, 1975.

[211] Felix Oswald, Aravindan Varadarajan, Holger Lill, Erwin J.G. Peterman, and Yves J.M. Bollen. MreB-Dependent Organization of the E. coli Cytoplasmic Membrane Controls Membrane Protein Diffusion. *Biophys. J.*, 110(5):1139–1149, 2016.

[212] Ryota Iino, Ikuko Koyama, and Akihiro Kusumi. Single molecule imaging of green fluorescent proteins in living cells: E-cadherin forms oligomers on the free cell surface. *Biophysical journal*, 80(6):2667–2677, 2001.

[213] Mohit Kumar, Mario S Mommer, and Victor Sourjik. Mobility of cytoplasmic, membrane, and DNA-binding proteins in Escherichia coli. *Biophys. J.*, 98(4):552–9, mar 2010.

[214] J Schuster, F Cichos, and C Von Borczyskowski. Diffusion measurements by single-molecule spot-size analysis. *The Journal of Physical Chemistry A*, 106(22):5403–5406, 2002.

[215] Johan Elf, Gene-Wei Li, and X Sunney Xie. Probing transcription factor dynamics at the single-molecule level in a living cell. *Science*, 316(5828):1191–4, may 2007.

[216] Hannah H Tuson and Julie S Biteen. Unveiling the inner workings of live bacteria using super-resolution microscopy. *Analytical chemistry*, 87(1):42–63, 2014.

[217] Ji Yu, Jie Xiao, Xiaojia Ren, Kaiqin Lao, and X Sunney Xie. Probing gene expression in live cells, one protein molecule at a time. *Science*, 311(5767):1600–1603, 2006.

[218] Christian L. Vestergaard, Paul C. Blainey, and Henrik Flyvbjerg. Optimal estimation of diffusion coefficients from single-particle trajectories. *Phys. Rev. E*, 89(2):022726, feb 2014.

[219] Daniel Thédié, Romain Berardozzi, Virgile Adam, and Dominique Bourgeois. Photoswitching of Green mEos2 by Intense 561 nm Light Perturbs Efficient Green-to-Red Photoconversion in Localization Microscopy. *J. Phys. Chem. Lett.*, 8(18):4424–4430, 2017.

[220] Germán E. Piñas, Vered Frank, Ady Vaknin, and John S. Parkinson. The source of high signal cooperativity in bacterial chemosensory arrays. *Proc. Natl. Acad. Sci.*, 113(12):201600216, 2016.

[221] Christian L Vestergaard. Optimizing experimental parameters for tracking of diffusing particles. *Physical Review E*, 94(2):022401, 2016.

[222] Jason E Gestwicki, Allison C Lamanna, Rasika M Harshey, Linda L McCarter, Laura L Kiessling, and Julius Adler. Evolutionary conservation of methyl-accepting chemotaxis protein location in bacteria andarchaea. *Journal of Bacteriology*, 182(22):6499–6502, 2000.

[223] George H Wadhams and Judith P Armitage. Making sense of it all: bacterial chemotaxis. *Nature Reviews Molecular Cell Biology*, 5(12):1024–1037, 2004.

[224] Ariane Briegel, Davi R Ortega, Elitza I Tocheva, Kristin Wuichet, Zhuo Li, Songye Chen, Axel Müller, Cristina V Iancu, Gavin E Murphy, Megan J Dobro, et al. Universal architecture of bacterial chemoreceptor arrays. *Proceedings of the National Academy of Sciences*, pages pnas–0905181106, 2009.

[225] T Duke and D Bray. Heightened sensitivity of a lattice of membrane receptors. *Proc. Natl. Acad. Sci. U. S. A.*, 96(18):10104–8, 1999.

[226] Victor Sourjik and Howard C Berg. Binding of the Escherichia coli response regulator CheY to its target measured in vivo by fluorescence resonance energy transfer. *Proc. Natl. Acad. Sci. U. S. A.*, 99(20):12669–12674, 2002.

[227] Mingshan Li and Gerald L Hazelbauer. Adaptational assistance in clusters of bacterial chemoreceptors. *Molecular microbiology*, 56(6):1617–1626, 2005.

[228] Robert G Endres and Ned S Wingreen. Precise adaptation in bacterial chemotaxis through "assistance neighborhoods". *Proceedings of the National Academy of Sciences*, 103(35):13040–13044, 2006.

[229] Yuhai Tu, Thomas S Shimizu, and Howard C Berg. Modeling the chemotactic response of escherichia coli to time-varying stimuli. *Proceedings of the National Academy of Sciences*, 105(39):14855–14860, 2008.

[230] Thomas S Shimizu, Yuhai Tu, and Howard C Berg. A modular gradient-sensing network for chemotaxis in escherichia coli revealed by responses to time-varying stimuli. *Molecular systems biology*, 6(1), 2010.

[231] Milena D Lazova, Tanvir Ahmed, Domenico Bellomo, Roman Stocker, and Thomas S Shimizu. Response rescaling in bacterial chemotaxis. *Proceedings of the National Academy of Sciences*, 108(33):13870–13875, 2011.

[232] Robert Mesibov, George W Ordal, and Julius Adler. The range of attractant concentrations for bacterial chemotaxis and the threshold and size of response over this range: Weber law and related phenomena. *The Journal of general physiology*, 62(2):203–223, 1973.

[233] Oren Shoval, Lea Goentoro, Yuval Hart, Avi Mayo, Eduardo Sontag, and Uri Alon. Fold-change detection and scalar symmetry of sensory input fields. *Proceedings of the National Academy of Sciences*, page 201002352, 2010.

[234] Bernardo A Mello and Yuhai Tu. Effects of adaptation in maintaining high sensitivity over a wide range of backgrounds for escherichia coli chemotaxis. *Biophysical journal*, 92(7):2329–2337, 2007.

[235] Yevgeniy V Kalinin, Lili Jiang, Yuhai Tu, and Mingming Wu. Logarithmic sensing in escherichia coli bacterial chemotaxis. *Biophysical journal*, 96(6):2439–2448, 2009.

[236] Vered Frank and Ady Vaknin. Prolonged stimuli alter the bacterial chemosensory clusters. *Mol. Microbiol.*, 88(3):634–644, 2013.

[237] Jeffrey E Segall, Michael D Manson, and Howard C Berg. Signal processing times in bacterial chemotaxis. *Nature*, 296(5860):855, 1982.

[238] Victor Sourjik and Howard C Berg. Binding of the escherichia coli response regulator chey to its target measured in vivo by fluorescence resonance energy transfer. *Proceedings of the National Academy of Sciences*, 99(20):12669–12674, 2002.

[239] Johannes M Keegstra, Keita Kamino, François Anquez, Milena D Lazova, Thierry Emonet, and Thomas S Shimizu. Phenotypic diversity and temporal variability in a bacterial signaling network revealed by single-cell fret. *ELife*, 6:e27455, 2017.

[240] Remy Colin, Christelle Rosazza, Ady Vaknin, and Victor Sourjik. Multiple sources of slow activity fluctuations in a bacterial chemosensory network. *ELife*, 6:e26796, 2017.

[241] Annette H Erbse and Joseph J Falke. The core signaling proteins of bacterial chemotaxis assemble to form an ultrastable complex. *Biochemistry*, 48(29):6975–6987, 2009.

[242] Ekaterina Korobkova, Thierry Emonet, Jose MG Vilar, Thomas S Shimizu, and Philippe Cluzel. From molecular noise to behavioural variability in a single bacterium. *Nature*, 428(6982):574, 2004.

[243] Franziska Matthäus, Marko Jagodič, and Jure Dobnikar. E. coli superdiffusion and chemotaxis—search strategy, precision, and motility. *Biophysical journal*, 97(4):946–957, 2009.

[244] Marlo Flores, Thomas S Shimizu, Pieter Rein ten Wolde, and Filipe Tostevin. Signaling noise enhances chemotactic drift of e. coli. *Physical review letters*, 109(14):148101, 2012.

[245] Mingshan Li and Gerald L Hazelbauer. Cellular stoichiometry of the components of the chemotaxis signaling complex. *Journal of bacteriology*, 186(12):3687–3694, 2004.

[246] Hanna Salman and Albert Libchaber. A concentration-dependent switch in the bacterial response to temperature. *Nature cell biology*, 9(9):1098, 2007.

[247] Yevgeniy Kalinin, Silke Neumann, Victor Sourjik, and Mingming Wu. Responses of escherichia coli bacteria to two opposing chemoattractant gradients depend on the chemoreceptor ratio. *Journal of bacteriology*, 192(7):1796–1800, 2010.

[248] Moriah Koler, Eliran Peretz, Chetan Aditya, Thomas S. Shimizu, 2, and Ady Vaknin. Long-term positioning and polar preference of chemoreceptor clusters in *E. coli*. *Nature Communications*, *in press*, 2018.

[249] Victor Sourjik and Howard C Berg. Receptor sensitivity in bacterial chemotaxis. *Proceedings of the National Academy of Sciences*, 99(1):123–127, 2002.

[250] Victor Sourjik, Ady Vaknin, Thomas S Shimizu, and Howard C Berg. [17]-in vivo measurement by fret of pathway activity in bacterial chemotaxis. *Methods in enzymology*, 423:365–391, 2007.

[251] Makio Tokunaga, Naoko Imamoto, and Kumiko Sakata-Sogawa. Highly inclined thin illumination enables clear single-molecule imaging in cells. *Nature methods*, 5(2):159–161, 2008.

[252] Michael J Rust, Mark Bates, and Xiaowei Zhuang. Sub-diffraction-limit imaging by stochastic optical reconstruction microscopy (storm). *Nature methods*, 3(10):793–796, 2006.

[253] Max Born and Emil Wolf. *Principles of optics: electromagnetic theory of propagation, interference and diffraction of light*. CUP Archive, 2000.

[254] Travis J Gould, Vladislav V Verkhusha, and Samuel T Hess. Imaging biological structures with fluorescence photoactivation localization microscopy. *Nature protocols*, 4(3):291–308, 2009.

[255] Jean-Christophe Olivo-Marin. Extraction of spots in biological images using multiscale products. *Pattern recognition*, 35(9):1989–1996, 2002.

[256] Russell E Thompson, Daniel R Larson, and Watt W Webb. Precise nanometer localization analysis for individual fluorescent probes. *Biophysical journal*, 82(5):2775–2783, 2002.

[257] Bo Zhang, Josiane Zerubia, and Jean-Christophe Olivo-Marin. Gaussian approximations of fluorescence microscope point-spread function models. *Applied Optics*, 46(10):1819–1829, 2007.

[258] Kim I Mortensen, L Stirling Churchman, James A Spudich, and Henrik Flyvbjerg. Optimized localization analysis for single-molecule tracking and super-resolution microscopy. *nature methods*, 7(5):377–381, 2010.

[259] Paolo Annibale, Stefano Vanni, Marco Scarselli, Ursula Rothlisberger, and Aleksandra Radenovic. Quantitative photo activated localization microscopy: unraveling the effects of photoblinking. *PloS one*, 6(7):e22678, 2011.

[260] P Annibale, M Scarselli, A Kodiyan, and A Radenovic. Photoactivatable fluorescent protein meos2 displays repeated photoactivation after a long-lived dark state in the red

photoconverted form. *The Journal of Physical Chemistry Letters*, 1(9):1506–1510, 2010.

[261] Xavier Michalet. Mean square displacement analysis of single-particle trajectories with localization error: Brownian motion in an isotropic medium. *Phys. Rev. E - Stat. Nonlinear, Soft Matter Phys.*, 82(4):1–13, 2010.

[262] Andrew J. Berglund. Statistics of camera-based single-particle tracking. *Phys. Rev. E*, 82(1):011917, 2010.

[263] Elias M Puchner, Jessica M Walter, Robert Kasper, Bo Huang, and Wendell A Lim. Counting molecules in single organelles with superresolution microscopy allows tracking of the endosome maturation trajectory. *Proceedings of the National Academy of Sciences*, 110(40):16015–16020, 2013.

[264] R. M. Zucker. Quality Assessment of Confocal Microscopy Slide Based Systems: Performance. *J. Int. Soc. Anal. Cytol.*, 69(A):659–676, 2006.

[265] Silke Neumann, Linda Løvdok, Kajetan Bentele, Johannes Meisig, Ekkehard Ullner, Ferencz S. Paldy, Victor Sourjik, and Markus Kollmann. Exponential signaling gain at the receptor level enhances signal-to-noise ratio in bacterial chemotaxis. *PLoS One*, 9(4):1–11, 2014.

[266] Ady Vaknin and Howard C Berg. Osmotic stress mechanically perturbs chemoreceptors in escherichia coli. *Proceedings of the National Academy of Sciences*, 103(3):592–596, 2006.

[267] Dirk Landgraf, Burak Okumus, Peter Chien, Tania A Baker, and Johan Paulsson. Segregation of molecules at cell division reveals native protein localization. *Nature methods*, 9(5):480, 2012.

[268] Mingshu Zhang, Hao Chang, Yongdeng Zhang, Junwei Yu, Lijie Wu, Wei Ji, Juanjuan Chen, Bei Liu, Jingze Lu, Yingfang Liu, et al. Rational design of true monomeric and bright photoactivatable fluorescent proteins. *Nature methods*, 9(7):727–729, 2012.

[269] S. Wang, J. R. Moffitt, G. T. Dempsey, X. S. Xie, and X. Zhuang. Characterization and development of photoactivatable fluorescent proteins for single-molecule-based superresolution imaging. *Proc. Natl. Acad. Sci.*, 111(23), may 2014.

[270] Tamas Gaal, Benjamin P. Bratton, Patricia Sanchez-Vazquez, Alexander Sliwicki, Kristine Sliwicki, Andrew Vegel, Rachel Pannu, and Richard L. Gourse. Colocalization

of distant chromosomal loci in space in E. coli: a bacterial nucleolus. *Genes Dev.*, 30(20):2272–2285, 2016.

[271] Martial Marbouty, Antoine Le Gall, Diego I. Cattoni, Axel Cournac, Alan Koh, Jean-Bernard Fiche, Julien Mozziconacci, Heath Murray, Romain Koszul, and Marcelo Nollmann. Condensin- and Replication-Mediated Bacterial Chromosome Folding and Origin Condensation Revealed by Hi-C and Super-resolution Imaging. *Mol. Cell*, 59(4):588–602, 2015.

[272] Tung B K Le, Maxim V Imakaev, Leonid a Mirny, and Michael T Laub. High-Resolution Mapping of the Spatial Organization of a Bacterial Chromosome. *Science*, 731, oct 2013.

[273] Virginia S. Lioy, Axel Cournac, Martial Marbouty, Stéphane Duigou, Julien Mozziconacci, Olivier Espéli, Frédéric Boccard, and Romain Koszul. Multiscale Structuring of the E. coli Chromosome by Nucleoid-Associated and Condensin Proteins. *Cell*, pages 1–13, 2018.

[274] JM Van Helvoort, J Kool, and CL Woldringh. Chloramphenicol causes fusion of separated nucleoids in escherichia coli k-12 cells and filaments. *Journal of bacteriology*, 178(14):4289–4293, 1996.

[275] Julio E. Cabrera and Ding J. Jin. Active transcription of rRNA operons is a driving force for the distribution of RNA polymerase in bacteria: Effect of extrachromosomal copies of rrnB on the in vivo localization of RNA polymerase. *J. Bacteriol.*, 188(11):4007–4014, 2006.

[276] Martin Thanbichler and Lucy Shapiro. Chromosome organization and segregation in bacteria. *J. Struct. Biol.*, 156(2):292–303, nov 2006.

[277] Xindan Wang, Paula Montero Llopis, and David Z Rudner. Organization and segregation of bacterial chromosomes. *Nat. Rev. Genet.*, 14(3):191–203, feb 2013.

[278] Elizabeth a Libby, Manuela Roggiani, and Mark Goulian. Membrane protein expression triggers chromosomal locus repositioning in bacteria. *Proc. Natl. Acad. Sci. U. S. A.*, 109(19):7445–50, may 2012.

[279] Nick Gilbert and James Allan. Supercoiling in DNA and chromatin. *Curr. Opin. Genet. Dev.*, 25(1):15–21, 2014.

[280] Mahdi Golkaram, Stefan Hellander, Brian Drawert, and Linda R. Petzold. Macromolecular Crowding Regulates the Gene Expression Profile by Limiting Diffusion. *PLoS Comput. Biol.*, 12(11):1–16, 2016.

[281] Cheemeng Tan, Saumya Saurabh, Marcel P. Bruchez, Russell Schwartz, and Philip Leduc. Molecular crowding shapes gene expression in synthetic cellular nanosystems. *Nat. Nanotechnol.*, 8(8):602–608, 2013.

[282] Robert S Fuller, Jon M Kaguni, and Arthur Kornberg. Enzymatic replication of the origin of the Escherichia coli chromosome (oriC plasmids/dnaA gene/DNA replication). *Biochemistry*, 78(12):7370–7374, 1981.

[283] E. Sokolova, E. Spruijt, M. M. K. Hansen, E. Dubuc, J. Groen, V. Chokkalingam, A. Piruska, H. A. Heus, and W. T. S. Huck. Enhanced transcription rates in membrane-free protocells formed by coacervation of cell lysate. *Proc. Natl. Acad. Sci.*, 110(29):11692–11697, 2013.

[284] Tyler N. Shendruk, Martin Bertrand, Hendrick W. De Haan, James L. Harden, and Gary W. Slater. Simulating the entropic collapse of coarse-grained chromosomes. *Biophys. J.*, 108(4):810–820, 2015.

[285] Chanil Jeon, Youngkyun Jung, and Bae Yeun Ha. A ring-polymer model shows how macromolecular crowding controls chromosome-arm organization in Escherichia coli. *Sci. Rep.*, 7(1):1–10, 2017.

[286] M. Schaechter, O. MaalOe, and N. O. Kjeldgaard. Dependency on Medium and Temperature of Cell Size and Chemical Composition during Balanced Growth of Salmonella typhimurium. *J. Gen. Microbiol.*, 19(3):592–606, 1958.

[287] M. Scott, S. Klumpp, E. M. Mateescu, and T. Hwa. Emergence of robust growth laws from optimal regulation of ribosome synthesis. *Mol. Syst. Biol.*, 10(8):747–747, 2014.

[288] Teuta Pilizota and Joshua W. Shaevitz. Plasmolysis and cell shape depend on solute outer-membrane permeability during hyperosmotic shock in E. coli. *Biophys. J.*, 104(12):2733–2742, 2013.

[289] Renata Buda, Yunxiao Liu, Jin Yang, Smitha Hegde, Keiran Stevenson, Fan Bai, and Teuta Pilizota. Dynamics of Escherichia coli 's passive response to a sudden decrease in external osmolarity. *Proc. Natl. Acad. Sci.*, 113(40):E5838–E5846, 2016.

[290] Suckjoon Jun and Bela Mulder. Entropy-driven spatial organization of highly confined polymers: lessons for the bacterial chromosome. *Proc. Natl. Acad. Sci. U. S. A.*, 103(33):12388–93, 2006.

[291] Debasish Chaudhuri and Bela M. Mulder. Spontaneous helicity of a polymer with side loops confined to a cylinder. *Phys. Rev. Lett.*, 108(26):1–5, 2012.

[292] Renko De Vries. DNA condensation in bacteria: Interplay between macromolecular crowding and nucleoid proteins. *Biochimie*, 92(12):1715–1721, 2010.

[293] Conrad L Woldringh, Peter Ruhdal Jensen, and Hans V Westerhoff. Structure and partitioning of bacterial dna: determined by a balance of compaction and expansion forces? *FEMS microbiology letters*, 131(3):235–242, 1995.

[294] R. T. Dame. H-NS mediated compaction of DNA visualised by atomic force microscopy. *Nucleic Acids Res.*, 28(18):3504–3510, 2000.

[295] Anna S. Wegner, Kathelijne Wintraecken, Roberto Spurio, Conrad L. Woldringh, Renko de Vries, and Theo Odijk. Compaction of isolated Escherichia coli nucleoids: Polymer and H-NS protein synergetics. *J. Struct. Biol.*, 194(1):129–137, 2016.

[296] Chanil Jeon, Juin Kim, Hawoong Jeong, Youngkyun Jung, and Bae-Yeun Ha. Chromosome-like organization of an asymmetrical ring polymer confined in a cylindrical space. *Soft Matter*, 11(41):8179–8193, 2015.

[297] Ryan P. Joyner, Jeffrey H. Tang, Jonne Helenius, Elisa Dultz, Christiane Brune, Liam J. Holt, Sebastien Huet, Daniel J. Müller, and Karsten Weis. A glucose-starvation response regulates the diffusion of macromolecules. *Elife*, 5(MARCH2016):1–26, 2016.

[298] Peter R Cook. Predicting three-dimensional genome structure from transcriptional activity. *Nature genetics*, 32(3):347, 2002.

[299] Ulrike Dinnbier, Eva Limpinsel, Roland Schmid, and Evert P Bakker. Transient accumulation of potassium glutamate and its replacement by trehalose during adaptation of growing cells of escherichia coli k-12 to elevated sodium chloride concentrations. *Archives of Microbiology*, 150(4):348–357, 1988.

[300] Bettina Kempf and Erhard Bremer. Uptake and synthesis of compatible solutes as microbial stress responses to high-osmolality environments. *Archives of microbiology*, 170(5):319–330, 1998.

[301] Teuta Pilizota and Joshua W Shaevitz. Fast, multiphase volume adaptation to hyperosmotic shock by escherichia coli. *PLoS One*, 7(4):e35205, 2012.

[302] HE Kubitschek. Constancy of the ratio of dna to cell volume in steady-state cultures of escherichia coli br. *Biophysical journal*, 14(2):119, 1974.

[303] D Scott Cayley, Harry J Guttman, and M Thomas Record Jr. Biophysical characterization of changes in amounts and activity of escherichia coli cell and compartment water and turgor pressure in response to osmotic stress. *Biophysical Journal*, 78(4):1748–1764, 2000.

[304] Teuta Pilizota and Joshua W. Shaevitz. Origins of escherichia coli growth rate and cell shape changes at high external osmolality. *Biophys. J.*, 107(8):1962–1969, 2014.

[305] Cedric Cagliero and Ding Jun Jin. Dissociation and re-association of RNA polymerase with DNA during osmotic stress response in Escherichia coli. *Nucleic Acids Res.*, 41(1):315–326, 2013.

[306] Vittore F Scolari and Marco Cosentino Lagomarsino. Combined collapse by bridging and self-adhesion in a prototypical polymer model inspired by the bacterial nucleoid. *Soft Matter*, 11(9):1677–87, 2015.

[307] D. Joseph Clark and O. Maaløe. DNA replication and the division cycle in Escherichia coli. *J. Mol. Biol.*, 23(1):99–112, 1967.

[308] Luc Vincent, Luc Vincent, and Pierre Soille. Watersheds in Digital Spaces: An Efficient Algorithm Based on Immersion Simulations. *IEEE Trans. Pattern Anal. Mach. Intell.*, 13(6):583–598, 1991.

[309] Hu Cang, Anna Labno, Changgui Lu, Xiaobo Yin, Ming Liu, Christopher Gladden, Yongmin Liu, and Xiang Zhang. Probing the electromagnetic field of a 15-nanometre hotspot by single molecule imaging. *Nature*, 469(7330):385–388, 2011.

[310] Michael J Rust, Mark Bates, and Xiaowei Zhuang. Sub-diffraction-limit imaging by stochastic optical reconstruction microscopy (STORM). *Nat. Methods*, 3(10):793–795, 2006.